TECHNISCHE UNIVERSITÄT MÜNCHEN

Lehrstuhl und Prüfamt für
Grundbau, Bodenmechanik, Felsmechanik und Tunnelbau

Time-dependent compression behaviour of sands under oedometric conditions

Friedrich Christoph Levin

Vollständiger Abdruck der von der Ingenieurfakultät Bau Geo Umwelt der Technischen Universität München zur Erlangung des akademischen Grades eines

Doktor-Ingenieurs

genehmigten Dissertation.

Vorsitzender: Prof. Dr.-Ing. habil. Christian U. Große

Prüfer der Dissertation:

1. Prof. Dr.-Ing. Roberto Cudmani
2. Prof. Dr.-Ing. habil. Torsten Wichtmann
3. Prof. Itai Einav, Ph.D.

Die Dissertation wurde am 22.07.2020 bei der Technischen Universität München eingereicht und durch die Ingenieurfakultät Bau Geo Umwelt am 04.02.2021 angenommen.

Preface of the Editor

Friedrich Levin's research was motivated by the necessity of predicting time-delayed deformation of dumps in the Renish lignite mining area near Cologne, Germany. These dumps consist of silty to gravelly sands with a thickness of several hundred meters and show increase of settlements over decades, which affect the serviceability of infrastructure founded on them. The time-dependent deformations result mainly from the pseudo-viscous properties of the sands. Although rate-effects are usually disregarded in natural coarse-grained soils, their consideration can be crucial in man-made deposits as open cast mining dumps, tailings and landfills. Other than the rate-dependent behaviour of soft soils, which has been extensively investigated in the literature, the viscous behaviour of granular soils is in the focus of current research and has not been fully understood yet. So far, constitutive models for unified simulation of creep, relaxation and rate dependency are not available.

Friedrich's critical analysis of the experimental data from the literature is comprehensive and demonstrates the complexity of the research topic. The experimental contribution of Friedrich is outstanding and includes the investigation of the rate-dependent behaviour under oedometric conditions, including sands with different fine contents, different pressures and densities as well as different loading boundary conditions. Such a comprehensive database is so far unique in this topic. Meticulously, Friedrich investigates inaccuracy sources related to soil sample preparation, assesses errors of the measurements and demonstrates the repeatability of the experimental results. He shows the distinctive features of the rate-dependent behaviour of coarse granular soils and the shortcomings and limitations of available fine-grained models to capture them.

Friedrich's experimental effort does not finish in the lab. He analyses available time-settlement measurements on dumps in the Renish lignite mining area near Cologne and derives creep coefficients from the field data, which agrees reasonably well with the lab values. The fact that stagnation of creep strains occurs after few days in the lab, while it is not observed in the field data even after several years could not be conclusively explained and remains an open question for future research. Based on this unique experimental database, he develops and validates a numerical model to predict the time-delayed settlements of sandy dumps of the Renish lignite mining area using an elasto-visco-plastic constitutive model for fine-grained soils.

Owing to the huge effort and the time required to plan, carry out, evaluate and interpret the experiments in the lab and the field, Friedrich does not manage to develop a constitutive model to simulate all the distinctive features of behaviour of coarse-grained soils observed in the laboratory, but he establishes a comprehensive base for their future developments.

With his research, Friedrich has made an important contribution to better understanding the rate-dependent behaviour of granular soils. In the era of digitalization and computer simulations, Friedrich's work demonstrates once more the fundamental role of experimental research, especially of laboratory testing in modern geotechnical engineering.

Roberto Cudmani

Abstract

The time-dependent behaviour of sands is studied using oedometric loading tests. It is tested with respect to creep, strain rate dependency and stress relaxation. The soil type, the density, the stress level and the loading strain rate are varied. The tests reveal stress and density dependent creep behaviour, different rate dependent responses ranging from temporary rate effects to permanent rate effects and stress relaxation, which is stress-dependent but independent of the relative density of the sands. Stress relaxation is more pronounced in clean sands than creep. Viscous behaviour of sands cannot be described by the classical isotache-concept. Long-term field measurements on open cast mining dumps in the Renish lignite mining area are evaluated to study the creep behaviour of sands in the field. The field measurements are compared to the laboratory test results. Creep in the laboratory is about 50% smaller than in the field. A method to determine creep-coefficients describing the creep deformations in the field using laboratory test results and data about the in situ relative density is presented. Three constitutive models are reviewed with respect to their capabilities of modelling the stress and time-dependent compression behaviour of sands. A modified version of the visco-hypoplastic model after GUDEHUS (2004) can predict the stress and density dependent compression creep behaviour of sands in element tests using a constant viscosity index I_v. However, none of the reviewed models can simulate all experimentally observed viscous behaviours of sand. A finite element implementation of the Soft Soil Creep model after VERMEER & NEHER (1999) is used to study its capabilities for modelling the creep settlements of open cast mines in the Renish lignite mining area. The requirements within the boundary value problem for successful prediction of the creep settlements and the limitations of the model are discussed.

Keywords: Sand, viscosity, creep, rate dependency, stress relaxation, open cast mine, dump.

Kurzfassung

Das zeitabhängige Verhalten von Sanden wird mittels Ödometerversuchen untersucht. Dabei werden Kriechen, Ratenabhängigkeit und Spannungsrelaxation betrachtet. Die Bodenart, die Dichte, das Spannungsniveau und die Belastungsdehnungsrate werden variiert. Die Versuche zeigen ein spannungs- und dichteabhängiges Kriechverhalten, unterschiedliche geschwindigkeitsabhängige Reaktionen von temporären Geschwindigkeitseffekten bis hin zu permanenten Geschwindigkeitseffekten und Spannungsrelaxation, die zwar spannungsabhängig, aber unabhängig von der relativen Dichte der Sande ist. Die Spannungsrelaxation ist bei reinen Sanden stärker ausgeprägt als das Kriechen. Das viskose Kompressionsverhalten von Sanden kann nicht mit dem klassischen Isotachenmodell beschrieben werden. Zur Untersuchung des Kriechverhaltens von Sanden im Feld werden langfristige Feldmessungen an Tagebaukippen im Rheinischen Braunkohlerevier ausgewertet. Die Feldmessungen werden mit den Ergebnissen der Laborversuche verglichen. Das Kriechen im Labor ist in etwa 50% geringer als im Feld. Eine Methode zur Bestimmung von Kriechbeiwerten, die die Kriechverformungen im Feld beschreiben, anhand von Laborversuchsergebnissen und Daten zur relativen Dichte in situ wird vorgestellt. Drei Stoffmodelle werden im Hinblick auf ihre Fähigkeiten zur Modellierung des spannungs- und zeitabhängigen Kompressionsverhaltens von Sanden überprüft. Eine modifizierte Version des visko-hypoplastischen Modells nach GUDEHUS (2004) kann das spannungs- und dichteabhängige Kompressions- und Kriechverhalten von Sanden in Elementversuchen unter Verwendung eines konstanten Viskositätsindex I_v ermitteln. Keines der untersuchten Modelle kann jedoch alle experimentell beobachteten viskosen Verhaltensweisen von Sand simulieren. Eine Finite-Element-Implementierung des Soft Soil Creep Modells nach VERMEER & NEHER (1999) wird im Hinblick auf die Modellierung der Kriechsetzungen von Tagebauen im Rheinischen Braunkohlerevier verwendet. Die Voraussetzungen innerhalb des Randwertproblems zur erfolgreichen Vorhersage der Kriechsetzungen und die Grenzen des Modells werden diskutiert.

Schlagwörter: Sand, Viskosität, Kriechen, Ratenabhängigkeit, Spannungsrelaxation, Tagebau, Kippe.

Table of contents

Symbols

Latin symbols (A – Z)

Symbol	Name	Unit
B	index for saturation of the soil sample in triaxial testing	
B_p	breakage potential	
B_r	HARDIN's relative breakage factor	
B_t	total breakage	
c'	effective cohesion	Pa
C	oedometric creep-coefficient with reference to ε and $\ln()$	
C_α	oedometric creep-coefficient with reference to e and $\log_{10}$	
$C_{\alpha,ref}$	reference oedometric creep-coefficient	
$C_{\alpha,ref,0}$	reference oedometric creep-coefficient at the densest state	
C_B	BUISMAN creep-coefficient	
C_c	oedometric compression index with reference to e and $\log_{10}$	
C_c^*	curvature coefficient	
C_s	oedometric recompression index with reference to e and $\log_{10}$	
C_u	uniformity coefficient	
d	diameter	mm
$d_{Fe,min}$	minimum FERET diameter	mm
$d_{Fe,max}$	maximum FERET diameter	mm
D_R	relative density (reference to e_{min} and e_{max})	
D_r	reference strain rate	
d_{10}	diameters where 10% of the soil is finer	mm
d_{50}	diameters where 50% of the soil is finer	mm
e	void ratio	
$\dot{e}$	change of void ratio with time	1/s
e_c	critical state void ratio	
e_{c0}	critical state void ratio at zero stress	
e_d	void ratio at maximum density	
e_{d0}	void ratio at maximum density and zero stress	
e_i	void ratio and minimum density	
e_{i0}	void ratio and minimum density and zero stress	
e_{max}	maximum void ratio	

Symbol	Name	Unit
e^*_{max}	maximum void ratio determined by collapse method	
e_{min}	minimum void ratio	
E	energy	J
E_s	oedometric modulus	Pa
$E_{s,ref}$	reference oedometric modulus	Pa
e_0	initial void ratio	
F	force	N
f (Section 3.3.3)	ratio of shear strength and yield stress at contact points between grains	
f_b	stress dependency factor (barotropy)	
f_d	density dependency factor (pycnotropy)	
f_e	density dependency factor (pycnotropy)	
f_v	viscosity factor	
h_F	part of the pores of the coarse grained fraction filled with fine grained material	
h_{ini}	initial sample height	mm
h_s	granular hardness	Pa
h_{sr}	reference granular hardness	Pa
I_d	pressure-adjusted relative density	
I_v	viscosity index	
$I_{v,jumo}$	viscosity index from sudden strain rate jump	
$I_{v,relax}$	viscosity index from stress relaxation	
k_α	OSTERMAYER creep-coefficient	
K_0	earth pressure coefficient at rest	
$K_{0,nc}$	earth pressure coefficient at rest in normal consolidated state	
$K_{0,oc}$	earth pressure coefficient at rest in overconsolidated state	
M	gradient of critical state line	
m *(Section 3.2)*	OHDE exponent	
m (Section 3.3.1.2)	gradient of the creep curves in $\log\dot{\gamma}$ - $\log t$ - representation	
m (Section 6.2.3)	defines the loosest state isotropic compression curve as the reference isotropic compression curve	
n	exponent of the BAUER compression law	
n_G	porosity of the coarse-grained fraction	
p'	mean effective stress	Pa

Symbol	Name	Unit
p'_e	equivalent mean effective stress	Pa
p'_{ee}	equivalent stress on the reference isochrone τ_{ref}	Pa
p'^{eq}	equivalent mean effective stress	
p'^{eq}_e	equivalent mean effective stress on reference isochrone	Pa
p'^{eq}_{e0}	initial equivalent mean effective stress on reference isochrone	Pa
p'_{e0}	initial mean effective stress on reference isochrone	Pa
p'_{ref}	reference mean effective stress	
p'_0	initial mean effective stress	Pa
q	deviatoric stress	Pa
q_u (Section 3.3.3)	yield stress at contact points between grains	Pa
R	stress ratio	
R (Section 4.1.1)	radius of the sample	mm
R^2	coefficient of determination	
r_e	relative void ratio	
s (Section 3.3.3)	shear strength at contact points between grains	Pa
S	settlements	mm
S_F	parameter for the filling of the pores of the coarse grained fraction by fine grained material	
S_r	saturation	
t_{EOM}	time of end of measurements	s
t_{EOP}	time of end of primary consolidation	s
T_{max} (Section 3.3.3)	transferable tangential forces at grain contacts	N
t_{obs}	time of start of observation	s
t_{ref}	reference time	s
t^*_{ref}	$t^*_{ref} = t_{ref}$ for $t_{obs} \leq 20$ d and $t^*_{ref} = t_{obs}$ for $t_{obs} > 20$ d	s
t_{zero}	zero point in time where the dump can in average be considered to be in a normally consolidated state (usually the time of end of dumping)	s
t_0	start time	s
u	vertical displacement	mm
V_p	pore volume	m^3
V_s	solid volume	m^3
w	water content	
w_L	liquid limit	

Symbol	Name	Unit
w_P	plastic limit	

Greek symbols (α – ω)

Symbol	Name	Unit
α (hypoplasticity)	density dependency factor (pycnotropy)	
β	density dependency factor (pycnotropy)	
$\dot{\gamma}$	shear strain rate	1/s
γ	shear strain	
$\dot{\varepsilon}_a$	axial strain rate	1/s
ε_a	axial strain	
ε^e	elastic strain	
ε^{ir}	irreversible (plastic) strain	
ε^{pl}	plastic strain	
$\dot{\varepsilon}_r$	radial strain rate	1/s
ε_r	radial strain	
$\dot{\varepsilon}_v$	volumetric strain rate	1/s
ε_v	volumetric strain	
$\dot{\varepsilon}^{vis}$	viscous strain rate	1/s
ε^{vis}	viscous strain	
$\dot{\varepsilon}_1$	major principle strain rate	
$\dot{\varepsilon}_3$	minor principle strain rate	
η	dynamic viscosity	Pa · s
ω	exponent of stress dependency of C_α	
κ^0	BUTTERFIELD coefficient of oedometric un-/ reloading	
κ^*	BUTTERFIELD coefficient of isotropic un-/ reloading	
λ	virgin compression index referenced to ε and $\ln()$	
λ_σ	ratio of the second and third invariant of the tensor $\widehat{\boldsymbol{T}}$	
λ^*	BUTTERFIELD coefficient of isotropic virgin loading	
μ	friction coefficient between steel and soil	
μ^*	creep-coefficient in SSC	
ν^*	kinematic viscosity	m^2/s
ν_{ur}	POISSON's ratio	
ρ	density	g/cm^3
ρ_s	density of solid particles	g/cm^3
σ'	effective stress	Pa
$\dot{\sigma'}_a$	axial effective stress rate	Pa

Symbol	Name	Unit
σ'_a	axial effective stress	Pa
$\sigma'_{a,ref}$	reference axial effective stress	Pa
σ'_c	effective confining pressure	Pa
σ_f	splitting tensile stress of a grain	Pa
$\dot{\sigma}'_r$	radial effective stress rate	N/s
σ'_r	radial effective stress	Pa
σ'_0	initial effective stress	Pa
τ_p	time at the end of primary consolidation (used in SSC-model)	s
τ_{ref}	reference isochrone (used in SSC-model)	s
ϑ_0	grain contact friction angle	°
φ'	friction angle	°
φ_{cc}	critical state friction angle	°
χ_u	unevenness factor of grains	
ω	gradient of $C_{\alpha,ref}$ with r_e	

Acronyms (A – Z)

Acronym	Name
CPT	cone penetration test
CSL	critical state line
CRS	constant rate of strain
ChRS	tests with sudden changes in the strain rate
EOM	end of measurement
EOP	end of primary consolidation
FM	following measurement
GSD	grain size distribution
GPS	global positioning system
LC	load controlled
LCC	limiting compression curve
m.a.s.l.	meter above sea level
ML	continous monotonic loading
OCR	overconsolidation ratio
NCL	normal consolidation line
P&N	positive – negative
RCL	reference compression line
$RDNS$	roundness
SBT	soil behaviour type
SBTn	normalized soil behaviour type
SEM	scanning-electron-microscopy
$SPHT\_K$	sphericity
SSC	soft soil creep
$SYMM$	symmetry
TCD	drained triaxial compression tests
TESRA	temporary effect of strain rate and acceleration

Tensors

Symbol	Name
$\vec{\boldsymbol{B}}$	potential function for definition of the direction of the creep strains
$\boldsymbol{D}$	strain rate tensor
$\boldsymbol{D}^{e}$	elastic strain rate tensor
$\boldsymbol{D}^{vis}$	viscous strain rate tensor
$\boldsymbol{E}$	elastic stiffness tensor
$\boldsymbol{I}$	unit tensor
$\boldsymbol{L}$	“linear stiffness tensor”
$\boldsymbol{N}$	“non-linear stiffness tensor”
$\boldsymbol{T}$	CAUCHY stress tensor
$\dot{\boldsymbol{T}}$	stress rate tensor
$\widehat{\boldsymbol{T}}$	normalized stress tensor
$\widehat{\boldsymbol{T}}^{*}$	deviator tensor

1 Motivation

The motivation for this study originates from the necessity to realistically predict time-dependent deformations of open cast mining dumps in the Renish lignite mining area near Cologne (Germany). These dumps consist of silty to gravelly sands and show time-dependent settlements under nearly constant overburden stresses of several decimetres over decades. The settlements can severely affect the performance of buildings and infrastructure constructed on them (LANGE, 1986, KOTHEN & KNUFINKE, 1990, VOGT *et al.*, 2013, LEVIN & VOGT, 2015). As an example, Figure 1.1 shows the construction of highway A44n on the Garzweiler open cast mining dump near Cologne. The highway was constructed immediately after dumping ended and while the soils still had great deformation potential (VOGT *et al.*, 2013). The time-dependent deformations result mainly from the viscous properties of the sands. In analogy to the viscosity of fluids, which denotes the relationship between the flow resistance of a fluid and the flow velocity, the term “viscosity” in soil mechanics refers to the dependence of the “macroscopic” stress-strain behaviour of soils on the stress and strain rate. According to this definition, the observed time-dependence of soil results from soil viscosity.

Figure 1.1: Construction of highway A44n on Garzweiler open cast mining dump near Cologne (Germany), printed with permission of RWE Power AG

In geotechnical design viscous effects of undisturbed naturally deposited granular soils are small and can usually be disregarded for the solution of common geotechnical problems. Nevertheless, in some special cases, e.g. the already mentioned open cast mining dumps, the proper consideration of time-effects in granular soils is crucial to fulfil the requirements of the serviceability limit state. Examples of long-term creep deformations in granular soils were reported by CHARLES-CRUZ *et al.* (2008) for the case of mine tailings and by CUDMANI *et al.* (2011) for a pier of a container terminal founded on a 20 m thick sand layer, which was compacted by vibro-flotation-densification. It still showed an increase of deformations over time after several decades. OSTERMAYER (1976) observed significant creep deformations in one-dimensional compression tests on mixed-grained gravels. He emphasizes

the importance of such deformations for the design of permanent anchors or highly sensitive structures (GUDEHUS, 1974). Other applications where creep strains of granular soil can be significant are heavily loaded mono piles or pile groups.

Especially in soft soils, the time- and rate-dependent behaviour is pronounced and can have the decisive influence on a structure in the long-term, causing deformations or even failure (e.g. VOGT, 2017). Therefore, the scientific investigations of these mechanisms already started in the first half of the 20th century (BUISMAN, 1936) and the rate-dependent behaviour is nowadays well understood. On a microscale, viscosity of soft fine grained soils is based on thermally activated processes, which can be described with the "rate process theory" originally developed for metals by GLASSTONE *et al.* (1941). The macroscopic viscous behaviour can be described using the law by NORTON (1929) and the isotache-concept by ŠUKLJE (1957) in the framework of elasto-viscoplastic or visco-hypoplastic constitutive models.
On the contrary, the viscous behaviour of granular soils is not yet well understood. Until now the modelling of the viscous effects of creep, relaxation and rate dependency within a unified constitutive model is not possible. The mechanisms behind the viscous behaviour of granular soils are fundamentally different from those of fine grained soils. According to experimental evidence found in the literature, the main driving mechanism of time-dependence in coarse grained soils is the degradation of contacts and grains, which is also called "static fatigue". This study may serve to better understand the viscous behaviour of granular soils.

All properties of soil undergo changes with time. They can affect the stiffness, the strength or the hydraulic conductivity and are strongly influenced by its viscous properties of soil. They are usually referred to as ageing in engineering time scales. Nowadays, the improvement of mechanical soil properties due to ageing cannot be predicted reliably and therefore, they are mostly disregarded in geotechnical engineering design. However, the consideration of ageing can be important in the context of the control of compaction (e.g. vibro-compaction) or for the verification of the capacity of offshore piles (KARLSRUD, 2012). It is widely accepted that both viscosity and ageing are based on similar mechanisms at the micro-scale and for this reason, there must be a link between soil viscosity and ageing effects (e.g. MESRI *et al.*, 1990, SCHMERTMANN, 1991, MITCHELL, 2008). If this link exists, measuring viscous effects can be the key to predict ageing. This study may serve as a basis of experimental data for further investigations on the relation between ageing and viscous properties of granular soils.

2 Introduction

The objective of this study is to better understand the time-dependent behaviour of granular soils on a micro- and a macroscale. Until now, research on time-dependent behaviour of granular soil has been focussed on one of the three characteristics of soil viscosity, i.e. creep, rate dependency or stress relaxation, analysing them separately. Creep is defined as the change of volumetric or shear deformations under constant effective stress. Rate dependency describes the reaction of the soil and especially of the stress-strain-response to different deformation- or loading-rates. And stress-relaxation – a change in stress over time – is a special type of rate-dependent behaviour in the case of zero strain rate.
This study looks on the one hand at the driving mechanisms of the time-dependent behaviour on the particle level and investigates the soil behaviour using oedometric element tests with respect to creep, rate-dependency and stress relaxation under different boundary conditions. On the other hand, the experimental findings from the laboratory are compared to the long-term deformation measurements from open cast mining dumps and the rather well known behaviour of soft soils. A major challenge for predicting the time-dependent behaviour of dumps is to derive the correct constitutive model parameters. It is known from experience that the time-dependent deformation behaviour of the dumped soils observed in laboratory testing is significantly different from the behaviour determined from long-term field measurements. A link between the field measurements and the laboratory test results is established and a concept is provided to determine the constitutive model parameters for the time-dependent behaviour from laboratory tests in case no long-term field measurements are available for calibration. Limitations of three existing constitutive models by VERMEER & NEHER (1999), NIEMUNIS (2002) and GUDEHUS (2004), which were developed on the basis of soft fine grained soil behaviour, when modelling the viscous behaviour of granular soils, are shown.

The investigation is structured as follows:
Section 3 reviews the findings from literature. The degradation of grains and the arrangement of the soil skeleton are key to understanding viscous effects in granular soil. The findings on the description and the influence of grain shape and soil skeleton properties are summarized. Furthermore, definitions of state parameters from literature describing the stress and density state of soils for rate-independent and rate-dependent materials are presented. The literature review on the time-dependent soil response addresses the viscous phenomena of creep and rate dependency, including relaxation. The findings from literature made in element testing are summarized prior to focussing on the micromechanical processes behind the viscous behaviour of granular soils. A short summary on ageing and the link to granular soil viscosity is given. Finally, the methods for analytical description of viscous behaviour are addressed extensively.

The laboratory test program presented in Section 4 was limited to oedometric compression tests. It included creep tests, constant strain-rate compression tests, tests with sudden changes in loading strain rate and relaxation tests as well as combined tests, in which multiple test conditions were

realized during the same test. The experiments involved several different sand types and varying states of initial relative density and degree of water-saturation. The test results are compared to one another and set in reference to fine grained soil behaviour known from literature. The applicability of well-established analytical approaches for the description of viscous behaviour presented in Section 3 is investigated and a relationship is proposed to describe the creep behaviour of granular soils including the stress- and density-dependency.

In Section 5, the evolution of deformations over time in open cast mining dumps in the Renish lignite mining area consisting of sands are analyzed. Different conditions influencing the deformation behaviour and its evaluation like the age, the thickness and the starting point of measurements after the end of dumping and duration of the measurements are assessed. Data from level gauges on the dump surface and data from level gauges in depths of up to 77 m below the dump surface as well as data from hydrostatic measurement lines in different depths of the dump are used for the analysis. A concept for determination of the creep-coefficient from field measurement data is introduced. The deformation measurement data from the field are compared to laboratory test results. It is shown how creep-coefficients for describing the time-dependent deformation behaviour of dumps can be determined using laboratory test results in combination with information about the in situ relative density of the dumped soils, without relying on long-term in situ deformation measurements.

Several constitutive models exist, which can simulate the viscous effects of creep, rate dependency and relaxation of soft fine grained soils. Most of them are based on the isotache-concept developed by ŠUKLJE (1957). In Section 6, three of these models are presented and their fundamentals are reviewed, compared and set into relation to the findings from laboratory tests presented in Section 4. The material models proposed by NIEMUNIS (2002) and GUDEHUS (2004) are based on the theory of visco-hypoplasticity, whereas the material model developed by VERMEER & NEHER (1999) is based on the theory of elasto-viscoplasticity. The material model proposed by GUDEHUS is subsequently modified for the simulation of the time-dependent compression behaviour of granular soils. Furthermore, prerequisites for the realistic modelling of the time-dependent dump deformations with the isotache-model for soft soils after VERMEER & NEHER (1999) are discussed.

3 A review of time- and stress-dependent deformation behaviour of granular soils

Deformations of granular materials result from the rearrangement of grains triggered and influenced by static and dynamic stress changes, water content variability, chemical processes and temperature fluctuations as the most important factors (MITCHELL & SOGA, 2005). From a geotechnical point of view, deformations caused by changes in the stress state, are the most significant. Deformations can be subdivided into instantaneous deformations and time-delayed deformations due to consolidation or deformations caused by viscous effects. Microscopically the deformation of granular soil results from the deformation of the particles themselves and the relative movements between particles (translation and rotation). Deformation of particles is defined as strain of the grains including grain degradation and breakage. Additionally, relative movements of the grains among each other and their rotation lead to deformation. Which deformation process dominates, depends on the one hand on granulometric properties of the grains like grain strength and on the other hand on state parameters of the assembly like density, structure, current stress state, particle shape and breakage taking into account the grains size distribution.
Previous studies have shown that the deformation mechanisms in fine grained and coarse grained soils are different, especially the processes dominating the time-dependent behaviour. In granular soils the viscous properties are influenced by the soil skeleton properties like particle shape, stiffness and strength and also by the state of the soil. Therefore, this section firstly addresses the different soil skeleton properties as well as state variables. It then describes the compression and swelling as well as the time-dependent deformation behaviour of granular soils from a macroscopic and from a microscopic point of view. Finally, the state of the art of the analytical description of viscous behaviour under oedometric conditions is summarized.

3.1 Granular soil skeletons

Granular soils are here defined as gravels, sands and non-plastic silts as well as mixtures of them. The deformation behaviour of any granular soil is primarily governed by the properties of its skeleton and its state in terms of density and stress and besides that by the liquid and gaseous phases within the assembly. The soil skeleton properties are mainly determined by particle size, shape, surface texture and size distribution. The mineral composition of the grains determines their strength and resistance to breakage due to loading or weathering. The interactions between grains are predominantly governed by mechanical contact-forces. Physicochemical repulsive and attractive forces are relatively small. Their relevance is highly dependent on the grain size and they only begin to exert a distinct influence on the behaviour when particle size reduces to 2 μm or less, i.e. in fine grained soils (MITCHELL & SOGA, 2005). Since the smallest particle size within the analyzed soils in this study is greater than 6 μm, the influence of physicochemical interparticle forces can be neglected.

3.1.1 Grain size distribution, grain breakage and degradation

Grain breakage or degradation and the change of the grain size distribution (GSD) during creep and during loading are considered important mechanisms of the viscous behaviour of granular soils. The GSD is described by cumulative curves showing the mass-percentage of the soil passing a certain grain diameter (i.e. sieve). The curves can be described by characteristic parameters like the uniformity coefficient C_u, the curvature coefficient $C_c{}^*$ or the diameters d_{50} and d_{10} where 50% and 10% of the soil are finer, respectively. The characteristics of a GSD can change due to breakage during loading or creep, as it will be shown in the element test results in Section 4. Particle damage was categorized by MESRI & VARDHANABHUTI (2009) as

– level I damage (abrasion or grinding of asperities),
– level II damage (breaking or crushing of particle surface protrusions and particle corners / edges) and
– level III damage (fracturing, splitting or shattering of particles).

These three descriptive terms will be later on used in this study. Breakage will be analyzed in this study by means of HARDIN's relative breakage factor B_r (HARDIN, 1985). B_r is defined as

$$B_r = \frac{B_t}{B_p}, \tag{3.1}$$

where B_t is the total breakage and B_p is the breakage potential (cf. Figure 3.1). B_p represents the area between the original gradation curve and the 0.074 mm sieve and B_t represents the area between the original and final gradation curve. B_r can vary between 0 (no breakage) and 1 (full breakage). The sieve 0.074 mm applied by HARDIN corresponds to the boundary between sand and silt according to the ASTM standard D6913. In this study, the breakage potential B_p will be determined by the area between the gradation curve and the 0.063 mm sieve, since this is the sand silt boundary used in the European standard DIN EN ISO 17892-4. Breakage is analyzed in high pressure compression and creep tests in Section 4.9.2.

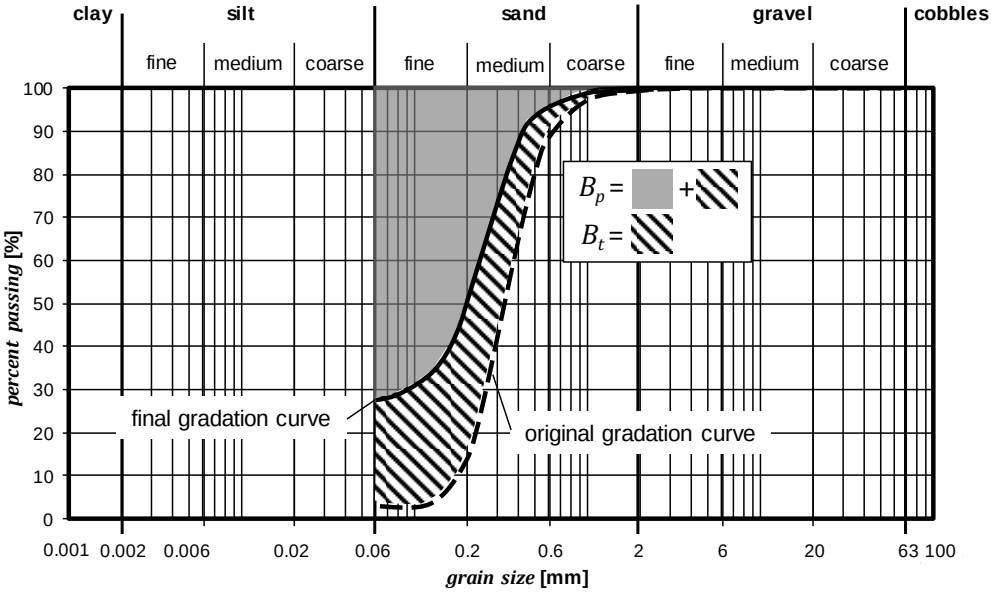

Figure 3.1: Determination of breakage potential B_p and total breakage B_t by HARDIN (1985)

3.1.2 Particle shape

The grain shape influences mechanical properties of soil, including compressibility, small-strain modulus, packing density, shear strength and viscous properties (MIURA *et al.*, 1997, MIURA *et al.*, 1998, CHO *et al.*, 2006, ENOMOTO *et al.*, 2009, CAVARRETTA *et al.*, 2017, MICHALOWSKI *et al.*, 2018). The description of the grain shape can be categorized into three different scales (cf. Figure 3.2):

– Morphology of the grains (large scale),
– roundness (intermediate scale) and
– surface texture (small scale).

Different descriptive parameters exist for each of these scales.

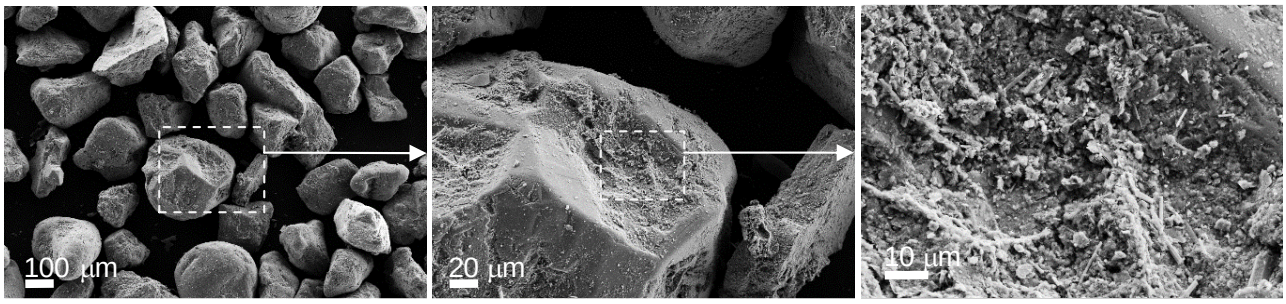

large scale (morphology) (magnification 50x) | intermediate scale (roundness) (magnification 200x) | small scale (surface texture) (magnification 1000x)

Figure 3.2: Scanning electron microscopy of medium quartz sand visualizing the scales of grain shape description [1]

Objectivity is not always easy to achieve when describing the grain shape, because it is very common to analyze the shape in the large and intermediate scale by comparing the grain appearance with tabulated grain outlines (POWERS, 1953 or KRUMBEIN & SLOSS, 1963). This method is subjective and shows large scattering in the determined shapes, depending on the individual person performing the classification (HRYCIW *et al.*, 2016). Another problem of describing the shape is the statistical representativeness of the analyzed grains, since the examination by means of a microscope is very cumbersome for a large number of particles. Nevertheless, modern optical methods allow for a great number of particles to be analyzed with respect to the large and intermediate scale. This was done in this study by means of a Camsizer©[2] (MOORE *et al.*, 2000). The parameters used in this study are the sphericity and roundness defined by KRUMBEIN & SLOSS (1963) as well as the symmetry (cf.Table 3.1 and Figure 3.3).

[1] The images were taken with the support of *Zentrum für Werkstoffanalytik Lauf GmbH (ZWL)*.
[2] a product of *Retsch Technology GmbH*

Table 3.1: Parameters for grain shape characterization used in this study

Sphericity KRUMBEIN & SLOSS (1963)	$SPHT\_K = \frac{d_{Fe,min}}{d_{Fe,max}}$	(3.2)
Symmetry	$Symm = \frac{1}{2}\left[1 + min\left(\frac{r_1}{r_2}\right)\right]$ with r_1 and r_2 being the distances between the centres of area and the edges of the grain in a given measuring direction. For asymmetric particles, symmetry is < 1. If the centre of the surface is outside the particle, i.e. $r_1/r_2 < 0$, then $Symm$ < 0.5.	(3.3)
Roundness KRUMBEIN & SLOSS (1963)	$RDNS = \frac{mean\ diameter\ in\ each\ corner}{largest\ inner\ diameter}$	(3.4)

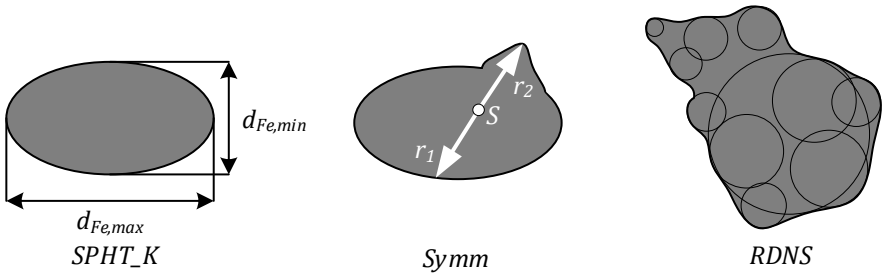

Figure 3.3: Schematic representations of *SPHT_K*, *Symm* and *RDNS*

The roughness or surface texture of grains (small scale) is only detectable with strongly magnifying microscopic analysis and it can change significantly within one assembly of grains. This is exemplified in Figure 3.4 for a medium quartz sand from the Garzweiler open cast mine used in this study, showing the changing surface textures.

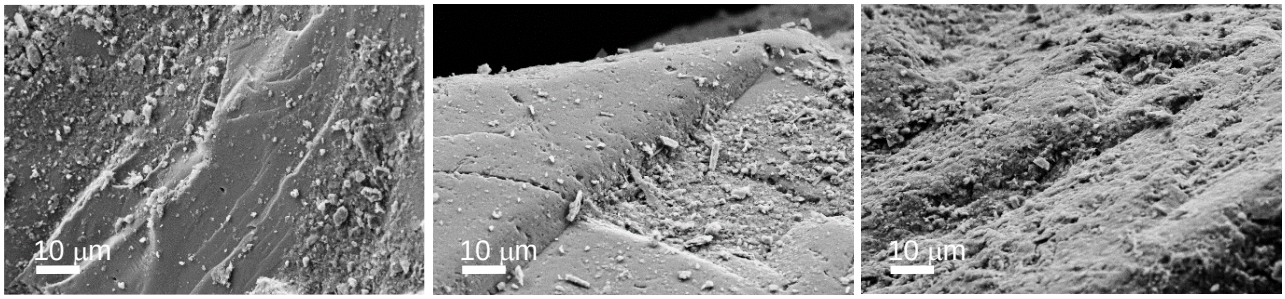

Figure 3.4: Scanning electron microscopy of pure medium quartz sand from Garzweiler open cast mine at 1000-fold magnification for visualization of different surface textures within one grain assembly including fine grained particles attached to the coarser grain surface

A method for quantifying the surface texture is to measure the surface elevations by atomic force microscopy. With this method an average value as a root mean square (RMS) of the surface elevations can be determined. MICHALOWSKI *et al.* (2018) used this method and determined RMS-values for different grains out of a batch of rounded Ottawa quartz sand varying between 321 nm and 621 nm leading to different creep behaviour of the single grains. The varying roughness of grains out of one batch determined by MICHALOWSKI *et al.* (2018) indicates that the surface texture of a single grain out of one assembly is not conclusive for the viscous response of the assembly. It is generally difficult to

establish a relation between the macroscopic behaviour of soil and the small scale grain shape. This can only be done for very homogenous grain assemblies or for single grains.
As the grain shape can only be described qualitatively, a unique relationship between it and constitutive parameters cannot be derived (HERLE, 1997). However, obvious tendencies in the deformation behaviour of a granular soil can be associated with the large and intermediate scale shape characteristics of grains (e.g. roundness and sphericity). Further details on the interrelation between grain shape and viscous properties are given in Section 3.3. The influence of the grain shape on the compression and creep behaviour of sands is analyzed in Sections 4.6, 4.7 and 4.9.2.

3.1.3 Particle strength

Since the mechanisms leading to viscous responses in granular soil are mainly related to particle degradation, the particle strength is an important controlling parameter. The particle strength of a single grain is influenced by the grain size, shape, mineralogy and imperfections like cracks or dislocations. The strength of a particle within a particle assembly is affected by the GSD. The strength of grains without any imperfections is limited by the mineral hardness and the grain shape only. In this case, the size of a particle would be irrelevant for its strength. However, nearly all natural soil particles have imperfections and the larger the particle, the more likely it is that its strength is reduced by the imperfections. CAVARRETTA *et al.* (2017) showed that breakage failure is sensitive to the relative curvature of the contacts $1/R^* = 1/R_1 + 1/R_2$ with R_1 and R_2 being the two averaged radii of curvature of the surfaces of the particles at the point of contact (cf. Figure 3.5).

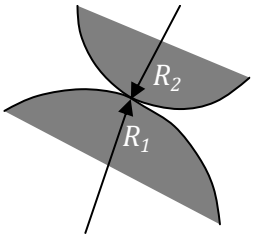

Figure 3.5: Radii at grain contact

If two particles consist of the same material, the crushing force is proportional to the relative radius of the contact. Smaller particles will tend to have larger relative radii and therefore show a greater strength. The particle strength of particles consisting of common minerals as a function of the particle diameter is shown in Figure 3.6. The strength, here described as the splitting tensile stress, decreases significantly with increasing diameter. It is inversely proportional to the diameter described by the relation

$$\sigma_f \propto \frac{1}{d^{\alpha}} \tag{3.5}$$

with d the characteristic diameter and α a correlation coefficient. For the materials in Figure 3.6 the exponent α is 0.844, 0.399 and 0.378 for Silica sand, Aio quartz sand and Aio feldspar sand respectively.

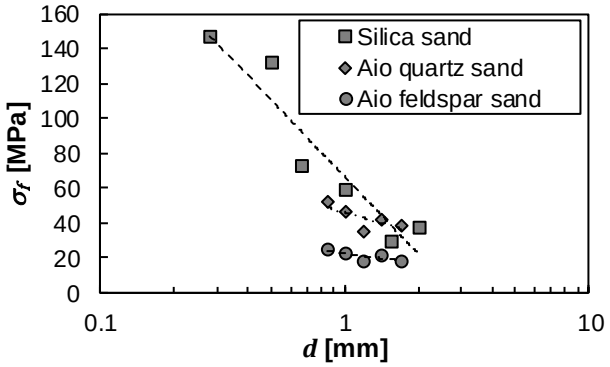

Figure 3.6: Particle strength of Silica sand, Aio quartz sand and Aio feldspar sand with respect to the particle diameter, data from NAKATA *et al.* (1999) and MC DOWELL & AMON (2000)

MIURA *et al.* (1997) demonstrate the dependence of particle strength on grain size by analyzing the potential of grain breakage of materials with the same mineralogy and grain shape but different mean grain size d_{50} and found clear trends towards increased potential of grain breakage with increasing d_{50}. They also analyzed the relationship between uniformity coefficient as well as angularity and potential of grain breakage and observed more breakage for increasing uniformity and angularity of the samples. Generally, these trends are explained by the reduction of the number of contact points between grains that consequently causes an increase of contact forces and the higher probability for larger grains to be weaker due to imperfections.

3.1.4 Particle stiffness

The interaction between grains and the load transfer in a grain assembly can be modelled in a simplified manner by a packing of perfect elastic uniform spheres of equal diameter $d = 2r$ as shown in Figure 3.7. The spheres are arranged in a simple cubic packing, which is characterized by a minimal packing density of

$$P = \frac{4/3\pi r^3}{a^3} = \frac{4/3\pi (a/2)^3}{a^3} = \frac{\pi}{6} \tag{3.6}$$

with r being the radius and a being the orthogonal distance between the centres of the spheres. It is assumed that the load transfer is limited to normal forces being transferred only in the vertical direction and that the contact behaves elastically. With these simplifications the contact point between two spheres can be described by the HERTZIAN contact radius (HERTZ, 1881)

$$a_r = \sqrt[3]{\frac{3Fr}{4E^*}} \tag{3.7}$$

with F being the force acting on the contact and E^* the contact stiffness (JOHNSON, 1985). The contact stiffness can be calculated via

$$E^* = \frac{E}{2(1-\nu^2)} \tag{3.8}$$

with E being the YOUNG'S modulus of the grains. The magnitude of the force acting on a grain contact is proportional to the number of grains in a fixed control volume loaded by a stress σ. When considering the simple cubic packing and no frictional contribution to the load transfer, only the vertical contact points transfer the load and the contact forces can be calculated by

$$F = \sigma \cdot \pi r^2 \,. \tag{3.9}$$

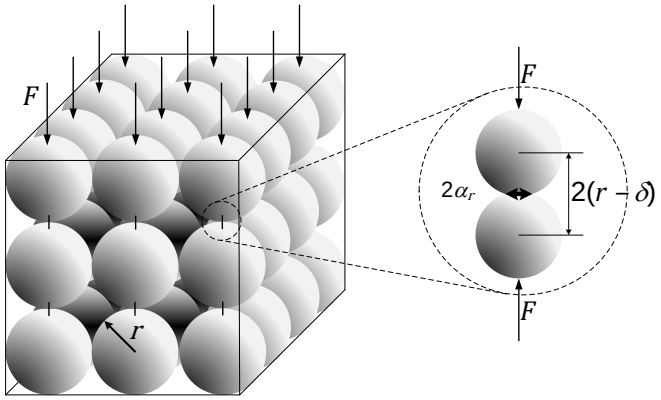

Figure 3.7: Loosest packing of spheres of equal diameter $d = 2r$ and detail of contact radius α_r

In this case and considering a HERTZIAN compression (i.e. linear elastic), the contact area between the grains is directly proportional to the applied force on the grain and therefore to the number of grains or the grain size. This also implies that the contact stress between the grains does not change with the grain size during HERTZIAN compression (cf. Figure 3.8 (a)). The development of contact force versus grain deformation

$$\delta = \frac{\alpha_r^2}{d/2} \tag{3.10}$$

is non-linear, because of the development of the contact radius (cf. Figure 3.8 (b)).
However, grains only show HERTZIAN contact behaviour within a small contact force range as experiments by ANTONYUK *et al.* (2005) showed (cf. Figure 3.9). They define a yield point, beyond which the material behaviour is softer than predicted by the HERTZIAN contact law, due to initiation of plastic deformations at the grain contacts. These plastic deformations initiate at relatively low contact forces (about 40% of the particle strength) and influence the viscous behaviour of grain contacts and therefore grain assemblies. In Section 3.3.3 it is shown that plastic deformations at the grain contacts trigger viscous behaviour of granular soils at low stresses far below the particle strength and that the material strength is time-dependent, i.e. it decreases under constant load. The conctact behaviour between the grains is key in understanding the time-dependent behaviour of granular soils. This will be further addresses in Sections 3.3 and 4.

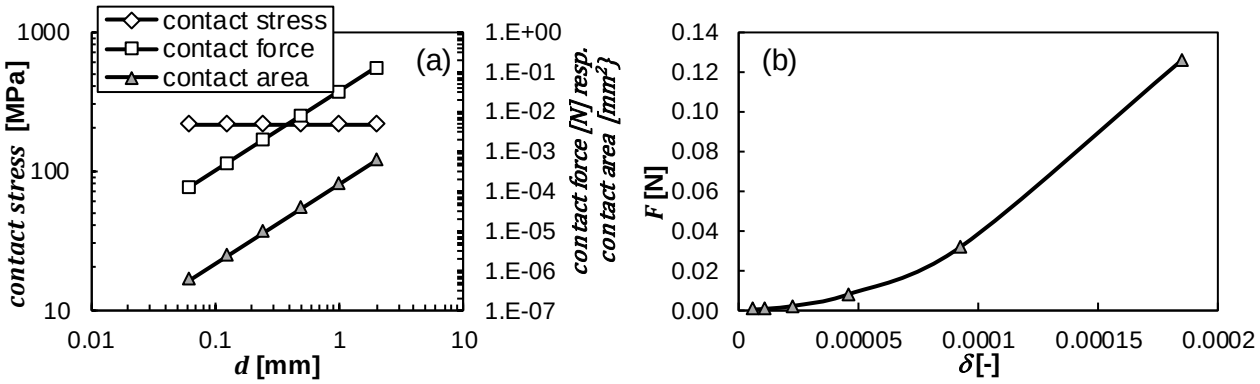

Figure 3.8: (a) Calculation of the contact area, contact force and contact stress between grains in a fixed control volume loaded by a constant stress considering HERTZIAN contacts and material parameters of quartz glass and (b) contact force versus grain deformation δ

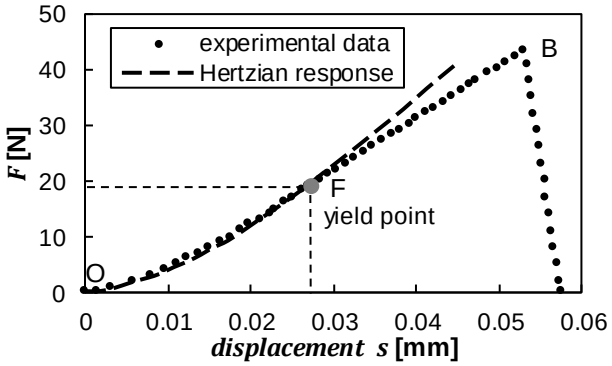

Figure 3.9: Force-displacement curve of Corundum-granulate (d = 1.7 mm): O-F elastic deformation and F-B elastic-plastic deformation (data from ANTONYUK *et al.*, 2005)

3.1.5 State variables

Besides the granulometric properties, the state of a soil, which is described by the stress state and the density, also controls its viscous response. To simplify the description of the state of a soil, which consists out of a huge number of grains and varying shape characteristics, macroscopic state descriptor quantities were introduced. They describe a physical condition of the soil, which can change with respect to a reference state, rather than a material property. Knowledge of the initial values and the evolution of the state variables is a pre-condition for modelling. The density is described by means of the void ratio defined as

$$e = V_p/V_s \tag{3.11}$$

with V_p as the pore volume – filled by gas (V_a) or liquid (V_w) – and V_s the solid volume in a soil. Alternatively the porosity n is used with

$$n = \frac{V_p}{(V_s + V_p)}. \tag{3.12}$$

To quantify the influence of the density of soil on its mechanical behaviour, the relative density D_R was introduced between 0 for very loose ($e = e_{max}$) and 1 for very dense ($e = e_{min}$),

$$D_R = \frac{e_{max} - e}{e_{max} - e_{min}}. \tag{3.13}$$

D_R is based on the definition of a minimum void ratio e_{min} and maximum void ratio e_{max}, whose determination is standardized for example by the German standard DIN 18126:1996-11. The descriptive terms of density, categorized by the relative density, are summarized in Table 3.2.

Table 3.2: Relative density description (Lambe & Whitman, 2012)

relative density D_R	descriptive term
0.00 – 0.15	very loose
0.15 – 0.35	loose
0.35 – 0.65	medium dense
0.65 – 0.85	dense
0.85 – 1.00	very dense

The behaviour of a granular soil does not only depend on its density, but also on the applied effective pressure. This can be taken into account by considering the change of the extreme void ratios e_i (loosest state), e_c (critical state) and e_d (densest state) with the pressure (cf. Figure 3.10). GUDEHUS (1996) therefore introduced the relative void ratio by

$$r_e = \frac{e - e_d}{e_c - e_d}. \tag{3.14}$$

r_e considers the change in extreme void ratios e_c and e_d with the pressure and relates the distance of the current state to the distance from the critical state line as the reference line. For r_e > 1, the soil is looser than the critical state and will behave contractive when sheared. For r_e < 1, the soil is denser than the critical state and will show dilatancy when sheared. And in case of r_e = 1, the soil is in the critical state. Contrary to the relative density D_R, with e_{min} and e_{max} determined at essentially zero pressure, the relative void ratio r_e is valid for a wide range of pressures. The boundaries e_i and e_d capture the minimum and maximum density state in an actually physically meaningful way. At a certain pressure and not considering macroporic structures, neither a looser state than e_i without the grains loosing contact nor a denser state than e_d without grains being damaged can be achieved. The limiting void ratios at nearly zero stress are referred to as e_{i0}, e_{c0} and e_{d0} for the void ratio in the densest, critical and loosest state respectively. The loosest state is achieved, when the grain sediments from a suspension to a state where the grains just touch each other to build a grain skeleton. VERDUGO (1992) proposed a procedure (called collapse method) to determine the loosest state e_i in sands. Therein, a sample with 5 wt-% partially saturated sand is carefully placed in a mould by spoon, the air is replaced by CO_2 and afterwards the sample is flooded at a minimal gradient, until it is almost, but not fully saturated. This leads to a collapse of the soil fabric and the loosest packing in a saturated state. The densest state of a soil can be reached under shearing cycles with small shear strain amplitude without change in the GSD (HERLE, 1997). The critical state void ratio describes the state of constant volume and constant stress a sample reaches under monotonic shear deformation at p' = constant. It divides the volumetric behaviour of a soil under shearing into a contractive and a dilative regime. Figure 3.10 shows the development of the extreme void ratios in isotropic compression.

Equivalent to the relative void ratio, the pressure-adjusted relative density is also used for the description of the density-state of granular soil

$$I_d = 1 - r_e = \frac{e_c - e}{e_c - e_d}, \tag{3.15}$$

for which the ranges in Table 3.2 also apply. Further references to the relative density in this study refer to (3.15).

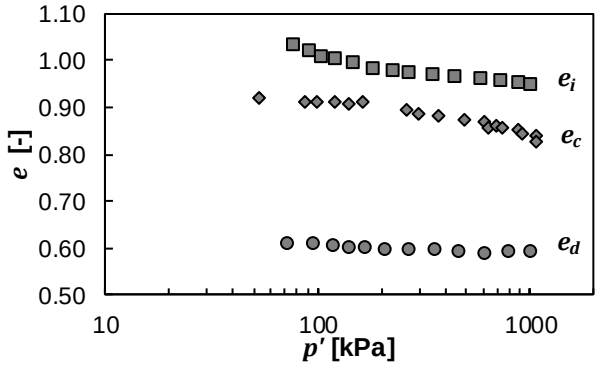

Figure 3.10: Development of extreme void ratio e_i (loosest state) e_c (critical state) and e_d (densest state) of Toyoura sand in isotropic compression (data from VERDUGO & ISHIHARA, 1996)

For the estimation of the void ratio at the densest state at nearly zero pressure e_{d0} of sands both VERDUGO (1992) and HERLE (1997) recommend to take the e_{min} value determined by standard procedure from DIN 18126:1996-11 respectively the ASTM D4254-16. For the critical state void ratio e_{c0}, it is advised to use the e_{max} value determined by the procedure from DIN 18126:1996-11 (HERLE, 1997). The determination of the void ratio in the loosest state at nearly zero pressure e_{i0} in the laboratory is difficult, because already the gravitational loading leads to a densification. From theoretical considerations of ideal packings HERLE (1997) advises to take $e_{i0} = 1.15 \cdot e_{max}$ as the loosest state void ratio for natural quartz sands. Data for clean sands from VERDUGO (1992) confirm this value (cf. Table 3.3).

Table 3.3: Values of e_{max} determined by ASTM D4254 - 16 and e^*_{max} determined by collapse method of different clean sands (data from VERDUGO, 1992)

Sand	e_{max} (determined by ASTM-standard, similar to DIN-standard)	e^*_{max} (determined by collapse method)	e^*_{max} / e_{max}
Toyoura	0.977	1.120	1.15
Chiba	1.271	1.411	1.11
Kiyosu	1.206	1.423	1.18
Kosaka	0.989	1.073	1.08
Kizugawa	1.030	1.170	1.14

e_{min} and e_{max} are influenced by the grain shape and the GSD. MIURA *et al.* (1997) give an overview and identify the following trends:

– Increasing e_{min} and e_{max} with decreasing d_{50},
– decreasing e_{min} and e_{max} with increasing uniformity and
– increasing e_{min} and e_{max} with increasing angularity and decreasing roundness.

The presented state variables provide a framework for the consideration of the influence of the density and stress state on the soil behaviour. This is sufficient for the description of the compressive and shearing behaviour, but it does not take into account the time-dependent behaviour. For the analysis of the time-dependent behaviour, another reference state, the so called reference compression line (RCL) is required, in analogy to the normal consolidation line (NCL) used in fine-grained soils. The definition of a RCL for granular soils is addressed in Section 6.

The state of a soil is generally defined by the stress state, the density and the preceding deformations. For sands and also fine grained soils it was discovered that after sufficiently long proportional strain paths from a distorted state, proportional stress paths are reached, independently from the initial stress state and initial strains. The proportional straining leads to a loss of influence of the preceding deformation and stress history in the soil. In this state, which was called “swept out of memory” (SOM) state (GOLDSCHEIDER, 1972 and GUDEHUS *et al.,* 1977), the state is defined by the void ratio and the stress only.
For rate-dependent material the strain rate needs to be constant as well, to remain on the same SOM-state. KRIEG (2000) investigated the influence of the previous deformation history on the creep behaviour of fine-grained soils under oedometric conditions. In the experimental investigation, three peat samples were left to creep starting from different initial states (p', e), which were achieved by unloading, creep and relaxation, respectively. The resulting creep behaviour was almost identical independently of the previous stress and strain history. KRIEG postulated the “extended swept out of memory” (ESOM) state for rate-dependent soils, in which the soil behaviour is uniquely defined by two of the three parameters σ', e and $\dot{e}$. According to these results, the behaviour of fine-grained soils appears to be independent of the strain and strain rate history. Whether this also applies for granular soils, will be addressed in Section 4.

3.2 Stress-dependent compression and swelling

3.2.1 Experimental results

Figure 3.11 shows results of oedometric compression tests by YAMAMURO *et al.* (1996) on a coarse angular quartz sand and a medium gypsum sand that represent very soft and very hard grains, respectively. The stresses exceed the stress range of conventional geotechnical problems. Figure 3.12 presents the respective C_c values of the two tests. It can be observed that the virgin $\Delta e - \log \sigma'$ behaviour of both materials is highly non-linear. The C_c values are approximately constant at stresses below 2 to 3 MPa and beyond that start to increase strongly to a maximum value of about 0.6 to 0.7 for both soils, which is comparable to C_c values of soft soils at low stresses smaller than 1 MPa. The gypsum sand reaches the maximum C_c value at about 10 MPa and the quartz sand at 40 MPa, which can be explained by the different mineral hardness of the soils. The large C_c values are due to level III damage (cf. Section 3.1.1) dominating the compression behaviour. At very high stresses the C_c values start to decrease again. Loose and dense samples of both soils reach a unified compression curve at high stresses. For the gypsum sand this curve is reached at about 3 MPa and in case of the

quartz sand at about 600 MPa. At sufficiently high stresses the compressive behaviour is only influenced by the GSD, particle shape and mineralogy. The initial density does not influence the compressive behaviour anymore.

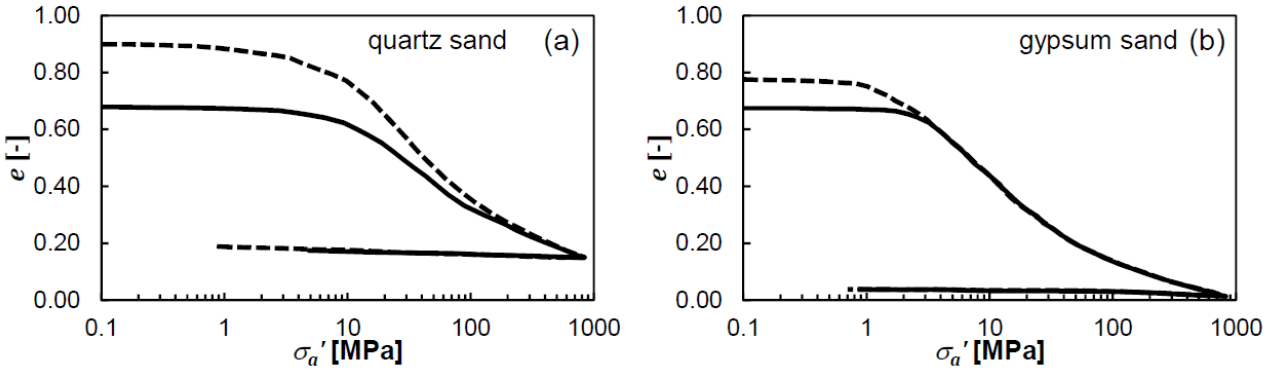

Figure 3.11: Oedometric compression test results of (a) loose and dense coarse angular quartz sand and (b) loose and dense medium gypsum sand (YAMAMURO *et al.*, 1996)

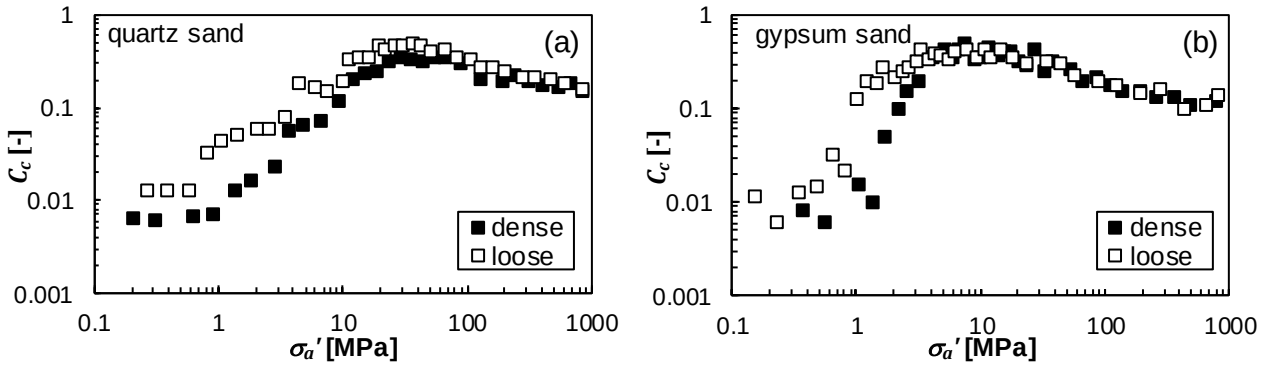

Figure 3.12: C_c evaluation of oedometer test in Figure 3.11 of (a) loose and dense coarse angular quartz sand and (b) loose and dense medium gypsum sand (data from YAMAMURO *et al.*, 1996)

Figure 3.13 presents results of the C_c evaluation from high pressure oedometric compression tests by MESRI & VARDHANABHUTI (2009). When comparing the carbonate sand and the angular to subangular quartz sand, the influence of the mineralogy on the compressibility is visible. As expected, the more brittle the material the higher is the compressibility at low stress. Angularity also influences the compressibility as can be observed when comparing the two quartz sands. The more angular material shows larger compression indices caused by the breaking of asperities of the grains. The test results show that a constant C_c is not applicable for granular soils even at small stresses.

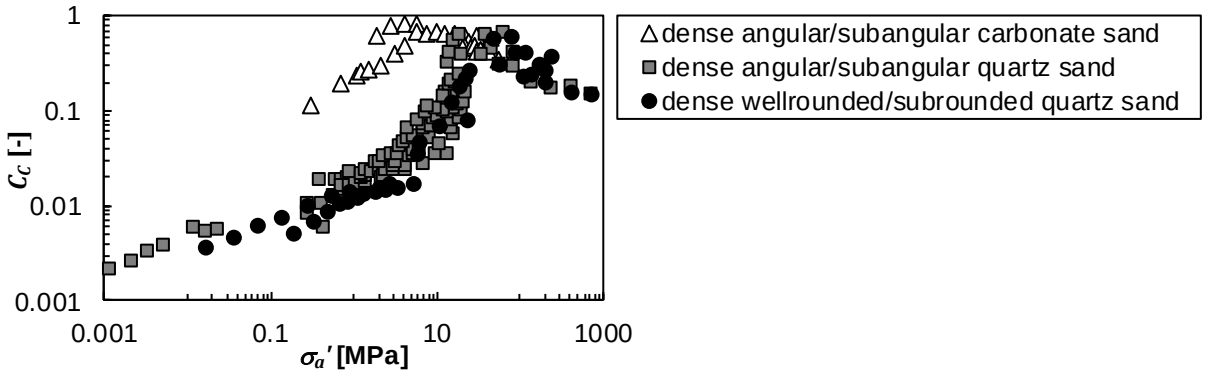

Figure 3.13: C_c values from high pressure oedometric compression test (data from MESRI & VARDHANABHUTI, 2009)

Figure 3.14 presents results of oedometric moduli ($E_s = \Delta\sigma'_a/\Delta\varepsilon_a$) from oedometer tests with medium well graded subrounded quartz sand (CHUHAN *et al.,* 2003), calcareous sand and Feldspar sand (PESTANA & WHITTLE, 1995). They represent a wide variety of sand types.

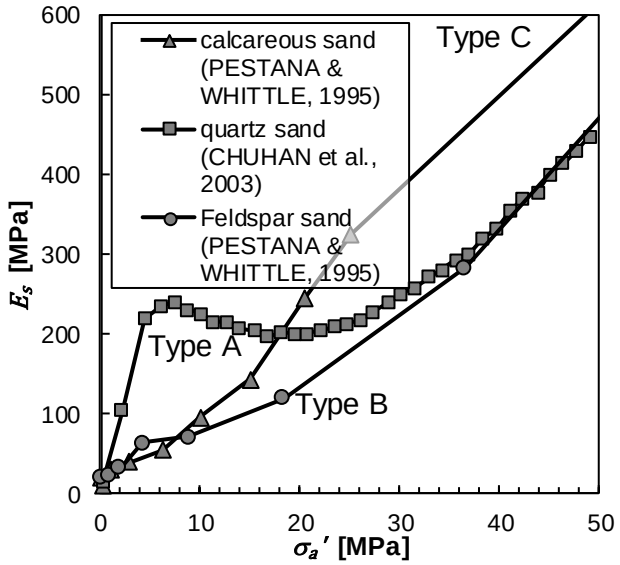

Figure 3.14: Oedometric modulus vs. axial stress, data from medium well graded subrounded quartz sand (CHUHAN *et al.,* 2003), calcareous sand and Feldspar sand (PESTANA & WHITTLE, 1995)

According to CHUHAN *et al.* (2003) and LAMBE & WHITMAN (2012), the virgin compression behaviour of sands under oedometric conditions can be categorized into three stress ranges:

1. Lower stress range (0 until approx. 5 – 15 MPa): Densification of the soil is primarily caused by relative movements and rotations of the grains, who have the tendency to get into a denser packing with more grain-to-grain contacts. The stiffness increases due to interlocking and the increased number of contact points. Surface abrasion and degradation can already happen in the lower stress range depending on the grain shape and strength, but they do not dominate the deformation mechanism (level I particle damage).

2. Intermediate stress range (approx. 5 – 15 MPa until 25 – 35 MPa): Increased breakage of entire grains leads to a reduced stiffness. Changes in the GSD towards a higher fine content are clearly

detectable. Stiffness decrease due to grain breakage exceeds stiffness increase due to a denser packing (level II and level III particle damage).

3. High stress range (above approx. 25 – 35 MPa): Fragments of the grains start to fill up the remaining void space, which leads to increased stiffness. Multiplication of grains through grain breakage leads to more grain-to-grain contacts and decreased stresses at contact points. This again leads to less frequent grain breakage and a continuously increasing stiffness in compression (level II and level III particle damage).

The boundaries of the stress ranges are dependent on the soil type and cannot be generalized very precisely. MESRI & VARDHANABHUTI (2009) observed that not all soils display the three phases in their stress-strain-behaviour. They therefore divide sands into three compression-types:

– Type A: Sands, which show all three stress-strain behaviours in the respective stress ranges. Generally these are soils with well rounded, hard grains.
– Type B: Sands that do not show a decrease of stiffness in the intermediate stress range. The bulk stiffness remains more or less constant within this range.
– Type C: Sands of this type exhibit grain breakage at relatively low stresses, which leads to a quick increase of the number of grain-to-grain contact points and a continuous increase of the bulk stiffness in all stress ranges. Sands with angular grains of low mineral hardness show this behaviour, e.g. carbonate sands.

The sands shown in Figure 3.14 represent the three compression types. Type A is clearly identifiable for the quartz sand. However, it is difficult to distinguish between type B and type C for the Feldspar and calcareous sand.

3.2.2 Analytical description of stress-dependent compression

A change in void ratio of a soil along with a change in the stress state influence its density and therefore stiffness, which changes during virgin-, un- and reloading. An early approach to describe the change in oedometric stiffness was proposed by OHDE (1939):

$$E_s = E_{s,ref}\left(\frac{\sigma'_a}{\sigma'_{a,ref}}\right)^m . \tag{3.16}$$

The approach can be derived from the mechanical behaviour of ideal elastic grains by HERTZ (1881) (HERLE, 1997) (cf. Section 3.1.4). The approach uses a reference stiffness $E_{s,ref}$ determined at a reference stress $\sigma'_{a,ref}$ (usually the atmospheric pressure of 100 kPa) and a power law depending on the acting effective axial stress σ'_a and the exponent m. For coarse to fine sand $E_{s,ref}$ at $\sigma'_{a,ref}$ = 100 kPa varies between 15 MPa and 70 MPa with exponent m between 0.65 and 0.8 (VON SOOS, 2009). When compared with Figure 3.14 this approach can be used for the description of the stiffness development at stresses below approximately 10 MPa. OHDE's model and alterations are an essential part of the well-established constitutive models, for example the Hardening Soil Model by SCHANZ *et al.* (1999), which was formulated in the plasticity framework for predicting the rate-independent mechanical behaviour of granular materials.

The most common approach to describe the one-dimensional compressive behaviour of soil under virgin loading respectively un- and reloading is the compression law of TERZAGHI (1925), as given by TAYLOR (1948), which relates the changes in void ratio with $\log \sigma'$

$$e - e_0 = C_c \cdot \log \frac{\sigma'}{\sigma'_0} \qquad \text{for loading and} \tag{3.17}$$

$$e - e_0 = C_s \cdot \log \frac{\sigma'_0}{\sigma'} \qquad \text{for unloading and reloading} \tag{3.18}$$

with C_c as the compression index and C_s as the swelling index. The oedometric stiffness E_s and the compression index relate by

$$E_s = \sigma' \frac{1 + e_0}{C_c} \cdot \ln(10)\,. \tag{3.19}$$

An alternative definition with the natural logarithm is also used:

$$e - e_0 = \lambda \cdot \ln \frac{\sigma'}{\sigma'_0} \qquad \text{or with the volumetric strain} \quad \Delta\varepsilon_v = \lambda \cdot \ln \frac{\sigma'}{\sigma'_0} \tag{3.20}$$

$$e - e_0 = \kappa \cdot \ln \frac{\sigma'_0}{\sigma'} \qquad \text{or with the volumetric strain} \quad \Delta\varepsilon_v = \kappa \cdot \ln \frac{\sigma'_0}{\sigma'}\,. \tag{3.21}$$

In many engineering applications C_c and C_s are regarded as constant in the relevant stress range, which is in good agreement with test results from fine grained soils. The compression behaviour of granular soils on a logarithmic stress scale is non-linear in all stress ranges in virgin loading as well as in unloading and reloading (BAUER, 1992, HAGERTY *et al.*, 1993, PESTANA & WHITTLE, 1995, BAUER, 1996, YAMAMURO, BOPP & LADE, 1996, CHUHAN *et al.*, 2003, MESRI & VARDHANABHUTI, 2009). Linearity can only be assumed for small stress increments (cf. Section 3.2.1).
A modification of the TAYLOR compression law was proposed by BUTTERFIELD (1979) for isotropic compression and swelling using the natural logarithmic strain measure (also called HENKY strain)

$$\varepsilon_v = \ln\left(\frac{1 + e}{1 + e_0}\right). \tag{3.22}$$

The BUTTERFIELD compression law reads

$$\varepsilon_v = \ln\left(\frac{1 + e}{1 + e_0}\right) = \lambda^* \ln \frac{p'}{p'_0} \qquad \text{for compression} \tag{3.23}$$

$$\varepsilon_v = \ln\left(\frac{1 + e}{1 + e_0}\right) = \kappa^* \ln \frac{p'_0}{p'} \qquad \text{for swelling and recompression} \tag{3.24}$$

with λ^* and κ^* as modified compression and modified swelling index respectively. The approach leads in some cases to a better linearization and therefore approximation of test results and is used

in constitutive models like Soft Soil Creep (SSC) by VERMEER & NEHER (1999) or the visco-hypo-plastic model by NIEMUNIS (2002), which were both developed for modelling the viscous behaviour of soft soils. These two models will be analyzed in Section 6.
Figure 3.15 shows a comparison between the two strain measures HENKY strain and the common engineering strain

$$\varepsilon_v = \frac{e_0 - e}{1 + e_0}. \tag{3.25}$$

Larger differences between the two strain measures can be expected at strains above approximately 15% (cf. Figure 3.15).

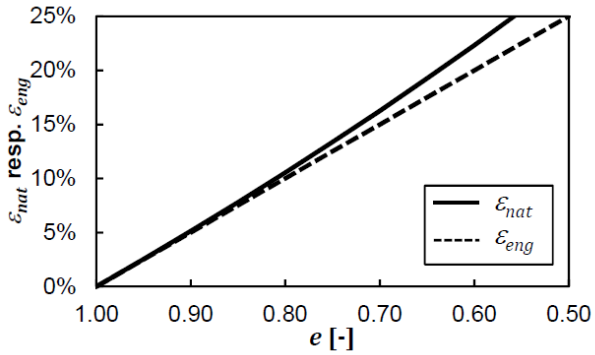

Figure 3.15: Comparison between engineering and natural strain

BAUER (1996) proposed an exponential compression law

$$\frac{e}{e_0} = 1/\exp\left[\left(\frac{tr\boldsymbol{T}}{h_s}\right)^n\right] = 1/\exp\left[\left(\frac{3p'}{h_s}\right)^n\right] \tag{3.26}$$

with h_s the granular hardness and the exponent n. $\boldsymbol{T}$ is the CAUCHY stress tensor describing the macroscopic stress state of the soil. Figure 3.16 shows examples of the influence of the parameters h_s and n on the compression curves. The BAUER compression law is applied in the family of hypo-plastic constitutive models and is especially suited for granular materials.

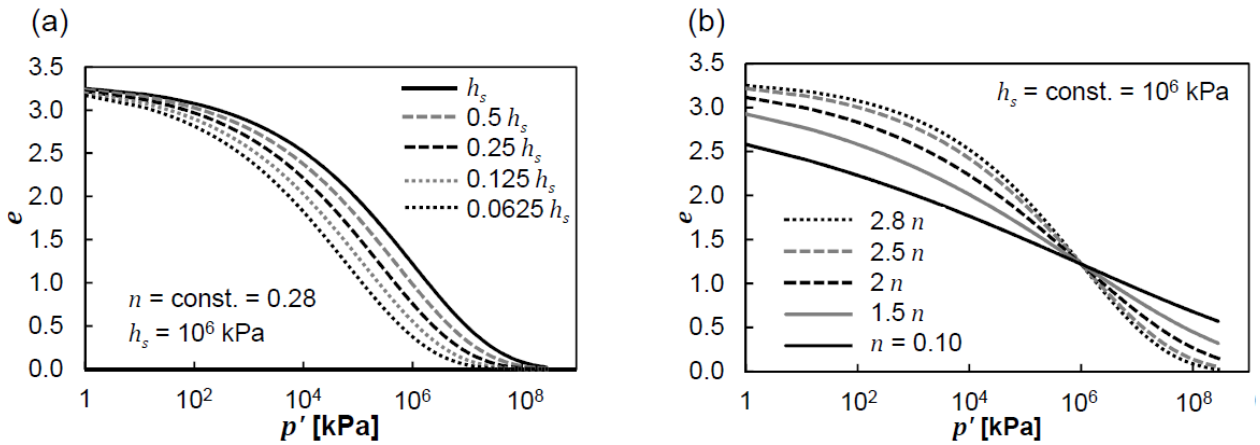

Figure 3.16: BAUER compression law with (a) different h_s at constant n and (b) different n at constant h_s

For constitutive modelling it is important to find a compression law that can reproduce the compressive behaviour in the entire stress range relevant for engineering applications. To precisely define this stress range is difficult, but stresses above 10.0 MPa are seldom met in geotechnical engineering applications. Most constitutive models (e.g. the hypoplastic models) also assume permanent grains as a requirement, because many constitutive parameters will change if the soil undergoes significant change in its GSD due to grain breakage. Other models that solely focus on compression behaviour use the unified compression curve (cf. Figure 3.11) as an asymptotic soil inherent state, also referred to as Limiting Compression Curve (LCC) (PESTANA & WHITTLE, 1995 and PESTANA & WHITTLE, 1998). However, to reach the LCC significant change in the GSD due to grain breakage is necessary and it is therefore not considered suitable for use in constitutive models.

3.3 Time-dependent soil response

The mechanical behaviour of soil is time-dependent. The magnitude of the time-dependent response highly depends on the soil type. Soft fine grained soils show a by orders of magnitude stronger time-dependency than granular soils. Time-dependency regarding the mechanical soil behaviour is usually referred to as creep – describing the time-dependent development of strains under constant effective stress – and the dependency of the stress-strain-relationship on the strain rate. The change of stress with time under constant strain – so called stress-relaxation – is a special case of rate dependency at zero strain rate. All three phenomena are an expression of the viscosity of soil. Viscosity is originally defined for gases and liquids as the relationship between shear resistance (or flow resistance) and the shear strain rate (or flow rate). It is distinguished between dynamic viscosity η and kinematic viscosity ν^* with

$$\eta = \frac{\tau}{\dot{\gamma}} \tag{3.27}$$

and

$$\nu^* = \frac{\eta}{\rho} \,. \tag{3.28}$$

τ is the shear stress, $\dot{\gamma}$ is the shear rate and ρ is the density. Fine grained soils can mostly be treated as highly viscous fluids in a simplified approximation.
This study focusses on the viscosity of grain skeletons where particles are in permanent contact. Suspensions are not considered. Viscosity in soil mechanics refers to the dependence of the macroscopic stress-strain behaviour of soils on the stress and strain rate.The viscosity of permanent grain skeletons is linked to shear forces at particle contacts and is mainly influenced by the frictional resistance between the particles and the time-dependent material strength of the grains. Viscous effects in granular soil are triggered and influenced by the rearrangement of force chains between the grains and static fatigue of the grains.

In the following sections creep, rate dependency and stress relaxation in granular materials and their experimental investigation in literature will be treated separately.

3.3.1 Creep

Time-dependent deformations of granular soils can be divided into three different types considering different mechanisms:

- Instantaneous deformation (particle rearrangement upon load-change),
- time-delayed deformation due to dissipation of excess pore-water pressure (primary consolidation) and
- time-delayed deformation under constant effective stresses (creep).

Contrary to creep, the dissipation of excess pore water pressure does not only depend on the properties of the pore fluid and soil, but also on the drainage conditions, permeability and drainage path. The time-dependency resulting from the interactions of pore water and grain skeleton deformations are therefore not of a constitutive nature and will not be a subject of this investigation.
Whether creep deformations already occur during primary consolidation (Hypothesis B) or if the start of creep falls together with the end of primary consolidation t_{EOP} (Hypothesis A), is still part of controversial discussion (cf. review in AUGUSTESEN *et al.,* 2004). However, the established constitutive models for prediction of viscous behaviour of soils are all based in Hypothesis B, which assumes that creep occurs during the primary consolidation process, which means that the strain at the end of primary consolidation depends on the soil layer thickness and is not unique. Nevertheless, this issue is not to be addressed here, because primary consolidation in granular soils finishes very quickly due to the comparably high hydraulic conductivity of the soils and creep deformations developed during the short consolidation time are small.
Creep of granular assemblies as well as the compression and shearing behaviour are dependent on the applied effective stress, the density, the mineralogy, the grain shape and the degree of saturation. The following general findings were made by several authors regarding the influence of these parameters. Creep deformations increase with

– increasing mean effective stress (e.g. COLLIAT-DANGUS *et al.*, 1988 and MIURA & YAMANOUCHI, 1975, KARIMPOUR & LADE, 2010)
– increasing deviator stress (e.g. MURAYAMA *et al.*, 1984, MEJIA & VAID, 1988),
– increasing loading strain rate (KARIMPOUR & LADE, 2010),
– decreasing relative density (e.g. COLLIAT-DANGUS *et al.*, 1988, LEUNG *et al.*, 1996 and LADE & LIU, 1998),
– increasing angularity and surface roughness of the grains (e.g. MEJIA & VAID, 1988, MICHALOWSKI *et al.*, 2018)
– decreasing mineral hardness (e.g. COLLIAT-DANGUS *et al.*, 1988, LV *et al.*, 2016) and
– with onset of grain crushing (e.g. COLLIAT-DANGUS *et al.*, 1988, LEUNG *et al.*, 1996, MESRI & VARDHANABHUTI, 2009, KARIMPOUR & LADE, 2010).

The dominating deformation mechanisms during creep in the respective stress ranges (low, intermediate, high) are the same as in stress-dependent compression postulated by CHUHAN *et al.* (2003) (cf. Section 3.2). Creep in granular materials can therefore not be described as a thermally activated process but rather as a process, which is triggered by the tendency of the grain assembly to move

into a more stable configuration for the load transfer, i.e. a configuration with least shear and most normal forces at the grain contacts (BOWMAN & SOGA, 2003). Depending on the stress level, this is accompanied by different deformation mechanisms, including degradation and breakage of grains and depends on the time-dependent material strength of the grains (WANG & MICHALOWSKI, 2015, MICHALOWSKI *et al.*, 2018).

The following sections analyze creep under compressive loading (i.e. isotropic or oedometric compression) and shearing separately and explain the mentioned findings regarding creep behaviour in more detail and concentrate on the proposed deformation mechanisms behind creep in granular soil.

3.3.1.1 Creep under oedometric and isotropic loading conditions

Oedometric creep tests by MEJIA & VAID (1988) on a loose angular quartz rich feldspar Tailings sand and a loose Ottawa quartz sand with round particles but similar GSDs show the different amount of creep strains measured after 20 min depending on the stress level and the angularity (cf. Figure 3.17 (a)). The larger creep strains of the Tailings sand are caused by the lower mineral hardness and higher angularity. The angularity is in the low stress range up to 1000 kPa more influential. An increase in angularity and surface roughness leads to an increased stress concentration on asperities and consequently to a higher rate of breakage and surface degradation (cf. Figure 3.18). The effect of increased asperity yield due to stress concentration predominates the stabilizing effect of increased interlocking of the rougher and more angular grains leading to increased creep strains.

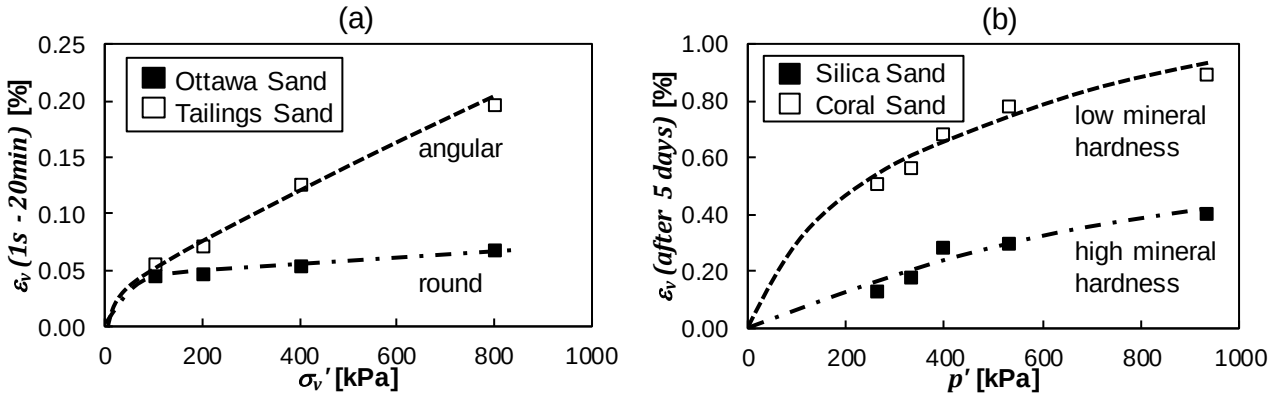

Figure 3.17: (a) Volumetric creep strains over axial stress in oedometric compression on a loose angular quartz rich feldspar Tailings sand and a loose round quartz Ottawa sand (data from MEJIA & VAID, 1988) and (b) volumetric creep strains over mean stress in triaxial loading at constant deviatoric stress of a silica sand and a coral sand with similar GSDs and angularity (data from LV *et al.*, 2016)

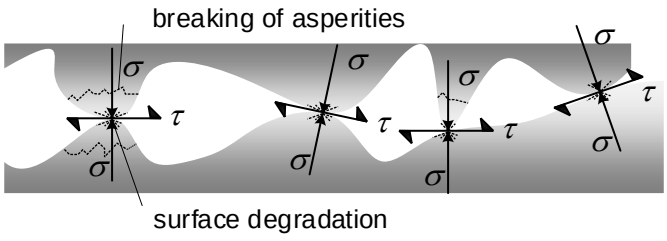

Figure 3.18: Stress concentration, breaking of asperities and surface degradation at rough angular grain contacts

To study the influence of mineral hardness on the creep behaviour LV *et al.* (2016) performed triaxial creep tests with constant deviatoric stress and different mean effective stress with maximum values of p' = 930 kPa on a coral and a silica sand with similar GSD and angularity. They also show larger creep strains at lower mineral hardness and increasing mean effective stress (cf. Figure 3.17 (b)). Isotropic compression creep tests by LADE & LIU (1998) on a subangular Antelope valley sand and maximum mean effective stresses of p' = 785 kPa emphasize the stress dependency of creep and show a linear trend with the logarithm of time within the maximum observation time of 5.4 d (cf. Figure 3.19 (a)).

Figure 3.19 (b) shows isotropic creep tests by KUWANO & JARDINE (2002) on subangular Ham River Sand (HRS), a clean medium quartz sand, and glass beads (GB) with round particles and similar GSD like HRS. The tests on HRS were prepared at loose to medium dense initial relative densities and show the reduced creep strains due to higher relative density. The test on glass beads was prepared at a similar density like the loose HRS. KUWANO & JARDINE trace the increased creep strains of HRS back to the angularity and micro-asperities of the sand that lead to a less stable, more time-dependent response.

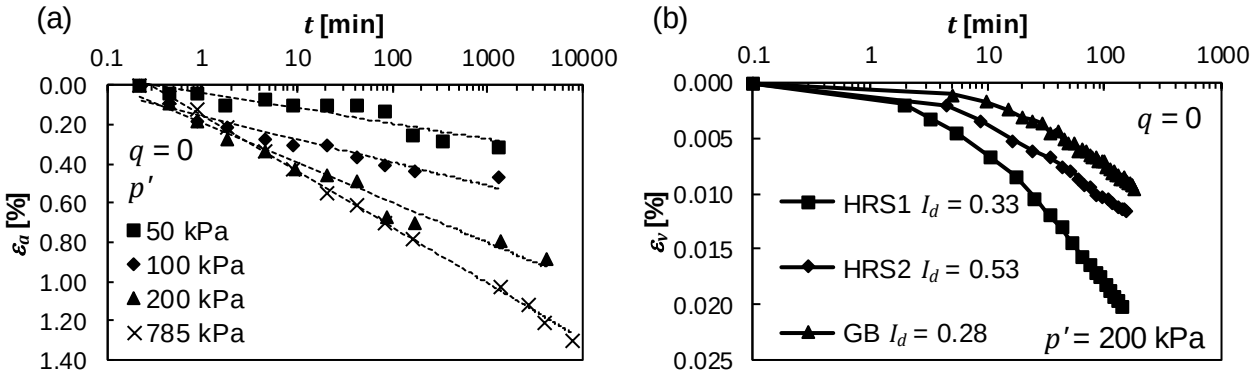

Figure 3.19: (a) Axial creep strains over time in a drained isotropic compression test on subangular Antelope valley sand (data from LADE & LIU, 1998) and (b) volumetric strains over time in a drained isotropic compression test at p' = 200 kPa on Ham River Sand (HRS) and glass beads (GB) (data from KUWANO & JARDINE, 2002)

Isotropic compression test results with different initial densities by COLLIAT-DANGUS *et al.* (1988) on a fine angular uniformly graded siliceous Hostun sand and a well graded medium calcareous sand are presented in Figure 3.20. The Hostun sand shows a strong increase of the creep strains at approximately 5 MPa, which is caused by the onset of level III particle damage. Such a distinction is not possible for the calcareous sand. In case of the Hostun sand, the influence of the differing initial densities is visible up to the maximum stress of 15 MPa. While for the calcareous sand the influence of the density on the creep strains is not clearly visible. The reason for these behaviours lies within the very different mineral hardness of the sands. In the siliceous Hostun sand larger amounts of level III grain damage do only happen at very high stresses (> 15 MPa). The calcareous sand is much more breakable and level III damage becomes the dominating deformation mechanism in creep at relatively low stresses. The density of the calcareous sand appears to only have negligible influence on the creep strains. The decrease of creep deformations at higher relative densities in the case of Hostun sand can be explained by the increased number of grain contacts to transfer the load and hence the decreased forces at grain contacts. This leads to less grain degradation. Above 5 MPa the

calcareous sand shows a decrease in the creep strains at increasing mean effective stress. This is also caused by the increased number of grain contacts due to the extensive degradation of the grains and hence the lower contact forces.

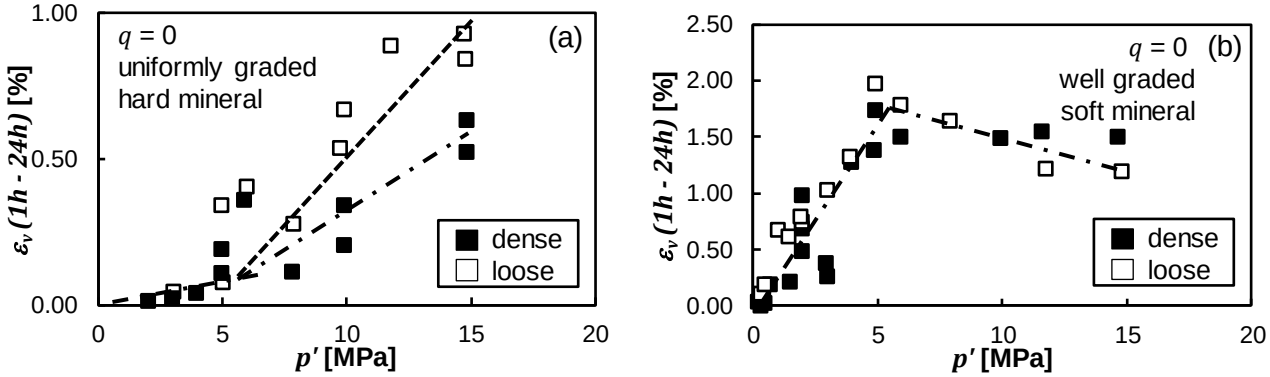

Figure 3.20: Volumetric creep strains over stress in isotropic compression on a (a) fine angular uniformly graded siliceous Hostun sand and (b) a well graded medium calcareous sand (data from COLLIAT-DANGUS *et al.*, 1988)

OSTERMAYER (1976) investigated the oedometric compression behaviour of mixed-grained soils and looked at the creep behaviour of the materials with variation of the fine content. More specifically, he looked at the ratio of the volume occupied by fine grained fraction to the porosity of the coarse-grained fraction n_G (cf. Figure 3.21). He defined a parameter for the filling of the pores of the coarse grained fraction by fine grained material

$$S_F = \frac{h_F}{n_G} \,, \tag{3.29}$$

where h_F is the part of the pores of the coarse grained fraction filled with fine grained material (cf. Figure 3.21). OSTERMAYER also defines the creep-coefficient k_α as

$$k_\alpha = \frac{\Delta s'}{\log(t_2/t_1)} \quad (t_2 > t_1) \tag{3.30}$$

with $\Delta s' = \Delta s / h_{ini}$ in the time interval from t_1 to t_2.

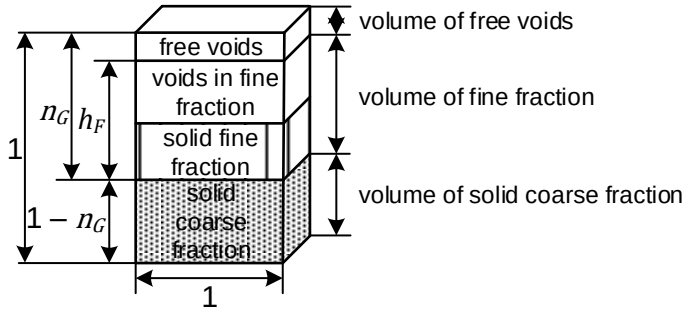

Figure 3.21: Definition of volume fractions and filling of voids in a mixed-grained soil (after OSTERMAYER, 1976)

His test results on a non-uniform sandy gravel with different filling ratios of the coarse grained voids and tests on fine grained soils with more than 60vol.-% clay and silt mixed with different proportions

of coarse grained soils are presented in Figure 3.22. OSTERMAYER defines for the tested soils the porosity of n_G = 0.4 as the threshold value, at which the load bearing coarse grain skeleton can no longer form and the coarse grains begin to swim in the fine grained soil matrix. The material behaviour changes from one of a granular soil to one of a fine grained soil. This threshold is of course not a fixed value and can vary significantly depending on the material properties. The results from the non-uniform sandy gravel, in which a load bearing grain skeleton exists, show that creep decreases with decreasing initial porosity and increasing degree of filling of the coarse grained voids with fine material. The fine fraction reduces the intergranular stresses in the coarse grain skeleton, which reduces the creep.

Above the threshold value of $n_{G,ini}$ = 0.4 the fine fraction dominates the load bearing behaviour of the soil. With further increase of the fine content the creep-coefficients of the tested soils strongly start to increase. In conclusion, the influence of the fine content on creep in OSTERMAYER's investigation is different whether a load bearing coarse grain skeleton can form or not. If the coarse grains form a load bearing grain skeleton, rising fine content reduces creep. But if the coarse grains begin to loose contact and swim in the fine grained soil matrix, rising fine content increases creep.

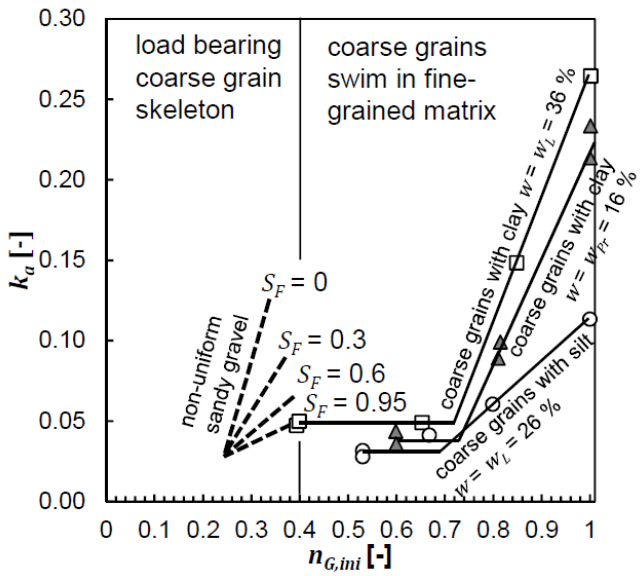

Figure 3.22: Creep-coefficients of mixed grained soils in dependence of the initial porosity of the coarse grained fraction $n_{G,ini}$ (data from OSTERMAYER, 1976)

3.3.1.2 Creep in deviatoric stress states

Creep rupture

MURAYAMA *et al.* (1984) investigated the creep behaviour of loose Toyoura sand in drained triaxial compression tests (TCD) under different deviatoric stress levels q and constant mean effective stresses p' (cf. Figure 3.23). They determined the creep strains by measuring the volume of drained pore water and the axial deformation. The creep rate increased with increasing mean effective stress p' and – as expected – with increasing stress ratio $R = q/p'$, until eventually creep rupture occurred. The applied stress ratios were below the ratio of time-independent failure R = 1.043. Tests with ratios

lower than R = 1.02 showed a constantly decreasing strain rate. The ones with stress ratios up to R = 1.032 also showed a decreasing strain rate but with reduction in the decrease towards the end of the test. Finally, stress ratios above R = 1.032 displayed a decreasing strain rate, which eventually became constant and then started to increase and ended up in creep rupture. The tests show that at stress ratios around R = 1.0 ($q/q_{failure}$ = 0.94), the soil reacts very sensitive and just a slight change in the stress ratio can lead to creep failure. A shortcoming of the tests were the rather short creep phases of only 20 minutes. This may lead to false conclusions about the stability with respect to creep rupture. The gradient of the creep curves in Figure 3.23

$$m = -\frac{\Delta \log \dot{\gamma}}{\Delta \log t} \tag{3.31}$$

with $\dot{\gamma} = \dot{\varepsilon}_1 - \dot{\varepsilon}_3$ ($\dot{\varepsilon}_1$: major principle strain rate, $\dot{\varepsilon}_3$: minor principle strain rate) and t the creep time is often applied to judge the possibility of creep failure. m-values below 1.0 can potentially lead to creep failure, while m-values equal and above 1.0 lead to a stabilization of creep. Results from literature show contradictory results regarding the strain rate development and the evaluated m-values (see review in AUGUSTESEN *et al.*, 2004). The use of m as an indicator value with respect to possible creep rupture should therefore be judged carefully.

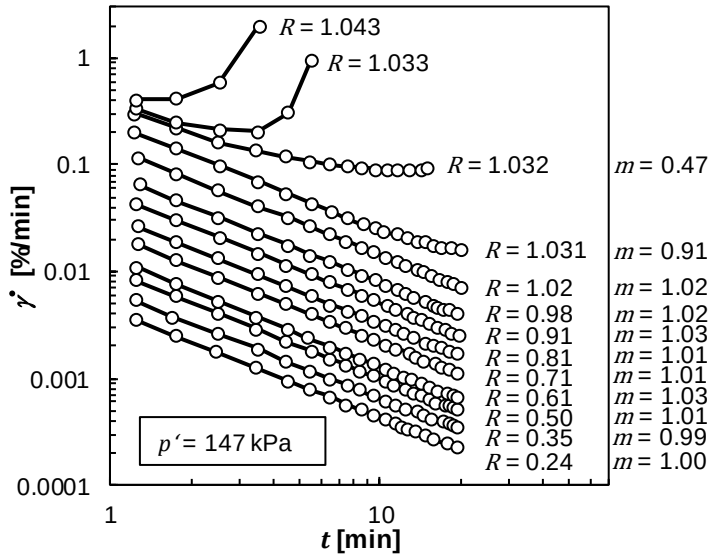

Figure 3.23: $\log(\dot{\gamma}) - \log(t)$ behaviour of sand under different stress ratios $R = q/p'$ (data from MURAYAMA *et al.*, 1984)

A possible explanation for creep rupture might be that the shear strength of the soil is reduced during the creep phase. Findings of MEJIA & VAID (1988), who performed TCD-tests with constant cell pressure σ_3 and changing vertical stresses σ_1' on Ottawa and Tailings sand and made similar observations regarding the creep rate like MURAYAMA *et al.* (1984), point in this direction. They looked at the volumetric creep behaviour and observed that at low stress ratios the creep deformations were contractive, while they were dilative at high stress ratios (R > 1.5), although the samples were prepared at a loose state and showed contractive behaviour during monotonic shearing. R = 1.5 was also the ratio at which maximum contraction occurred during monotonic shearing. At R = 1.65 creep rupture

happened, corresponding to the ratio at which failure unter monotonic loading occurred. During creep at high stress ratios the shear strength of the material is reduced due to grain degradation. This in turn can lead to a situation where the tangential forces at grain contacts increase while the normal forces decrease, ending up in creep rupture (cf. Section 3.3.3). Supporting this argumentation, KWOK & BOLTON (2013) mention the damage of the microstructure of the soil as a reason for creep rupture. KUHN & MITCHELL (1993) investigated creep rupture in a two-dimensional numerical discrete element model of an irregular packing of circular discs using a visco-frictional spring-dashpot contact model. They loaded the sample with different deviator stress levels while keeping the lateral stress constant and let it creep for up to 69 d. They found that the creep rate slows down if the overall ratio of tangential to normal contact forces decreases, whereas it accelerates and might lead to creep rupture when the ratio increases (cf. Section 3.3.3). As another explanation for the loss of shear strength during drained creep MITCHELL & SOGA (2005) mention the destruction of cementations at grain contacts during creep. But this does not explain creep rupture of freshly prepared samples that did not have the time to form cementation bonds.

Creep ruptures at constant total stresses under undrained conditions were observed by several authors (for a summary see MITCHELL & SOGA, 2005). Failure is explained by the reduction of the mean effective stresses due to developing pore water pressures, which leads to an increase of the stress ratio (cf. Figure 3.24). Thus, undrained creep tests with constant total stresses differ from creep tests under constant effective stresses. More details on undrained triaxial relaxation tests are presented in Section 3.3.2.

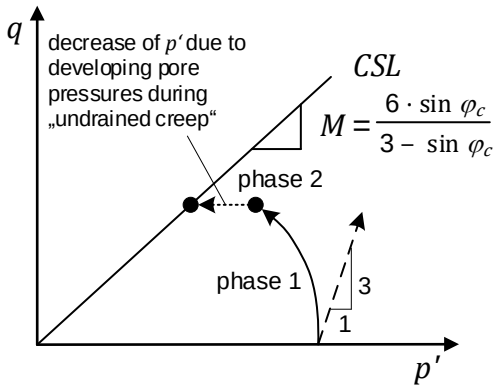

Figure 3.24: Stress path during undrained triaxial compression (phase 1) and so called “undrained creep” (phase 2)

Volumetric behaviour

According to MEJIA & VAID (1988), the ratio of deviatoric to volumetric strain rate during creep up to a stress ratio of about R = 1.13 remains constant. The strain direction is linked to the previously applied strain direction in monotonic shearing. LADE & LIU (1998) observed in TCD-tests on dense Antelope Valley sand at stress ratios far below the failure level that the strain directions in the creep phases approximately matched the ones in the previous strain controlled shearing phase. In contrast KUWANO (2001) saw in TCD-tests on Ham River sand at similar stress states and densities that the ratio of deviatoric to volumetric strains in the creep phase increased compared to the previous strain controlled shearing phase leading to higher deviatoric strains than volumetric strains in creep. Both

investigations showed a similar trend towards contractive or dilative behaviour in the creep phases, when correspondingly the shearing phases showed contractive or dilative behaviour.
BOWMAN & SOGA (2003) analyzed how the volumetric behaviour is linked to the soil type. They tested Leighton Buzzard clean silica sand, silica beach sand and imperfect glass beads in TCD-tests with creep phases of 21.6 h at p' = 600 kPa and q = 800 kPa (R = 1.33). They observed the following volumetric creep behaviour (cf. also Section 3.3.3):

a) Silica beach sand (most breakable, largest particles): Initially contractive then dilative.
b) Leighton Buzzard sand (smallest particles, angular): Dilative Creep.
c) Imperfect glass beads (least breakable, round): Very dilative in creep, because sliding and rolling are the dominant deformation mechanisms.

This behaviour corresponds well to the volumetric behaviour during monotonic shearing, where glass beads showed strong dilation, Leighton Buzzard sand was initially contractive then turned towards dilatancy and Silica beach sand behaved entirely contractive. The results by BOWMAN & SOGA show that the strain direction during creep can change in direction turning from contractive towards dilative behaviour. They confirm the findings by KUWANO (2001) mentioned before. BOWMAN & SOGA explain the volumetric creep behaviour with the different deformation mechanisms that dominate the creep phase depending on the material properties (cf. Figure 3.25). Little particle breakage and more particle sliding and rolling lead to dilative creep behaviour like for the glass beads (mechanisms 2 and 6 => 4). If breakage and asperity yield are dominant and only little sliding and rolling are happening, the behaviour in total is more contractive (mechanisms 1 and 5 => 3). Therefore, the volumetric creep in triaxial condition depends on the material properties, the stress state and the strain direction in the previous monotonic loading phase.

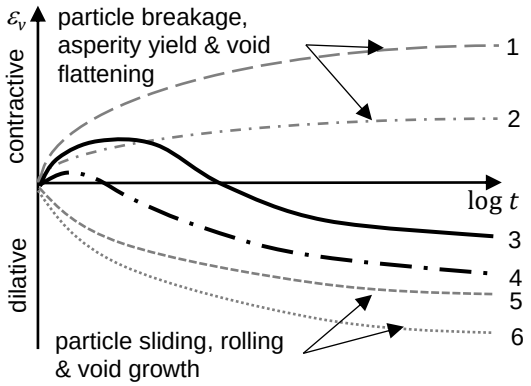

Figure 3.25: Different volumetric creep behaviour depending on material properties and the contributing deformation mechanisms (from BOWMAN & SOGA (2003) and modified)

3.3.2 Rate dependency

The rate-dependent behaviour of granular soils was extensively studied at the Tokyo University of Science by FUMIO TATSUOKA and his group (TATSUOKA *et al.,* 2002, DI BENEDETTO *et al.,* 2002,

TATSUOKA *et al.,* 2008, DUTTINE & TATSUOKA, 2009, ENOMOTO *et al.,* 2009, PENG *et al.,* 2010 and others). It can be described as very diversified and heterogeneous and as mostly non-isotache behaviour in terms of the isotache-concept by ŠUKLJE (1957). Basically four different types of rate-dependent behaviour were identified (cf. Figure 3.26):

– Isotache behaviour as it is well known from fine grained soils,
– temporary effect of strain rate and acceleration (TESRA) behaviour, in which the change of the stress-strain response following a sudden change of the strain rate (jump) is only temporary,
– combined behaviour of isotache and non-isotache type, where the stress change from a sudden change of the strain rate is not permanent, but does not vanish entirely and
– positive-negative (P&N) behaviour where the stress-strain response following a jump of the strain rate becomes stiffer, but with ongoing deformation drops below an unique rate-independent stress-strain curve (TATSUOKA *et al.,* 2008).

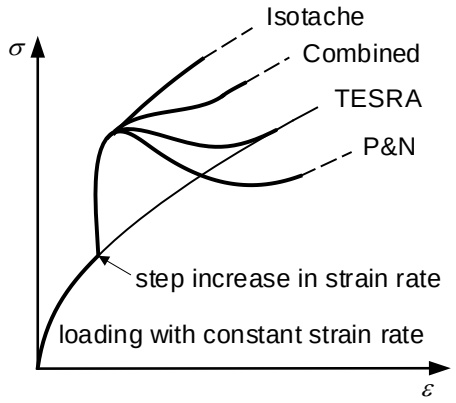

Figure 3.26: Rate-dependent stress-strain responses of granular soils (from TATSUOKA *et al.* (2008) and modified)

In isotache behaviour the stress change upon a sudden loading strain rate change remains constant under continued loading of the soil. It exists a unique relationship between the stress-strain-response and the strain rate. The isotache-concept can be illustrated by a series of parallel lines in an ε - $\log \sigma'$ - diagram (cf. Figure 3.27). They are isotaches – lines of equal strain rate – and isochrones – lines of equal creep time. Each creep isochrone corresponds to a constant strain rate. This means for a given material state (void ratio, stress state) an unique strain rate can be determined. This is further explained in Section 3.3.5.

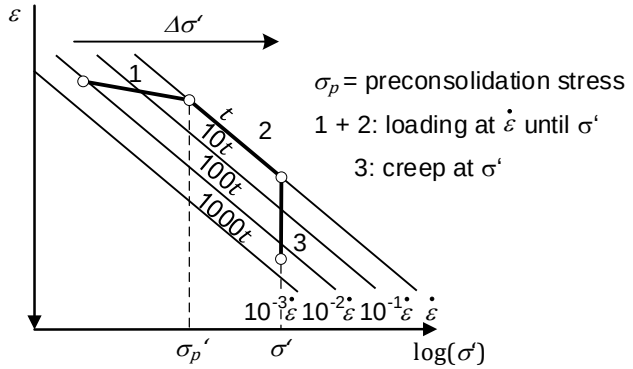

Figure 3.27: Illustration of the isotache-concept by ŠUKLJE (1957)

In TESRA-behaviour the change in stress $\Delta\sigma'$ that develops as the strain rate $\dot{\varepsilon}$ is changed stepwise decays eventually towards zero. The stress-strain behaviour during monotonic loading at a constant strain rate is independent of its value, the material is only temporarily rate-dependent. This means that to each pair of strain and effective stress an indefinite number of strain rates could theoretically be assigned. Combined type (TESRA + isotache) means that the stress change $\Delta\sigma'$ decays eventually towards a value larger than zero and P&N type means that a positive stress change $\Delta\sigma'$ upon increase in strain rate decays towards a negative value, so the strength during monotonic loading at constant $\dot{\varepsilon}$ decreases with an increase in $\dot{\varepsilon}$. Which rate-dependent behaviour a granular soil shows, depends primarily on the granulometric properties like GSD, grain shape, angularity and mineral hardness. ENOMOTO *et al.* (2009) looked extensively at the influences of these properties. Their findings are summarized in Table 3.4. Some general trends can be identified:

– Well graded angular soils show mostly isotache or TESRA behaviour,
– round well graded soils show combined or TESRA behaviour,
– angular poorly graded materials display TESRA or P&N behaviour and
– round poorly graded soils show P&N behaviour.

Depending on the deformation and applied deviator stress, it is also possible that soils show multiple types of rate-dependent behaviours during one test (TATSUOKA *et al.*, 2008).

Table 3.4: Granulometric influences on the rate-dependent behaviour of granular soils (after ENOMOTO *et al.*, 2009)

Influencing factor	Rate-dependent behaviour Isotache → Combined → TESRA → P&N
Particle shape (stiff particles)	More angular → more round
Grading	Well graded → poorly graded
Particle size	Smaller (clay) → larger (sand, gravel)
Particle crushability (mineral hardness)	More crushable → less crushable
Inter-particle bonding	Stronger → weaker → zero

TATSUOKA *et al.* (2002) and DI BENEDETTO *et al.* (2002) propose on the basis of their experimental results an extension of the isotache-concept – the so called TESRA-model –, which takes the temporary effect of a sudden strain rate change into account. An extension of the TESRA-model (TATSUOKA *et al.*, 2008) incorporates besides the TESRA behaviour all other strain rate-dependent behaviours via an additional constitutive parameter. It is based on the discretization of the strains into elastic (E) and irreversible strains, which again are subdivided into irreversible non-viscous strains (P) and viscous strains (V) (cf. Figure 3.28). For the E-P-part of the model hypoplastic or elastoplastic constitutive models can be used. The V-part is modelled by the modified TESRA-model. The model is however not capable of predicting different rate-type behaviours and is very difficult to calibrate. A Finite-Element-implementation was realized by PENG *et al.* (2010) and successfully tested by simulation of biaxial tests.

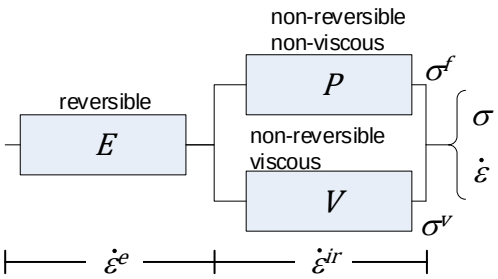

Figure 3.28: Non-linear elasto-viscoplastic three component TESRA-model by TATSUOKA *et al.* (2002)

GUDEHUS (2006) explains the temporary change in stiffness upon a jump in the strain rate by stress-fluctuations, which arise when the force chains in the grain skeleton suddenly buckle and rearrange. In this context, the term of a granular temperature is mentioned, which is a measure for the chaotic kinetic energy of the grain skeleton (HERRMANN, 1993 citey by GUDEHUS, 2006). The granular temperature depends on the critical state friction angle and the mean stress. It is however difficult to determine the granular temperature and other quantities depending on it (GUDEHUS, 2011). GUDEHUS demonstrates that, when replacing the absolute temperature by the granular temperature in the visco-hypoplastic model by NIEMUNIS (2002), the model is able to capture the rate-dependent behaviour during shearing. The model was so far only applied to element tests.

3.3.2.1 Stress relaxation

Stress relaxation – in the following also referred to as relaxation – is a special case of rate-dependent behaviour, during which the applied deformation of the soil specimen is kept constant in time. This implies for instance in a TCD-relaxation-test

– $\dot{\varepsilon}_{\mathrm{a}} = 0, \dot{\varepsilon}_r = 0$ and it follows $\dot{\varepsilon}_v = 0, \dot{\gamma} = 0$ and
– $\dot{\sigma}'_{\mathrm{a}} \neq 0, \dot{\sigma}'_r \neq 0$ and it follows $\dot{q} \neq 0, \dot{p}' \neq 0$.

The relaxation behaviour of fine grained soils can be described in the framework of the isotache-concept (cf. Section 3.3.5). However, experimental results of several authors suggest that this is not the case for granular soils (PHAM VAN BANG *et al.*, 2007, LADE, 2009, LADE *et al.*, 2010, KIKKAWA *et al.,* 2012, LADE & KARIMPOUR, 2014). LACERDA & HOUSTON (1973) performed TCD relaxation tests on Monterey quartz sand by keeping just the axial strain constant. They found a linear relationship between the relaxation of the deviator stress and the logarithm of time. The deviator and mean stress relaxed at a ratio of $\Delta q/\Delta p'$ = 3 / 1, following a drained unloading path. In their tests they observed a time period between initiation of the relaxation phase ($\dot{\varepsilon}_{\mathrm{a}}$ = 0) and the actual decrease of stress. This time period depends on the strain rate prior to relaxation – meaning a smaller time period at increasing strain rate –, which is in agreement with the findings on the influence of the loading strain rate on creep. PHAM VAN BANG *et al.* (2007) and LADE *et al.* (2010) made similar observations. These results were approved by LADE & KARIMPOUR (2014) in TCD relaxation tests on different sands. It was shown also that the relaxation-rate converged to a value independent of the prior strain rate.
While LACERDA & HOUSTON (1973) and KRIEG (2000) were able to link the relaxation behaviour of examined fined-grained soils to their creep behaviour, this was not possible for the examined relaxation and creep in sand. Generally, stress relaxation is much more pronounced in granular soils than

creep deformations or rate-effects following a jump in the strain rate. PHAM VAN BANG *et al.* (2007) performed relaxation tests in triaxial conditions with air-dried Hostun sand. They found that the relaxation magnitude is stress history and stress value-dependent. The direction of the stress change during relaxation (increase or decrease in stress) depends on the stress state, the stress path history as the distance from the last stress path reversal, the void ratio and the strain rate prior the relaxation phase.

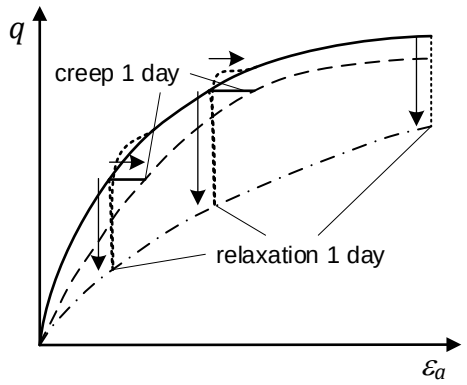

Figure 3.29: Schematic comparison between TCD creep tests and relaxation tests with periods of one day (adapted from LADE, 2009)

LADE (2009) compared results from drained triaxial compression creep tests to drained triaxial relaxation tests at the same deviatoric stress level. The creep and relaxation phases were both about one day long. As can be seen schematically in Figure 3.29, the corresponding stress-strain points obtained by creep and stress relaxation from the same stress and strain level did not match. The effect of constant strain on stress is far stronger than the effect of constant stress on strain. All authors mentioned so far, used TCD tests where volumetric strains still occurred during relaxation, because only the axial strain was controlled. The following boundary conditions apply in such a test: $\dot{\varepsilon}_1 = 0$, $\dot{\varepsilon}_2 + \dot{\varepsilon}_3 = \dot{\varepsilon}_v \neq 0$, $\dot{\sigma}_1' \neq 0$ and $\dot{\sigma}_3' = 0$. The volumetric strains occurring during such a test can lead to more relaxation. This can be seen in the test results from LADE *et al.* (2010). True relaxation tests ($\dot{\varepsilon}_1 = 0$, $\dot{\varepsilon}_3 = 0$, $\dot{\varepsilon}_v = 0$, $\dot{\sigma}_1' \neq 0$ and $\dot{\sigma}_3' \neq 0$) are easy to be carried out under undrained conditions. A comparison of drained to undrained triaxial relaxation tests by LADE & KARIMPOUR (2014) however showed very similar relaxation of the deviator stress q. The drained tests showed contractive behaviour while the undrained tests were in some cases dilative leading to negative excess pore water pressures. However, the excess pore water pressures were small compared to the mean stress level with a maximum ratio of excess pore water pressure to consolidation pressure of u/σ'_3 = 0.05. The development of only small excess pore water pressures means that the change in total stress nearly equals the change in effective stress according to

$$\sigma' = \sigma - u \tag{3.32}$$

and that the relaxation in undrained test conditions happens solely in the grain skeleton not affecting the pore water pressure. This was already found by LACERDA & HOUSTON (1973) who observed a ratio of $\Delta q/\Delta p'$ = 3 / 1 in TCU relaxation tests on different fine grained soils.

3.3.3 Micromechanical processes

Generally, the mechanical behaviour of a granular soil is governed by its structure and the acting effective stresses. Structure means the combined interaction between soil fabric, inter-particle forces and the soil composition in terms of the GSD, the particle shape and the surface roughness of grains as well as the interlocking between them. Fabric is the arrangement of particles and voids in a granular skeleton (MITCHELL & SOGA, 2005). The structure of a soil strongly influences the load transfer through the grain skeleton and its stiffness and strength. The load in granular materials is transferred through force chains that form an inhomogeneous network in the grain assembly (cf. Figure 3.30). Lightly loaded grain clusters provide lateral support to the heavily loaded force chains in between. The forces in the former are considerably lower than the forces in the latter. The ratio between longitudinal to lateral forces in the force chains depends on the contact friction angle ϑ_0 and the unevenness of the grain surface χ_u (EBER, 2006). The forces that are transferred by strong force chains can reach values of up to six times the mean force acting between grains in the sample (RADJAI *et al.*, 1996).

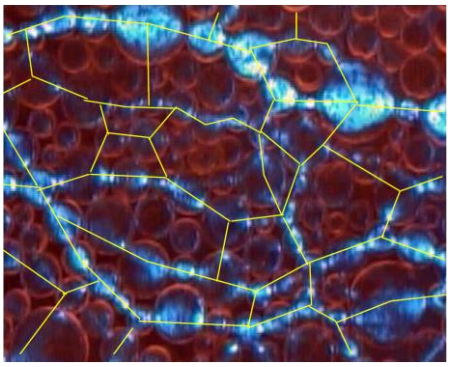

Figure 3.30: Load transfer in a grain assembly, experiments with polarized light through photoelastic disks (EBER, 2006)

During deformation, the force chains buckle and the structure of the granular material changes. The deformation may be triggered by an external loading stress or as in the case of creep by a time-dependent weakening of grains. From a micromechanical point of view, viscous effects in granular soils are a result of particle rearrangements due to translation and rotation of the grains, which are triggered by time-dependent surface degradation of the grains or crushing of entire grains (static fatigue) depending on the stress level (MEJIA & VAID, 1988, COLLIAT-DANGUS *et al.*, 1988, MESRI & VARDHANABHUTI, 2009, KARIMPOUR & LADE, 2010, KARIMPOUR & LADE, 2013). LEUNG *et al.* (1996), MCDOWELL & KHAN (2003) and LV *et al.* (2016) observed the effect of creep on the GSD by performing sieving analysis after creep stages of different duration and at different stress states. In line with these findings, GUDEHUS (2006) explains the viscous behaviour of granular soils by the chaotic kinetic energy emitted when force chains collapse due to loading (rate-dependent behaviour) or creep (static fatigue).

Following the static fatigue argumentation, JARDINE *et al.* (1999) claimed that force chains, which form during loading, can fail and rearrange with time without changing the mean effective stress. Creep can be understood as the gradual stabilization of this process in which force chains develop, buckle and fail. The failure of the force chains starts with particle rearrangements in the weakly loaded clusters. Because of the comparably low loading they can only support small shear forces at the grain

contacts. The rearrangement leads to a withdrawal of the lateral support from the strong force chains, which consequently buckle. This process slows down with time as more and more of the mean stress in the sample is transferred by normal forces and the network of strong force chains becomes self-supporting (cf. Figure 3.31). BOWMAN & SOGA (2003) were able to verify this mechanism with laboratory experiments on three different materials. They observed the change of particle orientation and variance of void sizes during creep phases in triaxial tests with durations of creep phases of up to four months. They linked ageing to microstructural changes. “Interlocking”, which is mentioned by MESRI *et al.* (1990) and SCHMERTMANN (1991) as being a mechanism for ageing, is described by BOWMAN & SOGA as a high level of edge-to-edge association of particles, providing shear and moment resistance. As a measure for interlocking the variance in void sizes is used. The greater the variance of the voids the more clustered and therefore interlocked are the particles. BOWMAN & SOGA (2003) found that grains rotate during creep in oedometric loading with their long axes towards a parallel orientation of the major principle stress trajectory. Having fallen under gravity during sample preparation, the orientation of the long axis of the grains is towards the horizontal, which is also the direction of the minor principal stress in oedometric loading. During creep with buckling of the force chains their orientation changes towards the vertical, which is the orientation of the major principle stress trajectory (cf. Figure 3.31). Furthermore, the increase of the variance in the void spacing during creep indicates the development of a more clustered and interlocked soil structure. The increased clustering of particles is also noticeable in a dilative creep behaviour, which was observed by BOWMAN & SOGA (2003) in triaxial creep tests. Especially very hard materials in a dense packing, where surface degradation and grain breakage are reduced, show a strong dilative creep behaviour, because their only possibility to move towards a more stable soil structure is through dilatancy (cf. Figure 3.25). This clustering is a mechanism behind the stress-strain response observed in oedometric and triaxial tests when the soil is loaded with constant strain-rate after a creep phase and the stress-strain curve overshoots the reference curve.

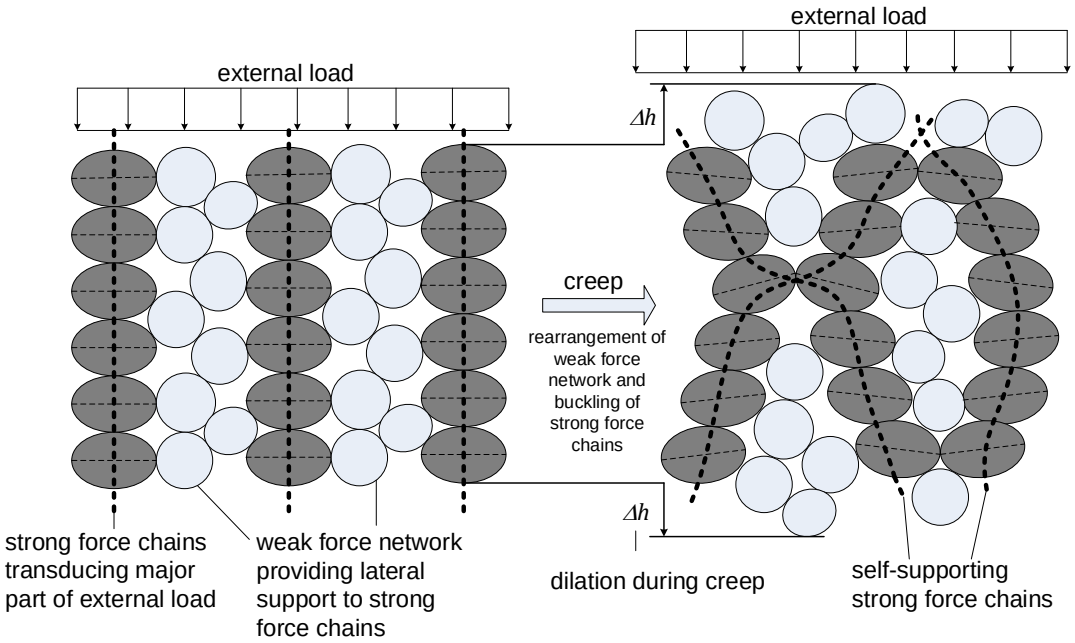

Figure 3.31: Rearrangement of force chains in a particle assembly during creep (from BOWMAN & SOGA (2003) and modified)

A decisive factor for the amount of creep deformations is the ratio of tangential to normal forces in the grain contacts. This again is dependent on the orientation of the force chain to the principle stress trajectory in the grain assembly. KUHN & MITCHELL (1993) demonstrate this by Discrete-Element-Analysis of a rectangular two-dimensional assembly of 1002 circular disks using a visco-frictional spring-dashpot-model for the grain contacts (cf. Section 3.3.1.2). Creep phases were initiated at different stress ratios between R = 0.2 and 1.4 lasting for up to 69 d. Stress ratios of $R \geq 1.0$ led to creep failure. They showed that a continuously decreasing creep rate was accompanied by a reduction of the ratio of tangential to normal forces in the grain contacts. The assembly of grains had the tendency to creep to an arrangement of force chains where as much of the loading forces as possible were transferred by normal forces. Meaning, the force chains tried to orientate parallel to the major principle stress trajectory. This is, based on the Adhesion Theory of Friction (TERZAGHI, 1925), also the state of maximum frictional stability of the grain assembly, because the maximum transferable tangential forces are directly proportional to the acting normal forces. On the other hand, KUHN & MITCHELL observed that creep failure was accompanied by an increase of the ratio of tangential to normal forces in the grain contacts.

A reason for the time-dependent buckling of force chains at constant effective stress is the time-dependent degradation of grains. This was shown by KARIMPOUR & LADE (2010) and KARIMPOUR & LADE (2013), who performed isotropic and triaxial high pressure creep tests ($\sigma_3{}'$ = 8000 kPa) on Virginia Beach sand (quartz-feldspar sand). They performed the creep phases at stages of equal amount of energy-input per volume applied to the soil rather than at the same deviator stress and mean stress. They state that particle crushing is related to the energy-input per volume. The energy-input was defined by KARIMPOUR & LADE as

$$E = \sum \sigma'_c \Delta\varepsilon_v + \sum q\, \Delta\varepsilon_a \tag{3.33}$$

with σ'_c as the effective confining pressure, $\Delta\varepsilon_v$ a volumetric strain increment, q the deviator stress and $\Delta\varepsilon_a$ an axial strain increment. They concluded that the amount of creep at equal energy-input depends on the prior loading strain rate. The presented GSDs after creep with different prior loading strain rate showed a correspondence between creep and the amount of grain crushing.

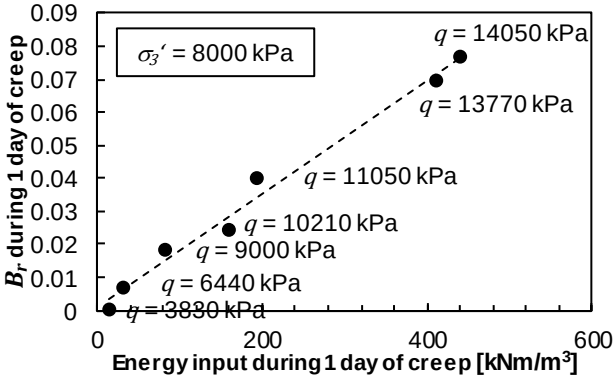

Figure 3.32: HARDIN's relative breakage factor B_r versus energy input during 24 h of creep at different deviator stresses (data from KARIMPOUR & LADE, 2013)

The triaxial creep tests on Virginia Beach sand by KARIMPOUR & LADE (2013) show a linear relationship between increasing energy-input and HARDIN's relative breakage factor B_r (cf. Equation (3.1)) during 24 h of creep (cf. Figure 3.32). With higher deviator stress the amount of crushing and therefore creep increased, caused by the higher energy-input.
However, it is doubtful if equal energy input at equal loading strain rate leads to equal amount of creep at the given definition of energy input of (3.33). If this would be the case, the description of the creep behaviour by the energy input would be valid. Considering for instance two triaxial tests loaded to the same energy state defined by (3.33) (cf. Figure 3.33). Test 1 was sheared under lower confining pressure than test 2 reaching a lower deviator stress in the critical state than test 2. In the critical state the volumetric strain, confining pressure and deviator stress are constant. The axial strain however can still be increased. Using the definition of (3.33) test 1 can reach the same energy input level like test 2 by increasing the axial strain, while all other parameters remain constant. However, the creep strains initiated at that point will most certainly be different in test 1 and 2, which makes the comparison of creep at equal levels of energy input difficult.

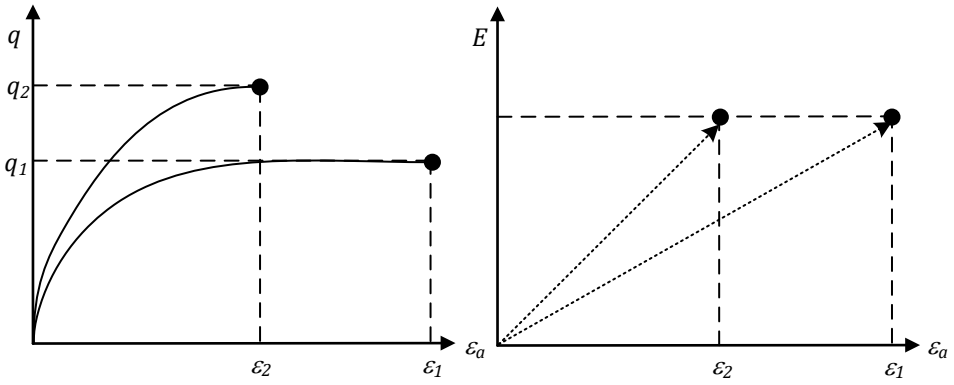

Figure 3.33: Schematics of two triaxial tests with equal energy input according to (3.33), but different stress – strain paths

It was found by several authors that the initial strain rate in creep depends on the previous loading-rate: The higher the strain rate, the higher the initial creep rate (cf. Figure 3.34). When creep begins after loading with a very low strain rate, it may take some time until creep strains become visible. Regardless of the loading strain rate, however, the two creep curves achieve the same gradient on a logarithmic time scale.

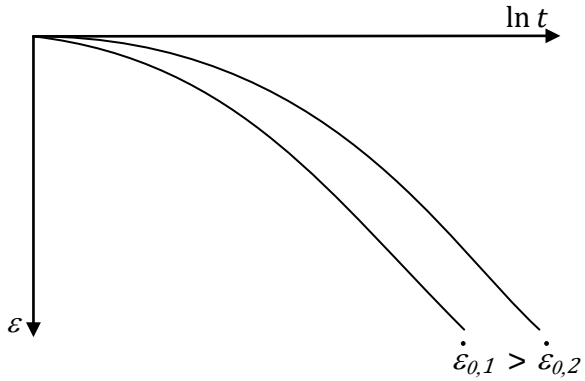

Figure 3.34: Creep after different loading strain rates

KARIMPOUR & LADE (2010) explain this by the different times the grain-assembly requires to adjust to the loading. At fast loading the grains do not degrade, because the time for weakening of the material (static fatigue) is too short. Consequently, more degradation occurs in the creep phase resulting in a higher creep rate on initiation of the creep phase. On the contrary, at lower strain-rate more degradation occurs and the grain-assembly becomes more stable during the loading stage. Therefore, the creep rate is lower at the beginning of the creep phase. The tests by KARIMPOUR & LADE all showed contractive volumetric behaviour during monotonic shearing. The strain directions in the creep phases approximately matched the ones in the previous strain controlled shearing phase, confirming the findings of LADE & LIU (1998).

The time-dependency of the particle strength even at very low constant forces was shown by MICHALOWSKI & NADUKURU (2012) and WANG & MICHALOWSKI (2015), who demonstrated that even strong minerals like quartz show a time-dependent weakening of the material at contact points. They loaded a single quartz grain with a constant force (0.65 N) against an iron plate and observed at different times the change of the grain surface texture by Scanning-Electron-Microscopy (SEM). A continuous change of the grain surface and a breakage of asperities were detected. Such degradation takes also place in the force chains at grain contacts, which consequently buckle even under constant mean effective stress. Further tests by MICHALOWSKI *et al.* (2018) with the same setup as mentioned before and with materials of different surface roughness show a strong dependency of creep at the particle contact on its surface roughness. The rougher a surface, the more stress concentrates on the micro-morphological features leading to increased grain damage and a stronger deformation of the grain. As postulated by the authors, during this process, the number of contact points per nominal contact area increases, which is associated with an increase in stiffness. If the stiffness at the grain contacts increases, while the vertical stress is constant during oedometric creep, the lateral stress must increase. They demonstrated this by oedometric creep tests in a soft oedometer, in which the lateral stress during creep was measured. They observed that the higher roughness of the grain surface and the therefore stronger degradation at the contact points led to larger change of the lateral stresses during creep. The structuration effects, including the contact-point-changes, proven by BOWMAN & SOGA (2003) lead to the increasing stiffness during creep.

3.3.3.1 Influence of saturation

The influence of saturation with fluid (mostly water) on creep strains showed in most cases in literature an increase of creep (e.g. MIURA & YAMANOUCHI, 1975, BRZESOWSKY *et al.*, 2014). However, some authors observed no influence of saturation (LEUNG *et al.*, 1996). MIURA & YAMANOUCHI (1975) performed oedometric loading tests on dry and wet Toyoura sand. They flooded the samples with fluids with different dipole moments and evaluated the resulting particle breakage after loading the sample with a constant stress of 40 MPa for 15 minutes. The tests showed increasing grain breakage and therefore creep strains if the samples were wet and if the wetting fluid had a large ratio of dipole moment to molar volume. The increasing grain breakage and therefore creep strains seem to result from elevated particle degradation due to the reduction of the surface energy of the grains caused by the dipole character of the fluids especially in pre-existing cracks of the grains. In order to lower the surface energy inside a crack the fluid has to be able to penetrate into the crack and wet it. Therefore

fluids with large ratios of dipole moment to molar volume induce the larger grain degradation (MIURA & YAMANOUCHI, 1975). BRZESOWSKY *et al.* (2014) report the same increase in creep under oedometric loading of a quartz sand and explain it by the term “stress corrosion cracking” established by ATKINSON (1979) and ATKINSON & MEREDITH (1981). It stands for a weakening of the Silicium-Oxygen-bonds of the quartz cristal by adsorption of water molecules onto its surface.
The creep tests by LEUNG *et al.* (1996) were performed with miniature piles in centrifuge testing. The piles were installed in medium dense fine uniformly graded angular silica sand. They were loaded by maximum loads of 609 N leading to maximum stresses at the pile base of 5.0 MPa. The creep tests with dry as well as with saturated sand showed the same amount of strains over time. The authors conclude that creep in sand is not influenced by water-induced chemical reactions, viscosity or moisture related effects. The results contradict many other studies. Furthermore, the testing of piles represents a boundary value problem in which other influences that cannot be further quantified can influence the deformation behaviour.
The effect of saturation with water and high-pH solutions was tested by MICHALOWSKI *et al.* (2018) showing an increase in creep with increasing pH-value of the fluid compared to the air-dry state. These findings support the already mentioned results of MIURA & YAMANOUCHI (1975) and BRZESOWSKY *et al.* (2014).

3.3.4 Ageing

Ageing lies not within the focus of this study, but the viscous behaviour of granular soils and ageing effects are closely linked as reported by several authors (JARDINE *et al.,* 1999, BOWMAN & SOGA, 2003, SUAREZ, 2012 and others). Therefore, ageing effects will be shortly addressed here, also as an outlook on possible future predictions of ageing effects and their consideration in engineering design through the possibility of measuring viscous effects in granular soil.
Different definitions of ageing with respect to time-dependent change of soil properties exist. Important is the differentiation between ageing mechanisms and ageing results. Generally, ageing can mean the change of any property of the soil with time. Also the time-scale has to be considered, in which the change takes place. Of course, with respect to geological time-scales soils and also rocks undergo fundamental changes in their properties, mostly by weathering or other metamorphoses. From an engineering point of view, the property changes concerning for example the stiffness, shear strength and liquefaction resistance of the soil as well as the hydraulic conductivity, which happen within engineering time-scales (i.e. days to less than 100 years), are most important. The effects of ageing can be positive or negative with respect to the considered boundary value problem. Chemical, microbiological and mechanical processes are considered mechanisms for ageing, which contribute to the time-dependent change of soil properties depending on the environmental conditions. Chemical and microbiological processes can lead to cementation of the grains by precipitation and deposition of e.g. carbonates, which are formed either by the metabolism of microorganisms or the chemical environment (STOCKS-FISCHER *et al.*, 1999). The cementations can lead to increased stiffness and shear strength and also to reduced hydraulic conductivity as ageing results. The influence of these two processes is heavily dependent on environmental factors like saturation and chemical composites of the soil and in the water. They have been seen as the key aging mechanisms, when explaining the time-dependent stiffness and strength gain of freshly deposited and densified granular soils

in the past (MITCHELL & SOLYMAR, 1984 and MITCHELL, 1986). More recent findings regard mechanical processes as the dominant mechanisms of ageing of coarse-grained soils, since ageing effects are also present in uncemented soils. Ageing effects are generally most prominent in granular soil just after the grain skeleton was intensively disturbed for instance by dynamic compaction, explosive compaction or pile driving (YORK *et al.*, 1995, KARLSRUD, 2012) and after deposition. The disturbance leads to a destruction of the existing soil structure, which redevelops over time after the disturbance ceased. This is closely connected with the micromechanical processes described in Section 3.3.3. Micromechanical processes used to explain ageing and creep are similar, i.e. static fatigue at grain contacts and grain breakage leading to rearrangement of force chains (cf. Section 3.3.3) (JARDINE *et al.,* 1999, BOWMAN & SOGA, 2003 and SUAREZ, 2012). This indicates that there must be a link between creep and ageing. However, creep deformations cannot always explain ageing to a full extent. Besides the apparent deformations, the change in the soil structure must also have an influence on the amount of ageing. So far no approach has been presented that can account for ageing effects within a framework of a constitutive model independently of specific boundary value problems.

3.3.5 Analytical description of viscous behaviour under oedometric conditions

Creep strains of fine grained soils in oedometric compression can be described by the logarithmic correlation between time and volumetric strain found by BUISMAN (1936)

$$\varepsilon - \varepsilon_0 = C_B \cdot log \frac{t}{t_{ref}} \qquad \text{with } t > t_{ref} \quad \text{(cf. Figure 3.35 (b))} \tag{3.34}$$

or similar

$$\varepsilon - \varepsilon_0 = C_B \cdot log \frac{t_{ref} + t}{t_{ref}} \qquad \text{with } t > 0 \text{ (cf. Figure 3.35 (a))} \tag{3.35}$$

where t_{ref} is a reference time and C_B is the correlation index called BUISMAN-coefficient. The difference between (3.34) and (3.35) is visualized in Figure 3.35. With (3.35) the creep strains converge towards a line with the gradient C_B. The time it needs for convergence depends on the chosen reference time. It can be approximated that it needs $10 \cdot t_{ref}$ for convergence. In case of (3.34) the creep strains are represented by a straight line with $\log t$ that originates from $t = t_{ref}$ and ε_0.

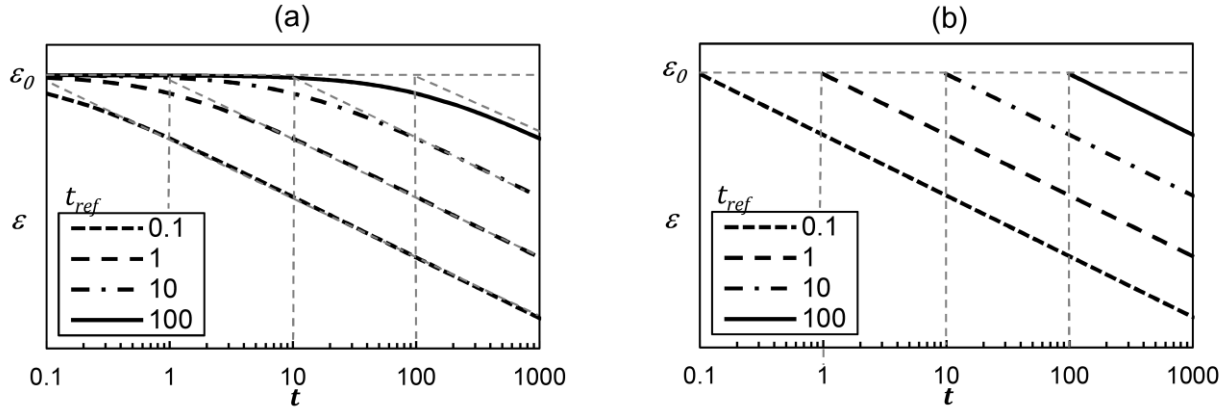

Figure 3.35: Graphical representation of (a) Equation (3.35) and (b) Equation (3.34)

The reference time for determination of C_B is in element testing often chosen to be t_{EOP} (cf. Figure 3.36) to detect creep settlements without the influence of consolidation.

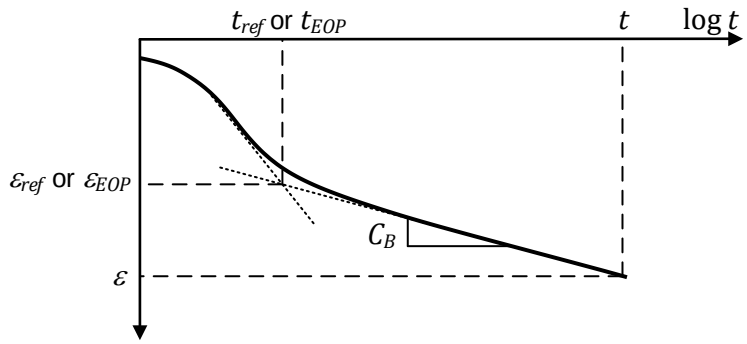

Figure 3.36: Typical strain over logarithm of time relation of saturated fine grained soil

Other formulations for determination of creep deformations use the void ratio or the natural logarithm instead of the logarithm to the base of ten:

$$e_0 - e_i = C_\alpha \cdot \log\frac{t_{ref} + t}{t_{ref}} \qquad \text{or} \tag{3.36}$$

$$\varepsilon - \varepsilon_{ref} = C \cdot \ln\frac{t_{ref} + t}{t_{ref}} \tag{3.37}$$

with C_α respectively C as the creep-coefficients and $t > 0$.
The approach by BUISMAN was developed further in the context of fine grained soil behaviour by BJERRUM (1967) and GARLANGER (1972) for consideration of stress- and time-dependent compression. GARLANGER presented the following σ' - e - t - relationship for oedometric loading conditions

$$e_0 - e_i = C_s \cdot \log\frac{\sigma'_{p0}}{\sigma'_0} + C_c \cdot \log\frac{\sigma'}{\sigma'_{p0}} + C_\alpha \cdot \log\frac{t_{ref} + t}{t_{ref}} \qquad (t > 0)\,. \tag{3.38}$$

The relationship from (3.38) is presented in Figure 3.37. The vertical distance between the displayed isochronic lines depends on the creep-coefficient. Approach (3.38) only allows for decoupled analysis of deformations in virgin loading, un- and reloading as well as of creep deformations. The initial preconsolidation stress σ'_{p0} and the reference time t_{ref} (i.e. time of the normal consolidated state $OCR = 1$), from which time-dependent strains start to develop, cannot be determined independently. Furthermore, the determination of the reference time t_{ref} cannot be related to a unique physical point in time, e.g. the end of primary consolidation (CHRISTIE & TONKS, 1985). Following Hypothesis B deformations due to creep and primary consolidation occur simultaneously at times $t < t_{EOP}$.

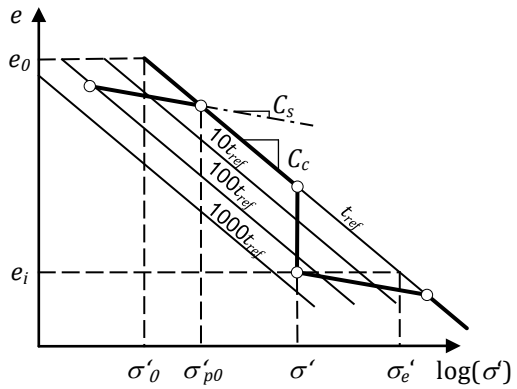

Figure 3.37: Graphical representation of the approach by GARLANGER (1972) for calculation of the stress and time-dependent void ratio change under oedometric loading conditions

Different approaches for the determination of the reference time have been proposed (e.g. JANBU, 1969 and CHRISTIE & TONKS, 1985), which will not be addressed here. Generally, any number of pairs of a reference time t_{ref} with the corresponding consolidation stress σ'_{p0} can be found. They have to be determined depending on the respective boundary value problem and element tests performed to calibrate model parameters.

BUISMAN mentions that C_B is proportional to the applied stress. For relevant stress ranges in engineering applications however, C_B is often assumed to be independent of the stress (KRIEG, 2000). Alternatively, MESRI & GODLEWSKI (1977), MESRI & CHOI (1979) and MESRI & CASTRO (1987) developed the C_α/C_c - concept for the description of the creep behaviour of soils, which is based on the stress and void ratio independence of the ratio of the creep-coefficient to the compression index

$$\frac{C_\alpha}{C_c} = \frac{\Delta e_{stress} \cdot \Delta\log(t)}{\Delta e_{time} \cdot \Delta\log(\sigma')} = \quad \text{constant} \tag{3.39}$$

in virgin loading as well as in un- and reloading. The concept was originally developed for soft soils. The parameters C_α and C_c can be evaluated as secant values according to Figure 3.38. The C_c-value at the end of primary consolidation and the C_α-value from the linear slope of the secondary compression curve in an e - $\log t$ - diagram are used for prediction of stress and time-dependent compression. Some soils do not show a constant C_α with time in secondary compression. In these cases it was found that the C_α/C_c -ratio remains not only constant with a change in consolidation stress but also with the change in time, since C_c also showed a change in time.

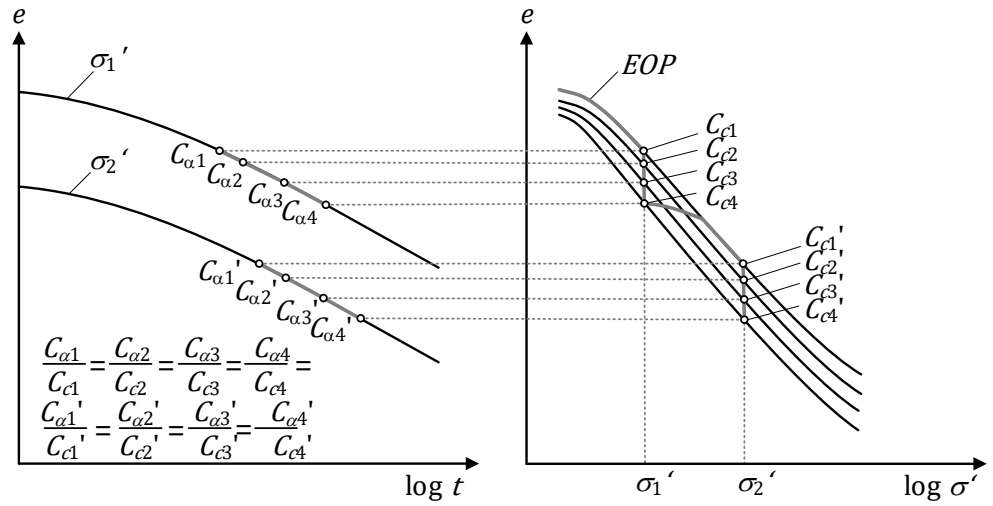

Figure 3.38: C_α / C_c - concept by MESRI & GODLEWSKI (1977)

With a constant C_α/C_c it is therefore possible to predict the stress and time-dependent shape of compression curves of soft soils. Based on oedometric test results MESRI *et al.* (1990) and MESRI & VARDHANABHUTI (2009) postulate the transferability of the C_α/C_c -concept to granular soils (cf. Figure 3.39). The C_α/C_c -ratio is assumed to be independent of the density and stress state of the soil. However, the test results presented by MESRI *et al.* (1990) show significant variation in the C_α/C_c -ratio (cf. Figure 3.39). The sample from Lake Michigan Beach Sand, which was tested by using medium-density specimens in a 6.35 cm diameter and 1.90 cm high stainless steel consolidation ring in the pressure range of 50 to 3000 kPa, shows only due to the different stress levels a variation of the C_α/C_c -ratio from 0.023 for low stresses to 0.015 for high stresses. Other presented test results have too few data points to judge the development of their C_α/C_c -ratio. Own oedometer tests on medium quartz sand MS in a stress range from 250 to 7500 kPa on very dense and medium dense samples presented in Figure 3.39 also show considerable variations in the C_α/C_c -ratio (cf. Section 4).

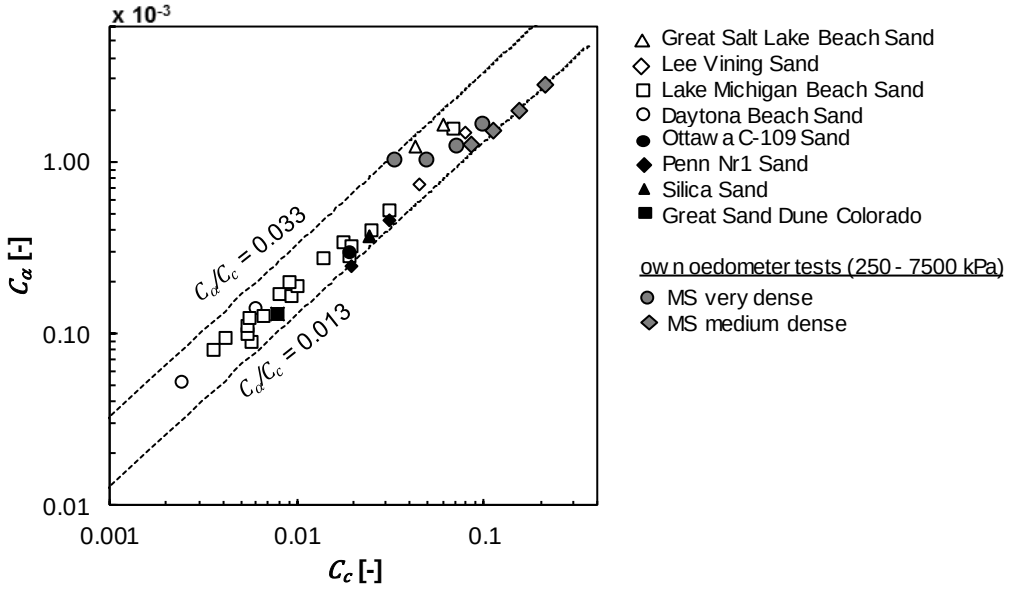

Figure 3.39: Results of C_α / C_c-ratios from oedometer tests on clean fine to medium sands (data from MESRI *et al.* (1990) and own tests)

Based on oedometric compression tests on soft soils ŠUKLJE (1957) recognized that after EOP, compression curves of equal strain rate $\dot{\varepsilon}$ are parallel when plotted in the e - $\log \sigma'$ - diagram. These isotaches can be derived from the test results of oedometric tests by

$$\dot{\varepsilon}(1+e)ln(10) = \frac{\partial \varepsilon}{\partial t}(1+e)ln(10) = \frac{C_\alpha}{t_{ref}+t} \quad (t>0) \tag{3.40}$$

which is the derivative of (3.36). Expression (3.40) emphasises the fact that creep time and strain rate are interconnected and that curves of equal creep time are also curves of equal strain rate in an e - $\log \sigma'$ - representation, which is the basis of the isotache-concept. The distance between two isotache or isochrone compression lines can be determined from

$$\frac{\sigma'_0}{\sigma'_i} = \left(\frac{\dot{\varepsilon}_0}{\dot{\varepsilon}_i}\right)^{C_\alpha/C_c} \qquad \text{(MESRI \& CHOI, 1979)} \tag{3.41}$$

or equivalently

$$\frac{\sigma'_0}{\sigma'_i} = \left(\frac{t_i}{t_0}\right)^{C_\alpha/C_c} \quad (t_i > t_0) \quad \text{(MURAKAMI, 1979).} \tag{3.42}$$

It was furthermore shown that the ratio of C_α/C_c is approximately equal to the viscosity index I_v by LEINENKUGEL (1976) and GUDEHUS & LEINENKUGEL (1978) (KLOBE, 1992)

$$I_v = \frac{C_\alpha}{C_c}. \tag{3.43}$$

LEINENKUGEL (1976) originally defined I_v from biaxial tests via

$$I_v = \frac{\tau_i/\tau_0 - 1}{\ln(\dot{\varepsilon}_i/\dot{\varepsilon}_0)} \tag{3.44}$$

with τ_i and τ_0 the shear stresses before and after a change in strain rate. KRIEG (2000) later defined I_v in the framework of a NORTON (1929) approach as

$$I_v = \frac{\ln\frac{\sigma'_0}{\sigma'_i}}{\ln\frac{\dot{\varepsilon}_0}{\dot{\varepsilon}_i}} = \frac{\ln\frac{\sigma'_0}{\sigma'_i}}{\ln\frac{t_i}{t_0}} \quad . \tag{3.45}$$

LEINENKUGEL (1976) showed that stress relaxation of fine grained soils could also be described by the viscosity index. Different approaches were proposed to describe stress relaxation analytically. It can be described by

$$\sigma'_i = \sigma'_0\left(1 - I_v \cdot \ln\frac{t_{ref}+t}{t_{ref}}\right) \quad (t>0) \qquad \text{(LEINENKUGEL, 1976 adapted by KRIEG, 2000),} \tag{3.46}$$

$$\sigma'_i = \sigma'_0 \left(\frac{t_{ref}}{t_{ref} + t} \right)^{I_v} \quad (t > 0) \qquad \text{(KRIEG, 2000),} \tag{3.47}$$

or similary

$$\sigma'_i = \sigma'_0 \left(\frac{t_0}{t} \right)^{I_v} \quad \text{from (3.45).} \tag{3.48}$$

with t_0 the starting time of relaxation and $t > t_0$. Relaxation according to (3.46), (3.47) and (3.48) is schematically shown in Figure 3.40. (3.46) and (3.47) give converging relaxation curves depending on the reference time. In case of (3.46) the relaxation approaches a constant slope, while (3.47) leads comparatively to slower relaxation over time. With (3.48) the relaxation curves pass through the pre-consolidation stress at the reference time and develop like with (3.47).

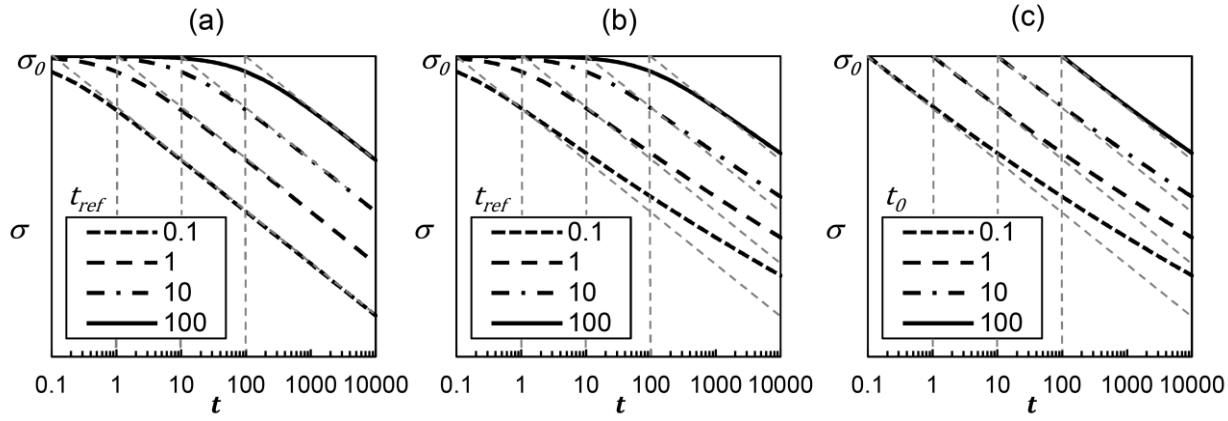

Figure 3.40: Relaxation according to (a) (3.46), (b) (3.47) and (c) (3.48)

As in creep, the relaxation behaviour depends on the preceding loading strain rate. This was found for fine grained soils (LACERDA & HOUSTON, 1973) as well as for granular soils (LADE & KARIMPOUR, 2014). Under consideration of (3.46), (3.47) and (3.48), the relaxation behaviour depends on the preceding stress rate $\dot{\sigma}$, which is in strain rate-controlled testing imposed by the loading strain rate. The derivative of (3.47) gives the stress rate

$$\dot{\sigma}' = \frac{I_v \sigma'_0}{t_{ref} + t'} \left(\frac{t_{ref}}{t_{ref} + t} \right)^{I_v} . \tag{3.49}$$

With t = 0 at the start of relaxation it follows

$$\dot{\sigma}'_{t=0} = \frac{I_v \sigma'_0}{t_{ref}} \tag{3.50}$$

and with

$$\dot{\sigma}'_{t=0} = \frac{\sigma'_0 (1+e) \ln(10)}{C_c} \dot{\varepsilon}_0 \tag{3.51}$$

as well as (3.43), (3.50) can be rewritten to

$$t_{ref} = \frac{C_\alpha}{\dot{\varepsilon}_0(1+e)\ln(10)}, \tag{3.52}$$

which is equal to (3.40). Hence, the stress rate at initiation of relaxation and the relaxation-reference time depend on the prior loading strain rate just like the creep rate. They can be described by the same approach.

Based on the finding of strain path and strain rate history independence of fine grained soils explained in Section 3.1.5, KRIEG (2000) concluded that creep, rate dependency and relaxation can be described by I_v with the interrelation

$$\underbrace{\overbrace{\left(\frac{\sigma'_0}{\sigma'_i}\right)}^{\text{compression}\rightarrow}}_{\text{relaxation}\rightarrow} = \underbrace{\overbrace{\left(\frac{\dot{e}_0}{\dot{e}_i}\right)^{I_v}}^{\text{creep rate}\rightarrow}}_{\text{rate dependency}\rightarrow} = \underbrace{\overbrace{\left(\frac{t_i}{t_0}\right)^{I_v} = \left(\frac{t+t_0}{t_0}\right)^{I_v}}^{\text{creep time}}}_{\text{relaxation time}} . \tag{3.53}$$

Figure 3.41 gives a graphical representation of Expression (3.53). No matter if the soil creeps for a time period of $t = t_i - t_0$ from the point σ'_i/e_0 or if it relaxes for the same period of time from the point σ'_0/e_i, it will always reach the same point σ'_i/e_i, as long as the soil is in a normal consolidated state in σ'_i/e_0 or σ'_0/e_i. Only the proportionality coefficients are not the same, respectively I_v and C_α. The same is true for a sudden change of the strain rate of the size

$$\frac{\dot{e}_0}{\dot{e}_i} = \frac{t_0}{t_i} . \tag{3.54}$$

For oedometric conditions also applies

$$\frac{\dot{\varepsilon}_0}{\dot{\varepsilon}_i} = \frac{\dot{e}_0}{\dot{e}_i} = \frac{t_i}{t_0} . \tag{3.55}$$

So, the current σ' is a unique function of instantaneous e and its rate $\dot{e}$. Any combination of void ratio e, effective stress σ' and rate of change of void ratio $\dot{e}$ is unique (DEGAGO *et al.*, 2011). Since the compression behaviour of fine grained soil in oedometric conditions is independent of the deformation rate history (cf. Section 3.1.5), two of the three parameters e, σ' and $\dot{e}$ are enough to describe the third and therefore the soil behaviour.

Equation (3.53) can be separated into the three appearances of soil viscosity:

Relaxation

$$\frac{\sigma'_0}{\sigma'_i} = \left(\frac{t_i}{t_0}\right)^{I_v}, \tag{3.56}$$

$\dot{e}$- and $\dot{\varepsilon}$-jump respectively

$$\frac{\sigma'_0}{\sigma'_i} = \left(\frac{\dot{e}_0}{\dot{e}_i}\right)^{I_v}, \tag{3.57}$$

and creep

$$\varepsilon_i - \varepsilon_0 = C \cdot \ln\left(\frac{t_i}{t_0}\right) = C \cdot \ln\left(\frac{\dot{e}_0}{\dot{e}_i}\right) \qquad \text{following (3.54).} \tag{3.58}$$

It follows

$$\lambda \cdot \ln\left(\frac{\sigma'_0}{\sigma'_i}\right) = C \cdot \ln\left(\frac{t_i}{t_0}\right) = C \cdot \ln\left(\frac{\dot{e}_0}{\dot{e}_i}\right) \qquad \text{or} \quad \frac{\sigma'_0}{\sigma'_i} = \left(\frac{t_i}{t_0}\right)^{C/\lambda} = \left(\frac{\dot{e}_0}{\dot{e}_i}\right)^{C/\lambda}. \tag{3.59}$$

Considering that the viscosity index I_v is equal to the ratio of C_α/C_c respectively C/λ for fine grained soils (KLOBE, 1992, KRIEG, 2000), (3.59) can be rewritten to

$$\frac{\sigma'_0}{\sigma'_i} = \left(\frac{t_i}{t_0}\right)^{I_v} = \left(\frac{\dot{e}_0}{\dot{e}_i}\right)^{I_v}, \tag{3.60}$$

which is equivalent to (3.41) and (3.42) with I_v from (3.45).
These descriptions of the time-dependent behaviour assume that the relationship between strain and logarithm of time is linear and that C_α/C_c is constant. This is true for fine grained soils in many cases and time spans for prediction of deformations of engineering structures.

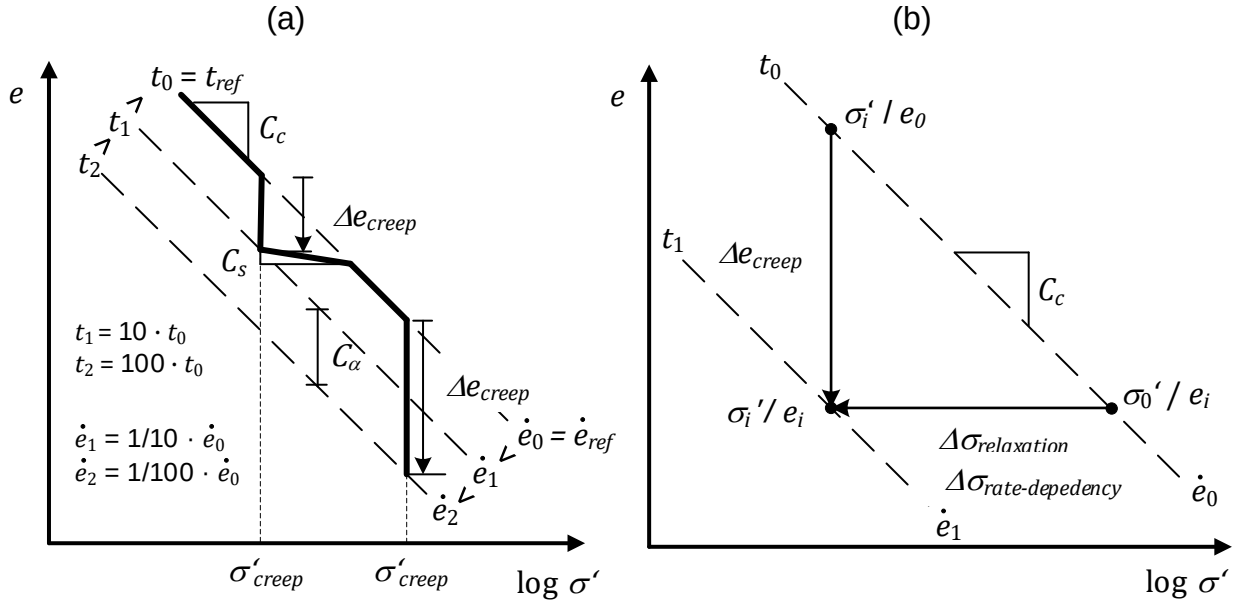

Figure 3.41: (a) Idealized stress-strain behaviour of fine grained soils, (b) relationship between creep, rate dependency and relaxation (according to KRIEG, 2000)

3.4 Conclusions

The review in this section shows that the time-dependent behaviour of sands is quite complex and common approaches to describe it, usually developed on the basis of data from fine grained soils, are not fit to describe it on all its aspects. Compared to the manifold data on fine grained soils the data set available on the time-dependent behaviour of granular soils is small. This thesis aims at

providing a data set on several different granular soils on the aspects of creep an strain rate dependent behaviour including stress relaxation. Such a data set is still missing in literature. Available publications just cover one or two of the named aspects. Such a data set can be a basis for future developments or the testing of constitutive models covering time-dependent behaviour of granular soils.

4 Element tests

The element tests investigate the influences of the state and different loading paths on the viscous behaviour for different types of sand. The soil state was varied with respect to the relative density, the stress state. The majority of the tests was conducted with air-dry samples but one test series compares the behaviour of air-dry and fully saturated samples. Since this study was motivated by the deformations of open cast mines in the Renish lignite mining area, the tested sands are representative for those encountered in the Garzweiler open cast mining dump. Other soils from the Munich area were used to investigate special influences of the soil type on viscous behaviour, for which the open cast mining sands were not suitable. In total, six different sand samples were investigated, four from the open cast mine and two from a quarry near Munich. The viscous behaviour of those samples was investigated under oedometric conditions exclusively.

4.1 Oedometer tests

Oedometer tests are commonly used in soil mechanics to investigate the soil behaviour in compression and swelling. The boundary conditions in an oedometer test depict the conditions in a soil body without surface inclination, as the vertical (axial) deformation is unconstrained, while the horizontal (radial) deformation is constrained. Hence, the boundary conditions in an oedometer test are $\dot{\varepsilon}_a \neq 0$ and $\dot{\varepsilon}_r = 0$. In oedometric tests cylindrical soil bodies are tested in a load- and / or deformation controlled manner (cf. Figure 4.1). It is assumed that the soil body deforms homogenously and therefore the volumetric strain of the sample can be measured by the axial strain component only ($\varepsilon_a = \varepsilon_v$). The stress state in the sample is also assumed to be homogenous and the vertical stress can be derived from the measured forces F. Laboratory tests with homogenous stress and strain distributions in the sample are called element tests.

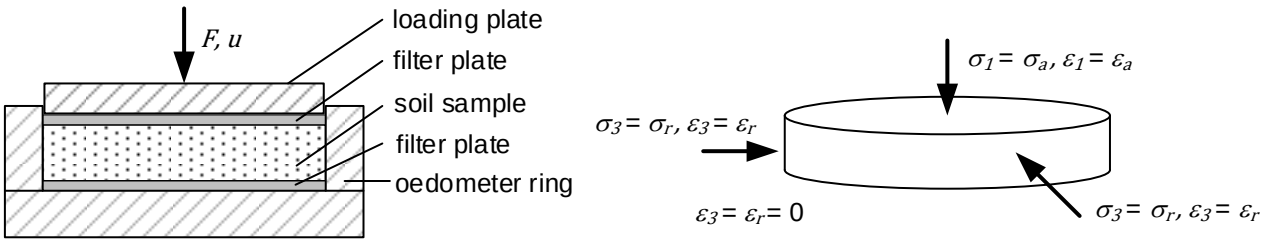

Figure 4.1: Sketch of fixed ring oedometer device and stress as well as strain definitions

During the test, the axial force F and the vertical displacement u of the loading plate are measured. Stresses and strains (natural strain definition) are calculated according to

$$\sigma_a = F/A \tag{4.1}$$

and

$$\varepsilon_a = -\ln\left(\frac{h_{ini} - u}{h_{ini}}\right) \tag{4.2}$$

with A being the sample area and h_{ini} the initial sample height. The void ratio is determined via

$$e = e_0 - \varepsilon_a(1 + e_0) \tag{4.3}$$

with e_0 being the initial void ratio. The axial and radial stresses and strains in the oedometer test are also the principal stresses and strains. The difference between axial and radial stresses in the sample leads to deviatoric stresses by

$$q = \sigma_a \cdot (1 - K_0) \tag{4.4}$$

with K_0 the ratio of radial σ_r to axial σ_a stresses. According to experimental evidence, K_0 in normally-consolidated ($K_{0,nc}$) and overconsolidated ($K_{0,oc}$) states can be estimated using the empirical relationship proposed by JAKY (1948)

$$K_{0,nc} = 1 - sin\varphi'_p \tag{4.5}$$

and MAYNE & KULHAWY (1982)

$$K_{0,oc} = K_{0,nc} \cdot OCR^{sin\varphi'_p}\,. \tag{4.6}$$

with φ'_p being the peak friction angle. (4.6) was introduced for granular and fine grained soils and derived from K_0 measurements in loading and unloading. A change in OCR can be caused by a load change ($OCR = \sigma'_0/\sigma'_i$) or by creep according to (3.42). If loading continues after a creep phase, the stress-strain relationship is controlled by the unloading-reloading stiffness until the normal consolidation line is reached. This was already presented by many authors and was again confirmed by the investigations of MICHALOWSKI *et al.* (2018), who link the change of K_0 with creep time to ageing effects (cf. Section 3.3.3).

4.1.1 Limitations of oedometer tests

The homogenous stress and strain distribution in an oedometer test is only an assumption. In reality, stresses and strains are not homogenous and the test results can be influenced by several errors. The friction between the oedometer ring and the sample leads to a shear stress acting against the vertical stress and strain at the edge of the sample. Other sources of stress inhomogeneity are an uneven sample surface, density variations in the sample, a tilting of the top cap or unwanted radial strains of the oedometer ring leading to a violation of the oedometric boundary conditions. The three latter influences can be remedied by careful sample preparation and the choice of an appropriately stiff oedometer device. The influences of an uneven sample surface and the wall friction act antagonistic with respect to the optimal sample dimensions. The influence of the wall friction becomes larger with an increasing ratio of sample height to sample diameter (HERLE, 1997), while the influence of an uneven sample surface becomes smaller. The uneven sample surface leads to increased settlements due to punctual induction of the stresses from the top cap. On the other hand, the wall friction leads to a reduction of the settlements. Both lead to an inhomogeneous stress and strain field. The sample dimensions need therefore to be optimized with respect to the two influences. Wall friction increases

proportional to the vertical stress and becomes even greater upon unloading due to interlocking effects leading to a larger ratio of horizontal to vertical stresses (OSTERMAYER, 1976). Detailed analysis of errors and the influence of wall friction and sample surface were performed by MUHS & KANY (1954), OSTERMAYER (1976) and BAUER (1992). An optimal sample dimension was found to be diameter to height of five to one. In this study, with sands (0.063 mm < grain size < 2.0 mm), 20 mm in height and 100 mm in diameter were applied.

BAUER (1992) presents an approach for estimating the amount of shear stress due to wall friction neglecting the small dead weight of the sample derived from the vertical equilibrium equation on an infinitesimal thin element of soil in an oedometer test via

$$\frac{d\sigma_z}{dz} + \frac{2\mu K_0}{R}\sigma_z = 0 \qquad \text{(JANSSEN, 1895)} \tag{4.7}$$

with μ the friction coefficient between steel and soil, R the radius of the sample and K_0 the ratio of radial to axial stresses (cf. Figure 4.2).

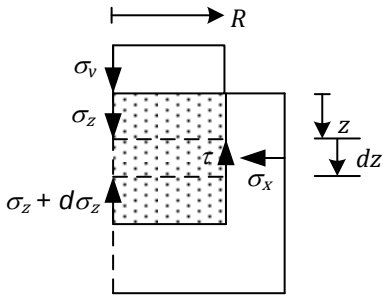

Figure 4.2: Stresses acting on an infinitesimal thin element of soil in an oedometer test with fixed ring during loading

Solving the differential equation (4.7) leads to

$$\sigma_z(z) = \sigma_v \cdot exp\left[-\frac{2\mu K_0}{R}z\right] \tag{4.8}$$

with σ_v the applied stress on the sample. The approach

$$\tau(z) = -\mu K_0 \sigma_z(z) \tag{4.9}$$

gives the vertical distribution of shear stresses on the oedometer ring. The presented approach is only an assumption, because it neglects the influence of the relative movement between soil and wall on the ratio τ/σ_x, considers the stress applied on the sample as constant on its surface and applies K_0 also as constant. However, it still can give an estimate of the stress variations within the oedometric specimen at the test ring. Figure 4.3 presents the relative stress reduction during virgin loading of a specimen with ratio of height to diameter of 0.2 considering different K_0-values and friction coefficients. Taking a friction coefficient between the stainless steel wall and Karlsruhe sand of μ = 0.2 to 0.3 as reported by BAUER (1992), the reduction in vertical stress between the top and bottom of a sample is approximately 5 to 13% depending on the roughness of the steel wall and the K_0-value.

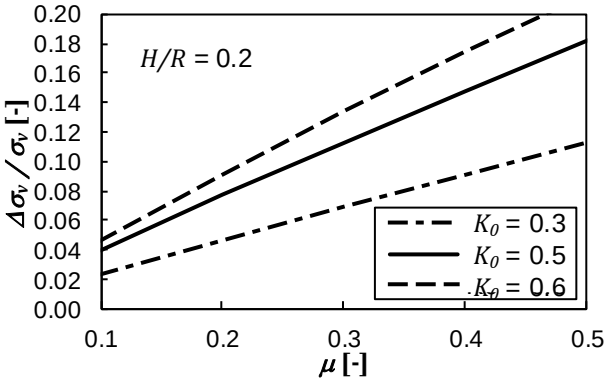

Figure 4.3: Influence of wall friction on the change of the vertical stress at the bottom of the sample $\Delta\sigma_v$ in comparison to the applied vertical stress σ_v during virgin loading in a fixed ring oedometer

Results of an own 3D finite-element analysis of an oedometer test with a ratio of height to diameter of 0.2 using the MOHR-COULOMB constitutive model, considering influences of wall friction, restraining effects in the corners of the oedometer ring, expansion of the oedometer ring and the small gap between top cap and oedometer ring are presented in Figure 4.4 and give a more detailed picture of the strain and stress distribution within an oedometer specimen (for more details on the simulation see Appendix A.3).

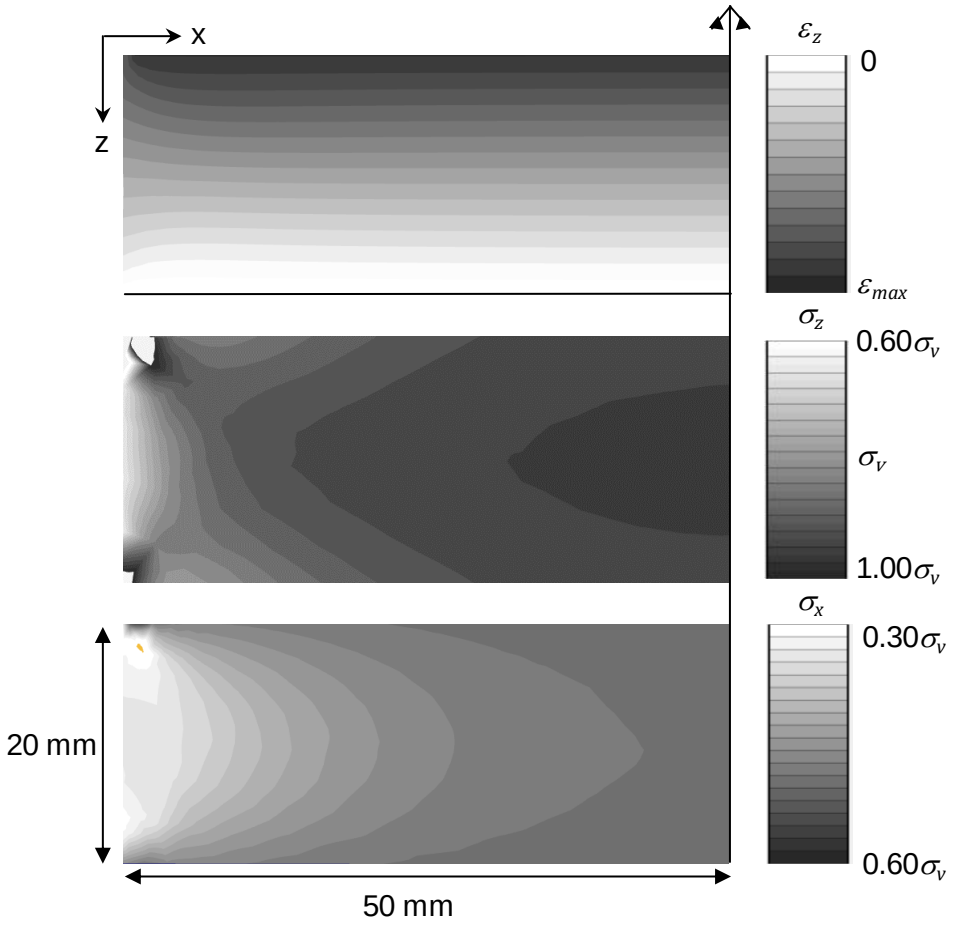

Figure 4.4: Qualitative distribution of strains, vertical and horizontal stresses within an oedometric specimen calculated with a finite-element analysis using the MOHR-COULOMB constitutive model

The results indicate that the stress distribution within the sample is quiet inhomogeneous and that a simple correction of the stress to account for friction is not possible. They also suggest that the reduction of vertical stresses due to friction at the oedometer ring might be larger than estimated by the approach of BAUER (1992). However, the influence of wall friction reduces strongly towards the centre of the specimen. The correction of the vertical stresses by estimating or measuring the wall friction in the oedometer test as suggested by OSTERMAYER (1976) is therefore not of much merit, because reduction of the vertical stresses in an averaged way may lead to an underestimation of stresses in the centre of the specimen. In this study, the test results are therefore judged knowing the shortcomings of the test setup rather than making corrections which cannot capture the complexity of the real stress and strain distribution. A viable option for reducing the influence of the wall friction is for instance the use of a floating oedometer ring (BAUER, 1992). Another option is to perform oedometer tests in the triaxial apparatus by controlling the cell pressure in order to fulfill the condition $\dot{\varepsilon}_r$ = 0. A floating ring oedometer was not available for this study and tests in the triaxial apparatus are time consuming and the available measurements of radial and horizontal strains do not fulfill the accuracy required for compression, relaxation and creep tests on sands.
Temperature fluctuations and inaccuracies resulting from the loading or measuring devices can also influence the test results. All tests were therefore performed under temperature controlled conditions with a maximum temperature fluctuation during one day of 0.5 °C and during one month of 2.0 °C (cf. Figure 4.5). Vertical deformation of the sample was measured with a resolution of 1.0 μm in most tests and one test series – especially the relaxation tests – was performed with a measuring resolution of 0.025 μm.

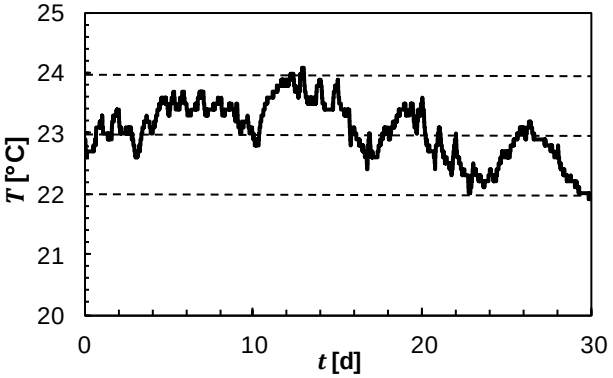

Figure 4.5: Ambient temperature variation during one month in the laboratory where the element tests were performed

The load-controlled (LC) tests were conducted with weights acting on a lever arm system with a ratio of one to ten, ensuring a truly constant vertical load on the specimen during creep. The strain-controlled tests including the relaxation tests were performed in a computer-controlled electromechanical load-frame driven by a stepper-motor using a 60 kN s-shape load cell (cf. Figure 4.6). A possible machine influence on the stress-strain curve due to inertia upon strain rate change was evaluated by loading a system of plate-springs and found to be negligible. In addition, a possible stress-relaxation resulting from the load-frame was checked and also found to be negligible. The $\dot{\sigma}'_a$ = 0-criterion during creep was fulfilled by the load frame with an accuracy of 0.01% at the highest stress of 7500 kPa and 0.09% at the lowest stress of 250 kPa applied in the strain controlled tests. Especially in the

relaxation tests the zero-strain criterion has to be fulfilled with high accuracy, because even small deformations lead to large stress fluctuations in the stiff sand samples. To ensure the zero strain rate criterion and also to be able to apply a truly constant rate of strain (CRS) to the sample taking into account the inevitable deformations of the load frame, the deformation transducer was mounted in the way presented in Figure 4.6. Thereby the deformations of the load-cell and the load-frame were being recorded by the deformation transducer and were compensated by the frame accordingly. This led in some tests to small stress jumps but guaranteed the zero deformation criterion with a very high precision of 10^{-4}% of the initial sample height.

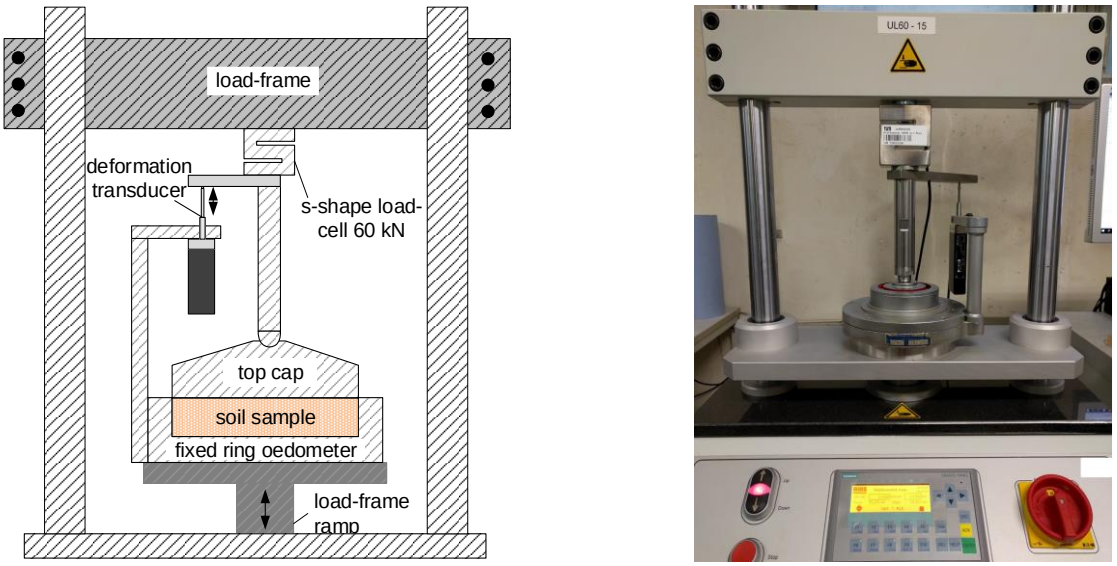

Figure 4.6: Sketch and photograph of the oedometer cell with deformation transducer in the electromechanical load-frame

4.2 Investigated materials

The soils studied were four sands from the Garzweiler lignite mine near Cologne (Germany) with subangular to rounded particles and two sands from a quarry near Munich (Germany) with angular to subangular grains. The sands from Garzweiler were a fine sand (FS) with 6.4wt-% content of fines, a medium sand (MS) with 2.8wt-% content of fines, a silty sand (SU) and a very silty sand (SU*) with 14wt-% and 25wt-% silt content respectively. The sand SU* was produced by taking the fraction of particles smaller than 0.125 mm from sample SU. MS, FS, SU and SU* were chosen as representative specimen for the Renish lignite mining areas. The sands from Munich were a silty sand (SU2) with 46wt-% silt content and a well graded sand (SW) with 25wt-% silt content and 20wt-% gravel content both from the same quarry. The tests performed with these two specimens focus on the influence of the mean grain size and fine content on the viscous behaviour, as the samples from Garzweiler are not appropriate to investigate these influences. Soils FS, MS, SU* and SU2 were uniform and SU as well as SW non-uniform. All samples were poorly graded. The mineralogical components of the sands from Garzweiler were 93 to 97% quartz and 3 to 7% orthoclase. The sands from Munich had 41% dolomite, 30% calcite, 22% quartz, 3% albite, 2% kaolinite and 1% orthoclase as well as 1% muscovite. Table 4.1 summarizes the classification characteristics, Figure 4.7 shows micrographs of the sands and Figure 4.8 presents the GSDs.

Table 4.1: Classification characteristics of investigated materials

Origin	Sample name	C_u	C_c*	Content < 0.063 mm [wt-%]	d_{50} [mm]	e_{min}	e_{max}	ρ_s [g/cm³]
Garzweiler	FS	1.38	1.09	6.4	0.170	0.776	1.144	2.614
	MS	2.11	0.99	2.8	0.340	0.628	1.088	2.604
	SU	5.13	3.11	14.3	0.170	0.755	1.154[3]	2.630
	SU*	2.33	4.25	25.0	0.075	0.622	1.181	2.665
Munich	SU2	3.26	0.74	46.0	0.069	0.683	1.200†	2.728
	SW	13.33	0.53	24.9	0.200	0.381	0.700	2.720

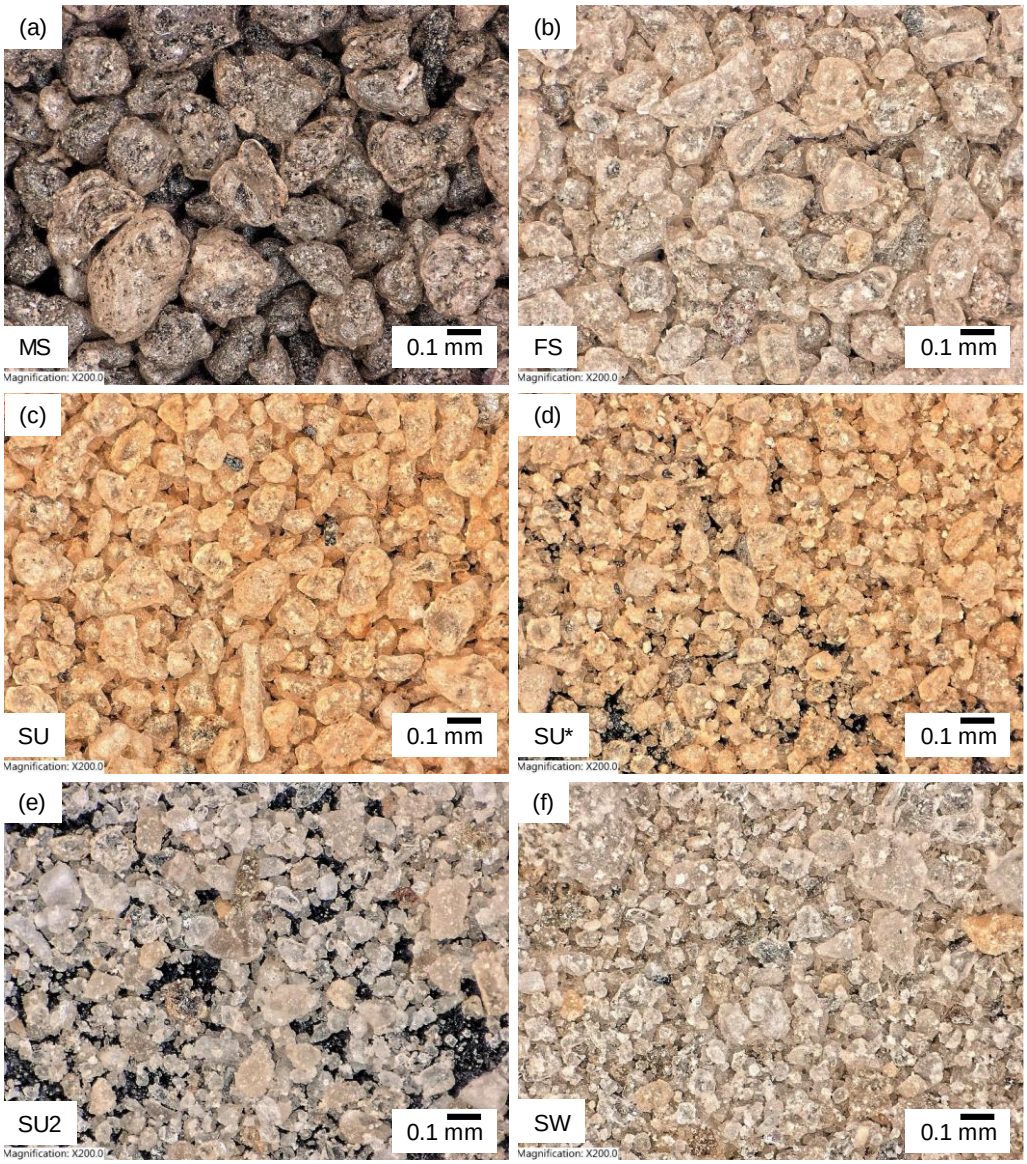

Figure 4.7: Optical micrographs of (a) MS, (b) FS, (c) SU, (d) SU*, (e) SU2 and (f) SW

[3] † SU, SU*, SU2 and SW were classified by e_{min} and e_{max}, because the fines (by definition content < 0.063 mm) consisted predominantly of coarse non-plastic silt particles resulting in a soil behaviour comparable to that of fine sands.

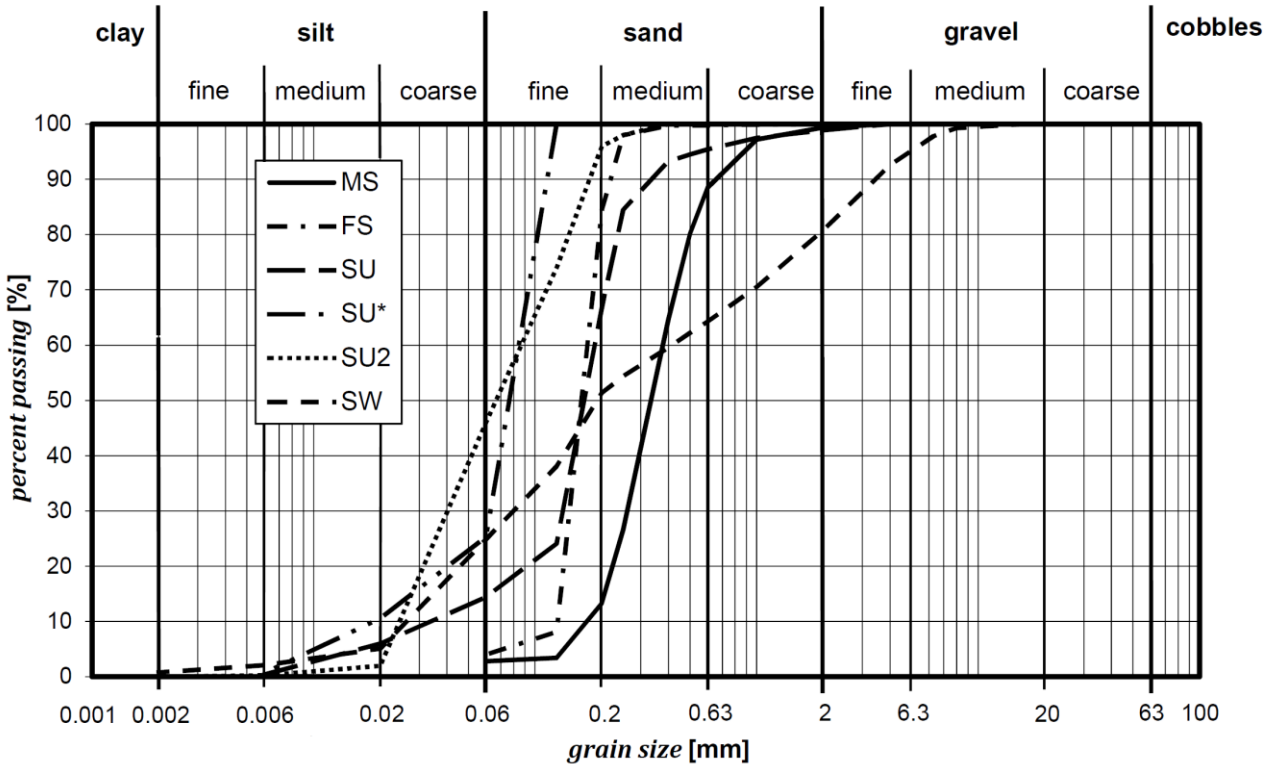

Figure 4.8: GSDs of investigated soils: MS, FS, SU, SU*, SU2 and SW

The grain shape characteristics of the soils were investigated by means of a Camsizer-analysis (cf. Section 3.1.2). The values $RDNS$ and $SPHT\_K$ are used to categorize the samples with the chart of KRUMBEIN & SLOSS (1963) (cf. Figure 4.9 and Table 4.2). The four samples from Garzweiler are very similar in shape, rather spherical with medium roundness. The samples from Munich are characterized by more or less the same sphericity but with lower roundness. The symmetry value $Symm$ lies for all sands above 0.8 indicating rather symmetrical grains. The micrographs in Figure 4.7 show that the surface texture of the grains of all tested sands is rather rough.

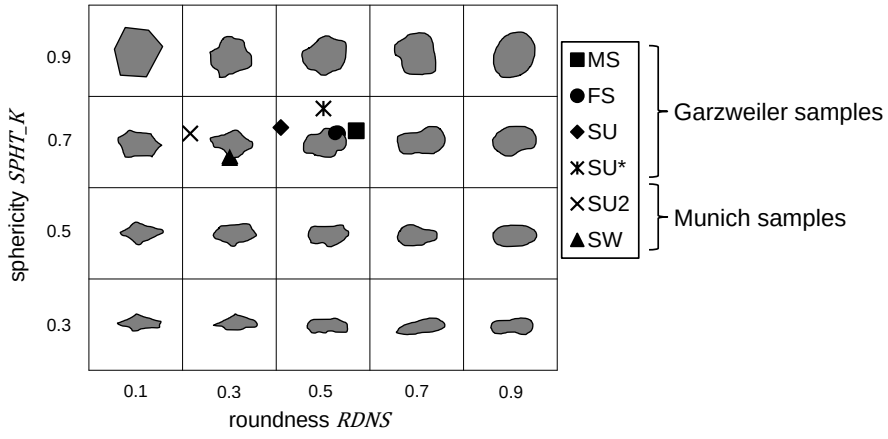

Figure 4.9: Ordering of the investigated soil samples into the diagram after KRUMBEIN & SLOSS (1963)

Table 4.2: Parameters for grain shape characterization used in this study

	MS	FS	SU	SU*	SU2	SW
$SPHT\_K$	0.723	0.716	0.730	0.772	0.717	0.666
$RDNS$	0.570	0.530	0.409	0.500	0.215	0.392
$Symm$	0.883	0.861	0.867	0.875	0.841	0.806

4.3 Experimental program

A total of 76 load-controlled, 51 strain rate-controlled, 14 stress-relaxation, 7 tests with combined control, one long-term (2 weeks), 15 high pressure strain rate-controlled oedometer tests and 24 high pressure strain rate-controlled oedometer tests with a one hour creep phase at the maximum vertical effective stress were performed, from which representative test results are presented. A summary of all performed oedometer tests is listed in Appendix A.4. The boundary conditions for different testing procedures used in this study are summarized in Table 4.3.

Table 4.3: Stress rate and strain rate boundary condition during oedometric compression tests with different testing procedures

Creep test	Strain rate-controlled test	Relaxation test
Condition: $\dot{\sigma'}_a = 0$ $\dot{\varepsilon}_a \neq 0, \dot{\varepsilon}_r = 0$ it follows: $\dot{\varepsilon}_v \neq 0$ $\dot{\sigma'}_r \neq 0$ (change of K_0) it follows: $\dot{q} \neq 0\,, \dot{p} \neq 0$	$\dot{\varepsilon}_a \neq 0, \dot{\varepsilon}_r = 0$ it follows: $\dot{\varepsilon}_v \neq 0$ $\dot{\sigma'}_a \neq 0, \dot{\sigma'}_r \neq 0$ it follows: $\dot{q} \neq 0\,, \dot{p} \neq 0$	Condition: $\dot{\varepsilon}_a = 0, \dot{\varepsilon}_r = 0$ it follows: $\dot{\varepsilon}_v = 0$ $\dot{\sigma'}_a \neq 0, \dot{\sigma'}_r \neq 0$ it follows: $\dot{q} \neq 0\,, \dot{p} \neq 0$

The following oedometer test series were performed:

Creep tests:

- LC creep tests with incremental loading with variation in initial density on MS, FS, SU and SU2 for investigation of the influence of the initial density state and stress state on the creep behaviour in the vertical effective stress range up to 2000 kPa.
- Creep after CRS tests with variation in initial density on MS, SU and SU* for verification of the test results of the LC tests and investigation of the loading behaviour after a creep phase in the vertical effective stress range up to 7500 kPa.
- Creep after different loading strain rate tests on sand MS for investigation of the influence of the loading strain rate on the subsequent creep rate in the vertical effective stress range up to 7500 kPa.

Tests on strain rate dependency:

- CRS tests with 1000-fold difference in the constant loading strain rates for investigation of its influence on the stress-strain response of sand MS (2.8wt-% fine content) and sand SU2 (46wt-% fine content) and determination of the influence of the fine content on the rate dependency in the vertical effective stress range up to 2000 kPa.

- Strain rate-controlled tests with sudden 1000-fold changes of the loading strain rate (ChRS) on MS, SU, SU* and SU2 for investigation of the influence of a sudden change in the loading strain rate and the influence of the fine content on the rate-dependent behaviour in the vertical effective stress range up to 7500 kPa.

Relaxation tests:

- Relaxation after CRS tests with variation in initial density on MS, SU and SU* for investigation of the influence of the initial density state and stress state on the relaxation behaviour in the vertical effective stress range up to 7500 kPa.
- Relaxation tests with different loading strain rates on sand MS for investigation of the influence of the loading strain rate on the subsequent relaxation rate in the vertical effective stress range up to 7500 kPa.

Combined tests:

- Combined tests with creep after different loading strain and stress paths for determination of the influence of the strain history and strain rate history on the subsequent creep behaviour of sand MS and sand SU* in the vertical effective stress range up to 7500 kPa.

Tests on additional features of viscous behaviour:

- A long-term CRS creep and relaxation test with phase durations of one week for investigation of the long-term behaviour in creep and relaxation of sand MS at vertical effective stresses of 4000 and 7500 kPa.
- CRS high pressure tests with and without creep at maximum vertical effective stresses of 300 MPa for investigation of the grain degradation as dominant creep mechanism in sand MS.
- LC creep tests on sand SW and several fractions of its GSD for determination of the influence of the GSD on the creep behaviour in the vertical effective stress range up to 2000 kPa.
- LC creep tests on sand MS with fully saturated samples to investigate the influence of water on the creep behaviour in the vertical effective stress range up to 2000 kPa.

With the creep tests, the tests on strain rate dependency and the relaxation tests the viscous response of granular soil is investigated in the aspects relevant for development of model approaches for time-dependent material behaviour. To the knowledge of the author, no experimental data set covering all three mechanisms of viscosity exists so far for granular soils. The test series on other influencing factors, with by no means a claim to completeness, give an insight into long-term (one week) influences, granulometric factors, influence of water content and behaviour in the high pressure regime.

Additional element tests like drained triaxial compression tests (TCD) for determination of shear parameters (cf. Appendix A.5) and soft oedometer tests for determination of the earth pressure coefficients at rest K_0 were performed to derive necessary model parameters. The soft oedometer ring was equipped with strain gauges to measure the forces in the ring to determine the radial stresses.

4.4 Sample preparation and repeatability

Sample preparation of dry sand samples in oedometer tests can be performed by three different techniques: Funnel deposition, deposition by dispersion of the sand through sieves with different opening width as well as drop height and a technique proposed by BAUER (1992) to deposit the soil homogenously above a sieve positioned at the bottom of the specimen which is – after deposition – pulled up through the sample. It should thereby homogenously loosen the specimen. The technique of funnel deposition allows for the preparation of loose to very loose samples. A disadvantage of the preparation technique is the inhomogeneous deposition of particles. The outer part of the sample consist of courser particles than the inner part, because the courser grains roll down the heap created by the funnel and accumulate at its lower / outer part. Studies reported by BAUER (1992) investigate the inhomogeneous particle distribution. The disadvantage of the two techniques using sieves for dispersion or loosening of the sample is that they can only be properly applied to very poorly graded soils, because the opening width of the sieve should not be much larger than the largest grain size to create loose samples. For samples which are not very poorly graded, the opening width of the sieve must be large to avoid particles from getting stuck. However, the large opening width entails that no significant loosening is achieved.

All three preparation techniques were tested for the investigated soils. It was found that even for the poorly graded sands MS and FS the preparation techniques using sieves were not expedient, because either the sieves were too narrow so that grains got stuck during preparation or the opening width was too large to prepare loose samples. Therefore, dry funnel deposition was used for sample preparation.

The sample size in the standard oedometer devices was 100 mm in diameter and 20 mm in height. All specimens were air-dry, prepared by funnel deposition and carefully levelled with a steel ruler. The necessary levelling of the soil with a steel ruler remedied the effect of inhomogeneous particle distribution within the sample, because finer particles in the center were also distributed to the outer part of the sample. With this preparation technique minimum well reproducable relative densities of approximately I_d = 0.3 (loose) were achieved. Very loose specimen could not be prepared with a good reproducability, because already the levelling with the steel ruler led to a densification of the soil. For the preparation of dense samples the specimens were compacted by laterally tapping the side of the oedometer with a hammer in a symmetrical pattern. The prepared maximum relative density was I_d = 1.0 (very dense).

For a precise determination of the initial relative density of the samples, the pre-mounted vertical displacement transducer was set to zero at an exact sample height of 20 mm, measured with an especially made aluminium dummy. The settlement resulting from the application of the loading plate prior to initiation of the deformation recording could thereby be determined. To demonstrate sample preparation repeatability, Figure 4.10 shows a CRS test and a ChRS test of specimen with the same density and loading sequence. To check the repeatability, a loose density was chosen as it is most susceptible to deviations from sample preparation. The stress-strain curves shown in Figure 4.10 are essentially the same, showing the high degree of accuracy and repeatability reached in sample preparation.

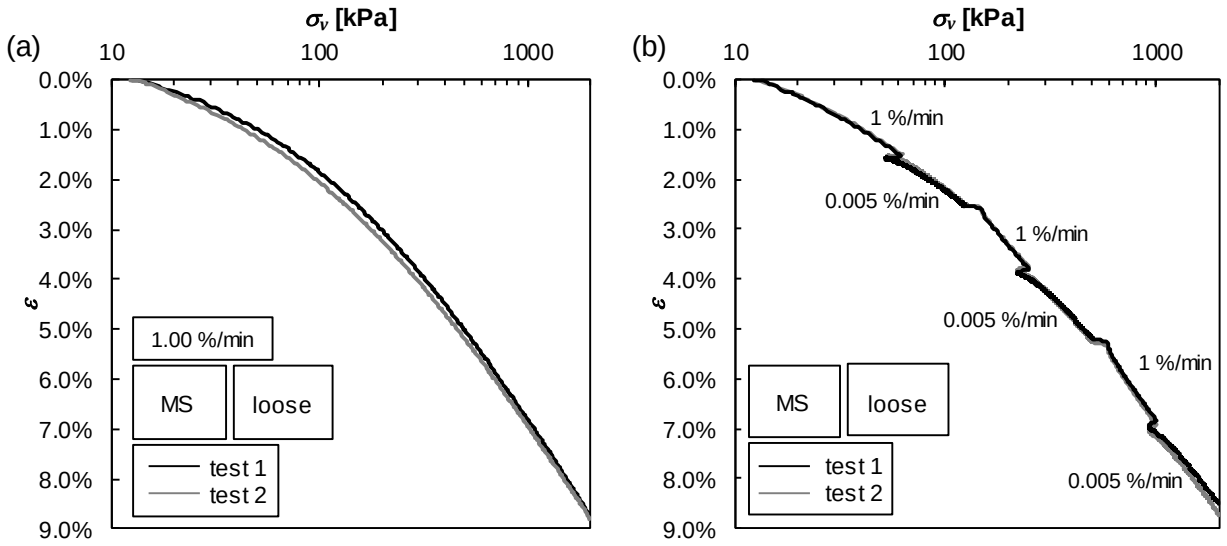

Figure 4.10: (a) Two CRS tests (strain rate of 1%/min each) with loose density and (b) two tests with loose density and 200-fold sudden stepwise changes of the strain rate

4.5 Evaluation methods

Definition of natural strain was used (cf. Equation (4.2)). The difference between engineering strain and natural strain in the strain range of oedometer tests is however very small (cf. Section 3.2). A simple approach for evaluating the results from the conducted experiments is to look at the volumetric deformations due to stress changes, creep and imposed strain rate separately.

For the evaluation of the change in void ratio Δe with vertical stress the compression index C_c for loading and the swelling index C_s for unloading / reloading were used as defined by (3.17) and (3.18). In LC tests, the indices were evaluated as secant moduli 60 s after a sudden stress change $\Delta\sigma$. In CRS tests they were evaluated continuously during loading.

Creep was evaluated using the parameter of secondary compression C_α from (3.36), which describes the change in void ratio on a logarithmic time scale or C from (3.37) which describes the change in strain on a logarithmic time scale. The creep-coefficients were evaluated from the linear slope of the $\log(t)$ - e and $\ln(t)$ - ε curve respectively. Furthermore, creep and compression were evaluated using the ratio C_α/C_c from (3.39) according to MESRI & GODLEWSKI (1977) and MESRI & CASTRO (1987). They postulated this ratio to be independent from time, stress and density for fine grained soils as well as for granular soils (cf. Section 3.3.5).

ChRS and relaxation tests were evaluated using the viscosity index I_v by KRIEG (2000) from (3.45), which is a correlation coefficient between the change in stress upon a change in the strain rate respectively relaxation time and creep time (cf. Section 3.3.5).

4.6 Creep after incremental loading

4.6.1 Test results

LC tests were performed with vertical effective stress steps of 125 kPa, 250 kPa, 500 kPa, 1000 kPa and 2000 kPa. At each stress level the soil was left to creep for 24 h. In some tests the samples were unloaded after the creep phase at the maximum applied stress of 2000 kPa.

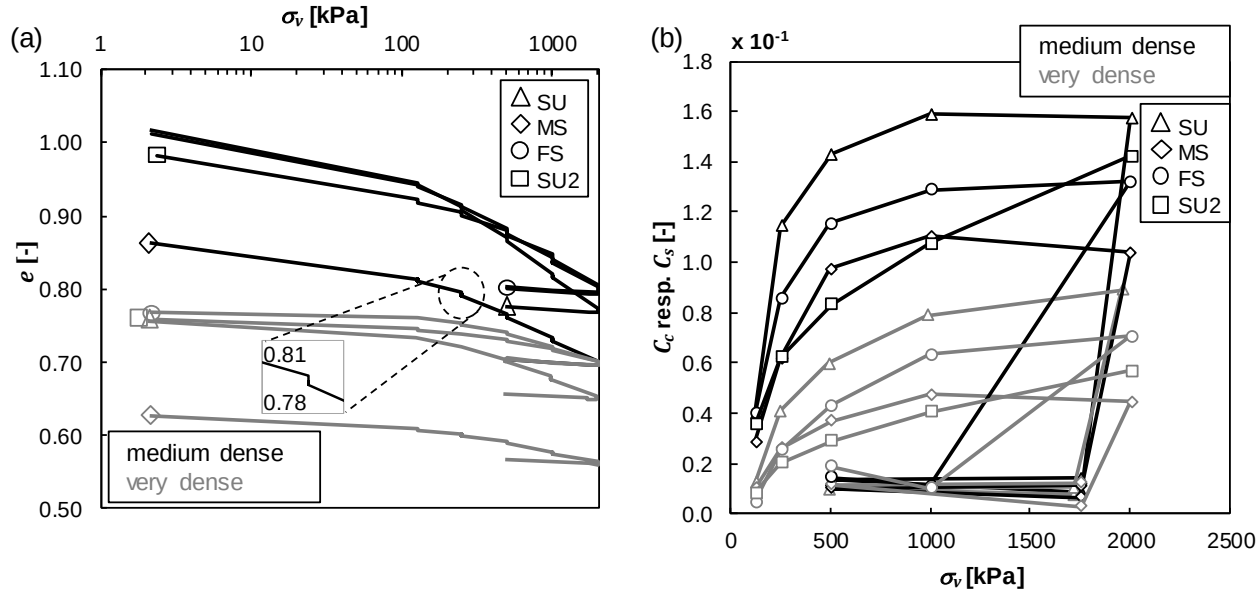

Figure 4.11: (a) Semi-logarithmic virgin compression and unloading curves of medium dense and very dense samples of FS, MS, SU and SU2, (b) C_c and C_s evaluation of all three soils with respect to the vertical stress

Figure 4.11 (a) shows the semi-logarithmic plot of the development of the void ratio e with the applied vertical effective stress σ_v during virgin loading, creep and unloading for representative test results for medium dense and very dense samples of the sands FS, MS, SU and SU2. The creep stages are visible as vertical lines at each load stage (cf. magnified section in Figure 4.11 (a)). Figure 4.11 (b) shows the obtained values of C_c and C_s according to (3.17) and (3.18). C_c increases strongly with rising vertical effective stress σ_v. The increase $\Delta C_c/\Delta\sigma_v$ becomes considerably smaller with rising vertical effective stress. The values are dependent on the initial relative densities of the samples and on the granulometric properties of the soils. The density change from medium dense to very dense reduces C_c for all samples by approximately 50%. As expected, C_c is generally lower with decreasing fine content of the soils with exception of SU2, where the grain shape and mineralogy are very different compared to the other sands. The swelling indices of all three soils vary between C_s = 0.003 and 0.018. An influence of the density on the swelling index is not observable in the test results.
Figure 4.12 (a) / (b) and Figure 4.13 (a) / (b) show the ratio of void ratio to initial void ratio e/e_0 on a logarithmic time scale. The compression curves can be approximated by a linear trend with respect to the logarithm of time. Therefore, an evaluation of the creep strains using (3.36) in the considered time interval is valid. Figure 4.14 depicts the evaluation of the creep-coefficient C_α as a function of the applied vertical stress. C_α increases with the vertical effective stress in a similar manner as the

compression index C_c and the intensity of creep depends on the initial relative density. Similar observations regarding the development of creep strains with increasing mean stress were made by MEJIA & VAID (1988), LADE & LIU (1998), KUWANO & JARDINE (2002) and LV *et al.* (2016) (cf. Section 3.3.1.1). The three Garzweiler sands show slightly larger creep-coefficients for the sands FS and SU with higher fine content. More influential are the grain shape and mineralogy in which the Garzweiler sands are very similar. Sand SU2 consists out of weaker minerals than quartz and shows especially in the medium dense sample a more stress sensitive creep response. This is caused by more grain and contact degradation. Creep strains of all samples are strongly reduced after significant unloading to OCR = 1.14 to 4 and with the applied measurement equipment difficult to resolve.

Figure 4.15 presents the evaluation of the C_α/C_c -ratio from the LC tests. Depicted by dashed lines are ranges of C_α/C_c for each soil. Dotted dashed lines indicate the deviation of C_α/C_c from a constant soil-specific value according to a best-fit correlation for the obtained test results. In the diagrams, the fine content (< 0.063 mm) is given. With decreasing fine content the deviation of C_α/C_c from a constant soil-specific value increases. This is mainly because in the tests the increase of C_c with the vertical stress is larger than the increase of C_α. At a fine content of 14.3wt-% as in sand SU, the ratio C_α/C_c approaches an almost constant value and at a fine content of 46wt-% (SU2) the soil behaviour can be very well described with one constant C_α/C_c -ratio.

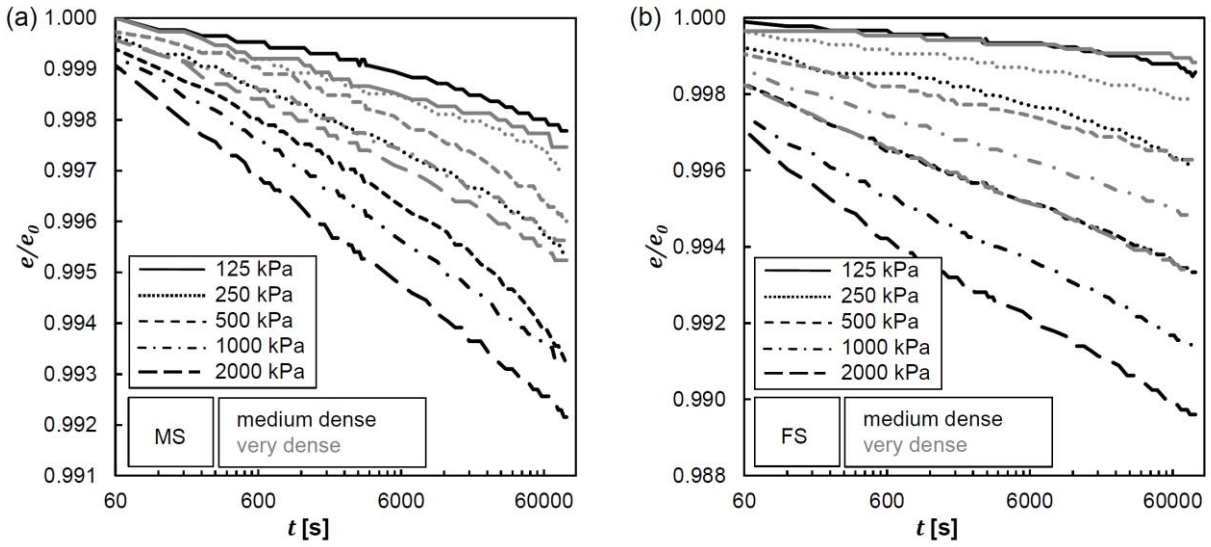

Figure 4.12: Void ratio to initial void ratio e/e_0 as a function of the logarithm of time of medium dense and very dense samples of (a) MS and (b) FS

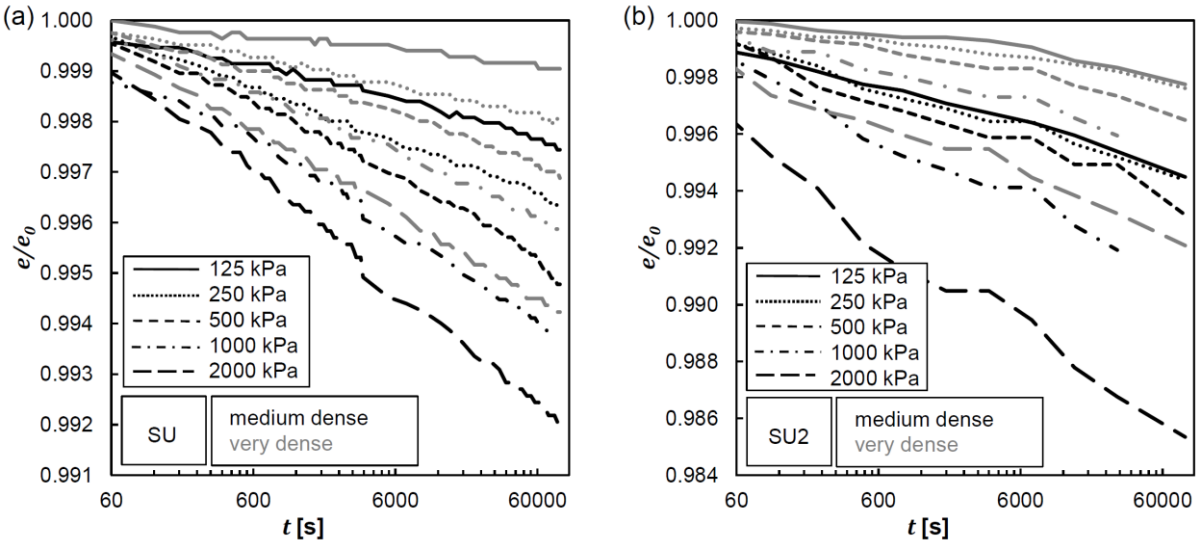

Figure 4.13: Void ratio to initial void ratio e/e_0 as a function of the logarithm of time of medium dense and very dense samples of (a) SU and (b) SU2

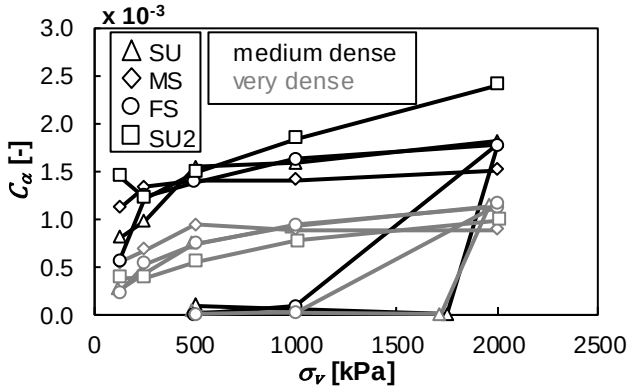

Figure 4.14: Creep-coefficient C_α of all soils in virgin loading and unloading with respect to the vertical stress evaluated as a best fit of (3.36) to the test data between 60 s and 86400 s

The evaluation of the C_α/C_c -ratio development with applied vertical stress is shown in Figure 4.16. In case of the sands SU and SU2, the dependence on stress and density is small and the specification of a constant C_α/C_c -ratio seems to be acceptable in a wide stress and density range. The sands FS and MS show a large difference in the values especially at lower stresses up to 1000 kPa. Generally, the denser specimen show higher C_α/C_c -ratios and the ratios decrease with rising vertical stress. At stresses larger than 1000 kPa the C_α/C_c -ratios remain constant. Considering the C_α/C_c -ratio as a descriptor value for the viscous behaviour of granular soils, as it is used for fine grained soils (cf. Section 3.3.5), this would mean, the viscosity decreases with increasing stresses and increasing density, which apparently contradicts the observed creep behaviour. In fact, the experiments show that creep deformations increase with rising stress and decreasing density. Therefore, the experimental results in Fig. 4.15 question whether the C_α/C_c -ratio alone is an appropriate indicator of the viscous response of granular soils. This issue will be further addressed in Section 4.7.1.

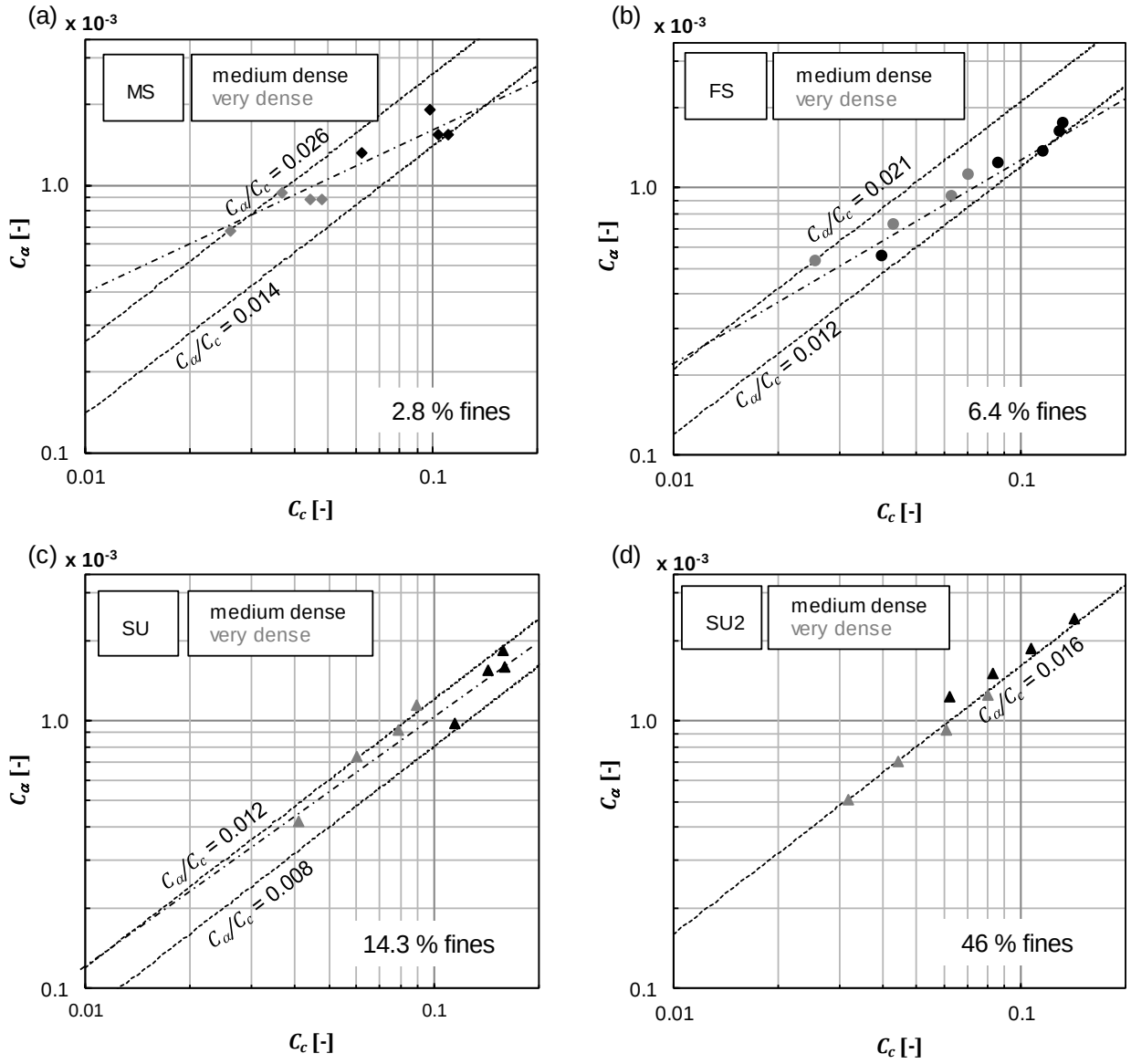

Figure 4.15: C_α / C_c - evaluation for (a) MS, (b) FS, (c) SU and (d) SU2

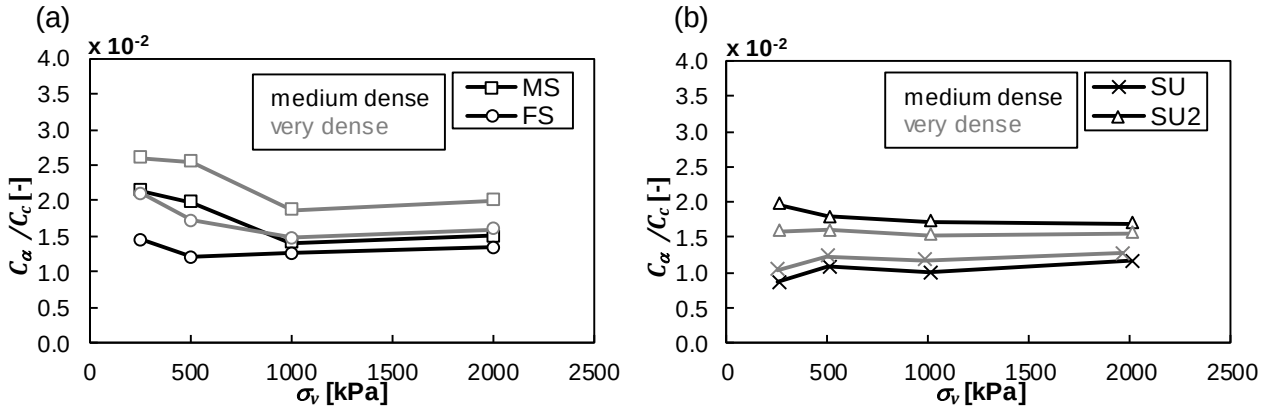

Figure 4.16: Development of C_α / C_c with the applied vertical stress for (a) MS and FS as well as (b) SU and SU2

4.6.2 Influence of pressure and density state on oedometric creep

The laboratory test results presented in Section 4.6 as well as the findings of other authors (cf. Section 3.3) show that the creep rate of granular soils depends on the mean stress level and the density. For further evaluation, the influence of pressure and density state have to be analyzed separately in order to distinguish between their respective influences on the creep rate. For this purpose, the creep-coefficient developments in the presented tests were evaluated with respect to isobaric lines (p' = const.) and lines of equal relative void ratio r_e = constant (cf. Figure 4.17). The mean stress p' was calculated using the K_0-values of the sands determined with a soft oedometer. The values are in good agreement with the approach by JAKY (1948) (4.5) considering the friction angles of the soils determined in TCD tests (cf. Table A.9.2, Appendix A.9). The evaluation was performed with respect to p' for purpose of generalization, assuming that the influence of the deviatoric stress in the oedometer test on the amount of creep strains is small and that it has no influence on general behavioural trends of the granular soils. p' is assumed to remain constant during the oedometric creep phases.

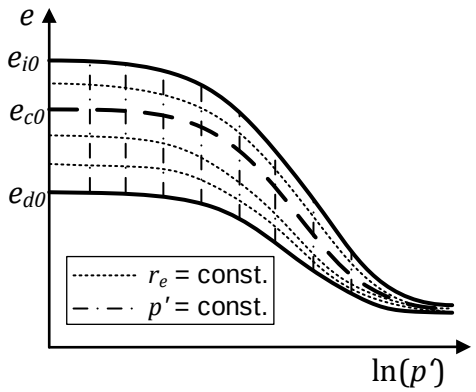

Figure 4.17: Lines of constant relative void ratio r_e and of constant pressure p' in the e - lnp' - plane

The analysis was performed with respect to the relative void ratio to capture the density dependent behaviour over a wider range of pressures considering the change of the extreme void ratios with the pressure (cf. Section 3.1.5). The compression law by BAUER (1996) (3.26) was used to calculate the development of the extreme void ratios e_c and e_d for determination of r_e. The calibration of the parameters h_s and n was done by back-calculation of a loose and a dense oedometer test of each sample with an element test driving routine of the hypoplastic model by VON WOLFFERSDORFF (1996). The exponent n was calculated by

$$n = \frac{\ln\left(\frac{e_1 C_{c2}}{e_2 C_{c1}}\right)}{\ln\left(\frac{{p_2}'}{{p_1}'}\right)} \tag{4.10}$$

with e_1 and C_{c1} as void ratio and compression index at low pressure ${p_1}'$ and e_2 and C_{c2} at high pressure ${p_2}'$ in the considered stress range (HERLE, 1997)(cf. Figure 4.18).

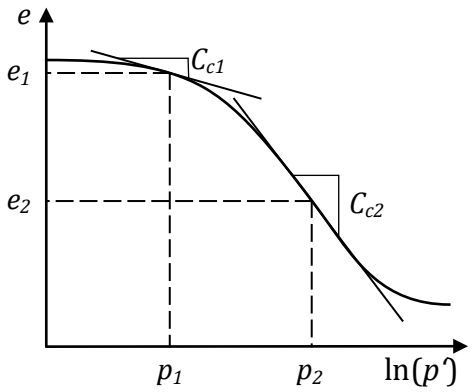

Figure 4.18: Determination of n from a compression curve of a loose oedometer test

h_s was determined independently of n by fitting model and test results. The summary of the parameters for the BAUER-compression law and e_{d0} and e_{c0} for the three Garzweiler sands MS, FS and SU is presented in Table 4.4.

Table 4.4: Parameters for the BAUER-compression law and e_{d0} and e_{c0}

	MS	FS	SU
n	0.22	0.18	0.5
h_s [MPa]	380	900	30
$e_{d0} = e_{min}$	0.630	0.776	0.755
$e_{c0} = e_{max}$	1.090	1.144	1.153

Figure 4.19 presents the results of the analysis with respect to isobaric lines (p' = const.) and lines of equal relative void ratio r_e. With respect to the relative void ratio at constant pressure the development of C_α can be represented by linear interpolations (cf. Figure 4.19 (a), (c) and (e)). The gradient of C_α over r_e increases with p'. The distance between the isobars indicates the sensitivity of the creep-coefficient to the mean pressure. FS and SU show a larger pressure dependency than MS. Generally, the creep rate is more pressure sensitive at high relative void ratios (low relative densities) than at low relative void ratios. The only exception in this respect is the sand MS, where the pressure sensitivity appears equal at low and high relative void ratios. The creep-coefficient shows considerable scattering at the lower pressures, which is related to the overall very low deformation rate at this stress level, which leads to larger scattering due to measurement inaccuracy and slight fluctuations of external influences like temperature. The influence of the pressure level at constant relative void ratio on the creep-coefficient C_α is presented in Figure 4.19 (b), (d) and (f). The experimental data can be fitted by hyperbolic functions. The interpolations show the same development of the gradient with the pressure for the range of relative void ratios considered. Some results of FS and SU show deviating trends, which is caused by experimental scatter.

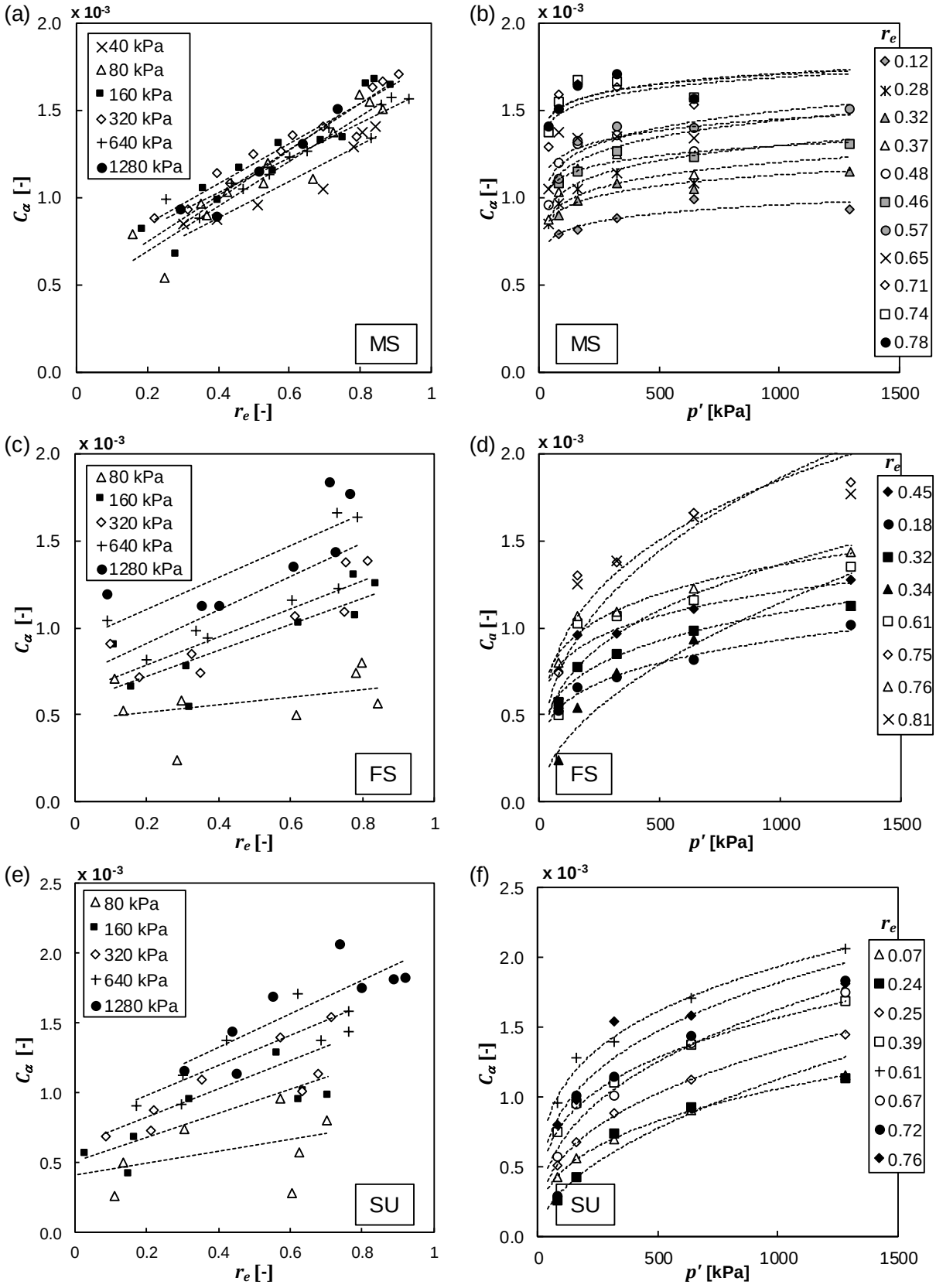

Figure 4.19: Development of the creep-coefficient C_α as a function of the relative void ratio r_e at different mean pressures with linear interpolation of the test data (left) and the mean pressure at different relative void ratios with hyperbolic interpolation of the test data (right) of (a / b) MS, (c / d) FS and (e / f) SU

4.6.3 Empirical concept for the creep-coefficient determination

Based on the large number of incremental loading tests presented before and the previous evaluation in Section 4.6.2 an empirical approach for calculating the density and stress-dependent creep-coefficient of a granular soil in oedometric compression was developed. It is limited to a stress range in which the soil undergoes level I and level II grain damage only (cf. Section 3.2). This stress range is most relevant for geotechnical engineering applications. Several established constitutive models, e.g. the family of hypoplastic models, derive parameters from grain assembly properties, which requires that the grain is permanent and the GSD does not undergo major changes during loading. Therefore, for future applications of the proposed approach this limitation should be considered.
As was presented, the creep-coefficient increases with the vertical stress and decreases with increasing density in oedometric testing. A schematic drawing of the development of the creep-coefficient in the C_α - p' - r_e - space is shown in Figure 4.20. The creep-coefficient increases linearly with the relative void ratio and hyperbolically with the mean stress p' (cf. Section 4.6.2).

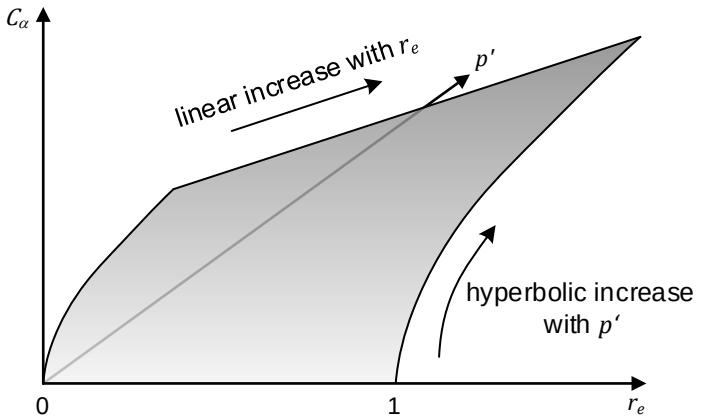

Figure 4.20: Schematic drawing of creep-coefficient development in the C_α - p' - r_e - space depicted from test results in Figure 4.19

The stress-dependent creep-coefficient developments from test results on MS, FS and SU at different relative densities are plotted in Figure 4.21. The data can be fitted by hyperbolic regression curves, which best fit the pressure dependency of the creep-coefficient. The pressure dependent regression was calculated according to

$$C_\alpha = C_{\alpha,ref}\left(\frac{p'}{p'_{ref}}\right)^\theta \tag{4.11}$$

with $C_{\alpha,ref}$ as reference creep-coefficient at the reference pressure p'_{ref} and θ as exponent. The reference pressure has to be chosen according to the best fit of the data and according to the relevant pressure range. The exponent θ can be fixed as a constant for each investigated soil and controls the pressure sensitivity of the creep-coefficient. For θ < 1.0 the creep-coefficient increases hyperbolically and for θ = 1.0 it increases linearly with p'. An exponential increase with θ > 1.0 was not detected for tests within the pressure range of level I and level II grain damage. As mentioned before, sands FS and SU show a much more pronounced pressure sensitivity than sand MS.

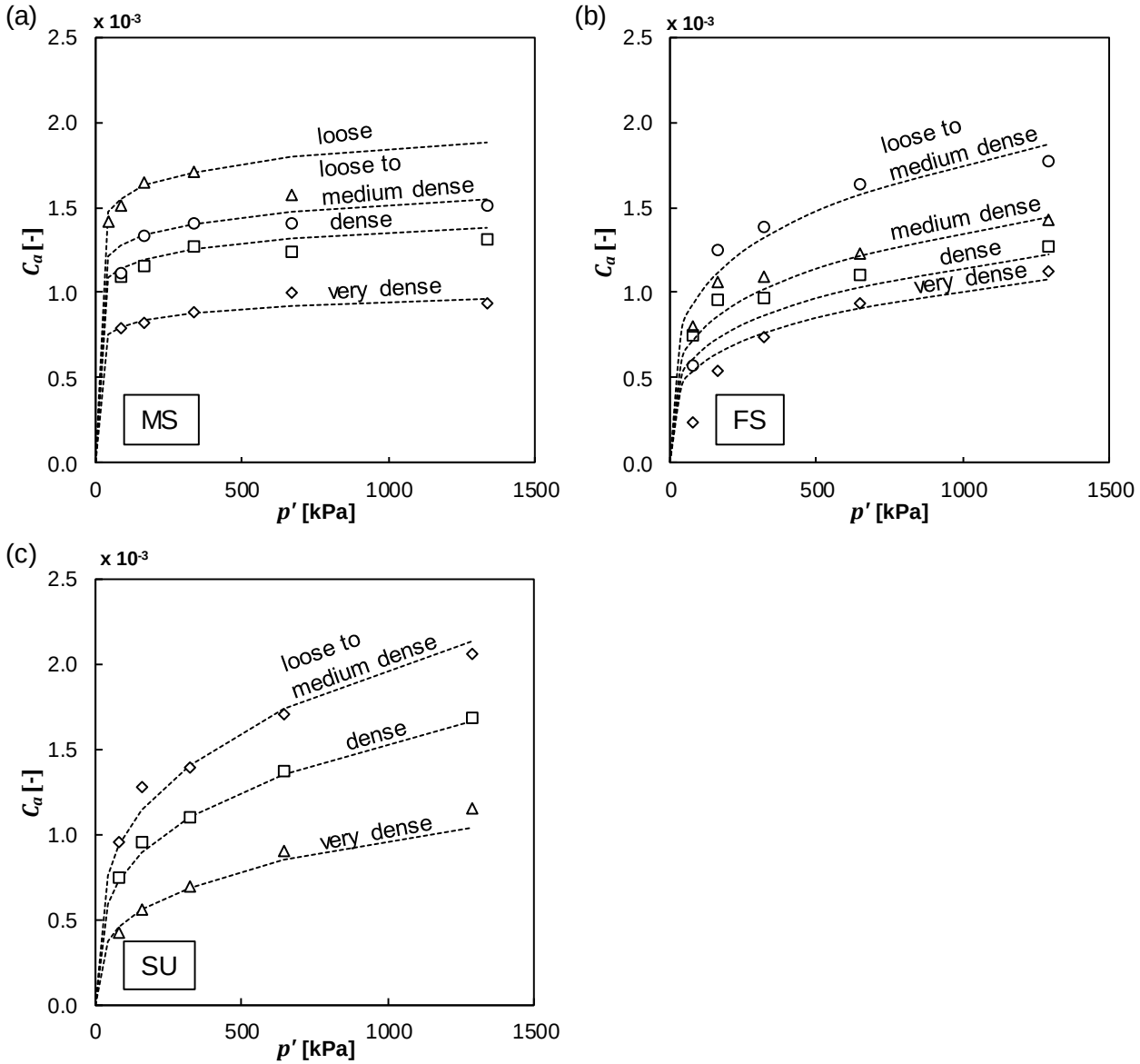

Figure 4.21: Stress-dependent increase of the creep-coefficient C_α at different densities with hyperbolic regression curves of (a) MS, (b) FS and (c) SU

As was presented, the development of the creep-coefficient with the relative void ratio at a specific pressure can best be approximated by a linear regression. Therefore, the reference creep-coefficient in (4.11) is calculated in dependence of the relative void ratio to incorporate the density dependency of creep by the following approach

$$C_{\alpha,ref} = \omega \cdot r_e + C_{\alpha,ref,0} \,. \tag{4.12}$$

ω defines the gradient of $C_{\alpha,ref}$ with r_e and $C_{\alpha,ref,0}$ is the axis intercept at the densest state r_e = 0. Test results showed that even at the densest state the sands still creep. A summary of the linear regressions of the data according to (4.12) for sands MS, FS and SU is presented in Figure 4.22 along with the respective parameter combinations of ω and $C_{\alpha,ref,0}$ as well as the coefficients of determination. A summary of all input parameters for (4.11) and (4.12) is shown in Table 4.5.

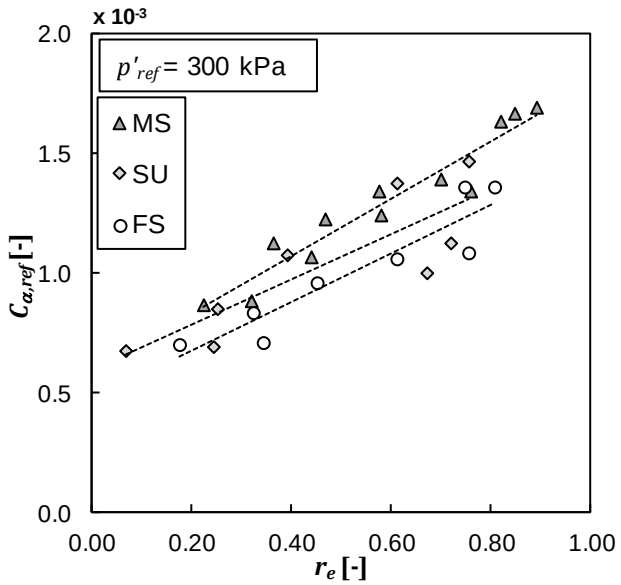

MS:
$C_{\alpha,ref}$ = 0.0012 · r_e + 0.0006
R^2 = 0.92
at p'_{ref} = 300 kPa
FS:
$C_{\alpha,ref}$ = 0.001 · r_e + 0.0005
R^2 = 0.86
at p'_{ref} = 300 kPa
SU:
$C_{\alpha,ref}$ = 0.0009 · r_e + 0.0006
R^2 = 0.71
at p'_{ref} = 300 kPa

Figure 4.22: Reference creep-coefficient values of MS, FS and SU as a function of the relative void ratio at a reference mean effective stress of p'_{ref} = 300 kPa with the corresponding linear regression curves and their coefficients of determination

Table 4.5: Parameters θ, ω and $C_{\alpha,ref,0}$ for MS, FS and SU at p'_{ref} = 300 kPa

	MS	FS	SU
θ	0.07	0.25	0.30
ω	0.0012	0.0010	0.0009
$C_{\alpha,ref,0}$	0.0006	0.0005	0.0006

Figure 4.23 presents the development of the normalized creep-coefficient $C_\alpha/C_{\alpha,ref}$ of sand FS. The normalization eliminates the density dependency of C_α and the pressure dependent behaviour can be calculated by

$$\frac{C_\alpha}{C_{\alpha,ref}} = \left(\frac{p'}{p'_{ref}}\right)^{\theta} . \tag{4.13}$$

The coefficients of determination between the interpolation and the data points of sand FS in Figure 4.23 vary between R^2 = 0.78 and R^2 = 0.97 with a mean value of R^2 = 0.91. For the sands MS and SU the mean value of the coefficient of determination is R^2 = 0.63 and R^2 = 0.96 respectively. It justifies the representation of the influence of the density by the development of a reference creep-coefficient.

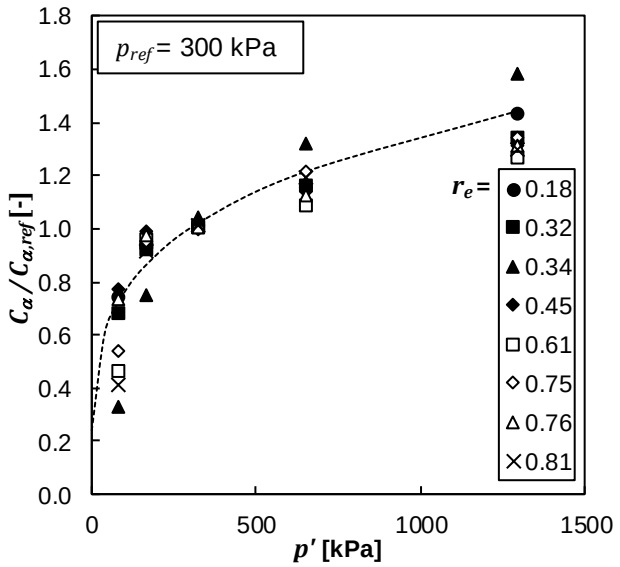

Figure 4.23: Development of normalized creep-coefficient C_α / $C_{\alpha,ref}$ of sand FS with the pressure p', regression calculation by Equation (4.13) with θ = 0.25

Inserting (4.12) into (4.11) gives

$$C_\alpha = \left[\omega \cdot r_e + C_{\alpha,ref,0}\right]\left(\frac{p'}{p'_{ref}}\right)^\theta , \tag{4.14}$$

which describes a plane of possible C_α - values in the C_α - p' - r_e - space as shown in Figure 4.20. A three-dimensional representation of (4.14) in the C_α - p' - r_e - space calculated exemplarily for sand FS is presented in Figure 4.24.

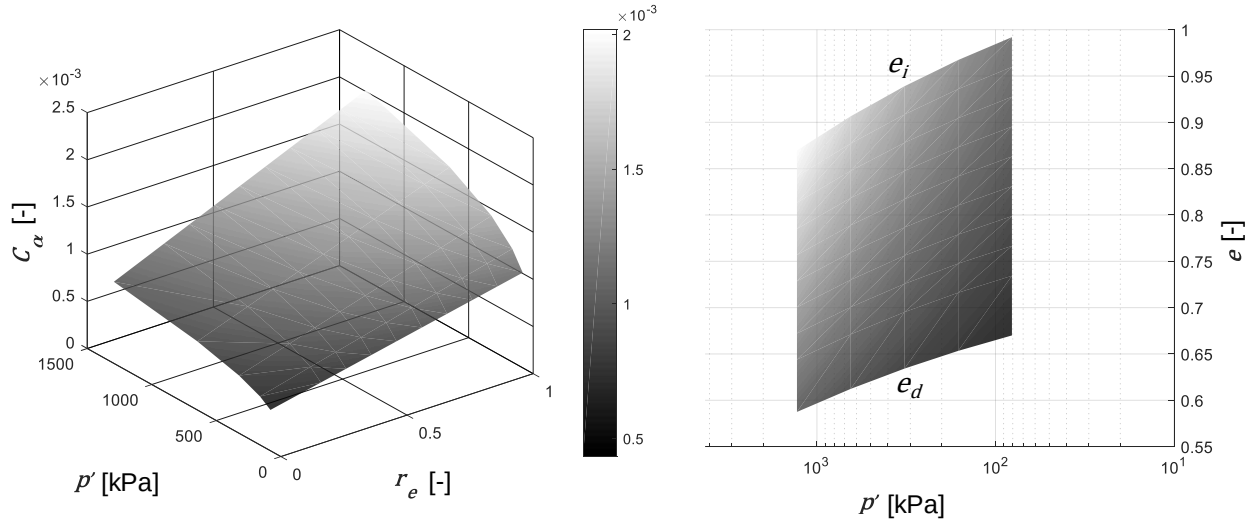

Figure 4.24: Development of C_α with the pressure p' and the relative void ratio r_e of sand FS calculated with ω = 8 · 10^{-4}, θ = 0.25, p'_{ref} = 300 kPa and $C_{\alpha,ref,0}$ = 6 · 10^{-4}

The C_α - developments of FS calculated with (4.14) and projected on the p' - C_α - plane and the r_e - C_α - plane are presented in Figure 4.25 along with representative test results. The creep-coefficient evolution with respect to the pressure and the relative void ratio can be well approximated by (4.14). The pressure-dependent behaviour shows very little deviation. The data on the development with the

relative void ratio shows scatter and deviations from the approximation by (4.14). However, the general trend and the magnitude of the creep-coefficient are predicted satisfactory. Results for the other two sands MS and SU are shown in Appendix A.6.

(a)

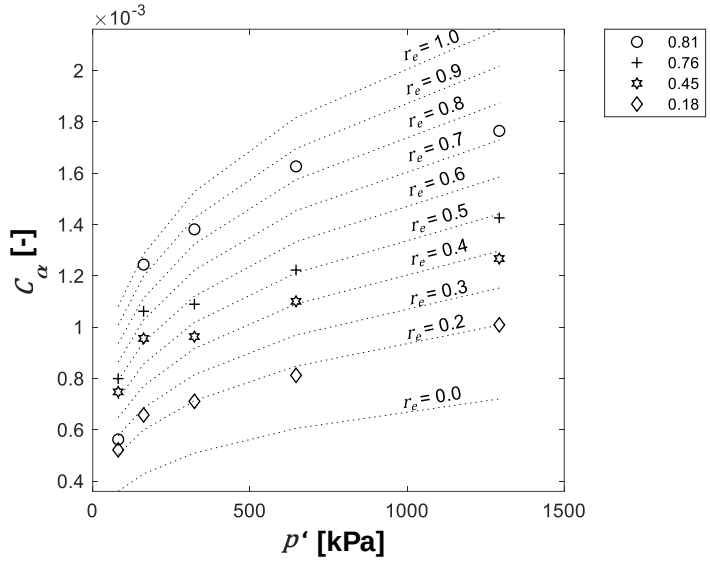

(b)

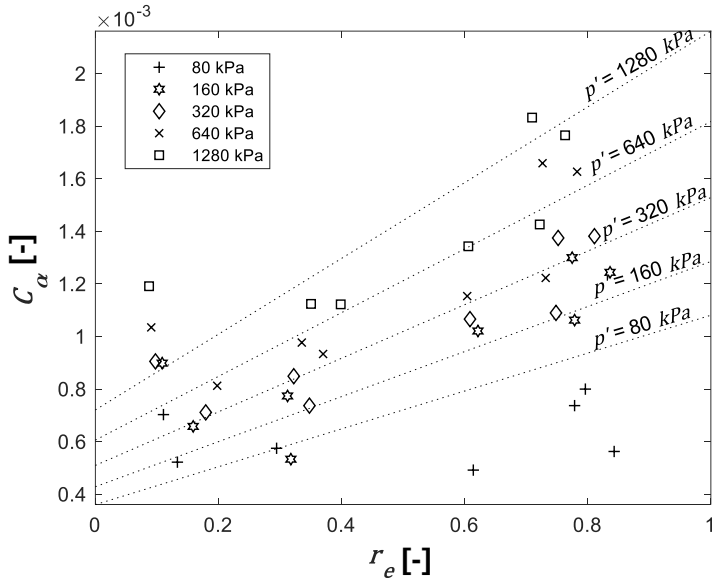

Figure 4.25: (a) Development of C_α with the pressure p' and (b) with the relative void ratio r_e of sand FS calculated with ω = 0.001, θ = 0.25, p'_{ref} = 300 kPa and $C_{\alpha,ref,0}$ = 0.0005

The calibration of the presented approach needs two oedometer tests or two isotropic compression tests including creep phases of at least 24 h on a loose ($r_e \approx 0.8$ to 1.0) and a very dense ($r_e \approx 0$) sample in the stress range considered. p'_{ref} has to be chosen for the best fit of the available data in the stress range considered. ω and $C_{\alpha,ref,0}$ can be calibrated by plotting the evaluated creep-coefficients of a very loose and a very dense oedometer test at the pressure level of p'_{ref} against the relative void ratio and evaluating the gradient and the axis intercept of the linear interpolation between the two points. θ is calibrated by plotting the evaluated creep-coefficients of a very loose and a very

dense oedometer test against the pressure p' and using θ and the fixed value of p'_{ref} to best fit the data of both tests.
This calibration procedure assumes that the relative void ratio changes only marginally during oedometric testing. A truly constant r_e occurs only in isotropic compression tests, which can also be used for calibration, but are more complicated to perform. Generally, the more tests with different density states and creep stress levels can be used for calibration, the better the parameter set. The above mentioned procedure uses the minimum required number of tests.

4.7 Strain rate-controlled tests

The strain rate-dependent material response in the previously presented results of incremental loading tests can only be analyzed in the creep phases. Strain rate-controlled loading and relaxation tests are not feasible in an incremental loading setup. The behaviour of the soil under constant rate of strain, a sudden change in the strain rate and continued loading after creep or stress relaxation with the boundary condition of zero strain rate have to be analyzed in strain rate-controlled testing. The following tests were performed (cf. Section 4.3):

– Creep after CRS,
– creep after different strain rates,
– CRS tests,
– ChRS tests,
– relaxation after CRS,
– relaxation after different strain rates and
– combined tests.

4.7.1 Creep after constant rate of strain

Creep after constant rate of strain was analyzed similarly to the LC incremental loading tests. The sands MS, SU and SU* were tested at low and high density to determine the influence of the GSD, the stress and density. By taking these three sands, the influence of a different mineralogy and largely also the influence of the grain shape were eliminated as influencing factors. The loading strain rate in all tests was 1.0%/min and creep phases of 24 h were performed at 250, 1000, 4000 and 7500 kPa vertical stress. The compression curves and creep strains are presented in Figure 4.26. All soils regardless of their fine content show a pronounced stress dependency of the creep strains and a strong reduction in the creep strains from a medium dense to a very dense or dense initial state, which is in agreement with the results from incremental loading tests (cf. Section 4.6). The soils SU and SU* with higher content of fines both follow nearly perfectly linear trends on a logarithmic time scale during the 24 h creep phases. Only sand MS shows an under-linear behaviour with increasing creep time. This indicates that the creep strains in sand MS may ultimately stagnate in time. This will be further addressed in Section 4.9.1.
With continued loading after creep, all soils react with their reloading stiffness. This is caused by the structuration in form of a rearrangement of force chains and a more stable load transfer state in the sample that develops during creep and can be deemed as an apparent preconsolidation reported for

normally consolidated clays (BJERRUM, 1967). This state is characterized by a low ratio of tangential to normal forces at the grain contacts (cf. Section 3.3.3). It can also be seen as a form of ageing. The structuration is destroyed with continued loading and the reloading stiffness gradually decreases until the virgin loading regime is reached again. In case of medium dense sand MS loaded at a strain rate larger than the creep rate, an overshooting of the normal consolidation line can be observed, while the other two soils show no such behaviour. The overshooting is due to a temporary shift in the yield point as a result of the structuration.

As it was also shown in Section 4.6, the compression curves follow in general a linear trend with respect to the logarithm of time, despite the slight deviation of sand MS. Therefore, an evaluation of the creep strains using (3.36) in the considered time interval is reasonable. The evaluated creep-coefficients are shown in Figure 4.27 (a). All soils show a stress and density dependency of the creep-coefficients. The difference in the coefficients between the medium dense and very dense respectively dense samples increases at higher stresses. When comparing the creep-coefficients of MS and SU to the ones analyzed from the incremental loading tests in Section 4.6, the values up to 2000 kPa are very similar, showing that the loading-rate – in LC tests the loads are instantly applied – has no influence on the long-term creep behaviour.

The increase of creep strains in 24 h with higher vertical effective stress from 250 to 7500 kPa is largest for sand SU with an increase of 300% and 340%, followed by SU* with an increase of 215% and 229% for the very dense or dense and medium dense samples respectively. The creep strains of MS increase by 63% and 122% for the very dense and medium dense samples respectively.

The denser samples show a decrease of the stress sensitivity of the creep strains. This is caused by the increased number of contact points between the grains that reduce the contact forces in the denser samples leading to reduced contact degradation and lower creep strains. In the tests in Section 4.6, the difference in the GSDs did not show much influence on the creep-coefficients up to a vertical stress of 2000 kPa (cf. Figure 4.14). However, the creep tests going to vertical stresses of 7500 kPa presented here, show a significant difference in the creep behaviour starting from stresses larger than 1000 kPa caused by the GSD. Sand SU has the highest compressibility and also shows the highest amount of creep strains. Soil MS shows the lowest creep deformations. The creep strains of sand SU* are in between the ones of SU and MS. This is surprising, as it would be expected that the soil with the highest fine content would also show the largest creep. It goes however hand in hand with the compressibility, where SU* shows a lower compressibility than SU, despite of the much higher fine content. An explanation for this behaviour could be the increased tendency of sand SU to form aggregates from coarser and finer particles, which was observed during sample preparation. These aggregates are destroyed during loading and creep leading to a higher compressibility and more creep strains.

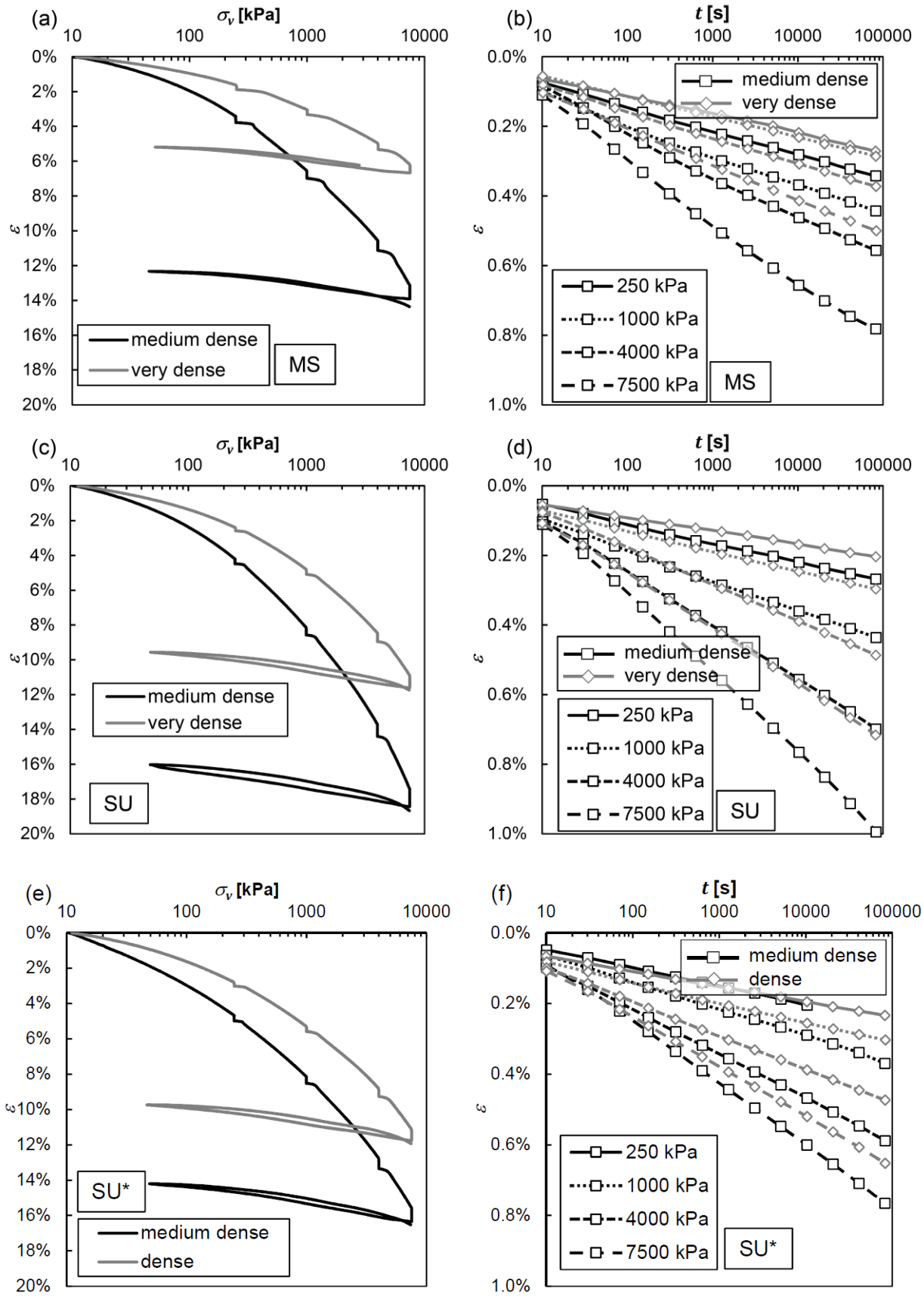

Figure 4.26: Creep after CRS of 1.0%/min at medium dense and very dense respectively dense state of (a)/(b) MS (2.8wt-% fines), (c)/(d) SU (14.3wt-% fines) and (e)/(f) SU* (25wt-% fines)

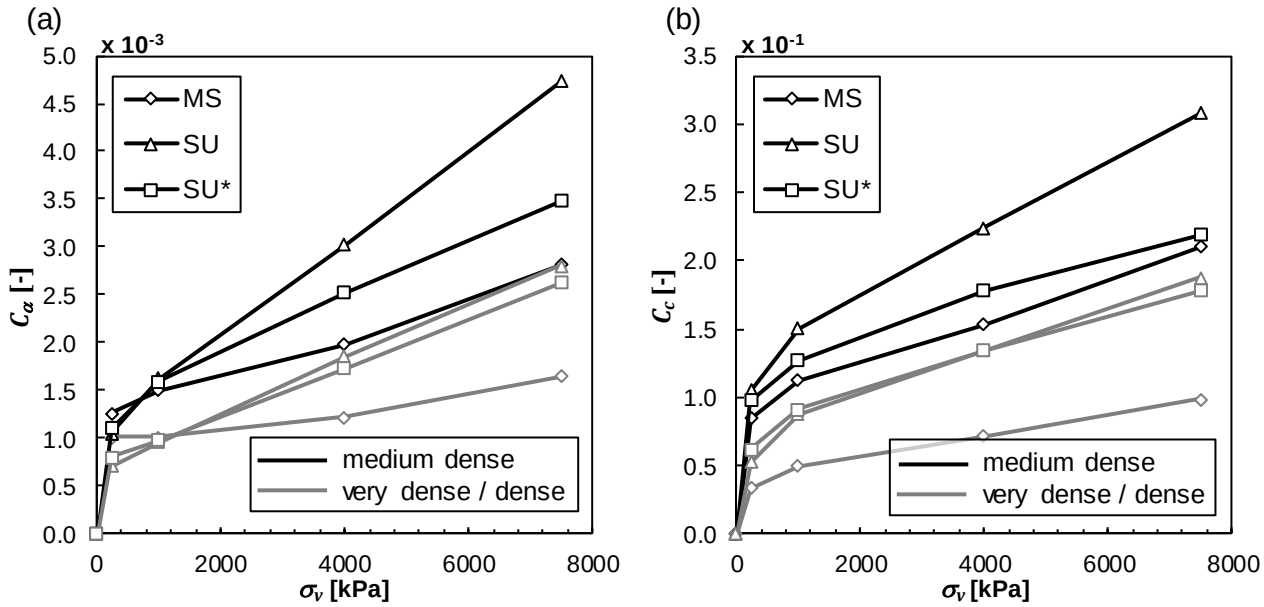

Figure 4.27: (a) Creep-coefficients after CRS of 1.0%/min and (b) compression indices at the creep stress level of medium dense and very dense samples of MS, SU and SU*

Figure 4.27 (b) shows the compression index at the vertical effective stresses where creep phases were performed. Evaluation of the C_α/C_c -ratio of the presented tests is shown in Figure 4.28. Generally, the results confirm the findings of the incremental loading tests in Section 4.6 and show the very good reproducibility of the test results. For the sands with high fine content the representation of the viscous behaviour can be approximated with a constant C_α/C_c -ratio. The variations of C_α/C_c with density and in the stress range up to 7500 kPa are very small. In case of sand MS it can again be seen that the C_α/C_c -ratios decrease with rising pressure and increase with rising density, as it was also shown in Section 4.6. The stress-dependent variation is more pronounced in the very dense sample than in the medium dense sample, where the ratio is almost constant. At stresses larger than 1000 kPa the C_α/C_c -ratios of the very dense sample converge to a value of 0.018 and of the medium dense sample to 0.013. The compression index C_c is more sensitive to density changes than the creep-coefficient C_α resulting in a change of C_α/C_c -ratios for sand MS. Similar for the stress dependency, the compression indices at low stresses show larger gradients than the creep-coefficients leading to the high C_α/C_c -ratio especially for the very dense specimen of sand MS (cf. Figure 4.27). As mentioned in Section 4.6, when taking the C_α/C_c -ratio as the descriptive parameter for the viscous behaviour, this would mean a large viscosity of the material at lower stresses and higher densities, which contradicts the soil behaviour in the presented laboratory tests and from experience.

As the experiments show, creep increases with higher stresses and lower densities. Such behaviour cannot be described by the evaluated C_α/C_c -ratio as it does not reflect this behaviour. In case of the tested clean sand MS, C_α and C_c are not influenced by stress and density change in the same way, leading to a change in the C_α/C_c -ratio. Therefore, as was already explained in Section 4.6 and shown here again, a precise description of the viscous soil behaviour of clean sands with the C_α/C_c -ratio alone is not applicable. Also in case of the sands SU and SU* the increase in creep with rising stress and reduced density cannot be described by just a constant C_α/C_c -ratio.

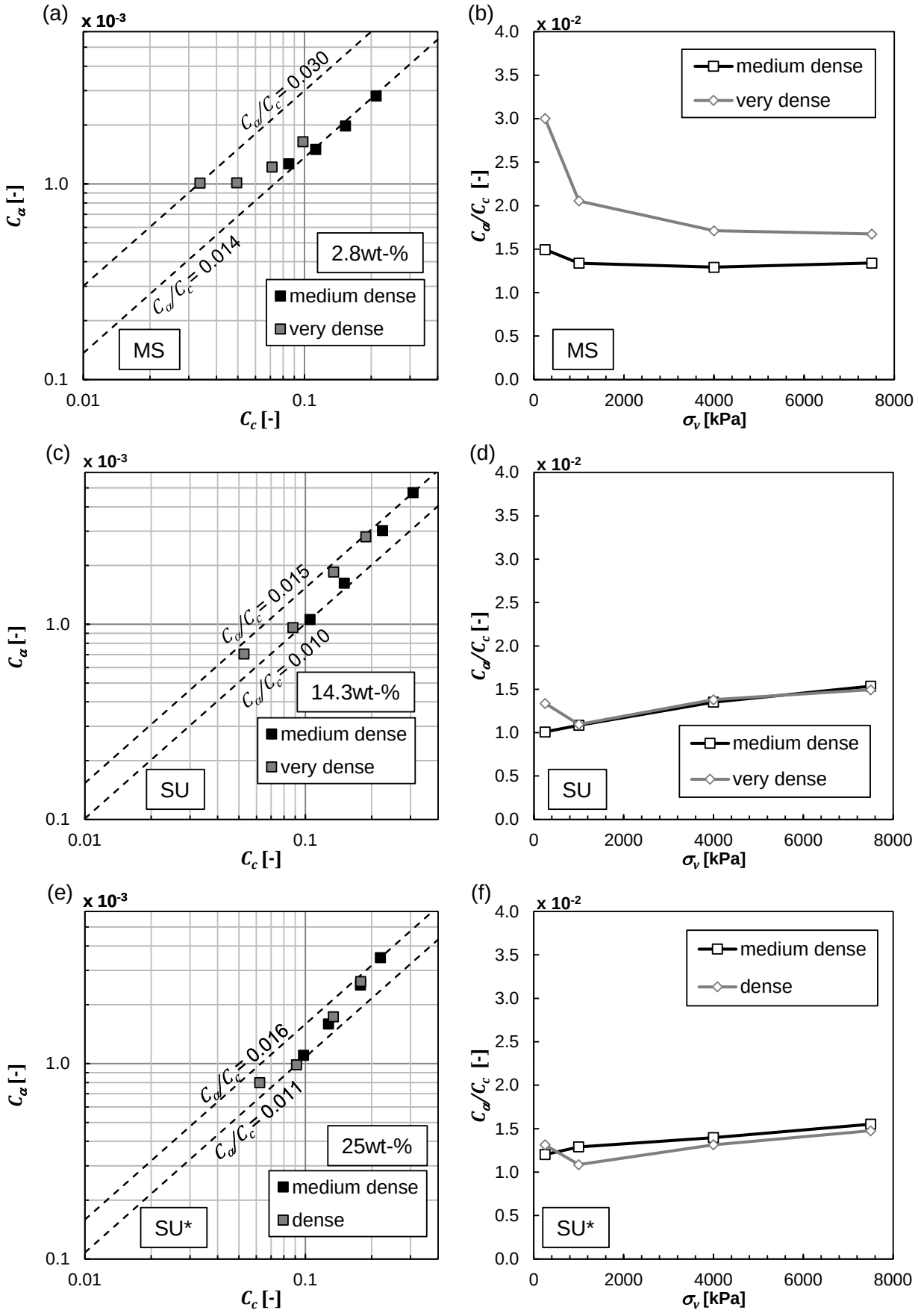

Figure 4.28: C_α / C_c - evaluation of (a)/(b) MS, (c)/(d) SU and (e)/(f) SU*

Conclusion

It can be summarized from the results presented in this section and in Section 4.6 that the creep behaviour of the investigated materials is highly stress and density dependent and that the assumption of a constant creep-coefficient is not valid. Also in the lower stress ranges up to approximately 2000 kPa, the creep-coefficients vary significantly with stress. A constant C_α/C_c -ratio is only valid for sands with a fine content larger than about 14wt-%. In his study about the one-dimensional compressibility of mixed-grained soils OSTERMAYER (1976) gives a threshold value of the fine content, above which the compressive behaviour of the soil changes from one of a granular soil to one of a fine grained soil (cf. Section 3.3.1.1). Between 15 and 25wt-% a load-bearing coarse grain skeleton still ensures the load transfer, but compressibility increases. From a fine content of 30 to 40wt-% the coarse grains begin to swim in the fine content. The coarse grains can no longer form a load-bearing grain skeleton. OSTERMAYER's oedometer test results on creep of mixed grained soils presented in Section 3.3.1.1 also indicate that the influence of the fine fraction on the viscous behaviour is significant at contents much lower than 30 to 40wt-%. The change in the load transfer mechanism from a grain skeleton to a fine grained matrix might explain the witnessed behaviour transition. To transfer the boundaries of OSTERMAYER or similar values to the viscous behaviour of soil, it would need additional testing. But the experimental results of this study already show that even lower fine contents starting from about 14wt-% are sufficient to influence the creep behaviour of the soil in a way that the C_α/C_c -ratio becomes nearly density and stress independent. A possible explanation could be the accumulation of fine particles on the coarse grains, which influences the mechanical behaviour at the contacts in the coarse grain skeleton.

4.7.2 Creep after different strain rates

During incremental loading tests the load is applied instantaneously and therefore the analysis of an influence of different loading strain rates on the creep behaviour is not possible. As shown in Sections 4.6 and 4.7.1, the development of creep deformations can be described using (3.36) respectively (3.37) during the 24 h creep phases. This implies the validity of (3.40) for the connection between creep strain rate and creep time. Hence, the strain rate at initiation of creep has to be equal to the prior loading strain rate.

To analyze the influence of the loading strain rate, tests with sand MS at medium relative density were performed with different loading strain rates prior to 24 h creep phases. The creep phases were performed at 250, 1000, 4000 and 7500 kPa with loading strain rates of 1.0, 0.1 and 0.01%/min. Figure 4.30 presents the compression curves of the three tests and the evaluated creep-coefficients. Figure 4.31 shows the time-dependent development of the creep strains. First of all, the stress dependency of the creep strains can again be clearly seen. Secondly, depending on the loading strain rate the time-dependent compression curves are initially non-linear and need different time intervals to converge towards a linear trend with the logarithm of time. This is in agreement with the results of KARIMPOUR & LADE (2010) and KARIMPOUR & LADE (2013) presented in Section 3.3.3, whom explain the behaviour by the different times the grain-assembly requires to adjust to the loading. However, regardless of the loading strain rate and time it needs for convergence, the creep-coefficients at one stress level approach the same value, as can be seen in Figure 4.30 (b) and as was also shown in

Sections 4.6 and 4.7.1. The creep-coefficients were evaluated from the approximately linear sections of the creep curves. According to (3.40), the reference time depends on the loading strain rate via

$$t_{ref} = \frac{C}{\dot{\varepsilon}_0}, \tag{4.15}$$

with increasing reference time at decreasing loading strain rate $\dot{\varepsilon}_0$ (cf. Figure 4.29).

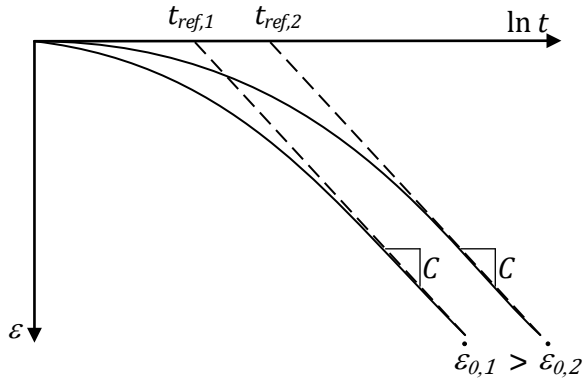

Figure 4.29: Creep reference time after different loading strain rates according to (4.15)

Since the creep-coefficient C is stress-dependent, also the reference time has to be stress-dependent according to (4.15) with a shorter reference time at lower stresses. Calculating the reference time for the three tested cases for the stress level of 7500 kPa using the determined creep-coefficients leads to values of t_{ref} = 4.5, 42 and 449 s at the loading strain rates of 1.0, 0.1 and 0.01%/min respectively. This is in good agreement with the values determined graphically from Figure 4.31 (b). As expected, a ten-fold difference in the loading strain rate leads to a ten-fold difference in the reference times with slight deviations due to inherent fluctuations in the laboratory tests. The reference time at 1.0%/min lies before the first measuring point at 10 s, which is why the creep curve already follows a constant gradient at the time of 10 s after load application. For comparison, the reference times at 250 kPa calculated with (4.15) using the determined creep-coefficients are t_{ref} = 1.8, 21 and 232 s at 1.0, 0.1 and 0.01%/min respectively. These results are also in good agreement with the graphically determined values (cf. Figure 4.31 (a)). They are smaller than the values at 7500 kPa due to the lower stress and therefore lower creep-coefficient.

Calculations of the creep strains with (3.37) using the determined reference times using (4.15) at 7500 kPa are presented in Figure 4.32. For the faster two strain rates the comparison between calculated and measured creep strains shows larger deviations, while they are very similar at the loading strain rate of 0.01%/min. This is most probably caused by the larger inaccuracy of the determination of the reference time at fast loading strain rates. The relative inaccuracies of the calculated creep strains in the cases of the faster strain rates become smaller with increasing observation time, because the creep curves run parallel, meaning the deviations are constant. However, fast loading strain rates have the advantage that the creep curves quickly converge to a straight line on a logarithmic time scale and the constant creep-coefficient can be determined after short creep phases. At very slow loading strain rates the point of convergence can be difficult to determine.

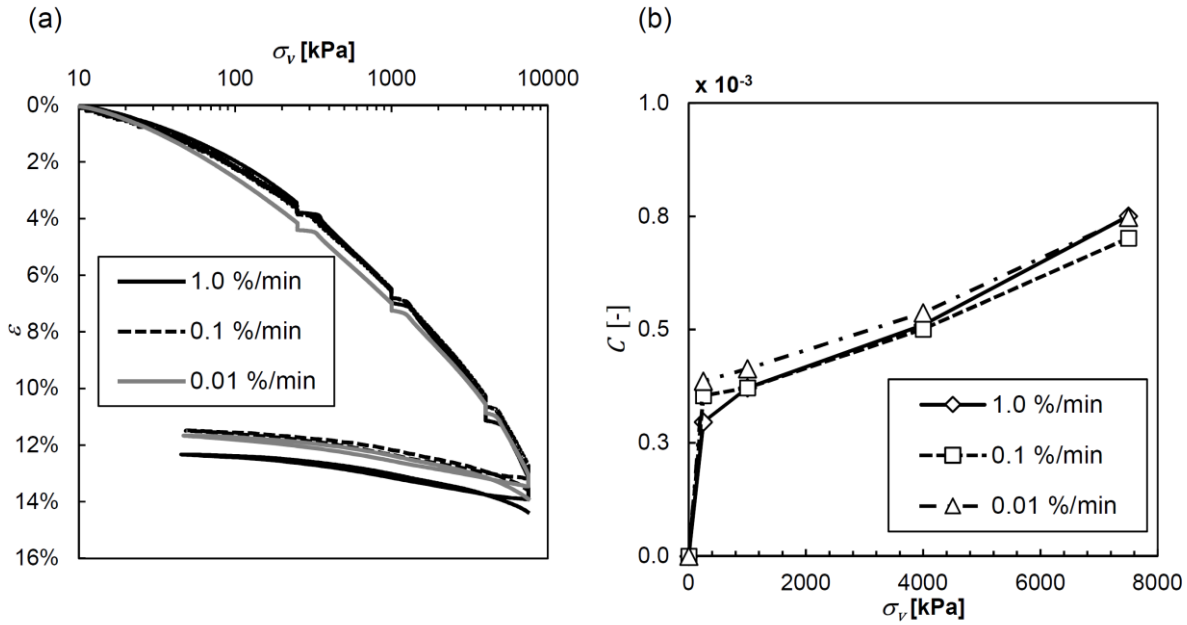

Figure 4.30: CRS-tests on medium dense soil MS with different loading strain rates and 24 h creep phases at 250, 1000, 4000 and 7500 kPa, (a) compression curves and (b) creep-coefficients evaluated in the approximately linear sections of the creep curves

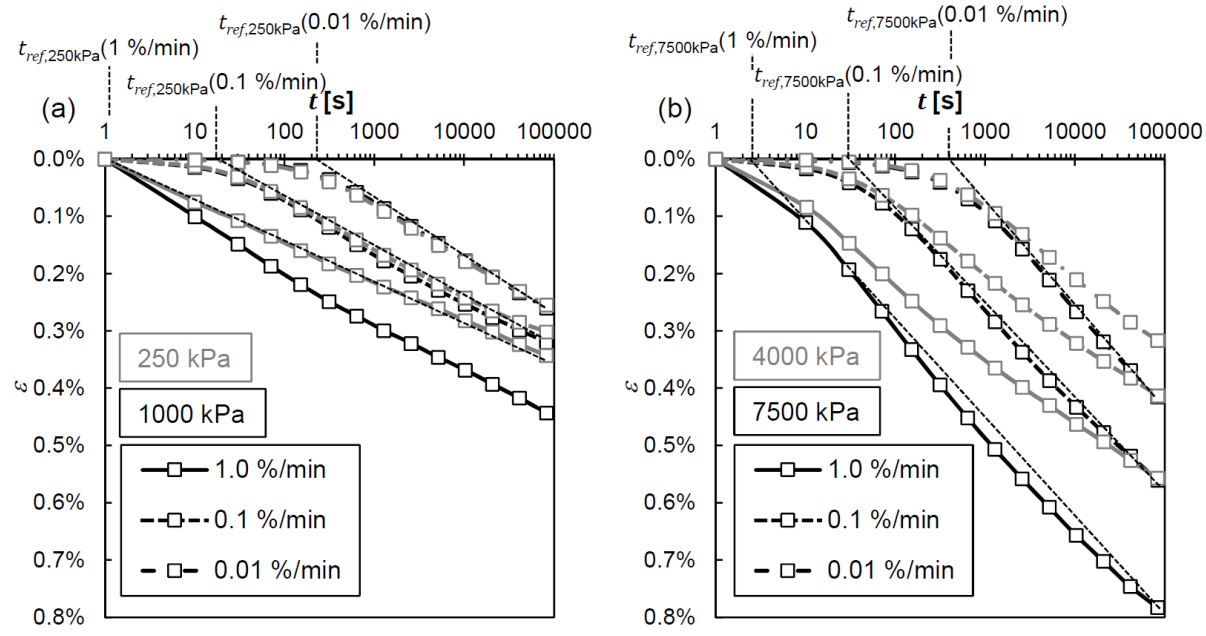

$t_{ref,250kPa}$(1 %/min) = 1.2 s
$t_{ref,250kPa}$(0.1 %/min) = 18 s
$t_{ref,250kPa}$(0.01 %/min) = 220 s

$t_{ref,7500kPa}$(1 %/min) = 2.5 s
$t_{ref,7500kPa}$(0.1 %/min) = 30 s
$t_{ref,7500kPa}$(0.01 %/min) = 400 s

Figure 4.31: Creep for 24 h at 250, 1000, 4000 and 7500 kPa after different loading strain rates

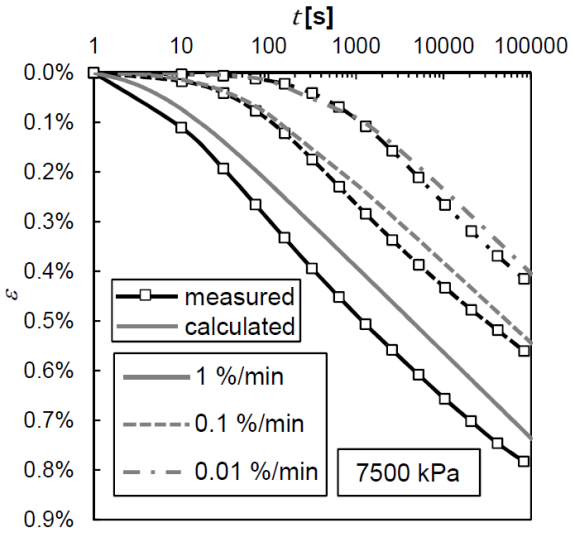

Figure 4.32: Creep for 24 h at 7500 kPa together with creep strains calculated with (3.37) and reference time determined by (4.15)

The results show that the behaviour of the tested sand follows in this respect (3.37) and (4.15). However, they again demonstrate the stress dependency of the creep strains or creep-coefficients, which means a changing reference time along the $\dot{\varepsilon}_0$-isotache or vice versa a changing strain rate along the reference isochrone. When considering the results from this section and Sections 4.6 as well as 4.7.1 the assumption of (3.53) respectively (3.58) that

$$C \cdot \ln\left(\frac{t_i}{t_0}\right) = C \cdot \ln\left(\frac{\dot{\varepsilon}_0}{\dot{\varepsilon}_i}\right) \tag{4.16}$$

does not apply to granular soils, because the equality of isochronic-lines and isotache-lines upon a stress change from σ_0 to σ_i is not given.

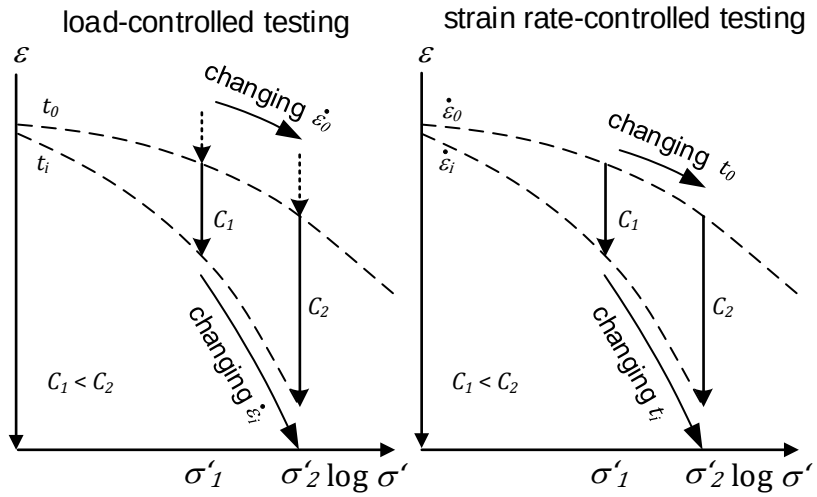

Figure 4.33: Consequences for the isotache-concept resulting from the findings in Sections 4.6, 4.7.1 and 4.7.2

A graphical representation of this conclusion is shown in Figure 4.33. In LC testing we can determine lines of equal creep time. Due to the lower creep-coefficient at the stress level σ_1 compared to σ_2, the strain rate after equal creep time at σ_2 is larger than at σ_1. In strain rate-controlled testing the imposed strain rate of $\dot{\varepsilon}_0$ decays slower at stress level σ_2 than at stress level σ_1. Therefore, the creep time t_0 along an isotache-line has to change. However, considering the same stress level, the creep behaviour can be described using (4.16) or (3.58).

4.7.3 Constant rate of strain tests

Previous studies on granular soils by TATSUOKA *et al.* (2002), DI BENEDETTO *et al.* (2002), LADE (2009), LADE *et al.* (2009), KARIMPOUR & LADE (2010) and LADE & KARIMPOUR (2014) reported no rate dependency of the stress-strain-relationship during CRS tests (cf. Section 3.3.2).
Figure 4.22 shows the results of CRS tests of sand MS with 2.8wt-% and sand SU2 with 46wt-% content of fines. The strain rate was varied by a factor of 1000 between 1.0 and 0.001%/min. While sand MS shows no visible dependency on the strain rate (cf. Figure 4.22 (a)), sand SU2 displays a well visible strain rate effect (cf. Figure 4.22 (b)). As expected, the faster the strain rate the stiffer is the specimen's reaction. To avoid effects from sample preparation as apparent strain rate effect, each CRS test was performed twice at the same density.
To rule out the possibility that the strain rate effect at a 1000-fold strain rate change is present, but just too small to be detected by the used measurement equipment, five points on the isotache-line of $\dot{\varepsilon}$ = 0.001%/min were calculated using (3.58) and are marked by boxes in Figure 4.34 (a).

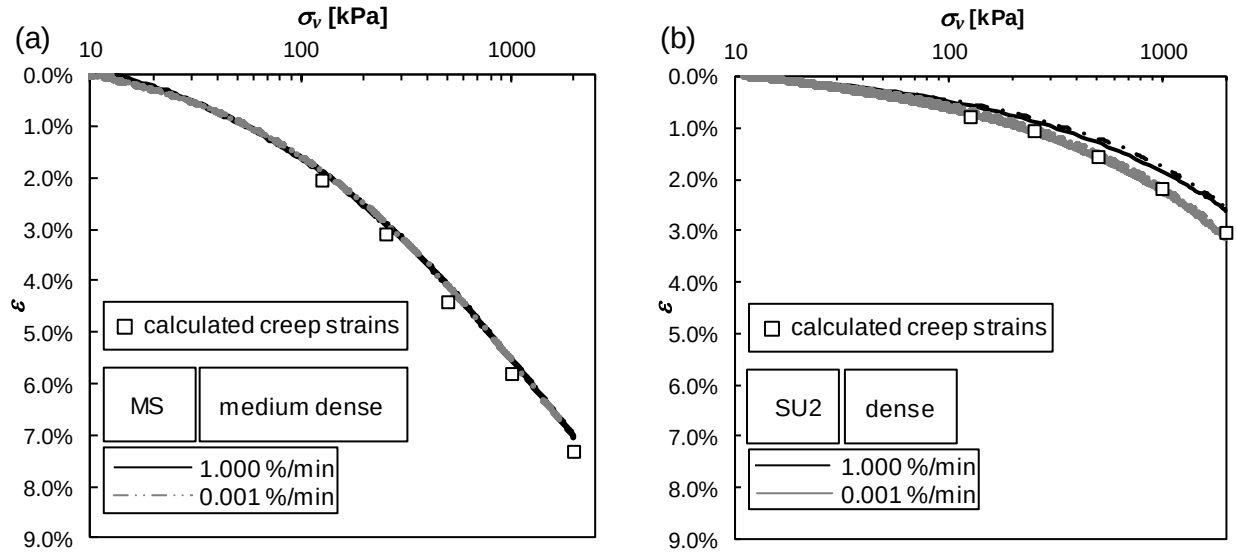

Figure 4.34: CRS tests on (a) MS and (b) SU2 by applying two strain rates with a ratio of 1000 and creep strains calculated using (3.58) marked by boxes

The validity of (3.58) at one stress level was shown in the previous Section 4.7.2. The needed creep-coefficients at each stress level were taken from the test results of medium dense sand MS presented in Section 4.6. It is obvious that the strain rate effect – if it would be present – could have been captured with the used measurement equipment. The same calculation was performed for the sand

SU2 with the test results from Section 4.6 (cf. Figure 4.34 (b)). The apparent rate-effect, which increases with stress, is in very good agreement with the calculated strains from (3.58) determined on the basis of the stress-dependent creep-coefficients. Consequently, for sand MS to each pair of σ' and e an indefinitely large number of strain rates could be theoretically assigned. Therefore, a unique relationship between σ', e and $\dot{\varepsilon}$, as defined by (3.53), does not exist for clean sands.

4.7.4 Tests with sudden changes in strain rate

To investigate the rate-effects further, tests with sudden stepwise changes in the strain rate (ChRS) were conducted. In ChRS-tests the strain rate was varied stepwise during loading at different stress levels. Figure 4.35 shows results of sand MS with medium relative density and (a) 200-fold as well as (b) 10-fold strain rate change. Upon a sudden strain rate change, there is a simultaneous variation in the vertical effective stress. After strain rate reduction stress decreases and after strain rate acceleration stress increases. The change of the stress-strain curve is reversible, since the compression curve approaches with ongoing straining the curve it would have gone through without a sudden change in the strain rate. This kind of behaviour was also reported by TATSUOKA *et al.* (2002) and DI BENEDETTO *et al.* (2002) and called TESRA ("Temporary Effect of Strain Rate and Acceleration") (cf. Section 3.3.2).

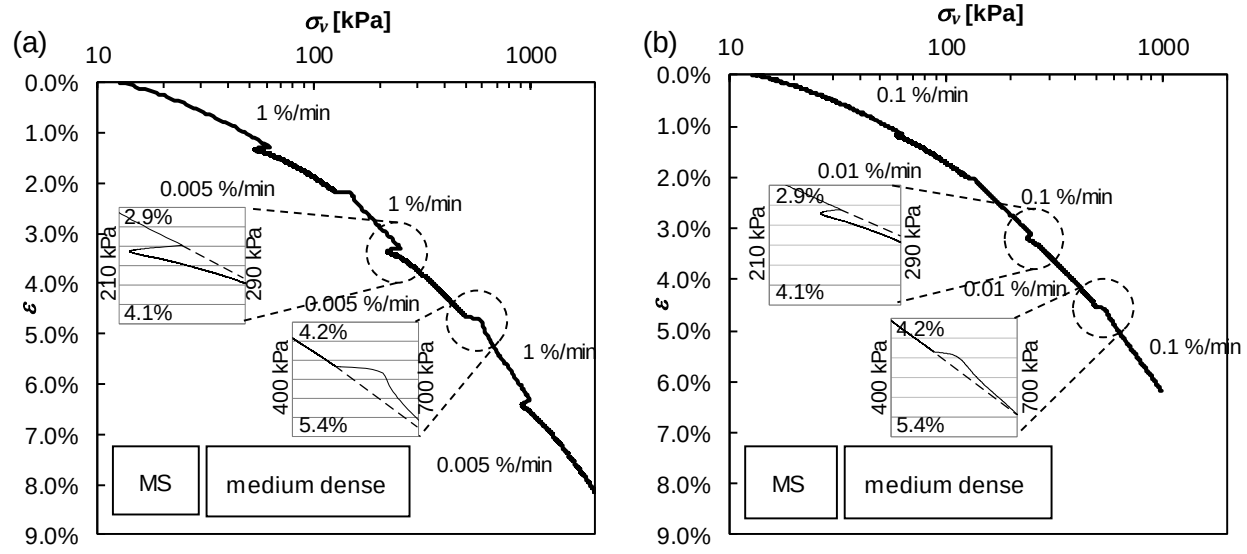

Figure 4.35: Strain rate-controlled tests including sudden changes in strain rate of MS with (a) 200-fold and (b) 10-fold change in strain rate

It can be seen from the two magnified sections in the diagrams, which have the same strain and stress sectors, that the intensity of the stress change depends on the difference in the strain rates. The larger the difference in the strain rates, the greater the change in stress. At deceleration stress relaxes, because the initial relaxation rate depends on the previous loading strain rate and is faster than the stress rate imposed by the slow loading strain rate. With continued straining the relaxation stress change vanishes as the relaxation rate decays quickly with rising OCR and becomes slower than the loading strain rate. Upon acceleration the stress increases temporarily, because the relocation rate of the grains does not immediately adopt from the previously slow imposed strain rate to the fast imposed strain rate leading to an interlocking effect. At continued straining the relocation rate

adopts and the interlocking effect and therefore the stress increase is lost. The reversibility of the strain rate effect is in agreement with the results of CRS-tests presented in the previous Section 4.7.3, where no rate-effect could be detected.

Figure 4.36 shows the results of sand SU2 in a dense state with (a) 200-fold and (b) 100-fold strain rate change. The viscous reaction of the soil is less pronounced than in sand MS. Contrary to the behaviour of sand MS, a change in the stress-strain curve at a sudden change of strain rate is permanent with continued straining. The intensity of the stress change depends on the difference in the strain rates as already identified for the sand MS (see the magnified sections in the diagrams).

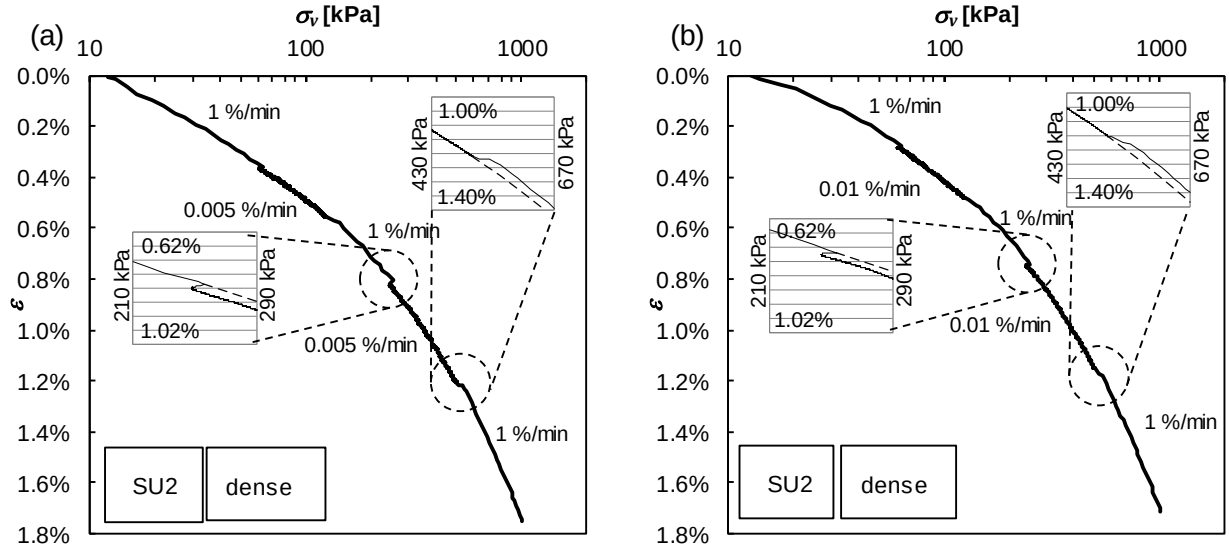

Figure 4.36: Strain rate-controlled tests including sudden changes in strain rate of SU2 with (a) 200-fold and (b) 100-fold change in strain rate

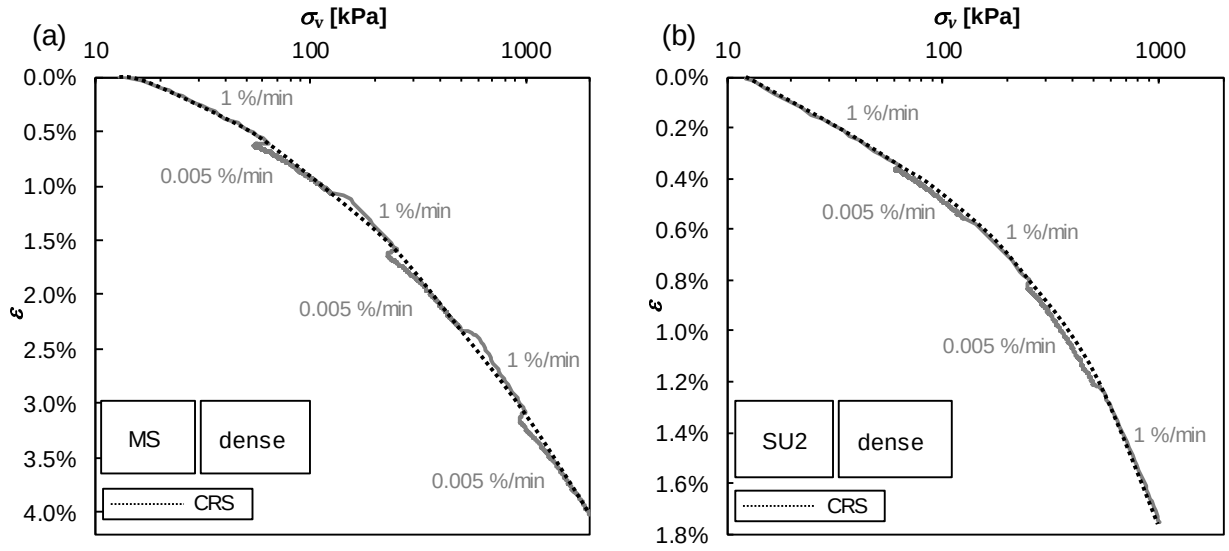

Figure 4.37: Strain rate-controlled tests including sudden changes in strain rate together with a CRS curve of (a) MS and (b) SU2 in a dense state

For further investigation of the viscous behaviour of the two sands at strain rate changes and in order to clarify whether they follow a TESRA behaviour or the stress changes upon strain rate jump are

permanent, Figure 4.37 depicts two diagrams from (a) sand MS and (b) sand SU2 in a dense state. A ChRS test and the CRS line corresponding to the initial strain rate are presented. It can be seen from Figure 4.37 (a) that after a sudden strain rate change the stress-strain curve of MS always approaches the CRS curve again, which indeed corresponds to TESRA behaviour. In the case of SU2 (Figure 4.37 (b)), it can be observed that the two lines remain seperated after a sudden strain rate change. The distance between the isotache-lines increases slightly with the vertical effective stress.

Three more tests on soil MS, SU and SU* with 1000-fold strain rate change at medium density and up to 7500 kPa vertical stress were conducted. The purpose was to see whether the permanent stress change is just not visible in case of soil MS, because of its low viscosity, or if the temporary nature of the stress change is of a constitutive character. SU and SU* with 14.3 and 25wt-% fine content were to determine a threshold value of fine content from which the soil behaviour changes from TESRA to a permanent stress change. The test results are presented in Figure 4.38.

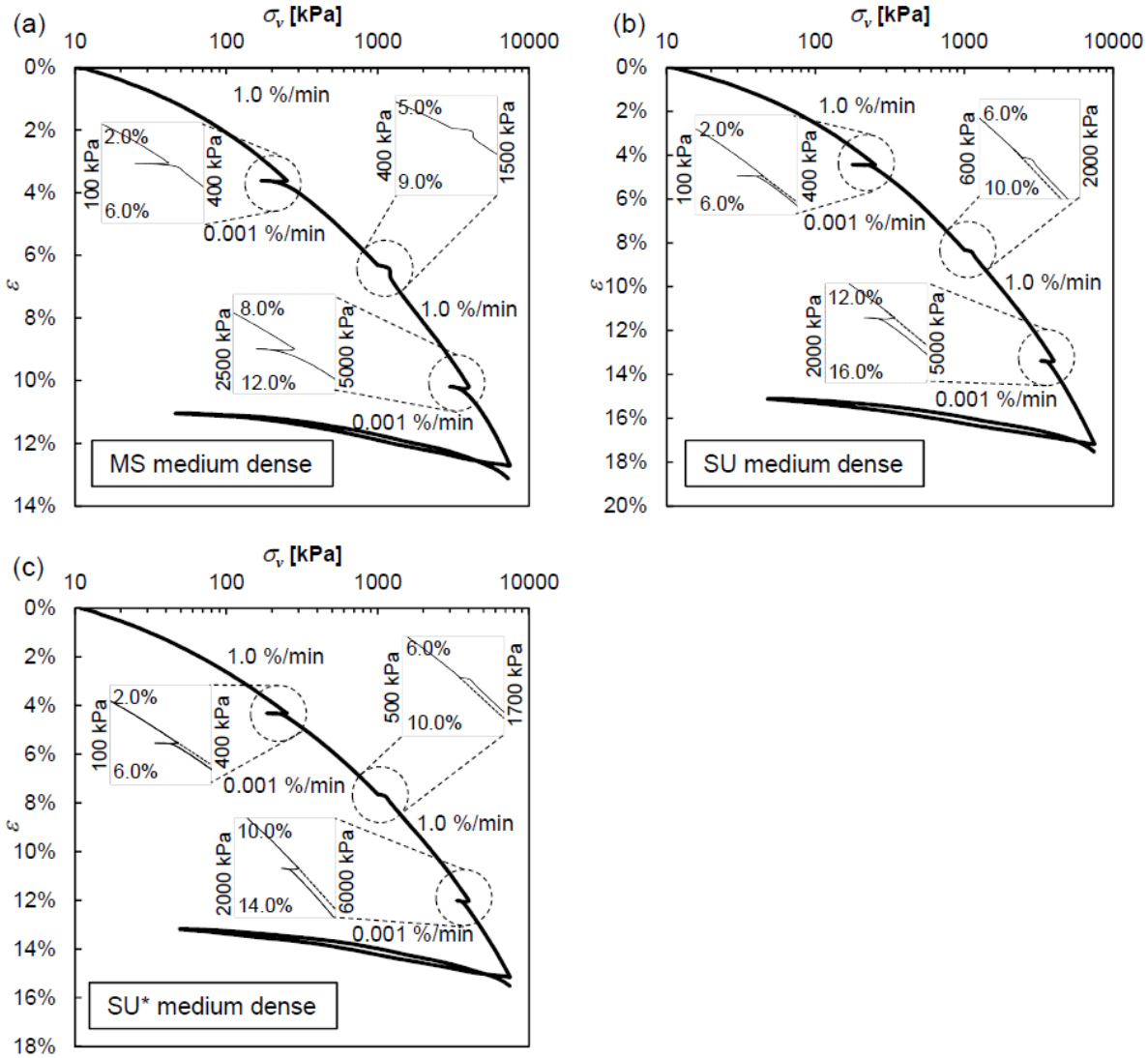

Figure 4.38: Strain rate-controlled tests including 1000-fold sudden changes in strain rate of (a) MS (fine content 2.8wt-%), (b) SU (fine content 14.3wt-%) and (c) SU* (fine content 25.0wt-%) in a medium dense state

The sudden changes in strain rate from 1.0%/min to 0.001%/min and vice versa were performed at 250, 1000 and 4000 kPa and are indicated by magnified images in the diagrams. In case of sand MS, the changes in stress upon sudden strain rate change are again clearly of a temporary nature and no seperate isotache-line can be determined. For soil SU and SU* with fine contents of 14.3 and 25wt-% respectively, a permanent change in stress can be identified. At deceleration to 0.001%/min, the increase in vertical effective stress is initially much slower than the relaxation-rate, which explains the strong stress decrease at almost constant strain. Upon acceleration of the strain rate the compression curve immediately reaches the new isotache-line after a slight overshooting.

Evaluation of I_v according to (3.45) is only possible if the relative stress jump upon strain rate jump remains constant with ongoing straining. Therefore, in case of sand MS I_v cannot be determined, because the relative stress jump is only temporary. For SU and SU* I_v was evaluated at each stress level where a sudden change in strain rate was applied using (3.45). Figure 4.39 presents the results for the two different densities with respect to the applied vertical stress. The I_v -values remain practically constant over the wide range of stresses from 250 to 4000 kPa and densities from medium dense to very dense. Table 4.6 presents the individual values of I_v and the mean value as well as the standard deviation divided by the mean value of each soil. A ratio of standard deviation to mean value of 14% can be considered as very small in the context of geotechnical laboratory testing. I_v can therefore be regarded as constant for the two sands with high fine content. Regardless of their different GSDs, both sands have nearly identical viscous responses to sudden changes in the strain rate. This indicates that the same mineralogy and similar grain shape of SU and SU* leads to similar I_v values.

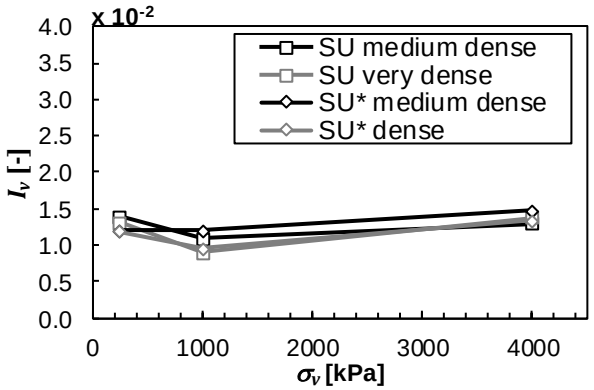

Figure 4.39: Evaluation of ChRS tests with 1000-fold strain rate change on SU and SU* in a medium dense and a very dense respectively dense state using I_v from (3.45)

Table 4.6: I_v for a 1000-fold strain rate change of SU and SU* in a medium dense and a very dense respectively dense state at different stress levels

Vertical effective stress [kPa]	I_v			
	SU		SU*	
	Medium dense	Very dense	Medium dense	Dense
250	0.014	0.013	0.012	0.012
1000	0.011	0.009	0.012	0.010
4000	0.013	0.014	0.015	0.013
Mean	0.012		0.012	
Standard deviation / mean	0.14		0.13	

Concluding, the test results show that sand MS has a TESRA-type response to sudden changes in the strain rate and (3.45) cannot be applied to describe its viscous response. In case of the sands SU and SU* with 14.3 and 25wt-% fine content respectively, the tests show a remaining stress change with continued straining after a sudden jump in the strain rate. The viscosity indices of SU and SU* evaluated with (3.45) are nearly constant in a wide range of stresses as well as densities. This is in agreement with the results on the C_α/C_c -ratios evaluated from creep tests (cf. Sections 4.6 and 4.7.1).

The observed transient effects of strain rate, just like the creep strains in the previous sections, are very small. Their pratical relevance is usually small too. As for the creep strains, which only have to be considered in engineering design at special boundary conditions like the mentioned open cast mining dumps, the strain rate effects are usually only relevant at large scales, maybe even in the explanation of tectonic movements and earthquakes. However, for the mechanical understanding of soil behaviour they are important, independent of their practical relevance.

4.7.5 Relaxation after constant rate of strain

Test conditions

A test series with almost identical boundary conditions like the creep tests after constant rate of strain compression (cf. Section 4.7.1) was conducted to evaluate the relaxation behaviour of different soil types, under different vertical effective stresses and varying density. The loading strain rate in all tests was 0.01%/min as opposed to 1.0%/min in the creep tests in Section 4.7.1. The slow loading strain rate was chosen to minimize the influence of the load frame for maintaining the condition $\dot{\varepsilon} = 0$. Tests with a loading strain rate of 1.0%/min showed a large influence of the load frame at the beginning of the relaxation phases. As an example, a comparison of the recorded deformations and stresses during a relaxation phase at 250 kPa with 0.01%/min and 1.0%/min loading strain rate is presented in Figure 4.40.

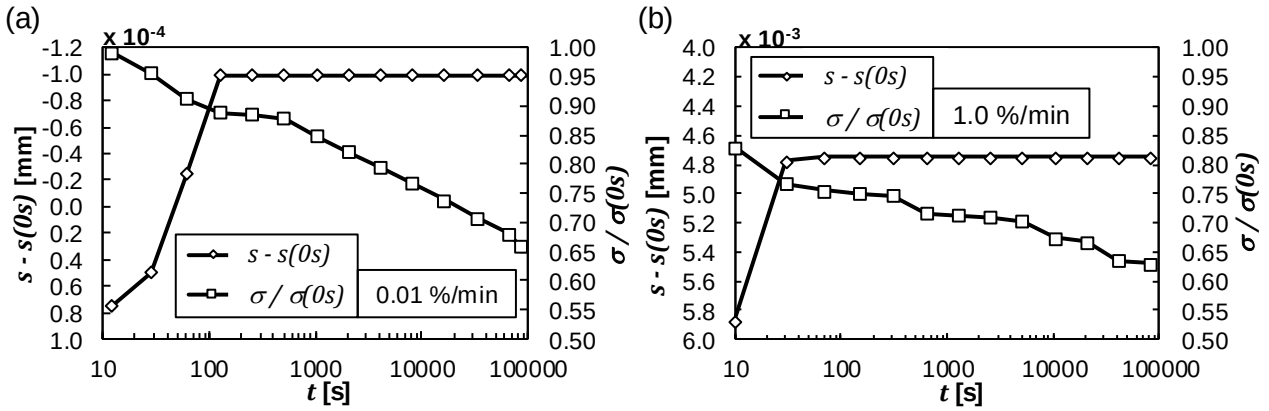

Figure 4.40: Relative deformations $s - s(0s)$ and normalized stress relaxation $\sigma / \sigma(0s)$ recorded during a relaxation phase of 24 h at 250 kPa with sand MS, with (a) 0.01%/min and (b) 1.0%/min loading strain rate

At initiation of the relaxation phase the load-frame stops, but the sample still has the tendency to deform. The deformation-rate depends on the prior loading strain rate, just like the creep rate as shown in Section 4.7.2. The deformation leads to a decrease in stress, which in turn results in a very

quick stagnation of the deformations, because the sample becomes overconsolidated. However, the stress decrease that is triggered by these initial deformations is due to unloading not due to relaxation. The deformations need to be compensated. In order to keep the initial deformations small, the load frame needs time to react. Therefore, it is recommendable to apply a small loading strain rate. In case of the sample loaded at 0.01%/min, the load cell expands only $0.8 \cdot 10^{-4}$ mm, because stress reduces only by approximately 1% in the first ten seconds. In case of the sample loaded at 1.0%/min the stress decreases by 18% and the measured deformations are approximately $5.8 \cdot 10^{-3}$ mm in the first ten seconds. The load-frame then tries to compensate the deformation, which can be seen by the decrease in relative deformation $s - s(0s)$ in Figure 4.40. In case of the fast loading strain rate, the frame does not compensate the entire initial deformation, but still moves $1.0 \cdot 10^{-3}$ mm, which leads to a large unloading stress decrease and not – as required – a relaxation stress decrease. With the loading strain rate of 0.01%/min it only reacts with an unloading of $1.8 \cdot 10^{-4}$ mm, which can be regarded as a tolerable value. It still influences the relaxation behaviour slightly, as can be observed by the non-linearity of the relaxation curve in Figure 4.40 (a). After about 120 s the deformations are kept constant, because the load-frame has now enough time to maintain the $\dot{\varepsilon} = 0$ condition as the relaxation rate has already slowed down significantly and the sample deformations are minimal due to the already large overconsolidation. This leads to a nearly constant slope of the relaxation curves over the logarithm of time. Generally, the results of the relaxation tests are sensitive to any change of the boundary conditions. This can be observed in the partly erratic relaxation curves of the tests presented in the following. Especially the results of the tests at high densities proved to be very sensitive.

Test results

The oedometer tests were performed with relaxation phases of 24 h at 250, 1000, 4000 and 7500 kPa vertical stress. The relative density was varied between medium dense and very dense, respectively dense in case of soil SU*. The results are presented in Figure 4.41 and Figure 4.42. Sand MS shows a decreasing normalized relaxation σ/σ_0 with increasing initial vertical effective stress. In case of sands SU and SU* the relaxation is almost independent of the stress level. For all soils the density does not influence the relaxation behaviour significantly. The evaluated viscosity indices are shown in Figure 4.43. The results confirm the observations from Figure 4.41 and Figure 4.42. The I_v values for MS decrease with rising vertical effective stress while I_v is constant in case of SU and SU*. For sand MS this dependency is qualitatively similar to the development of the C_α/C_c -ratios determined from creep tests in Sections 4.6 and 4.7.1, although the I_v values from relaxation tests are approximately 1.25 to 1.7 times larger than the C_α/C_c –ratios depending on the stress level. In case of sands SU and SU* the I_v -values from tests with sudden changes in strain rate are identical to the values from relaxation tests (cf. Section 4.7.4).

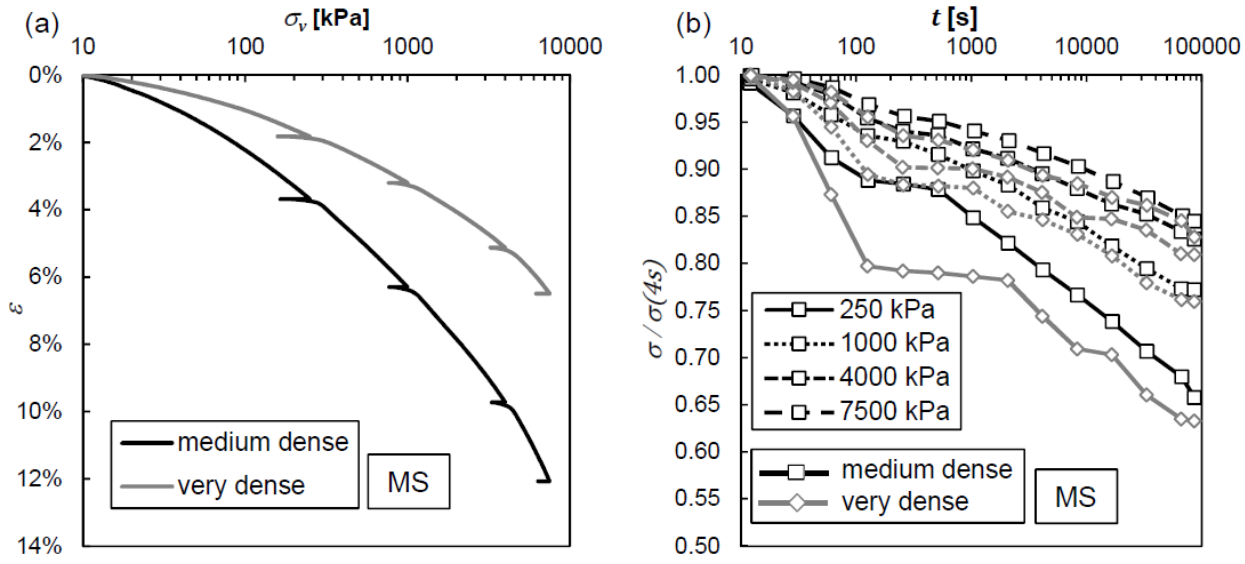

Figure 4.41: Stress relaxation after CRS at 0.01%/min at medium dense and very dense state of sand MS (2.8wt-% fines)

An explanation for the observed reduced normalized relaxation of sand MS can be found by assuming that the strain rate can be decomposed into an elastic and a viscous part according to a MAXWELL-rheological model. Considering the boundary condition of zero strain rate during relaxation, the following must hold for oedometric conditions:

$$\dot{\varepsilon} = \dot{\varepsilon}_v = \dot{\varepsilon}^e + \dot{\varepsilon}^{vis} = 0\,. \tag{4.17}$$

where $\dot{\varepsilon}_v$ is the volumetric strain rate, $\dot{\varepsilon}^e$ is the elastic part and $\dot{\varepsilon}^{vis}$ is the viscous part of the strain rate. Since the viscous strains will not be zero during relaxation, the granular skeleton must be unloaded for the elastic strains to compensate viscous strains and therefore follows

$$-\dot{\varepsilon}^e = \kappa^0 \frac{\dot{\sigma}'}{\sigma'} = \dot{\varepsilon}^{vis} \tag{4.18}$$

and

$$\dot{\sigma}' = \frac{\dot{\varepsilon}^{vis}}{\kappa^0} \cdot \sigma' \tag{4.19}$$

where σ' is the current stress and κ^0 is the oedometric swelling index, which can be calculated via

$$\kappa^0 = \frac{C_s}{(1+e_0)ln(10)} \tag{4.20}$$

with e_0 the initial void ratio.

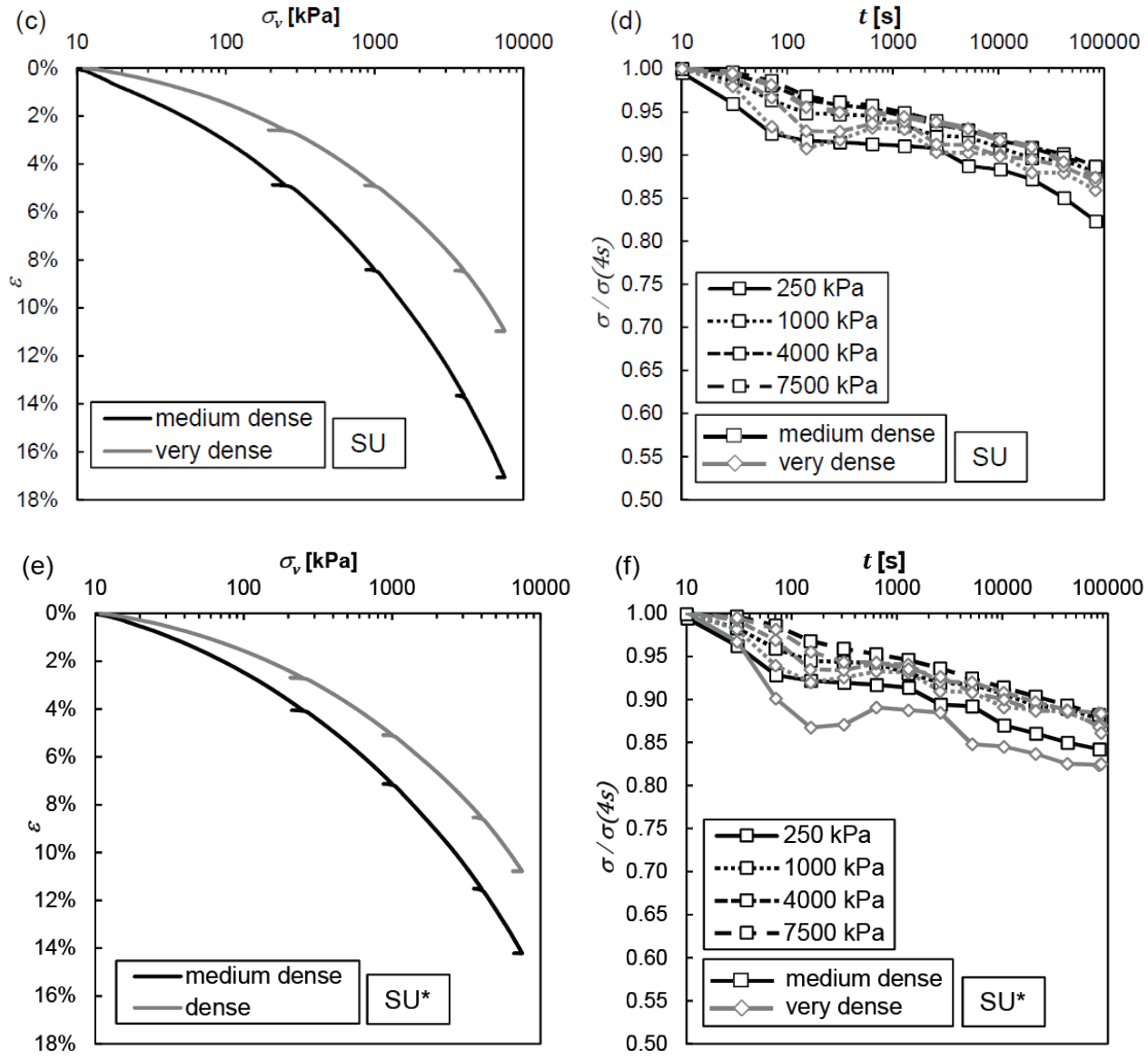

Figure 4.42: Stress relaxation after CRS at 0.01%/min at medium dense and very dense respectively dense state of (c)/(d) sand SU (14.3wt-% fines) and (e)/(f) sand SU* (25wt-% fines)

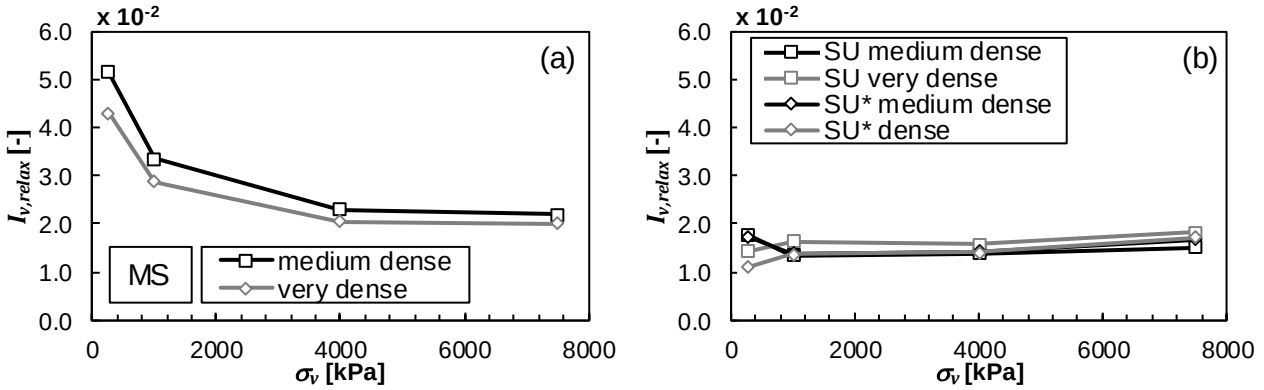

Figure 4.43: Viscosity indices determined from relaxation tests on (a) MS and (b) SU as well as SU*

The relaxation stress rate is influenced by the swelling index, the viscous strain rate and the current stress. Considering the test results from Section 4.6 on the creep behaviour after unloading (cf. Figure 4.14) it can be assumed that the creep-coefficient and thus the viscous strain rate $\dot{\varepsilon}^{vis}$ at overconsolidated states OCR > 1.2 in sands are very small and independent of the stress and the density. Under this assumption, the relaxation behaviour is only controlled by the elastic soil response. The swelling index κ^0 increases relative to and with rising preconsolidation stress in an oedometer test. Oedometer test results on medium dense and very dense sand MS with several unloading and reloading phases exemplify this for preconsolidation stresses of 125 to 7500 kPa (cf. Figure 4.44). The swelling index was determined as the mean value from the unloading and reloading curves between the preconsolidation stress and the minimal stress of 50 kPa. Inserting larger κ^0 into (4.19) leads to lower normalized relaxation stress rates.

While the compression index is strongly influenced by the density of the soil, the swelling index is almost independent of the density (cf. Figure 4.44 (b)). This corresponds well to the finding from Figure 4.42 (b), (d) and (f) that the density of the samples does not influence the relaxation behaviour. And it supports the conclusion that stress relaxation can be described by the swelling index κ^0.

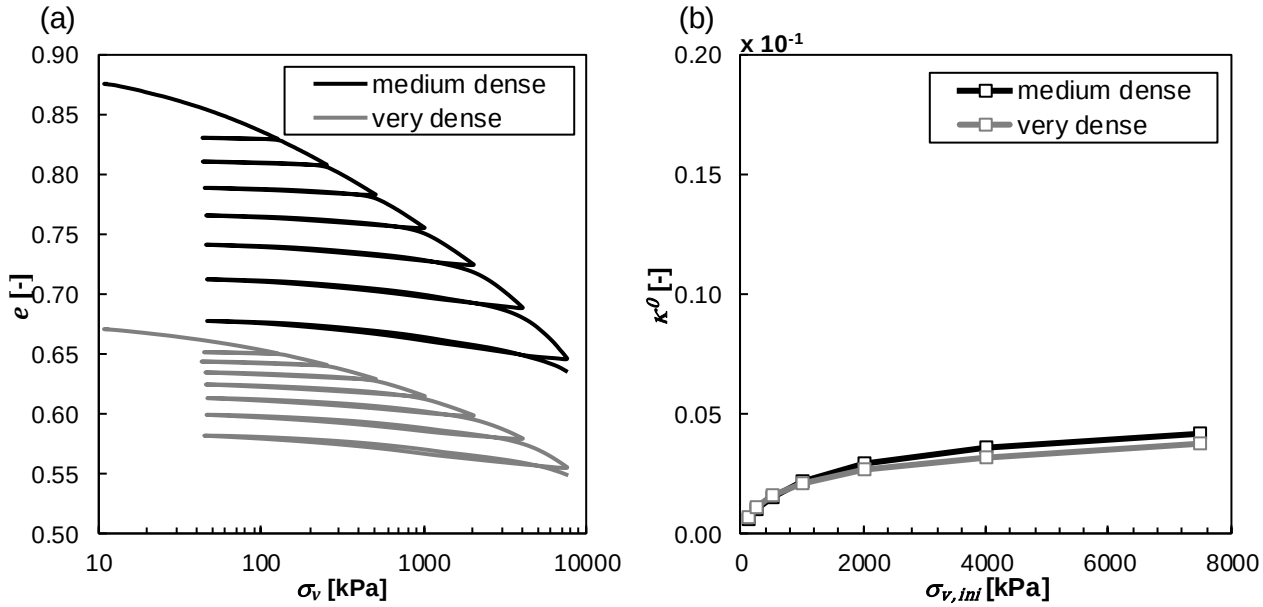

Figure 4.44: (a) Oedometer test on medium dense and very dense sand MS with unloading and reloading stages at 125, 250, 500, 1000, 2000, 4000 and 7500 kPa and (b) evaluated swelling index κ^0

For the soils SU and SU* the relaxation rate is independent of the initial stress and density, which is the behaviour expected for fine grained soils. However, the normalized stress relaxation σ/σ_0 after 24 h of SU and SU* still decreases with increasing vertical effective stress caused by an increase in the reference time t_{ref} at initiation of relaxation with rising stress. This can be seen in the later onset of the stress decrease with higher stresses (cf. Figure 4.42 (d) and (f)). The same is true for sand MS (cf. Figure 4.42 (b)). The dependency of the reference time on the stress level was also seen in the creep tests in Section 4.7.2. There, it was caused by the stress dependency of the creep-coefficient. The connection between reference time and relaxation is examined in more detail in Section 4.7.6.

4.7.6 Relaxation after different strain rates

It was shown that the initial creep strain rate of granular soils depends on the loading strain rate, the stress and the density (cf. Section 4.7.2). The behaviour can approximately be described by (4.15). It was shown by other authors that also the relaxation behaviour depends on the loading strain rate in a similar manner (LADE & KARIMPOUR, 2014) (cf. Sections 3.3.2 and 3.3.5 as well as Figure 4.45).

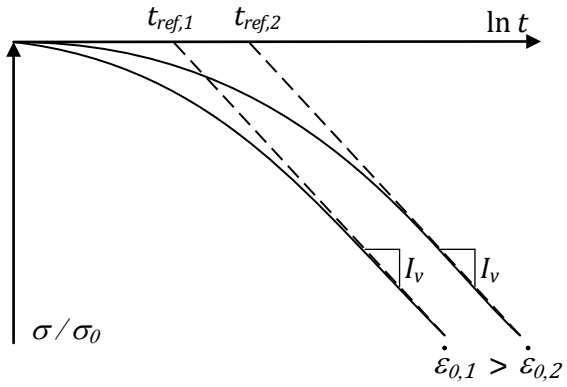

Figure 4.45: Relaxation after different loading strain rates

The assumption is that the stress rate at t = 0 (initiation of relaxation phase) can be determined via the preceding loading strain rate. To confirm this, a test series was performed, in which the samples were loaded at strain rates of 0.1%/min and 0.01%/min, similarly to the creep tests after different strain rates in Section 4.7.2. Medium dense specimen of sand MS were used and the relaxation phases lasted for 24 h at 250, 1000, 4000 and 7500 kPa. The normalized stress relaxation σ/σ_0 over the logarithm of time for the two strain rates are presented in Figure 4.46.

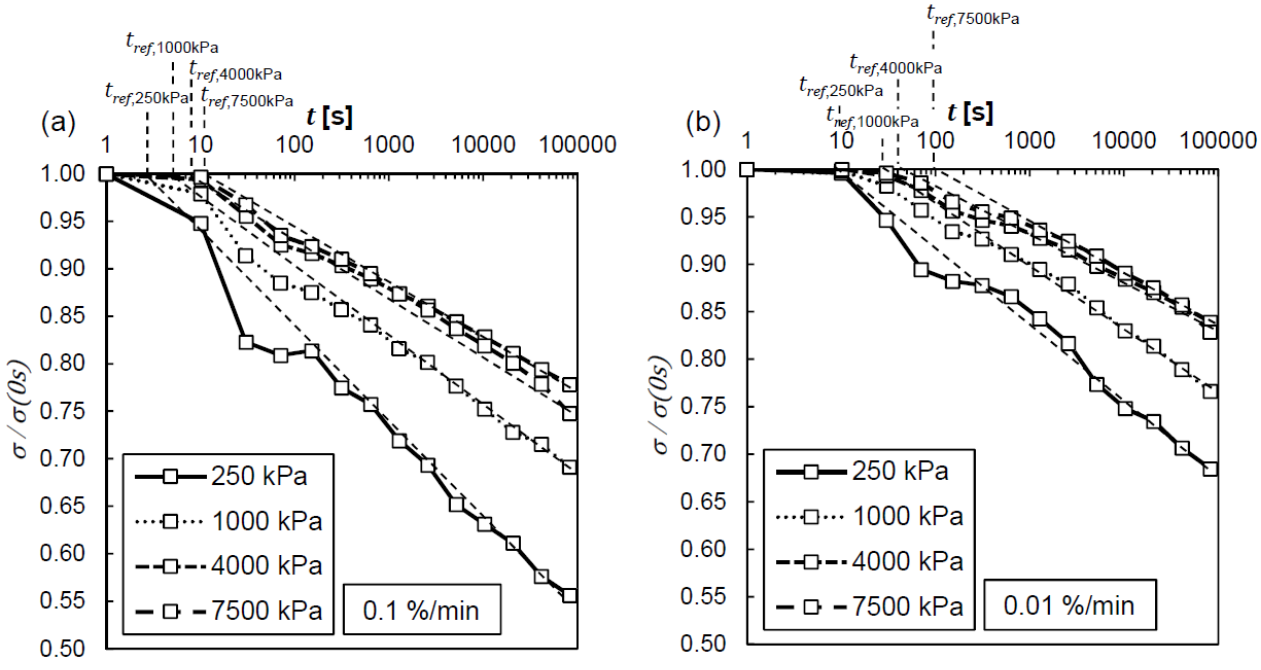

Figure 4.46: Normalized stress relaxation versus the logarithm of time for medium dense sand MS loaded at (a) 0.1%/min and (b) 0.01%/min

The test results show an influence of the loading strain rate on the relaxation behaviour. The reference time t_{ref} increases with decreasing loading strain rates. Furthermore, t_{ref} increases with the vertical effective stress, as was also observed in the relaxation tests presented in Section 4.7.5. Opposite to creep, the magnitude of the normalized stress relaxation σ/σ_0 decreases with the vertical effective stress. This is expressed by the decreasing viscosity index of sand MS and was explained in Section 4.7.5. However, at one stress level the relaxation behaviour can be described by a constant viscosity index. To verify this, the viscosity indices and reference times were determined at individual stress levels and used as input parameters for (3.47). The viscosity indices were determined from the linear sections of the test curves and the reference times were calculated according to (3.52) with

$$t_{ref} = \frac{I_v C_c}{\dot{\varepsilon}_0 (1+e) \ln(10)}. \tag{4.21}$$

The results at vertical stresses of 4000 and 7500 kPa are presented in Table 4.7. The analytical results using (3.47) with the input parameters from Table 4.7 are shown in grey colour in Figure 4.47. Only the two stress levels of 4000 and 7500 kPa are presented, because they were least influenced by the load-frame deformation compensation (cf. Section 4.7.5).

Table 4.7: Determined viscosity indices from relaxation test results and reference times according to Equation (3.47)

	I_v		t_{ref} [s]	
σ_0 [kPa]	0.1%/min	0.01%/min	0.1%/min	0.01%/min
4000	0.027	0.022	46	488
7500	0.034	0.025	93	719

The reference times show approximately a ten-fold change at a ten-fold difference in loading strain rate like in creep (cf. Section 4.7.2).

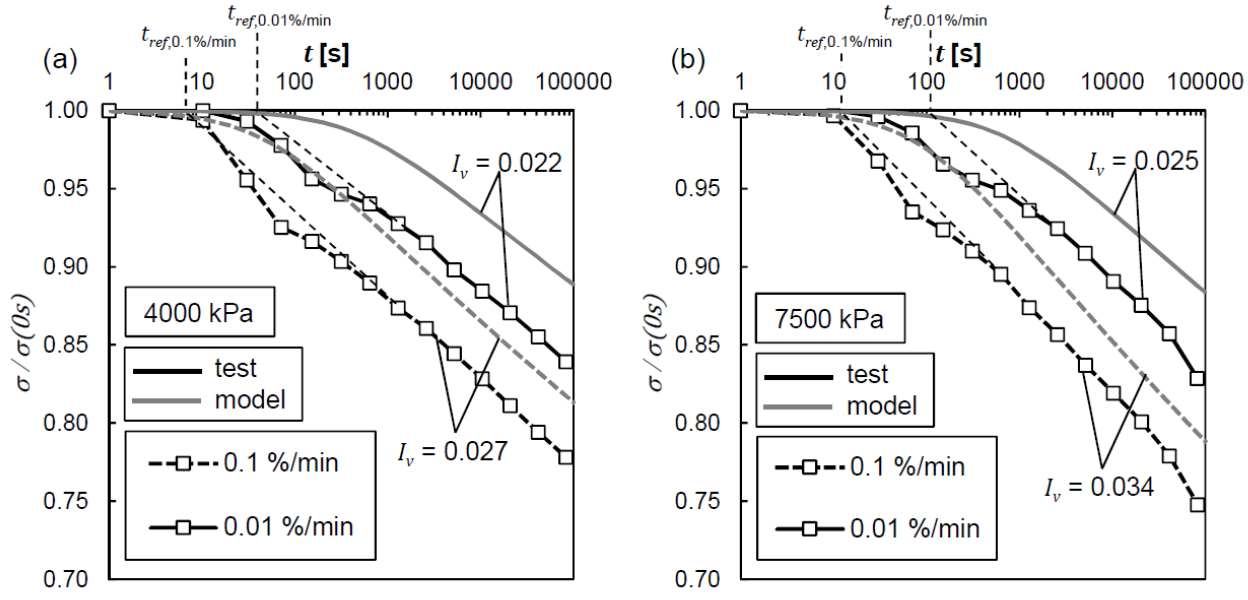

Figure 4.47: Stress relaxation over time of medium dense sand MS loaded at (a) 0.1%/min and (b) 0.01%/min

The calculated reference times are larger than the ones, which can be determined from the diagrams in Figure 4.46 or Figure 4.47. However, as for the creep strains presented in Section 4.7.2, the relative inaccuracies of the calculated stress relaxation become smaller with increasing observation time, because the relaxation curves run parallel, meaning the deviations are constant and become relatively smaller compared to the overall relaxation.
It can be concluded that the test results generally confirm the findings from literature that the relaxation stress rate depends on the previous loading strain rate. The relaxation curves converge independent from the loading strain rate to a constant viscosity index I_v. At one individual stress level and density state the relaxation can be described by (3.47) with a time-independent viscosity index and a reference time according to (3.52). A comparison between the creep and relaxation behaviour is given in Section 4.8.

4.7.7 Combined tests

It was shown in the previous sections that the time-dependent behaviour of granular soils cannot be described by the isotache-concept. Therefore, the relationship between σ', e, and $\dot{\varepsilon}$ cannot be predicted by equation (3.53). It is furthermore of interest, if the viscous response from a known state of σ', e and $\dot{\varepsilon}$, which was reached by different loading mechanisms, is the same. In other words, if the soil response is strain and strain rate history independent (cf. Section 3.1.5). Therefore, a test series on sand MS and sand SU* was conducted, in which overconsolidated states at equal OCR were reached by different loading paths including creep, relaxation and unloading. The behaviour in the subsequent creep phases was compared to evaluate the strain and strain rate history dependence. This test series was inspired by a test conducted by NIEMUNIS & KRIEG (1997) to check the validity of the isotache-concept for soft fine grained soils under monotonic deformation.

Test conditions

It was already shown that in strain rate-controlled testing the soil response of sand is strain rate independent or only temporarily dependent (cf. Sections 4.7.3 and 4.7.4). On the contrary, the creep strain and relaxation stress rate depend on the previous loading strain rate. Therefore, the loading mechanisms in the tests for the analysis of the influence of the strain history on the behaviour of sands are restricted to creep, relaxation and unloading. Unloading and relaxation can be considered as nearly identical mechanisms in this context. The target overconsolidated state was chosen to a low OCR = 1.072 to ensure that creep strains were still in a measurable range.
Sand MS and sand SU* were tested in a medium dense state to compare their behaviour. Sand SU* was chosen for comparison because it showed constant viscosity indices in the tests with sudden changes of the loading strain rate and relaxation tests. Sand MS was loaded with two different loading strain rates of 0.1%/min (test 1) and 1.0%/min (test 2). Sand SU* was loaded with a strain rate of 0.1%/min corresponding to test 1 on sand MS. The testing procedure of the combined tests is summarized in Table 4.8.
For the unloading and relaxation test phases the desired stress state at OCR = 1.072 can be determined straight forward via $OCR = \sigma'_0/\sigma'_i$. In case of the creep phase leading to OCR = 1.072, the determination of the required creep time was based on (3.37) and (3.41). The validity of (3.37) and

(3.41) is given at an individual density and stress state for which the coefficients C_α and C_c and thus C_α/C_c need to be determined (cf. Sections 4.6 and 4.7.1). The stress state can be determined via

$$\sigma'_i = 1/OCR \cdot \sigma'_0 \,. \tag{4.22}$$

The desired creep rate follows from (3.41) with

$$\dot{\varepsilon}_i = \dot{\varepsilon}_0 \left(\frac{\sigma'_0}{\sigma'_i}\right)^{C_c/C_\alpha} = \dot{\varepsilon}_0 \left(\frac{1}{OCR}\right)^{C_c/C_\alpha} , \tag{4.23}$$

where $\dot{\varepsilon}_0$ is the loading strain rate. Furthermore, the reference time t_{ref} in (3.37) needs to be determined, because creep does not instantly follow a linear trend on the logarithmic time scale. This needs to be done by fitting (3.37) to the experimental results in test phase 5. An exemplary determination of t_{ref} for sand MS in test 1 is presented in Figure 4.48. With the previously determined strain rate $\dot{\varepsilon}_i$ at the desired OCR the creep strain increment between $\dot{\varepsilon}_0$ and $\dot{\varepsilon}_i$ can be determined via

$$\Delta\varepsilon(OCR) = C \cdot \ln\left(\frac{\dot{\varepsilon}_0}{\dot{\varepsilon}_i}\right) . \tag{4.24}$$

Afterwards, the associated creep time t can be determined under consideration of t_{ref} by solving (3.37) for t

$$t\big(\Delta\varepsilon(OCR)\big) = t_{ref} \cdot \left[\exp\left(\frac{\Delta\varepsilon}{C}\right) - 1\right]. \tag{4.25}$$

And it follows

$$t_{creep}(OCR) = t_{ref} + t\big(\Delta\varepsilon(OCR)\big) \,. \tag{4.26}$$

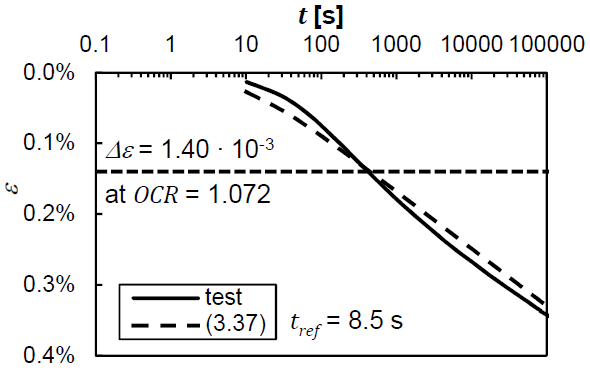

Figure 4.48: Determination of t_{ref} from (3.37) and $\Delta\varepsilon$ from (4.24) in case of sand MS test 1 phase 5

Table 4.8: Testing procedure for the oedometer tests with combined control

Phase		test 1	test 2	
1	loading with	0.1%/min	1.0%/min	to 250 kPa
2	unloading with	-0.01%/min	-0.1%/min	to 233 kPa (OCR=1.072)
3	creep for 24 h **(a)**			
4	loading with	0.1%/min	1.0%/min	to 1000 kPa
5	creep for	658 s (MS) or 3965 s (SU*)	67 s (MS)	(OCR=1.072)
6	creep 24 h **(b)**			
7	loading with	0.1%/min	1.0%/min	to 2000 kPa
8	unloading with	-0.01%/min	-0.1%/min	to 1865 kPa (OCR=1.072)
9	creep for 24 h **(c)**			
10	unloading with	-0.5%min	-0.5%min	to 50 kPa
11	loading with	0.1%/min	1.0%/min	to 4000 kPa
12	relaxation	to 3731 kPa	to 3731 kPa	(OCR = 1.072)
13	creep for 24 h **(d)**			
14	loading with	0.1%/min	1.0%/min	to 7500kPa
15	unloading with	-0.01%/min	-0.1%/min	to 6996 kPa (OCR=1.072)
16	creep for 24 h **(e)**			
17	unloading with	-0.5%min	-0.5%min	to 50 kPa
18	loading with	0.5%/min	0.5%/min	to 7500 kPa

Test results

The compression curves from the tests on sand MS and SU* are presented in Figure 4.49 (a) and (b) respectively.

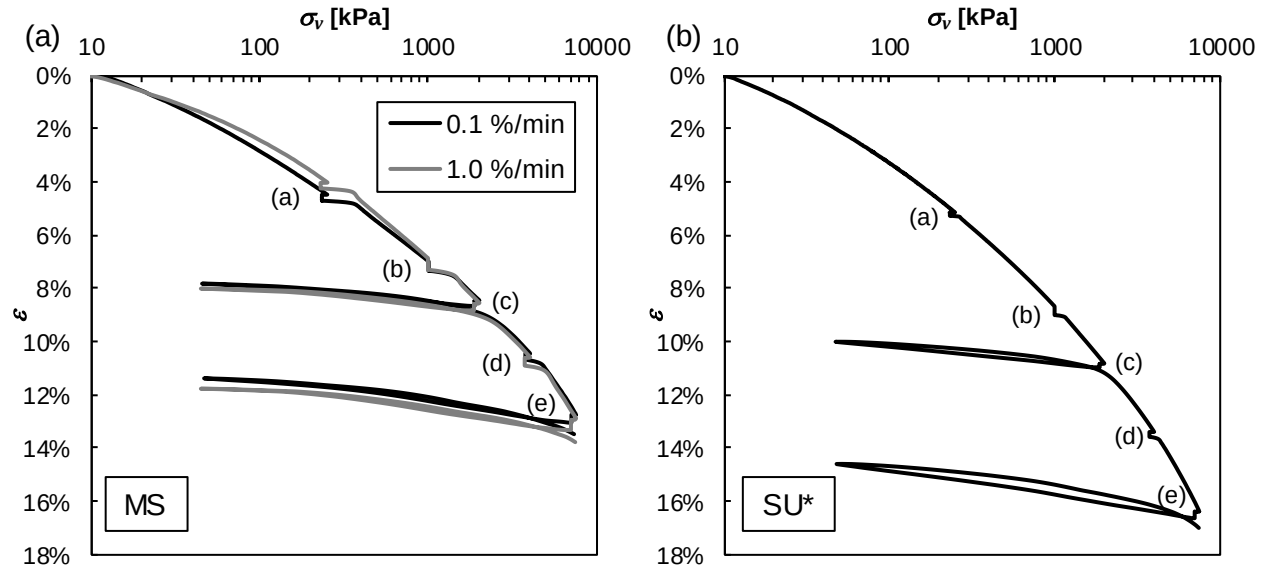

Figure 4.49: Combined tests on (a) sand MS and (b) sand SU* at medium dense relative density

For sand MS the necessary creep time to reach OCR = 1.072 was determined to be 67 s in case of 1.0%/min (test 2) and 658 s in case of 0.1%/min (test 1) loading strain rate, which is approximately a 10-fold just like between the strain rates. However, the test evaluation showed that in test 1 the

OCR = 1.072 was not accurately reached in the test phases. The following OCR-values were reached in the different test phases:

(a) OCR = 1.077
(b) OCR only indirectly determinable (see below),
(c) OCR = 1.067,
(d) OCR = 1.065 and
(e) OCR = 1.065.

The OCR in phase (a) is significantly larger than in the other phases. Therefore, phase (b) is evaluated as such that the average OCR = 1.0657 of phases (c), (d) and (e) is taken as a basis. This leads to a different time t_{creep} = 455 s. The correct determination of t_{creep} is very important for the right interpretation of test phase (b) in the context of strain and strain rate history independence of the sands, because this ensures the comparability to the other test phases where the OCR is reached by unloading.

The creep time can additionally be verified by determining it through the compression curve. The compression curve can be extrapolated beyond the creep stress level with the compression index determined at the creep stress level using (3.20). This is shown in Figure 4.50. The total strain reached at 1065.7 kPa (OCR = 1.0657) is 7.147%. Comparing this to the actual test data from the creep phase reveals a necessary creep time of 464 s to reach this strain, which is very close to the previously determined 455 s.

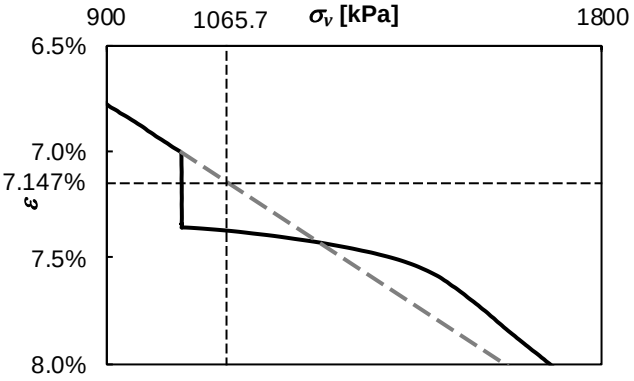

Figure 4.50: Determination of the necessary creep strain at 1000 kPa vertical effective stress to reach OCR = 1.0657

In case of the test on sand SU* the OCR-values reached were

(a) OCR = 1.078,
(b) OCR only indirectly determinable,
(c) OCR = 1.067,
(d) OCR = 1.066 and
(e) OCR = 1.065.

Just like for sand MS, phase (b) is evaluated as such that the average OCR = 1.066 of phases (c), (d) and (e) is taken as a basis. This leads to a time t_{creep} = 2513 s to reach OCR = 1.066 in phase (b).

Figure 4.51, Figure 4.52 and Figure 4.53 show the evaluated creep strains over time after the different loading mechanisms. As mentioned, the target OCR was not always precisely reached. The actual

values are presented in the legends of the diagrams. In phase (a) in all tests a significantly larger OCR was reached than in the other phases. This is caused by the sensitivity of controlling the stress condition at this comparably low stress level. If the desired stress state is only slightly missed, the change in the OCR is relatively large. Especially in phase (a) in test 1 the creep strains are considerably different from the beginning. Why they are larger than in the other phases despite the larger OCR and the lower stress level could not be clarified. Therefore, the evaluation is limited in all tests to the phases (b) to (e).

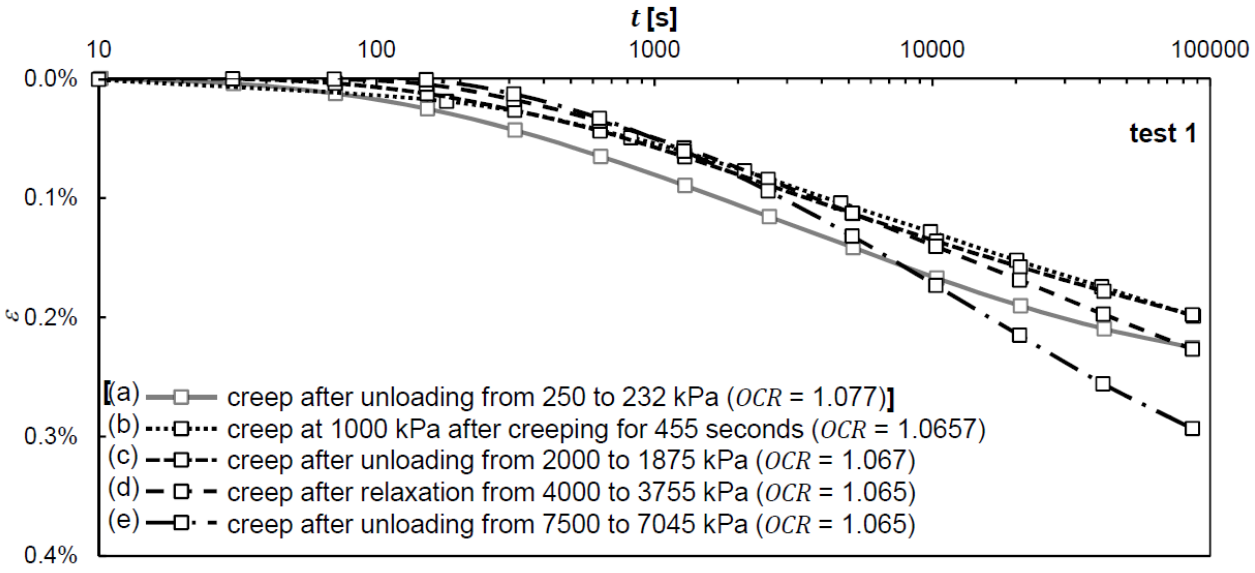

Figure 4.51: Creep after different stress and strain paths leading to an overconsolidated state of sand MS; test 1 (cf. Table 4.8)

The test results from test 1 and test 2 on sand MS (cf. Figure 4.51 and Figure 4.52) show an increase in the total creep strain occurring in 24 h with the stress level. The results show the already known pattern. Phase (b) and (c) in test 1 show almost identical creep strains. This is most likely caused by the slightly larger OCR of phase (c). The test results indicate that it makes no difference for the subsequent creep behaviour whether the initial overconsolidated state of the soil was reached by unloading, relaxation or creep. This conclusion is drawn because the strain rate in all tests on initiation of the creep phases is very similar and deviations between the creep strains only start to be observable from 600 s (test 2) and 2500 s (test 1) into the creep phase. It shows that the stress-dependent mechanism of static fatigue causing creep needs time to exert an influence on the particle strength, which varies in size depending on how high the stresses are. But it makes no difference if the initial state in the creep phase was reached by unloading, relaxation or creep. It is furthermore visible from test 2 that the loading strain rate has an influence on the subsequent creep rate even if an unloading or relaxation phase preceded the evaluated creep phase. Higher loading strain rate results in a larger creep strain rate in test 2 (cf. Figure 4.52).

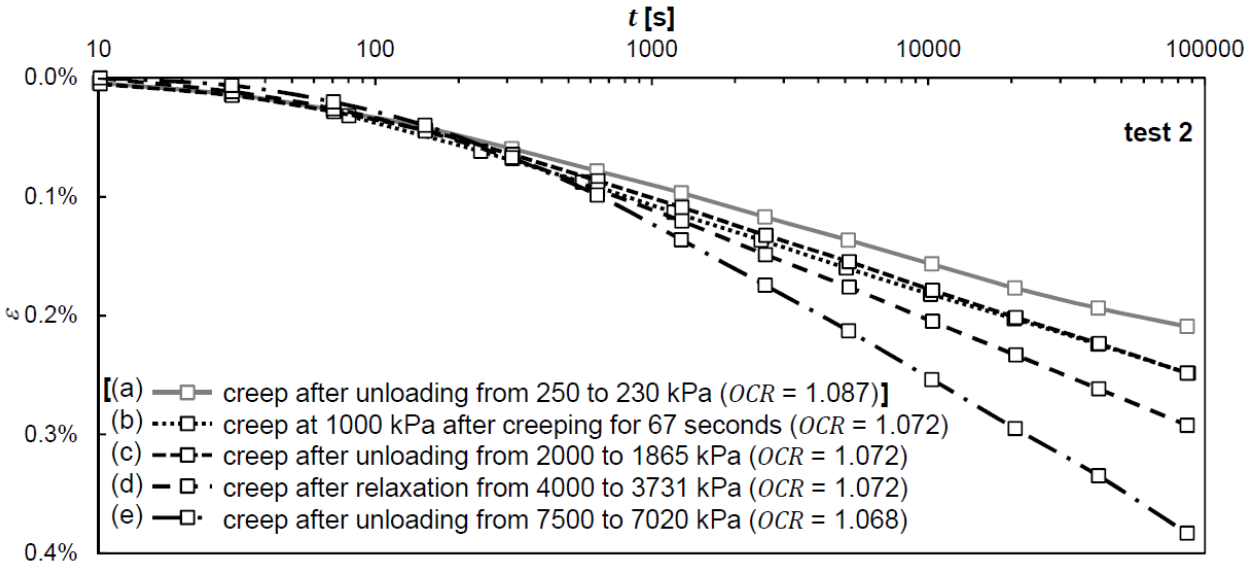

Figure 4.52: Creep after different stress and strain paths leading to an overconsolidated state of sand MS; test 2 (cf. Table 4.8)

The comparative test on sand SU* with 25wt-% fine content shows very similar results. The creep curves after unloading or relaxation show again initially very similar creep strain rates, which start to deviate depending on the stress level. An influence of the stress or strain history on the creep behaviour, other than the stress level, cannot be observed in a laboratory time scale.

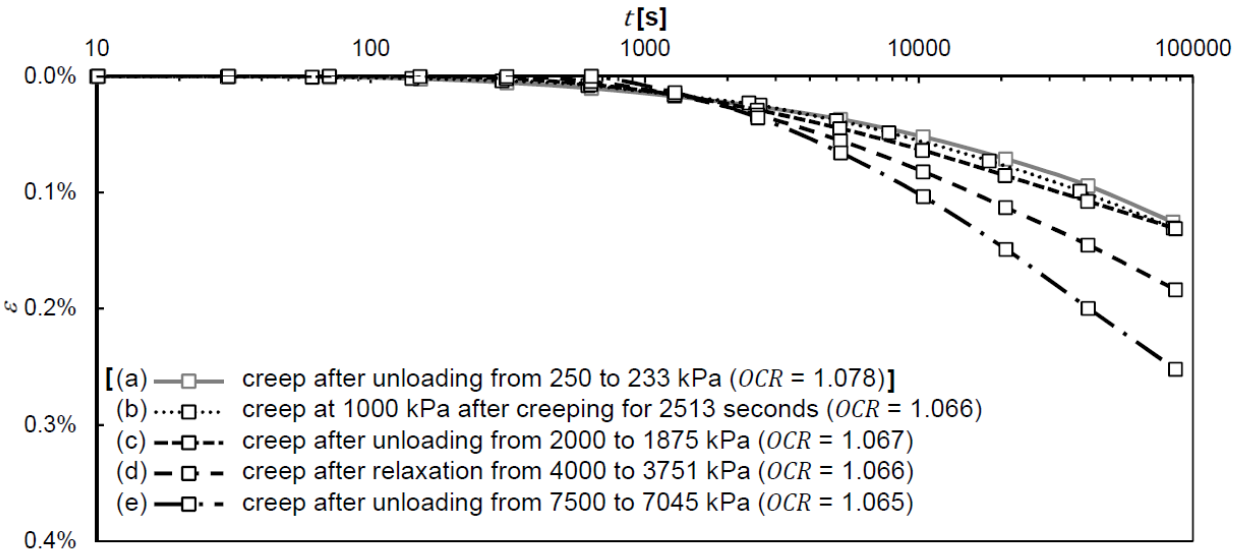

Figure 4.53: Creep after different stress and strain paths leading to an overconsolidated state of sand SU*; test 1 (cf. Table 4.8)

Evaluation of the test results after 5000 s of creep presented in Figure 4.54 show that the long-term creep behaviour is not influenced by the strain or strain rate history. Sand MS was compressed in test 1 with a strain rate of 0.1 %/min and in test 2 with 1 %/min. Nevertheless, the creep strains that developed between 5000 s and 24 h are nearly identical (cf. Figure 4.54 (a) and also Section 4.7.2). The influence of the different strain rates is only relevant shortly after the start of the creep phase

and in states with low overconsolidation ratio. At higher OCR the compression rate does not influence the creep rate anymore.

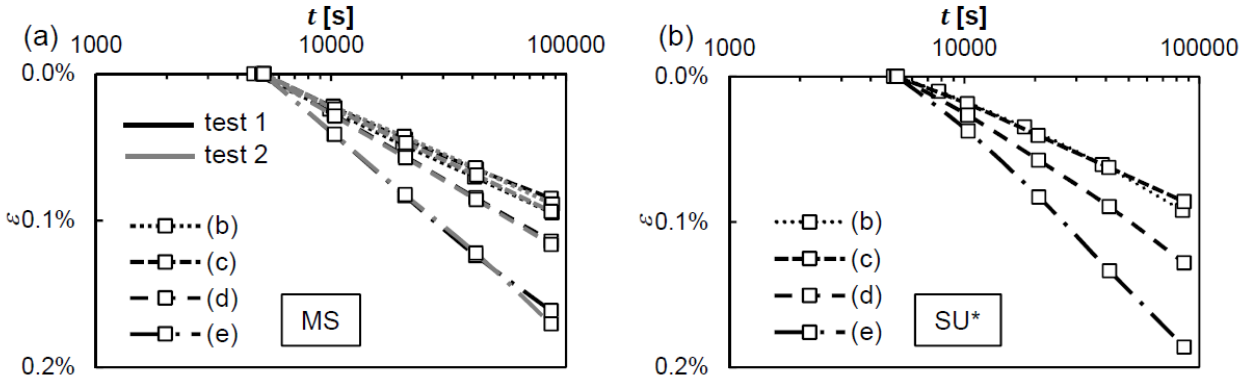

Figure 4.54: Creep after different stress and strain paths leading to an overconsolidated state of (a) sand MS and (b) sand SU* evaluated after 5000 s creep after reaching the overconsolidated state

The test results show that the creep behaviour of the sands does not depend on the previous strain or strain rate history in the investigated time scales. Only the stress level influences the long-term creep rate. The stress dependency leads to an inequality of isotaches and isochrones as was explained in Section 4.7.2. Due to the stress dependency of the viscous response and the not unique reference state in granular soils, all three state parameters σ', e and $\dot{\varepsilon}$ have to be known to fully describe the state of the soil.

4.8 Conclusions from incremental loading and strain rate-controlled tests

The conclusions from the previously presented test results in Sections 4.6 and 4.7 are summarized here. They are ordered in the same way as the sections:

Creep

– Creep of granular soils depends on the vertical effective stress and the density. With higher stress level creep increases. The same is true for decreasing density. This was to be expected, since the creep mechanism is based on static fatigue of the grains, which is directly correlated to the contact stress between the grains. The average contact stress increases with rising mean effective stress and decreasing density.

– Also sands with high fine content (14 to 46wt-%) show a pronounced stress and density dependency in the creep-coefficient. In this case the fine-particles were non plastic silts, in which the creep mechanism is also based on static fatigue and the dependencies on stress and density are therefore qualitatively the same as in the clean sand MS.

– The influence of the GSD and non-plastic silt content on the occurring creep strains is small in lower stresses up to 2000 kPa and becomes larger at higher stresses.

– The stress-dependent compressive behaviour is significantly softer with rising fine content.

– Creep at one stress level and one initial density can be described by a constant creep-coefficient in the original definition by BUISMAN (1936) and equivalent approaches presented.

– The C_α/C_c -ratio of sand MS and FS vary with density and stress. Test results from incremental loading tests and strain rate-controlled tests both show rising C_α/C_c -ratios with rising density and decreasing C_α/C_c -ratios with rising stress. The creep-coefficient and the compression index are influenced to different extent by stress and density changes. This leads to changes of the C_α/C_c –ratio. The description of the viscous behaviour of sand MS and FS with a constant C_α/C_c -ratio alone is therefore not valid.

– The variation of the C_α/C_c -ratios with stress and density significantly reduces with rising fine content of the sand (cf. Figure 4.55). Soils with a fine content larger than approximately 14wt-% show a sufficiently constant C_α/C_c -ratio over a wide range of stresses (up to 7500 kPa) and densities (medium dense to very dense).

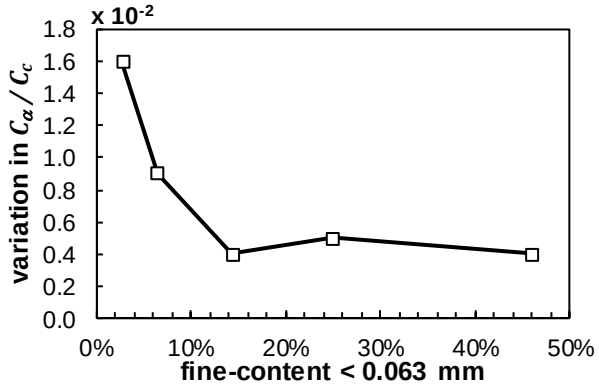

Figure 4.55: Variation in the C_α/C_c -ratio with changing fine content

– The influence of mean effective stress and density on creep of the tested sands can be taken into account by an empirical approach developed on the basis of a large number of oedometer tests. It describes the development of the creep-coefficient with varying mean effective stress and density in the C_α - p' - r_e - space. It is calibrated using two oedometer tests at high and low density including creep phases in the relevant stress range (cf. Section 4.6.3).

– Under consideration of the test results from Sections 4.6, 4.7.1 and 4.7.2, isotache and isochronic lines are not identical in granular soils. Due to the changing creep-coefficients at different stress levels, the equivalency of the lines in the sense of (3.53) or (4.16) is not given. This means, at one stress level a certain strain rate is matched to a different isochronic line than at another stress level. The equivalency can only be assumed at one stress level (cf. Figure 4.33).

Rate dependency

– The loading strain rate influences the subsequent creep strain rate according to the approach formulated in (4.15). Just after the creep phase starts, the creep strain rate is equal to the loading strain rate and tends to a stress-dependent creep rate with time.

– In CRS tests sands do not show a rate dependency in oedometric testing, i.e. a unique rate-independent compression line is followed. Therefore, isotache and isochronic lines are apparently not identical in granular soils. The relationship between σ', e, and $\dot{\varepsilon}$ cannot be described by the classical isotache-concept. This indicates that this relationship is more complex for sands than for fine-grained soils.

– Tests with sudden changes of strain rate on sand MS show a temporary rate effect, which disappears with increasing deformation after the strain rate jump. The compression curves approach the strain-rate independent compression curve obtained in the CRS tests. The behaviour of sand MS can be considered as TESRA.

– Sands SU, SU* and SU2 with 14.3, 25 and 46wt-% fine content respectively show a permanent stress change upon sudden strain rate change.

Relaxation

– Relaxation tests on sand MS showed an influence of the stress level on the normalized stress relaxation. With increasing vertical effective stress the normalized relaxation σ/σ_0 in 24 h was smaller. The viscosity index decreased and the reference time increased with the vertical effective stress.

– It can be assumed that the creep-coefficient and thus the viscous strain rate at highly overconsolidated states (OCR > 1.2) are very small and independent of the stress. Under this assumption, the relaxation behaviour is controlled by the elastic soil response.

– Assuming that the relaxation behaviour can be described by the swelling index κ^0, the smaller normalized relaxation at higher stresses can be explained by increasing swelling indices at higher preconsolidation stresses.

– At a given initial stress and density the relaxation of sand MS can be described by a constant viscosity index I_v.

– Tests on sands with more than 14wt-% fine content showed almost no stress dependency in relaxation. Only the reference time increases slightly with higher vertical effective stresses. The relaxation can be described by a stress and density independent viscosity index I_v.

– The influence of the initial density on the stress relaxation behaviour was negligible for all investigated sands

– The initial relaxation rate of the tested sands was influenced by the previous loading strain rate. With decreasing loading strain rate the reference time increases and the initial relaxation rate decreases. The interrelation follows (3.52) satisfyingly.

Combined behaviour

– Tests with combined control showed that the creep behaviour of sand MS and sand SU* after unloading, creep or relaxation does not depend on the previous stress or strain history in the investigated time scales. The creep behaviour was only influenced by the previous compression

rate and the stress level, but not by whether the starting point of creep was reached by unloading, relaxation or creep.

Comparison of the different viscous mechanisms

– When comparing the different viscous mechanisms in sand MS, it is obvious that the behaviour cannot be described by the interrelation of (3.53). This is caused by various reasons. Most important is the different prominence of the viscous behaviours. This can be seen in Figure 4.56 (a), where the viscosity indices from relaxation tests and the C_α/C_c -ratios from creep tests on sand MS are plotted. It is obvious that relaxation is much more pronounced and the variation in stress is large. I_v from tests with sudden changes in the strain rate cannot be determined, because the effect is only temporary.

– Contrary, sands SU and SU* with 14.3 and 25wt-% silt content show a constant $I_v = C_\alpha/C_c$. This is demonstrated by the comparison in Figure 4.56 (b), showing the viscosity indices and the C_α/C_c -ratios from creep, relaxation and jump-tests of sand SU. The values are constant under consideration of the wide range of stresses and densities. The same is true for sand SU*.

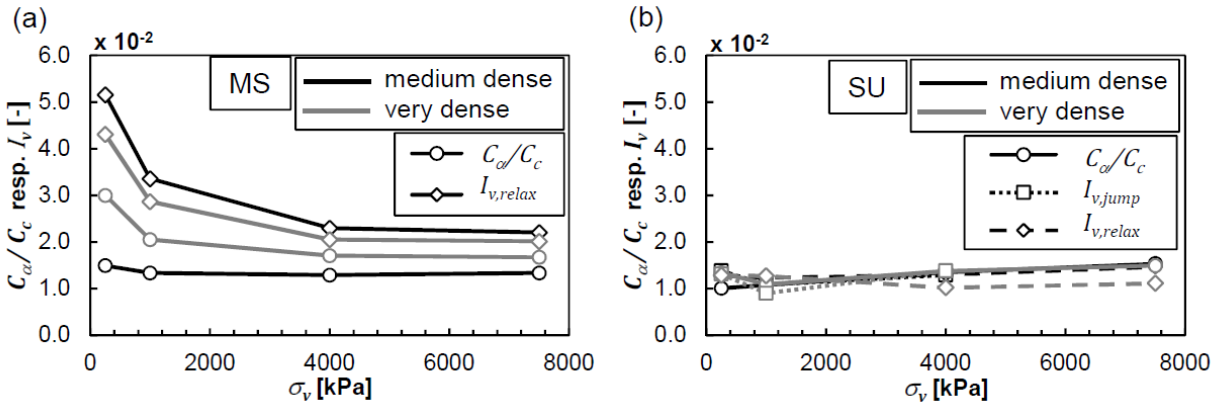

Figure 4.56: Comparison of I_v and C_α/C_c from evaluation of different viscous mechanisms of (a) sand MS and (b) sand SU

4.9 Additional features of viscous behaviour

In this section different factors influencing the viscous behaviour of sand besides the vertical effective stress, the density and the loading strain rate are analyzed experimentally. The investigation focusses on the following aspects:

– long-term creep and relaxation,
– influence of very high pressures on compression and creep,
– influence of mean grain size and
– influence of the water content on creep.

The following results give indications of the soil response with varying properties and testing conditions.

4.9.1 Long-term creep and relaxation test

Introduction

Experiments show that for fine grained soils, especially in highly plastic and organic clays, the change of the void ratio / volumetric deformation with time follows a semi-logarithmic relationship with a constant slope for periods of months and years. For a period of one month KRIEG (2000) confirms the constant slope of the creep curve over the logarithm of time with oedometer tests on organic silt. A unique oedometer test by BRANDL (2015) performed on organic silt with a creep phase of 42 a at 681 kPa shows a continuous increase in deformations (cf. Figure 4.57). Although the creep-coefficient, i.e. the slope of the curve in the semi-logarithmic diagram, decreases with time, a stagnation of the deformation did not occur so far. Despite external influences making the measurements of deformations of approximately 1.0 mm over more than 40 a questionable, the test shows that creep in fine grained organic soils does not stagnate over very long time periods.

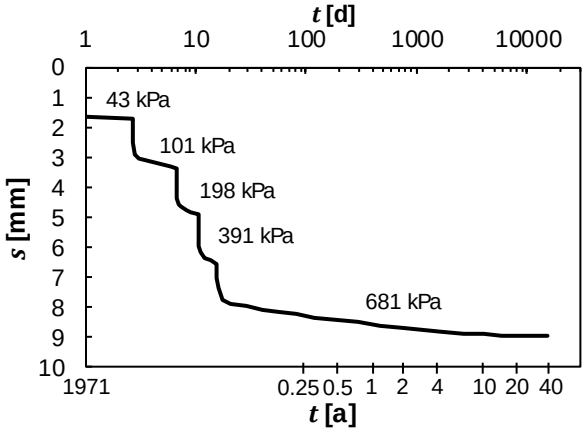

Figure 4.57: Long-term oedometer test with a duration of the last creep phase of 42 a on organic clayey silt (data from BRANDL, 2015)

As mentioned in Section 3.3.4, ageing effects cause an increase of stiffness and a more stable granular skeleton with external loading being transferred predominantely by normal forces at the grain contacts. Therefore, ageing is expected to counteract creep and to lead to stagnation of deformations in both fine-grained and coarse-grained materials. Due to the singnificantly smaller creep of granular soils, stagnation is expected to be reached much sooner than in fine-grained soils.

Test results

The stagnation effect can already be seen during the 24 h creep phases in the tests in Section 4.7.1. The tests on soils MS and SU* were evaluated to compare a clean sand to a sand with high fine content. Figure 4.58 shows the development of the creep-coefficient C during one day of creep at different stress levels of both sands. While SU* shows more or less constant creep-coefficients at the different stress levels over time, soil MS shows a decreasing trend with time in all stress levels with an increasing gradient towards higher stresses.

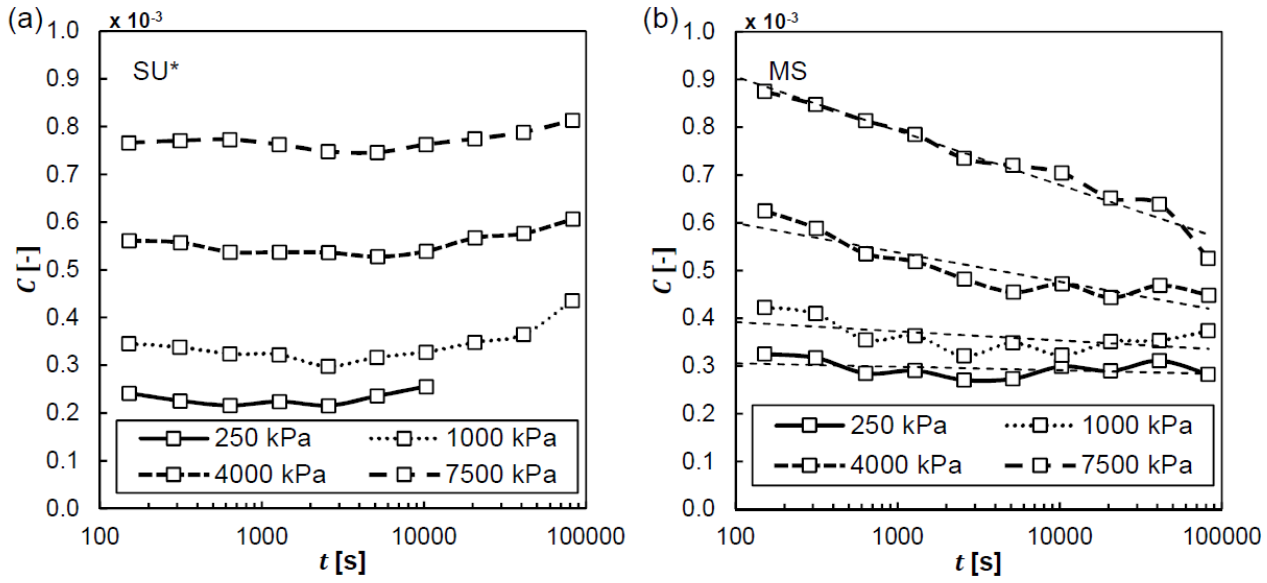

Figure 4.58: Development of the creep-coefficient during creep phases of one day of (a) medium dense soil SU* and (b) medium dense soil MS

For further analysis, a long-term test was performed on medium dense sand MS. The sample was loaded by CRS with a strain rate of 1.0%/min until 4000 kPa and left to relax for one week and afterwards loaded again by CRS with a strain rate of 1.0%/min until 7500 kPa and left to creep for one week. The test results are presented in Figure 4.59. The relaxation behaviour converges towards a linear trend with the logarithm of time, which remains constant over the period of one week and can be well described by a constant viscosity index of I_v = 0.03 at σ_v = 4000 kPa. The creep strains at 7500 kPa also follow initially a rather constant linear trend (C = 0.00076) with the logarithm of time until about half a day after load application. After that, the gradient, i.e. the creep-coefficient, strongly decreases and reaches a value of C = 0.0002 after one week (cf. Figure 4.59 (b) and (d)). The test results show a significant reduction in the creep-coefficient indicating that the creep strains of sand in the laboratory will stagnate ultimately. This results from a change of the structure of the grain skeleton, which is charaterized by an increase of the number of grain contacts and the contact area and consequently, a reduction of the normal and shear stresses at the contacts during creep. The time interval in which a stagnation happens is strongly dependent on the soil properties.

On the contrary, measurements on the surface of an open cast mine consisting of sands, which are presented in Section 5, show constant creep-coefficients and therefore no tendency to stagnation during a period of 8.4 a. So far, this discrepancy cannot be explained. However, these deformations might not only be caused by creep, but also by additional effects like temporary changes in the water content or the atmospheric pressure due to changing weather conditions. Such slight changes in the stress state and density of the dump seem to be sufficient to slow the reduction of the creep-coefficient down significantly.

In relaxation a decrease in the viscosity index could not be observed. The stress decrease does not show signs of stagnation in the period of seven days of relaxation. Despite of the stress decrease and resulting restructuration of the force chains, under the macroscopic zero strain criterion, which is met during relaxation, no incipient stagnation is discernible in the time period investigated.

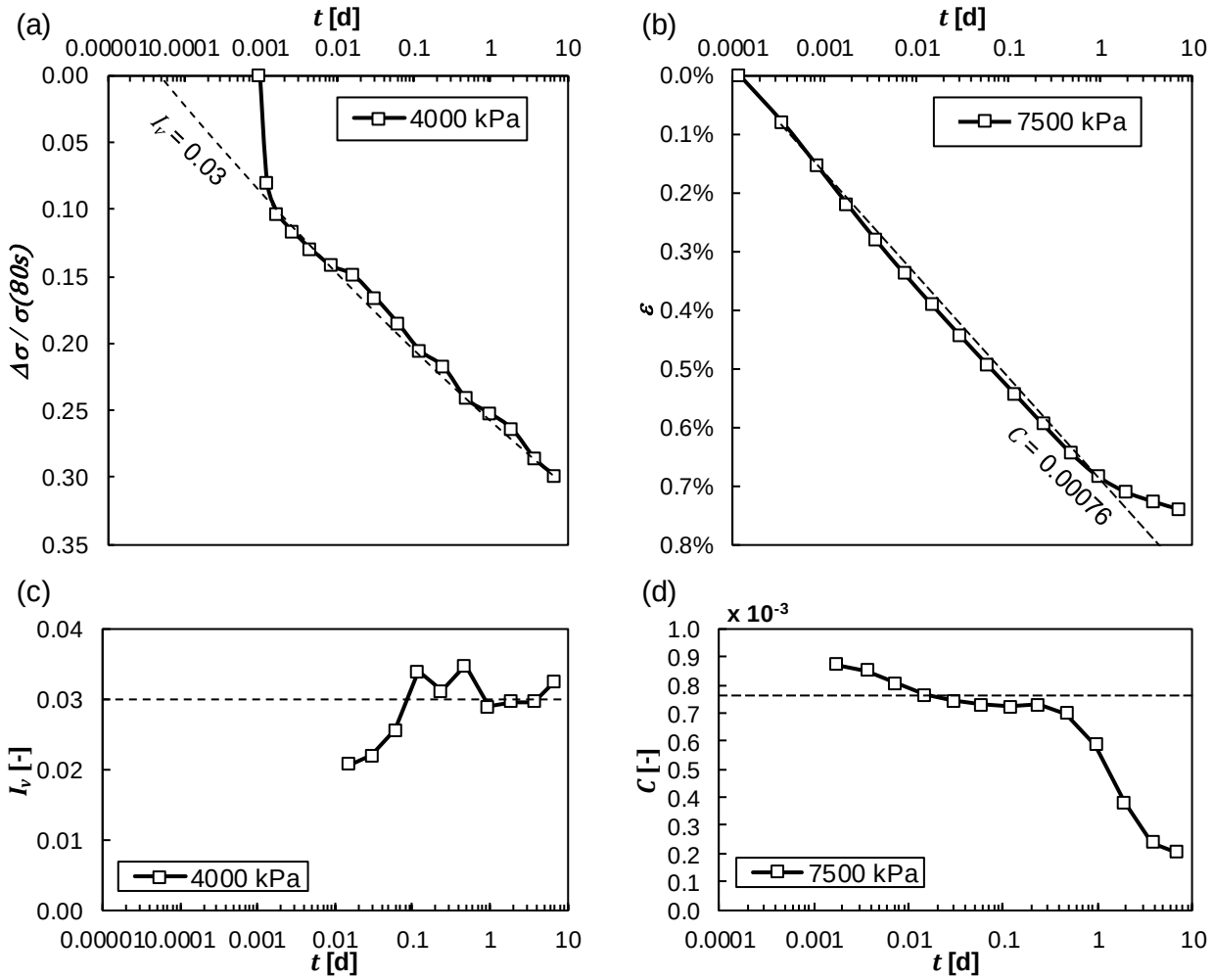

Figure 4.59: Oedometer test results on medium dense sand MS: (a) Development of the normalized stress change during one week of relaxation, (b) development of creep strains during one week of creep and (c) as well as (d) evaluation of the viscosity index and creep-coefficient over time respectively

4.9.2 High pressure tests

Introduction and test conditions

The mechanism of creep in granular material is based on static fatigue at the grain contacts triggering a rearrangement of the force chains and the grains without changing the macroscopic effective stress state in the soil (cf Section 3.3.3). At low stresses, these effects are difficult to observe, because changes in the GSD of hard materials like quartz sands are so small that they are not detectable by sieving analysis. The findings of MICHALOWSKI & NADUKURU (2012), WANG & MICHALOWSKI (2015) and MICHALOWSKI *et al.* (2018) demonstrated the microscopic degradations at a single grain contact at low stresses (cf. Section 3.3.3). At large stresses, static fatigue leads to breakage of entire grains (level III damage), visible in a change of the GSD. The underlying effect of breakage of entire grains and degradation of the grain contact is the same and is controlled by the time-dependent particle strength. To demonstrate the static fatigue effect for the Garzweiler sands during creep, the soils

were subjected to high vertical effective stresses of up to 340 MPa in a especially designed oedometer cell, followed by creep phases at different stress levels. Besides creep and static fatigue, the stress-dependent compressive behaviour and the development of the compression index C_c were analyzed.
The oedometer cell was produced from steel with a wall thickness of 50 mm. The steel surface was hardened to prevent quartz grains as good as possible from penetrating into the walls. The sample size was 100 mm in diameter and 30 mm in height. A finite element simulation of the oedometer cell for estimation of the lateral deformations while applying 340 MPa vertical effective stress yielded 0.07 mm or 0.07% maximum lateral deformation. The specimen were prepared air-dry. For performing the tests, a 300-ton hydraulic load frame was used. The used load cell only delivered precise measurements at stresses above 1.0 MPa, which is why the evaluation starts at this stress.

4.9.2.1 Stress-dependent compression

In a first test series, samples of MS, FS and SU were loaded by CRS at 0.5 mm/min up to 340 MPa. The compression curves and evaluated C_c -indices are presented in Figure 4.60. The compression curves in the $e - \log \sigma_v$ - plane converge towards a unique linear line with a nearly constant slope, i.e. compression index. The compression index increases from about 0.10 at 1.0 MPa to approximately 0.4 at 340 MPa. This increase is not caused by reloading, because samples are in a virgin loading state, but by intensified damage to the grains. The point of maximum curvature of the compression curves – indicated with a black dot in the diagrams – marks the point beyond which entire grains increasingly start to break (level III damage) (NAKATA *et al.*, 2001, CHUHAN *et al.*, 2003). At lower stresses the compressive behaviour of the soil is predominantly influenced by its structure, which in this case differs between the samples due to their different initial densities. At stresses beyond the point of maximum curvature, the influence of the soil structure diminishes and the particle strength, which is a material- and not a state-parameter, becomes increasingly important. It is influenced by the grain shape, the mineralogy and preexisting flaws of the grains. The compression curves converge and the influence of the initial state on the compressive behaviour of the sample gradually disappears. The points of maximum curvature of the looser samples lie between 10 and 15 MPa and of the denser samples between 15 and 20 MPa, which corresponds well to the transition between the intermediate and high stress range defined by CHUHAN *et al.* (2003) and LAMBE & WHITMAN (2012) (cf. Section 3.2). The increase in the stress level at the point of maximum curvature caused by increased specimen relative density was also reported by HAGERTY *et al.* (1993), whom explain this behaviour on the basis of more interparticle contacts, lower average interparticle forces, and, consequently, less extensive crushing. PESTANA & WHITTLE (1995) and (1998) called the converged compression curves the Limiting Compression Curve (LCC), which they assume as a reference state for their compression law (cf. Section 3.2).
The detailed analysis of the stress-dependent change of the GSD at different stress levels was performed with the sand MS. Different specimen were prepared at the same medium dense relative density loaded with the same deformation rate of 0.5 mm/min to vertical stresses of 10, 50, 100, 200 and 300 MPa. The tests were terminated after reaching each vertical stress and the soil sample was sieved. The GSDs along with an evaluation of the relative breakage B_r according to HARDIN (1985) (cf. Section 3.1.1) and the results of the analysis on the grain shape are presented in Figure 4.61. At

10 MPa the crushing of grains is not very pronounced and only detectable for grains larger than 0.15 mm in diameter. The deformation behaviour is governed by level I and level II grain damage. At 50 MPa and beyond, crushing (level III damage) starts to increase strongly. This correlates well with the position of points of maximum curvature between 10 and 20 MPa. The relative breakage shows a hyperbolic trend with the vertical stress, which means that the susceptibility to grain degradation decreases with the grain size: The larger the number of grains and the interparticle contacts per volume unit, the lower the interparticle forces.

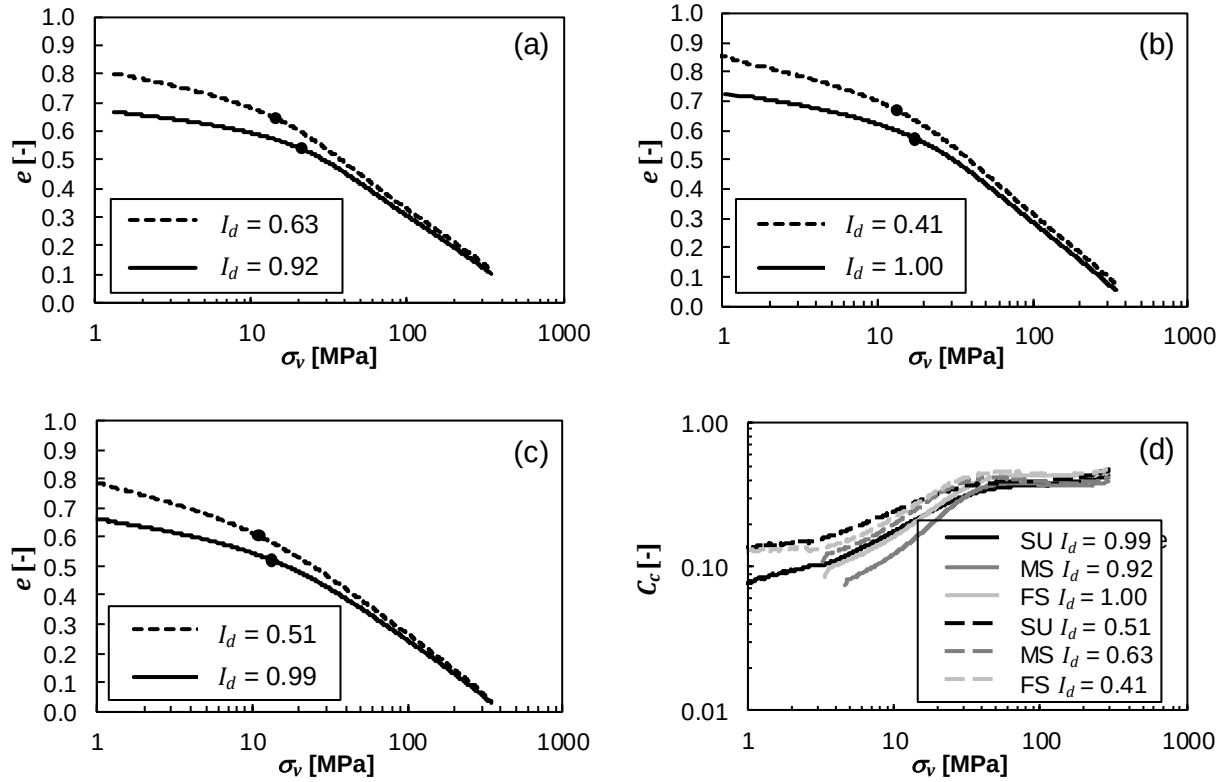

Figure 4.60: Compression curves of (a) MS, (b) FS and (c) SU from two different initial densities up to 340 MPa with indicated points of maximum curvature and (d) the development of the compression index C_c with the pressure

Micrographs with 200-fold magnification presented in Figure 4.62 show the increasing degradation of the grains at the different stress levels and confirm the sieving analysis. At 10 MPa no degradation is visible in the micrograph. From 50 MPa the breakage is plainly visible and the broken particles appear in white color and more angular than the intact grains. At 100 and 200 MPa more and more fine particles are visible and at 300 MPa the coarser particles left, swim in a matrix of fine particles. An investigation of a change in the grain shape was performed with an optical method by means of a Camsizer (cf. Section 3.1.2), but only for the fraction of grains larger than 0.125 mm. Particles smaller than 0.125 mm tend to form aggregates, which falsifies the Camsizer results. The results show that the sphericity stays more or less constant while the roundness is reduced.

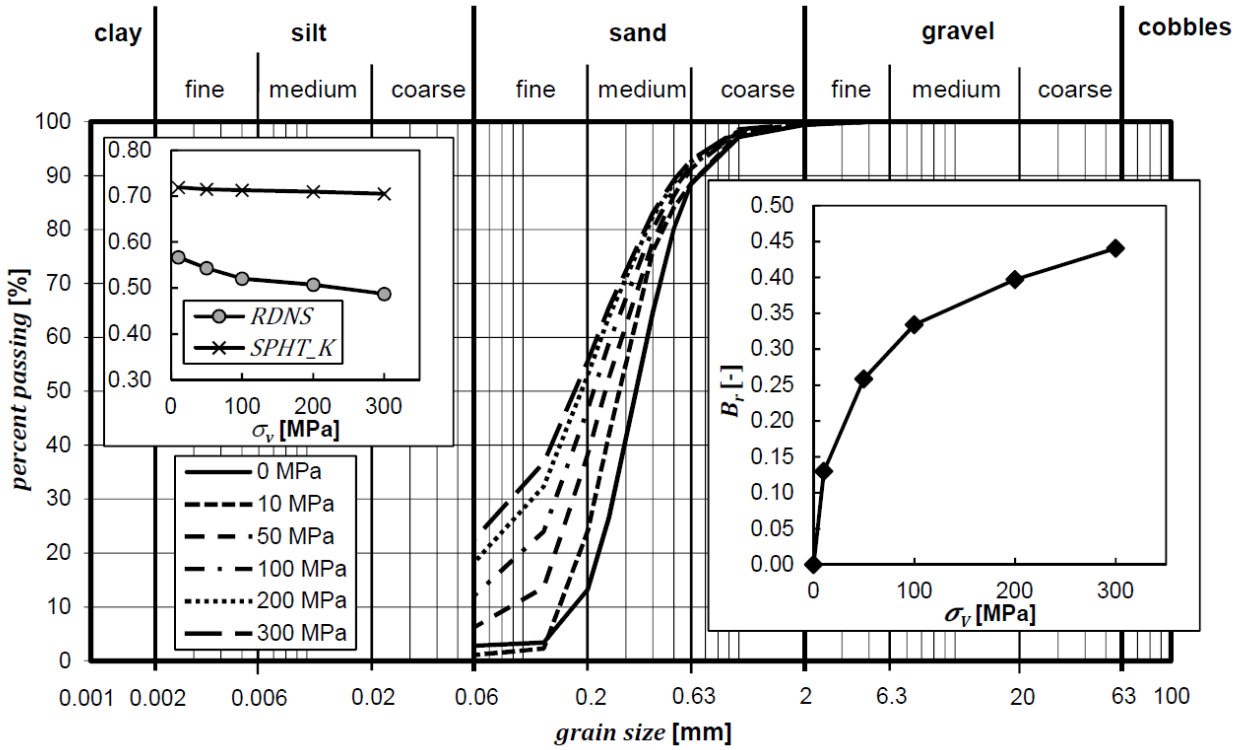

Figure 4.61: GSDs of initially medium dense samples of MS loaded to stress levels of 10, 50, 100, 200 and 300 MPa, development of the relative breakage B_r and development of the roundness *RDNS* and sphericity *SPHT_K* with the vertical stress

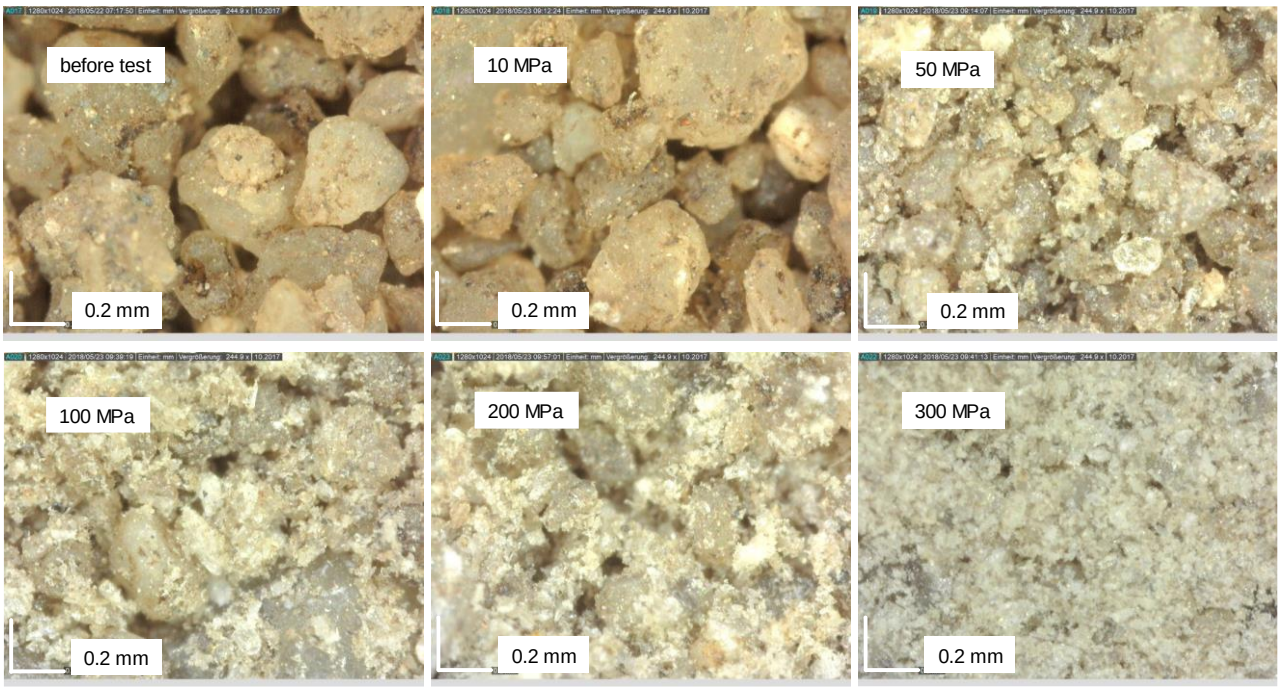

Figure 4.62: Micrographs with 200-fold magnification of MS after oedometric loading to vertical pressures of 10, 50, 100, 200 and 300 MPa

To compare the influence of the relative density on the grain degradation during compression, a series of tests on medium dense and very dense samples of the sand MS were performed. The GSDs were again determined after loading to 10, 50, 100, 200 and 300 MPa. The respective GSDs along

with the evaluated relative breakage are presented in Figure 4.63. In all tests, except the one with 300 MPa vertical effective stress, the medium dense samples show more breakage than the very dense samples. This can again be explained by the reduced number of contacts and therefore larger contact forces in the medium dense sample and corresponds well to the position of the points of maximum curvature. This influence seems to remain until 200 MPa, but vanishes at 300 MPa. When looking at the compression curves in Figure 4.60 it is also obvious that the medium dense samples need to go through a larger change in void ratio to reach the LCC, which is accompanied by more grain degradation.

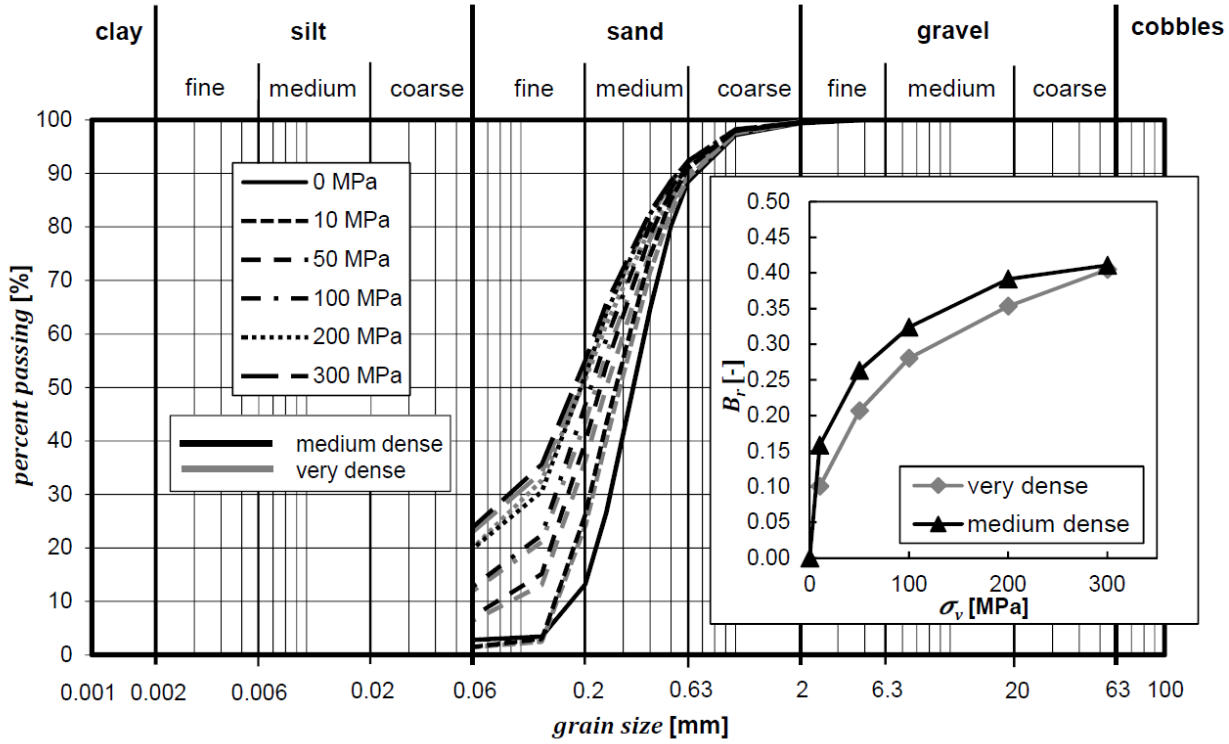

Figure 4.63: GSDs of initially medium dense and very dense samples of MS loaded to stress levels of 10, 50, 100, 200 and 300 MPa and development of the relative breakage B_r with the vertical stress

4.9.2.2 Time-dependent compression

The previously presented results on the stress-dependent compressive behaviour serve as a basis for comparison to samples, who were left to creep for 1.0 h at vertical effective stresses of 10, 50, 100, 200 and 300 MPa. The creep time was limited to one hour to avoid damaging the hydraulic load frame maintaining the very high stresses. Soil MS was prepared at the same medium dense relative density as before and the samples were left to creep at different stress levels. Afterwards, the GSDs were evaluated and compared to the ones without a creep phase. The different GSDs along with a comparison of the relative breakage are presented in Figure 4.64. At 10 and 50 MPa the difference in the GSDs is detectable by the larger fine content < 0.063 mm of the samples with a creep phase. In the tests with higher vertical effective stresses the difference between the GSD lies within the accuracy of a sieving analysis. The evaluation of the relative breakage B_r shows a most notable difference at 10 MPa. The limited creep time of one hour is the reason why the change in the GSD

is not more pronounced. However, the differences between 10 and 50 MPa are detectable and are caused by static fatigue as the creep mechanism. The point of maximum curvature of the compression curve, which marks the onset of major level III particle damage, is also located between 10 and 50 MPa, confirming the conclusions of NAKATA *et al.* (2001) and CHUHAN *et al.* (2003) (cf. Figure 4.60).

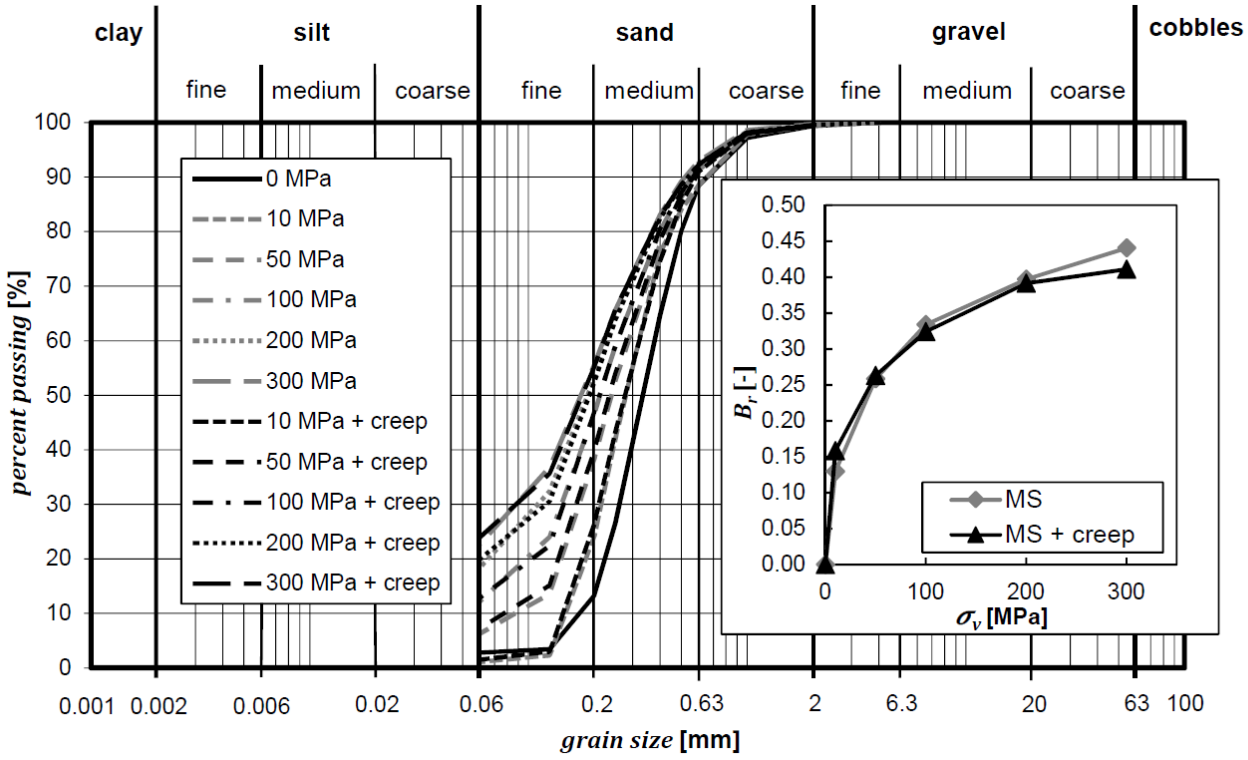

Figure 4.64: Comparison of GSDs of initially medium dense samples of MS loaded to effective vertical stresses of 10, 50, 100, 200 and 300 MPa with and without a creep phase of approximately one hour and comparison of the relative breakage B_r

The evolution of the creep strains with time is shown in Figure 4.65. The increase of the strain follows a linear trend in the semi-logarithmic scale and can therefore also be evaluated using (3.37). Note that the creep strains at 100, 200 and 300 MPa are smaller than at 50 MPa. The creep-coefficient evaluation is presented in Figure 4.66 along with results from tests at lower vertical effective stresses of 0.25, 1.0 and 4.0 MPa presented in Section 4.7.1.

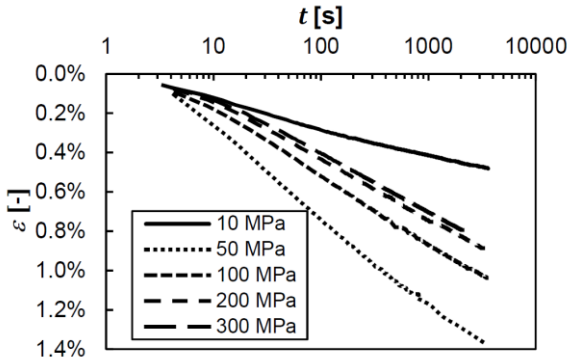

Figure 4.65: Creep strains at different vertical effective stresses of the high pressure tests on medium dense sand MS

The creep-coefficients of the high pressure tests were evaluated between 100 s after load application and the end of the creep phases. The results are displayed in two diagrams, one for the whole stress range up to 300 MPa with a logarithmic stress scale and one up to 50 MPa with a linear stress scale. The analysis shows a hyperbolic increase until 10 MPa, as also observed in Sections 4.6.1 and 4.7.1, and a stronger increase up to 50 MPa. At 100, 200 and 300 MPa the creep-coefficients, i.e. the creep deformations, decrease. This can also be observed in the reduced creep strains in Figure 4.65. These results agree qualitatively very well with the findings of COLLIAT-DANGUS *et al.* (1988) presented in Section 3.3.1.1, which show an increase of the creep-coefficient of calcareous sand below and a decrease above a threshold stress of 5 MPa. As expected, this threshold stress is lower than the value of 50 MPa for the quartz sand MS. This demonstrates the influence of the different mineral hardness of the materials on static fatigue as the creep mechanism. The decreased creep deformations at stresses above 50 MPa can also be a reason for the not detectable difference between the GSDs with and without creep at these stress levels.

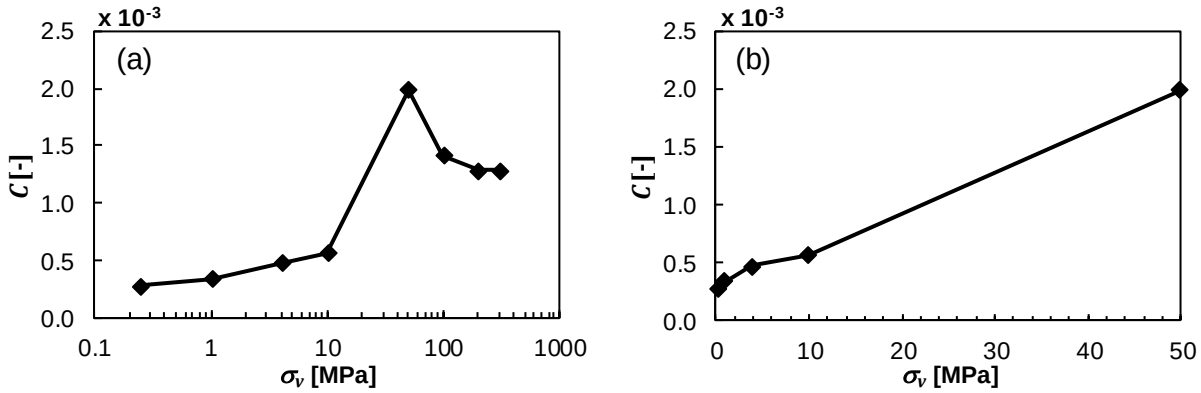

Figure 4.66: (a) Creep-coefficients up to 300 MPa on a logarithmic stress scale and (b) the creep-coefficients up to 50 MPa on a linear stress scale of medium dense sand MS

At high stresses the time-dependent degradation of grains (level III damage), which can be identified and quantified through the changes of the GSD, becomes the predominant mechanism of creep deformation. At low stress levels degradation of the grains is also occurring, but this only affects the grain contacts and is not producing measurable changes of the GSD and the grain shape. Degradation of contacts can only be proven on inspection of the static fatigue of single grains (MICHALOWSKI & NADUKURU, 2012, WANG & MICHALOWSKI, 2015 and MICHALOWSKI *et al.*, 2018).

The particle strength is a time-dependent parameter, which reduces quicker at higher stress levels. But at very high stress levels and upon continued fragmentation of the grains the creep strains start to decrease. This could be due to two reasons. First, the increased number of contact points superimposes the increased external loading of the samples, which in total reduces the contact forces between the grains and thus the grain degradation and creep. The development of the relative breakage B_r (cf. Figure 4.63 and Figure 4.64) shows a reduced susceptibility to grain breakage with increased number of grains and grain contacts at higher stresses, which supports this conclusion. Second, the surfaces of the freshly broken particles tend to be smooth with little asperities that can degrade, causing a reduction in contact degradation and thus creep. The observed behaviour could be due to one of the two reasons or due to a mixture of the two.

4.9.3 Influence of the grain size distribution on creep

The influence of the granulometric properties, described by the grain shape, the grain size, the texture and the grain mineral, on the mechanical behaviour of soil has been shown by the literature review in Section 3.

The four sands from the Garzweiler open cast mine MS, FS, SU and SU*, having similar grain shape characteristics and mineralogy but different fine content showed similar creep behaviour (cf. Sections 4.6 und 4.7). To clarify the influence of the GSD on the creep behaviour of sands, a well graded sand from the Munich area with angular to subangular particles (soil SW) (cf. Section 4.2) was tested in LC oedometer tests. To analyze how the GSD influences the tendency to creep, the soil SW was separated into different size-fractions by sieving. The fractions range from > 2 mm, 0.5 – 2 mm, 0.2 – 0.5 mm, 0.063 – 0.2 mm and < 0.063 mm. The respective GSDs are presented in Figure 4.67 along with the original GSD of SW. This procedure guaranteed similar granulometric properties for each analyzed size-fraction in terms of mineralogy, grain shape as well as grading and uniformity. Only the GSD was changed and therefore its influence on the creep behaviour can be evaluated in isolation.

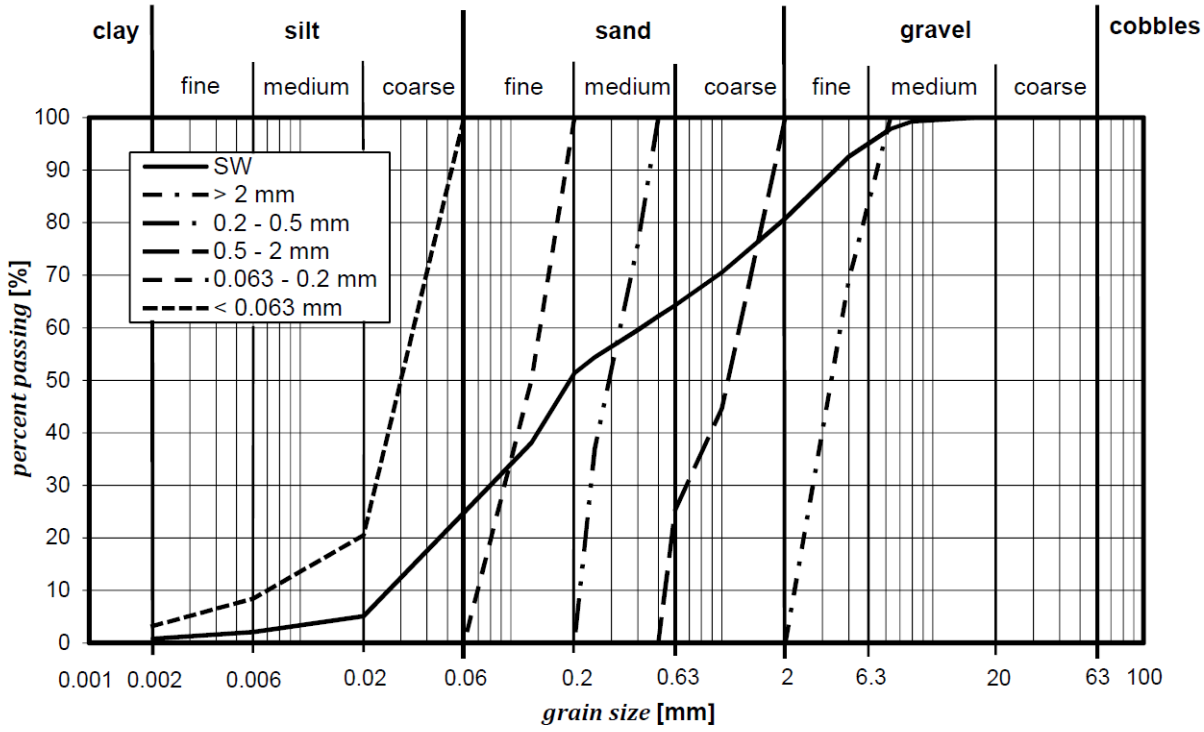

Figure 4.67: GSDs of SW and the size-sections > 2 mm, 0.5 – 2 mm, 0.2 – 0.5 mm, 0.063 – 0.2 mm and < 0.063 mm

The minimum and maximum void ratios of each grain size-fraction were determined according to DIN 18126:1996-11 (cf. Table 4.9) and the samples were prepared in the oedometer test devices as described in Section 4.4 with the same medium dense relative density. The size fraction < 0.063 mm could not be classified by means of the minimum and maximum void ratio. The samples of this frac-

tion were prepared air-dry with two different masses without knowing the exact relative density. However, as expected, the creep behaviour of the fraction < 0.063 mm did not show a dependency on the prepared density.

Table 4.9: Minimum and maximum void ratios of SW and its grain size-fractions

	SW	> 2 mm	0.5 – 2 mm	0.2 – 0.5 mm	0.063 – 0.2 mm	< 0.063 mm
e_{min}	0.381	0.495	0.525	0.717	0.603	-
e_{max}	0.700	0.720	0.822	0.954	1.085	-

The incremental load steps were 125, 250, 500, 1000 and 2000 kPa followed by 24 h creep phases at each load-step. The results were evaluated with respect to the creep-coefficient value according to (3.37) and are presented in Figure 4.68. The mean grain size d_{50} was chosen as the characterizing value of the different GSDs. The different markers at each d_{50} give the creep-coefficient values for each vertical effective stress. The minimum and maximum stresses of 125 kPa and 2000 kPa are interpolated by the dashed lines. As can be observed, the tendency to creep is inversely proportional to d_{50} by

$$C \propto \frac{1}{{d_{50}}^{\alpha}} \tag{4.27}$$

with α = 0.397 in this case.

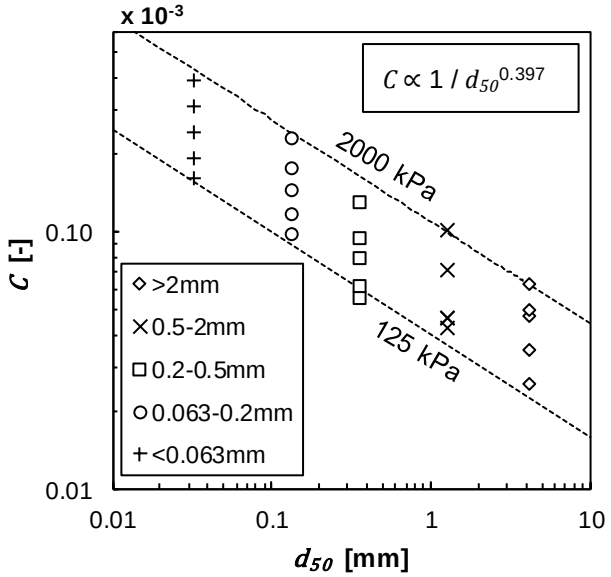

Figure 4.68: Creep-coefficients at each stress level versus grain size d_{50} of the fractions of sand SW

The presented results show that creep deformations reduce with increasing mean grain size. However, findings regarding the influence of the grain size on the particle strength presented in Section 3.1.3 show that the particle strength σ_f is inversely proportional to the grain size (cf. Equation (3.5)). Additionally with increasing grain size less grain contacts transduce the mean sample loading and thus the contact forces have to increase. Both findings point into the opposite direction compared to the results in Figure 4.68.

A hypothetical explanation of the observed behaviour could be that the stresses up to 2000 kPa applied in the creep tests are too small to cause major particle breakage. Degradation of asperities

(level I and level II damage) is thus the triggering mechanism of creep. The reduced number of contact points in the coarser grain assemblies results in a reduced number of loaded surface asperities that can potentially degrade, which leads to reduced creep deformations. The effect of the decreased number of possibly failing asperities outweighs the effect of increased contact forces in the coarser grain assemblies. Results of OSTERMAYER (1976) presented in Section 3.3.1.1 point into the same direction. He found that the creep-coefficients reduce strongly with increased content of coarse material in a primarily fine grained soil (cf. Figure 3.22).

4.9.4 Effect of full saturation on creep

In literature exist contradictory statements about the influence of the water content on creep (cf. Section 3.3.3.1). Some authors found an increasing grain degradation and creep due to full saturation, while others could not observe any effect.

An LC oedometer test series was performed to get an indication of the influence of full saturation on the oedometric creep behaviour. Two test series were conducted with soil SU at different initial dry densities, one with air-dry samples and one with fully saturated samples. The air-dry samples were prepared as described in Section 4.4. The saturated samples were also prepared air-dry and then flooded from bottom to top with demineralized water after positioning the top filter plate. The saturation process led to slight collapse in the very loose samples. Loading was performed in five steps by doubling the load every 24 h up to 1000 kPa. The creep-coefficients were evaluated using (3.37) from the linear section of the compression curves between 100 s after load application and 24 h. The stress-dependent development of the creep-coefficients is presented in Figure 4.69.

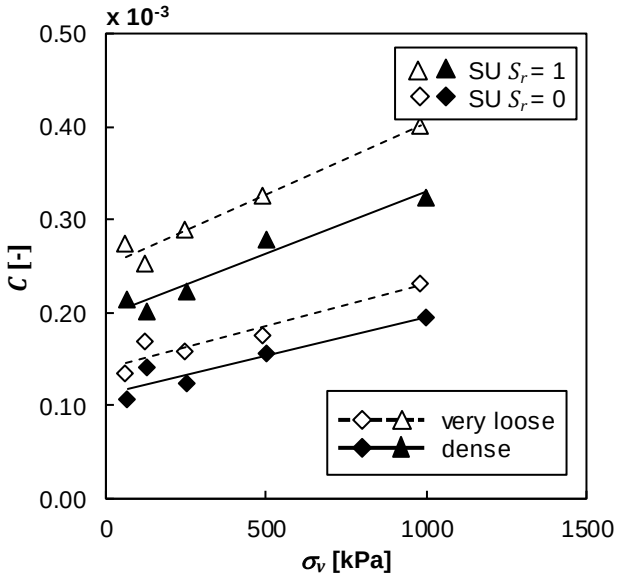

Figure 4.69: Effect of full saturation (S_r = 1) on the creep behaviour of very loose and dense samples of sand SU

It can be seen that the creep-coefficients approximately double for the saturated samples, although the initial density of the saturated samples is slightly higher due to the collaps upon saturation. Also the stress sensitivity of the creep-coefficient increases, because the gradient with stress is higher. This is the case for both relative densities tested. The results confirm the conclusions of MIURA &

YAMANOUCHI (1975) and BRZESOWSKY *et al.* (2014) and can be explained by increased “stress corrosion cracking”, which stands for a weakening of the Silicium-Oxygen-bonds of the quartz crystal by adsorption of water molecules onto its surface (ATKINSON, 1979) (cf. Section 3.3.3.1). The weakening of the bonds leads to more grain degradation and therefore creep in the saturated samples.

4.9.5 Conclusions

The main conclusions from the test results presented in Section 4.9 are summarized here:

Long-term creep and relaxation

– Creep of sand MS shows an under-linear trend on a logarithmic time scale. This results from a change of the structure of the grain skeleton, which is charaterized by an increase of the number of grain contacts and the contact area and consequently, a reduction of the normal and shear stresses at the contacts. It will ultimately lead to stagnation of the creep strains. The time interval in which a stagnation happens is strongly dependent on the soil properties. Clean sand shows a clearly visible reduction in the creep-coefficient during the first 24 h, while sand with high fine content does not.

– The long-term relaxation test with a duration of one week on the other hand, showed no reduction of the viscosity index, describing the relaxation process.

– This indicates that the deformations that happen during creep, but not during stress relexation, contribute to the stagnation of the viscous effect of creep.

High pressure tests

– At high pressures causing considerable grain breakage, compression curves of sand MS converge asymptotically to a unique compression curve, regardless of the initial density.

– The medium dense samples show more breakage in compression compared to the dense samples due to the reduced number of contact points and therefore higher contact forces between the grains.

– The relative breakage shows a hyperbolic trend with the vertical stress, which means that the susceptibility to grain degradation decreases with the grain size: The larger the number of grains and the interparticle contacts per volume unit, the lower the interparticle forces.

– Time-dependent grain degradation and breakage (static fatigue) is the creep mechanism in sands. With high pressure tests this is measurable by the time-dependent change of the GSD and the relative breakage.

– The increase in number of contact points at the smooth surfaces of the freshly broken grains at very high stresses outweighs the effect of stresses on creep. This leads to a decrease of the creep-coefficient at very high stresses > 50 MPa.

Influence of mean grain size

– As long as the stress level does not cause significant level III grain damage, the creep-coefficient is inversely proportional to d_{50}. The relation can be described by (4.27).

– At stress levels with level I and level II grain damage asperity yielding is the driving mechanism of creep. A reduced number of contact points in the coarser grain assemblies results in less surface asperities that can potentially degrade, which leads to reduced creep deformations.

Effect of full saturation

– Full saturation of the sand MS leads to an increase of the creep rate at the same stress level. According to ATKINSON (1979) and ATKINSON & MEREDITH (1981) this can be explained by the so-called “stress corrosion cracking”, which is caused by a weakening of the Silicium-Oxygen-bonds of the quartz crystal by adsorption of water molecules onto its surface. Consequently, degradation, plastic deformations at the grain contacts and creep increase.

5 Creep of open cast mining dumps in the Renish lignite mining area

Lignite open surface mining in large open cast mines contributes to about 25% of the total electricity production in Germany (FRAUNHOFER INSTITUT ISE, 2018). In order to gain the equivalent of 180 million tons of lignite per year a three- to fivefold magnitude of overburden is excavated and dumped, depending on the geological boundary conditions of the open cast mine. This results in a bulk flow of approximately 700 million tons per year. The dumps cover large areas of land that must be regained for nature reserve, agriculture, buildings and infrastructure. In the context of the reuse of dumps resulting from open cast mines, the aspect of long-term ground deformations plays an important role for the planning of infrastructure, such as roads and foundations for engineering structures like bridges and buildings. The long-term deformations of the dumps, their characteristics and predictions of the long-term deformations are the focus of this section.

The open cast mines Garzweiler and Zukunft West, which are in the focus of this study, are situated in the Renish lignite mining area east of Cologne (Germany) and reach depths of up to 185 m (cf. Figure 5.1). The lignite layers originate from the Neogene and Paleogene period (formerly called Tertiary period) and are intermitted by marine sand, clay and silt layers. They are overlain by fluvial sands and gravels from the Quaternary period (KLOSTERMANN, 2010). The dumped soils are therefore mostly marine sands from the Neogene and Paleogene period and fluvial sands and gravels from the Quaternary period (cf. Figure 5.1).

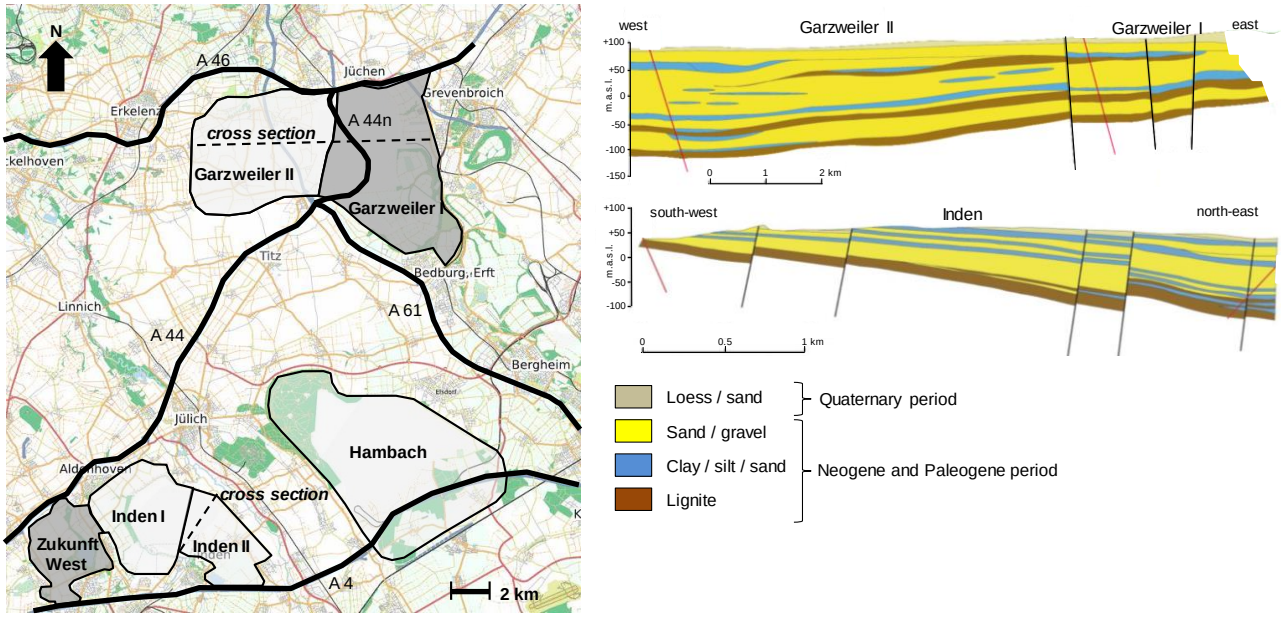

Figure 5.1: Location of the open cast mines Garzweiler and Zukunft West in the Rhenish lignite mining area west of Cologne (Germany), cross sections adapted from NEUROTH *et al.* (2016)

Dumps are created using large scale spreaders with a capacity of up to 200,000 m^3/d. During the dumping process, the soil is not compacted by additional technical measures. The density of the

dumped soil is influenced by the drop height, which varies between 10 m and 30 m, the mass flow from the spreader, the overburden stress (LANGE, 1986) as well as the water content. Field tests by means of cone penetration tests (CPT) with a maximum depth of 71.2 m show in average relatively low tip resistances corresponding to a loose relative density of the material (cf. Section 5.1.3). Therefore, the dumps exhibit a high compressibility. The loose state is one of the reasons for the long-term evolution of deformations that continue for many years after the end of dumping (KOTHEN & KNUFINKE, 1990, VOGT *et al.*, 2013, LEVIN & VOGT, 2015). During operation, the open cast mines are dewatered and the dumped sands are in an unsaturated state. Effective stress changes due to suction effects are however negligible compared to the effective overburden stresses acting in the dump. Therefore, it can be assumed that the long-term strains develop mainly under constant effective stresses. After operation of the mines, the dewatering will be stopped and the groundwater tables will rise back to their natural level. However, this study only takes the long-term deformations during operation of the mine into account. Possible deformations due to rising ground water tables are not considered. Infiltrating rain water, changes of weather conditions in form of atmospheric high- and low-pressure areas and seismic events have in principle also influence on the stress and density state and therefore the deformation of the dumped soil. The Renish lignite mining area lies within the seismic zone 3, which is a zone of high seismic activity for Germany. This means a probability of 10% of exceeding an event of intensity 7.5 on the European Macroseismic Scale in 50 a (mean return period of 475 a) (GRÜNTHAL & BOSSE, 1996). Based on the available measurement data it was however not possible to study the effect of seismic events on the dump settlements.

This study focusses on the long-term deformations of the dump during operation of the mines resulting mainly from creep of the dump material. Despite the fact that the creep strains in sand are very small compared to soft fine grained soils, the great thickness of the loose freshly dumped material leads to significant long-term surface deformations of the dumps. Field measurements show that the time-dependent surface settlements occuring after the end of dumping reach values of about 0.35 to 1.0% of the thickness of the dump (KOTHEN & KNUFINKE, 1990). The maximum settlement is assumed to be reached once the settlement-rate is below 1.0 cm/a, which can take time spans between approximately 10 to 50 a (KOTHEN & KNUFINKE, 1990). These values may correspond to very different strain rates depending on the depth of the dump. Taking the thickness of the considered open cast mines Garzweiler and Zukunft West of about 75 m (Zukunft West) to 185 m (Garzweiler) it corresponds to mean strain rates of about 0.01 to 0.005%/a and maximum settlements between 0.26 and 1.85 m. Differential settlements due to the different ages of the dumped soil layers and different materials have to be considered also and can be significant. An example of a cross-section through the Garzweiler dump along the axis of highway A44n, in which the different dumping layers and their respective dumping time are presented, is shown in Figure 5.2. The dumping layers can have very different thickness and extent, which additionally leads to differential settlements of the dump surface. Time-dependent settlements of the unscathed natural ground beneath the dump are small compared to the dump deformations (cf. Section 5.2.3).

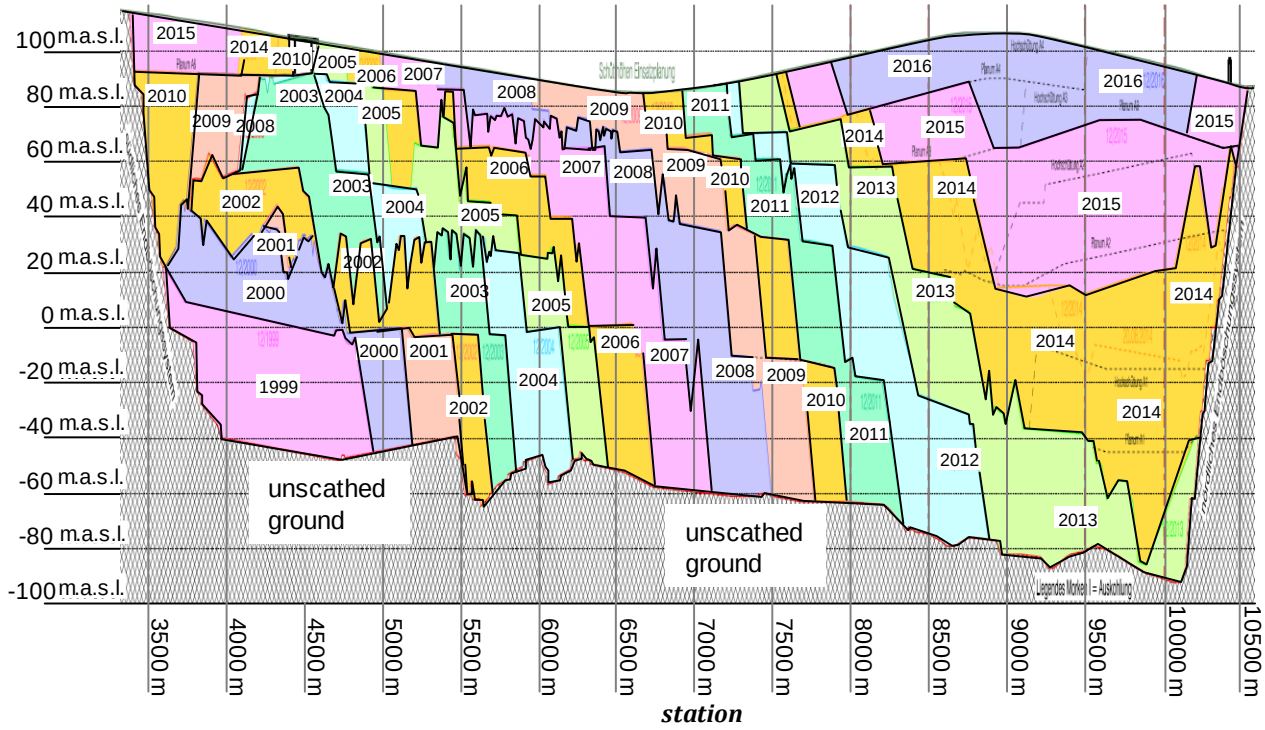

Figure 5.2: Cross-section through the Garzweiler open cast mining dump along the axis of highway A44n with dumping layers and their respective dumping year, RWE-Power AG

The time-dependent deformations of the dumps were studied using data sets, made available by the RWE Power AG. The data sets include soil classification data, settlement measurements and CPT records. They were evaluated in this study with respect to the influence of the soil type, the density, the age of the dump, the depths, the observation time-span and the overburden pressure.

The following sections will present an approach for a representative classification method of the dumped materials and show results of the different field settlement measurements of the Garzweiler dump. The measurements include level gauges on the dump surface, hydrostatic line measurements and level gauge measurements in different depth of the dump.

The evaluation of the field measurement data for estimation of creep-coefficients and dump conditions influencing the deformation behaviour are discussed and the creep behaviour in the field is compared to results from laboratory tests presented in Section 4. One focus of the analysis lies on the determination of the model parameters controlling creep from laboratory tests for constitutive modelling of the dump material. A method to determine creep-coefficients based on laboratory test results and the in situ density of the soil using the empirical concept for the creep-coefficient determination introduced in Section 4.6.3 is presented.

5.1 Classification and characterization of the soils at Garzweiler open cast mining dump

5.1.1 Classification by continuous sampling

For the interpretation of the measuring data from level gauges and hydrostatic measuring lines, it is very important to properly classify the dumped material. One effective way is to take samples continuously during the dumping process in areas of the dump where future construction is projected. This method is much more cost-effective than performing exploration drillings and penetration tests after dumping has ceased. Examples of continuous sampling along the axis of highway A44n built on the Garzweiler open cast mining dump are presented in the cross-section in Figure 5.3. The top view of the cross-section is presented in Appendix A.7. The presented cross-section corresponds to the one shown in Figure 5.2.

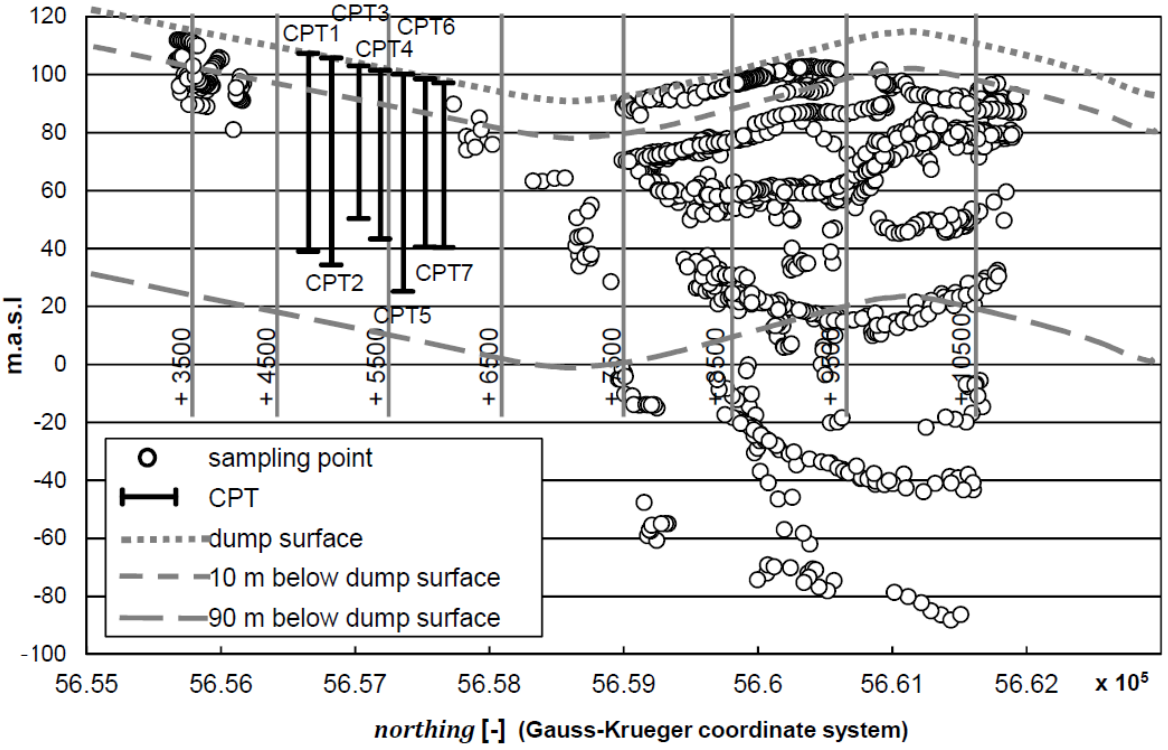

Figure 5.3: Cross-section through the Garzweiler dump along the axis of highway A44n with sampling points

The diagram shows the location of the collected samples in different depths beneath the dump surface. Samples were not taken uniformly in all areas of the cross-section. The areas where no samples were taken, were investigated with the aid of seven CPTs to a maximum depth of approximately 71.2 m below the surface. The samples were partly analyzed by sieving and partly by a so-called macroscopic classification. In the latter, the samples are analyzed considering their main fractions clay, silt, sand and gravel using visual and tactile methods. Sieving analysis served as a verification for the macroscopic classification. Overall, 1954 macroscopic classifications and 325 sieving analyses were performed on samples taken from the presented cross-section of the dump. The macroscopic classification and about one third of the sieving analyses were performed by the RWE Power AG. The other analyses were done in the laboratory of the Zentrum Geotechnik at the Technical

University of Munich. Figure 5.4 presents the results of the macroscopic classification. The results show that more than 90% of the samples have more than 40wt-% of sand and also more than 90% have less than 15wt-% fine content. The GSDs determined by sieving analysis presented in Figure 5.5 show that the majority of the samples are fine to coarse sands. The samples with a larger fraction of gravels were mostly found in the upper 10 m of the dump. The main dump body consists out of fine to coarse rather poorly graded sands.

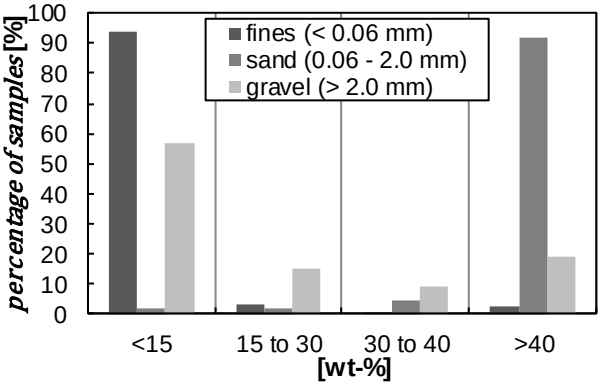

Figure 5.4: Distribution of grain size fractions of all samples classified by the macroscopic method in the dump section

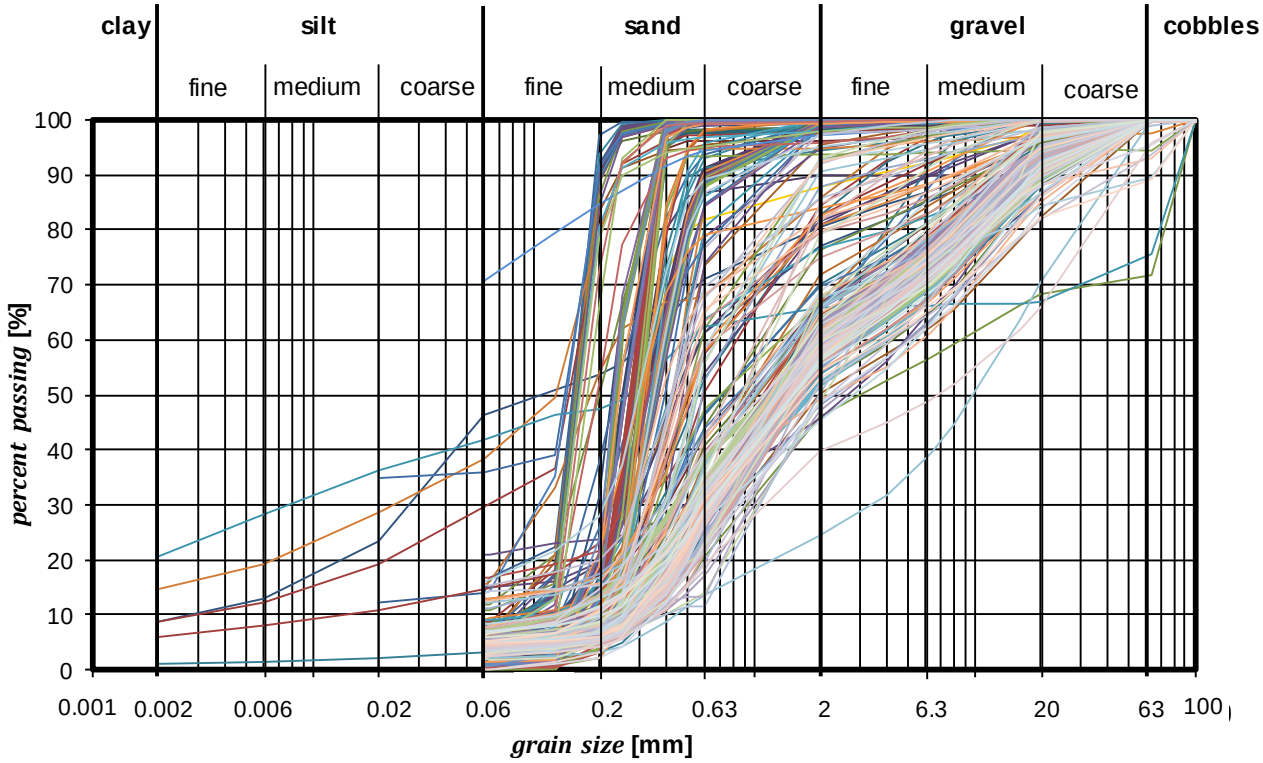

Figure 5.5: GSDs of 206 samples from the dump cross-section

5.1.2 Soil type determination by CPT interpretation

It is common to use CPT data for the interpretation of soil stratigraphy. Established methods for determining the soil type through the so called Soil Behaviour Type (SBT) were developed by

ROBERTSON *et al.* (1986), ROBERTSON (1990), ROBERTSON (2009) and ROBERTSON (2010). The methods were developed for naturally deposited soils and it was necessary to investigate, which method is suitable for classifying the dumped soils, which are characterized by a very loose state and a macroporic structure. CPT 1 to CPT 7 (cf. Figure 5.3) can be used for this task, because the soil profile is known from monitoring the dumping process and can be considered to be very similar to the soils classified via macroscopic classification in Section 5.1.1. Mostly sands with some gravels primarily at the top of the dump were deposited. The method by ROBERTSON (2010) determining the SBT and the method by ROBERTSON (1990) determining the normalized Soil Behaviour Type (SBTn) are compared. The SBT by ROBERTSON (2010) is an update of the version developed by ROBERTSON *et al.* (1986). Both methods determine the soil type through the tip resistance q_c and the friction ratio

$$R_f = \frac{f_s}{q_c} \tag{5.1}$$

with f_s the CPT sleeve friction. SBTn uses a normalization of q_c and R_f with

$$R_{fn} = \frac{f_s}{q_{cn} - \sigma_{v0}} \tag{5.2}$$

and

$$q_{cn} = \frac{q_c - \sigma_{v0}}{\sigma'_{v0}}, \tag{5.3}$$

where σ_{v0} is the total vertical overburden stress and σ'_{v0} is the effective vertical overburden stress. Figure 5.6 and Figure 5.7 show a comparison of the soil type determinations with the two methods for the case of CPT 1. The evaluation was done with the software CPET-IT version 1.7.6.42 with the input parameters summarized in Table 5.1. More comparisons of the two methods for CPT 2 to CPT 7 are summarized in Appendix A.7.

Table 5.1: Input parameters for CPT evaluation with the software CPET-IT version 1.7.6.42

Average interval	3
Ground elevation	0
Ground water table	100 m below surface
Probe radius	0.0219 m
Cone area ratio	0.80
OCR	1.0
Unit weight of water	10 kN/m³
Unit weight (of soil)	15.6 kN/m³ (cf. Section 5.1.3)

According to the SBT-method the dumped soils are mostly classified as sands, silty sands and sandy silts, while the SBTn-method classifies the dumped soils predominantly as fine grained soils like clay and silty clay and less as sands, silty sands and sandy silts. It is known however from the extensive macroscopic classification and sieving analysis on a great number of samples presented before that the dump consists predominantly of sands or silty sands. Therefore, the method by ROBERTSON (2010) is considered more suitable for classification of the dumped soils.

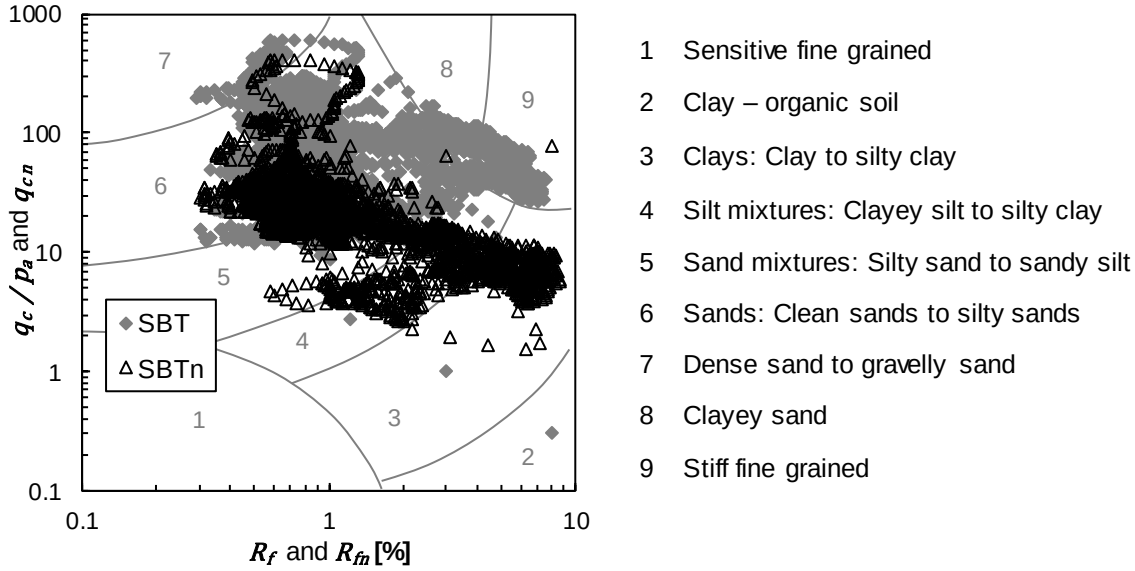

Figure 5.6: Comparison of SBT and SBTn in case of CPT 1

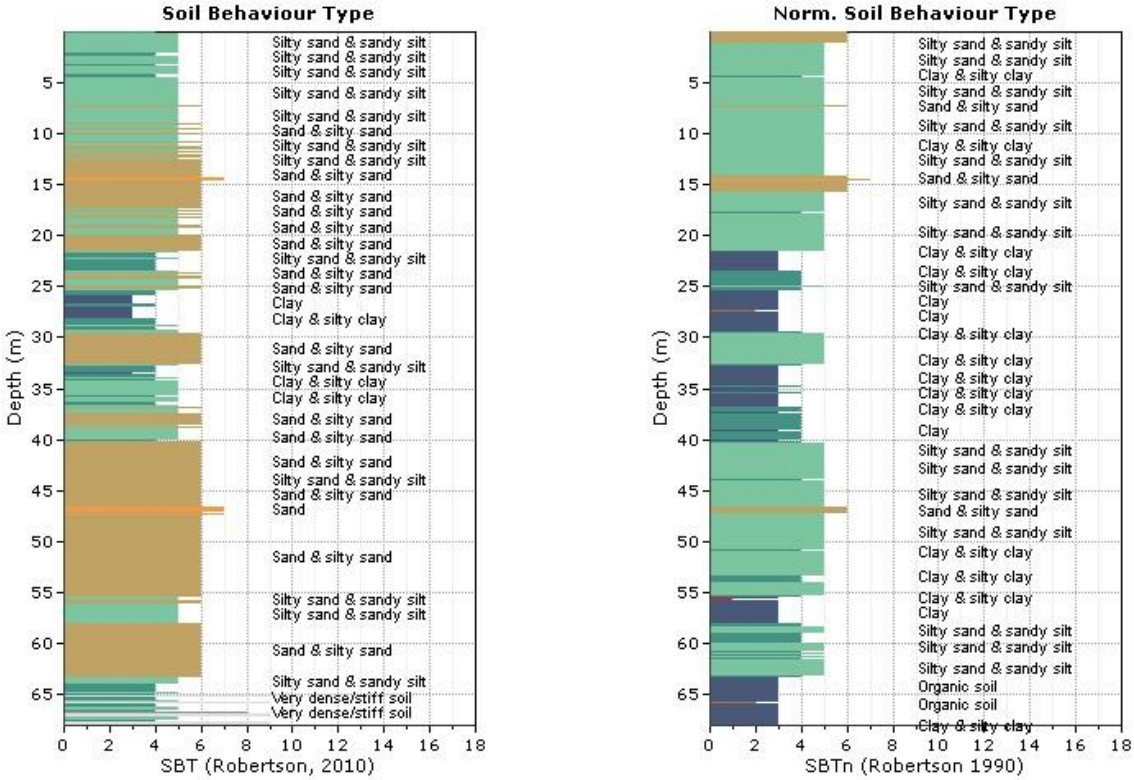

Figure 5.7: Soil profile with comparison of SBT (left) and SBTn (right) in case of CPT 1

5.1.3 Determination of relative density by CPT interpretation

The CPT-data was also analyzed with respect to the relative density using the method proposed by CUDMANI (2001), which is based on the numerical simulation of a cavity expansion and takes the mean effective stress increase with increasing depth of penetration into account:

$$q_c = \underbrace{\left[1.5 + \frac{5.8 \cdot {I_d}^2}{{I_d}^2 + 0.11}\right]}_{k_q} \underbrace{\left(a_1 + \frac{a_2}{a_3 + I_d}\right) {p_0}^{b_1 + \frac{b_2}{b_3 + I_d}}}_{p_{LS}} \tag{5.4}$$

with k_q as shape-factor, p_{LS} limiting pressure from cavity expansion, I_d pressure-adjusted relative density and a_1, a_2, a_3, b_1, b_2 as well as b_3 as coefficients for the approximation of the limiting pressure with respect to the initial pressure p_0. Equation (5.4) can be numerically solved for I_d and the input parameters a_1, a_2, a_3, b_1, b_2 and b_3 can be determined by the numerical simulation of a cavity expansion at different relative densities I_d and initial pressures p_0 using the hypoplastic constitutive model by VON WOLFFERSDORFF (1996). For a robust interpretation of the CPT results, the soil profile has to be known. Since no exploration drillings are available at the locations of the CPTs, it is assumed that the soil profile is homogenous. This assumption is warranted by the classification results from samples taken between stations 6500 m and 10500 m and the soil type determination from the CPT results themselfs presented before. I_d was determined from q_c as the average value of relative densities calculated with (5.4) using the determined coefficients and hypoplastic model parameters from sand MS as representative soil given in Table A.9.1 in Appendix A.9. The model parameters were determined from oedometer and triaxial tests. The results from CPT 1 to CPT 7 between stations 4500 m and 6500 m (cf. Figure 5.8) show generally medium to very low relative densities also in great depths. The depths in which the relative density increases to values larger than I_d = 0.6 correspond to the locations of compacted working planes, on which the large scale spreader was moving during the dumping process.

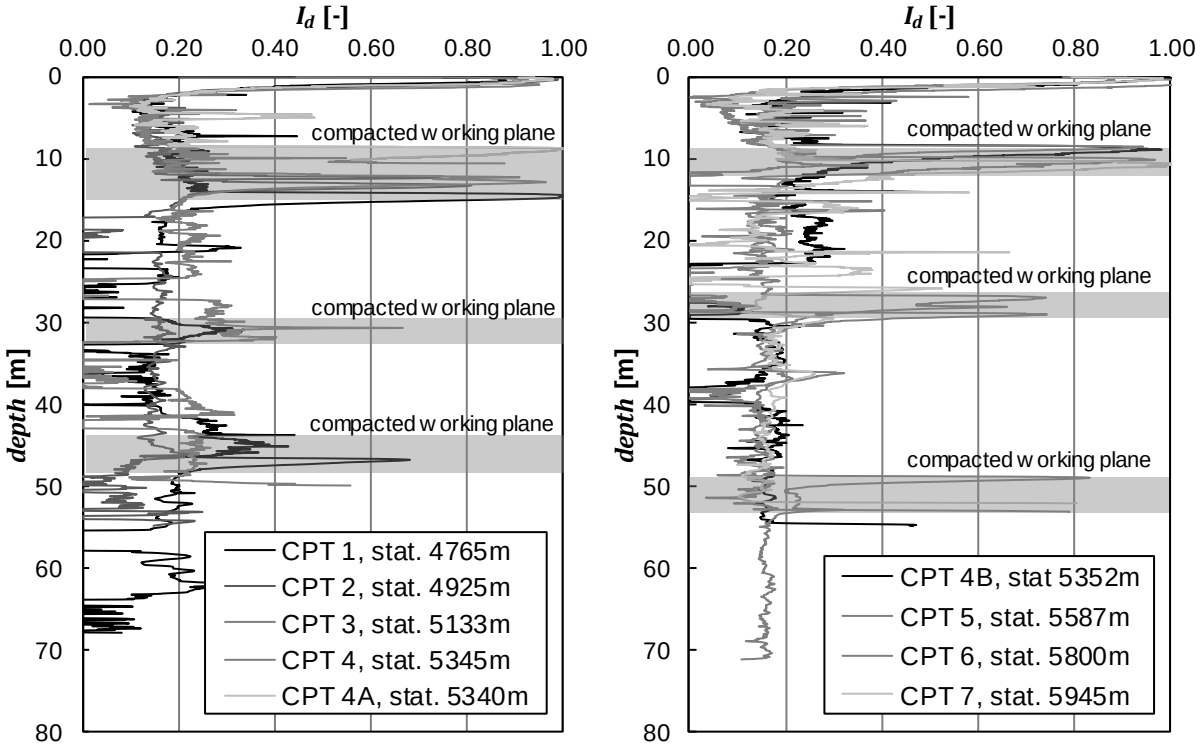

Figure 5.8: Relative density of the dump between station 4500 m and 6500 m evaluated from CPTs with the pressure compensated approach by CUDMANI (2001)

In summary, the soil classification of the dumped material indicates that the soil is rather homogenous in terms of soil type (poorly graded, fine to coarse sands with low fine-content) and relative density

(very loose to medium dense). The homogeneity is important for the following evaluation of the level gauges and hydrostatic line measurements. For a certain position within the dump it allows to interpret the data independent from the soil type and state. Other influences on the creep behaviour of the dump, which do not result from the soil type and relative density, can therefore be considered separately.

5.2 In situ deformation measurements

The prediction of deformations of open cast mining dumps is essential for the evaluation of possible subsequent uses. For a reliable long-term prediction, the deformation behaviour of the dumps has been monitored to analyze its behaviour and estimate input parameters for numerical modelling. To this end, several hundred level gauges and numerous hydrostatic measuring lines were installed on the surface and in certain depths of the considered open cast mining dumps to record settlements in different time intervals, some as often as once a day. The observation times vary in duration and in the time period between the end of dumping and the observation start. On this data basis, the time-dependent deformation characteristics of the dump are analyzed, concerning the development of the settlement-rate with increasing observation time or elapsed time since the end of dumping. Futhermore, associated questions whether the creep-coefficient C as defined by (3.37) can be assumed constant over time as well as independent of the depth of the dump is examined using the measurement data. Following this empirical analysis, concepts of modelling and the determination of creep-coefficients from the measurement data as well as various influencing variables on the determined C-values like the depth of the dump body and the observation time period are examined. The obtained findings provide empirical evidence about the applicability of the constitutive models illustrated in Section 6 for the prediction of time-dependent deformations of dumps consisting primarily of sand.
The following analysis defines several different time variables, which are summarized here and graphically explained in Figure 5.9:

- t_{zero}… zero point in time where the dump can be assumed to be in average in a normally consolidated state
- t_{ref}… reference time according to (3.37)
- t_{EOM}… time of end of measurement or observation
- t_{obs}… observation start

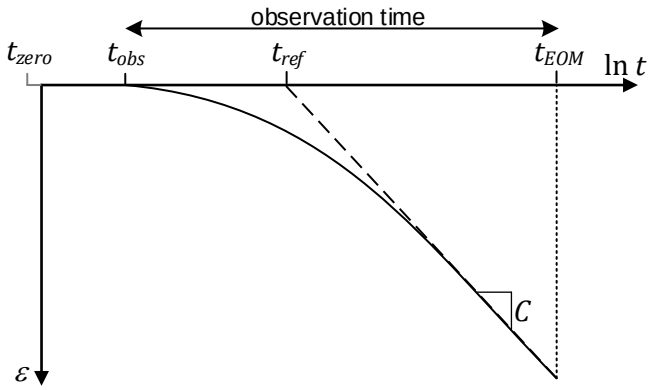

Figure 5.9: Schematical explanation of defined time variables

5.2.1 Surface settlement measurements on the Garzweiler open cast mining dump

The measured data sets of the level gauges on the surface of the dump are evaluated with respect to their time-dependent development. Diagrams are used, which represent the time axis in a logarithmic scale. The strains were calculated by dividing the settlements by the thickness of the dump. Also the unscathed naturally deposited soils show deformations due to the dumping process. They mostly occur during the dumping process as instantaneous settlements and the time-dependent deformations are negligible (cf. Section 5.2.3).

5.2.1.1 Concept for determination of the creep-coefficient from field measurement data

When evaluating laboratory tests for determination of a creep-coefficient (e.g. the parameter C) for the respective soil, the determination of the evaluation time span and the zero point in time, where creep starts, is apparently straight forward (cf. Section 3.3.5). The creep strains are usually evaluated in the time span between end of primary consolidation t_{EOP} and 24 h. At t_{EOP} OCR = 1.0 is assumed. This is a common specification, which makes results comparable.
In contrast, the evaluation of field measurement data holds the problem of an objective determination of the zero point in time, when the soil can still be assumed to be in a normally consolidated state and which makes results comparable. The determination of the zero point where a normally consolidated state can be assumed is important for determination of the creep-coefficient, because a different zero point can lead to an under- or overestimation of the creep-coefficient. The relevant creep deformations occur after the end of dumping. The question is, whether the end of dumping can be assumed as the zero point in time for the evaluation of the creep-coefficient? Due to the continuous dumping process the obtainable level of accuracy for the determination of a certain time when the end of dumping happened is difficult. Analysis show that the time when the end of dumping (zero point) is defined and the time when the first measurement data was collected as well as the length of the subsequent period of measurements (observation time) influence the evaluation of the creep-strains and hence creep-coefficients. The zero point in creep-time determines the value of the creep rate and therefore the creep-coefficient evaluated from the measured data (cf. Equation (3.40)).
During the dumping process the dump already creeps with a logarithmically decreasing creep rate. The strains at a certain point in the dump (point 1) develop as schematically presented in Figure 5.10. After dumping of layer 1 the soil creeps from time t_{zero} until time t_1 with a decreasing creep rate. Upon dumping of layer 2, the state of the soil in layer 1 is initially in the reloading regime, because creep causes overconsolidation, until it reaches the normal-consolidation-line (NCL). Overconsolidation induced by creep can be seen in the creep tests presented in Section 4.7.1 and can be explained by a structuration effect (cf. Section 3.3.3). When dumping of layer 2 finishes, creep of layer 1 starts again from the NCL with a rate of $\dot{\varepsilon}_{zero}$, because the instantaneous deformations caused by dumping reset the structuration effect.

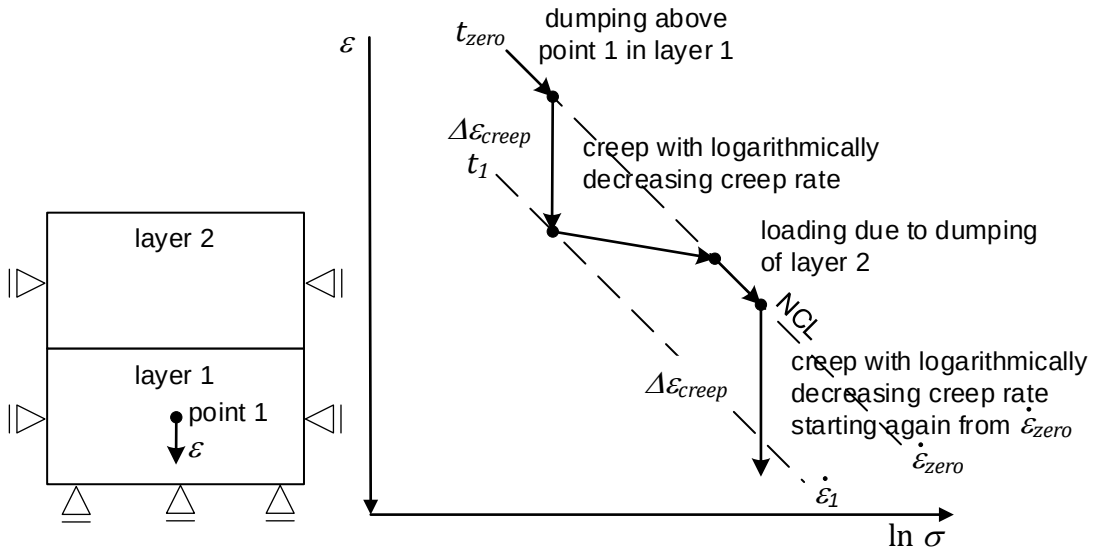

Figure 5.10: Schematic development of strains at point 1 in layer 1 during the dumping process

Whether the soil at the state of point 1 actually returns to a normally consolidated state depends on the loading and the resulting settlements caused by layer 2. In this explanation we assume the validity of the isotache-concept by ŠUKLJE (1957), although this concept is not valid for granular soils for all possible loading paths and significant changes of stress of several 100 kPa, as was explained in Section 4. Stress changes of this order of magnitude can occur during the dumping process in dump layers at the bottom of dumps exceeding e.g. 100 m in thickness. Nevertheless, the stress changes occurring after the end of dumping are small enough to remain within the applicability of the isotach-concept at least for the prediction of creep strains from the end of dumping.

The assumption that the dumped material reaches the NCL at the end of dumping and creep time can be considered to start from there has been confirmed by data from a settlement gauge installed in the open cast mining dump Zukunft West. The settlement gauge allows the measurement of settlements in different depths of the dump down to the unscathed natural ground at 77 m beneath the surface. The measuring levels are positioned in a vertical distance of approximately 5 m and are connected by a tube, which was continuously installed during the dumping process. Further details on the settlement gauge are given in Section 5.2.3. With the settlement gauge the instantaneous and the creep settlements in different depths of the dump were measured. The thickness of the dumping layers controls the stress change in the dump and therefore the instantaneous settlements. Usually, dumping layers have a thickness of 15 to 30 m and therefore induce significant additional stresses (250 to 500 kPa) and deformations over the entire depth of the dump. The dump at the location of the settlement gauge was constructed in three main layers with a thickness of about 24 to 30 m. The layers were dumped in short time intervals of just four to six days each. Figure 5.11 shows the instantaneous settlements and strains occurring in layer 1 during dumping of layer 2 and in layer 1 and 2 during dumping of layer 3.

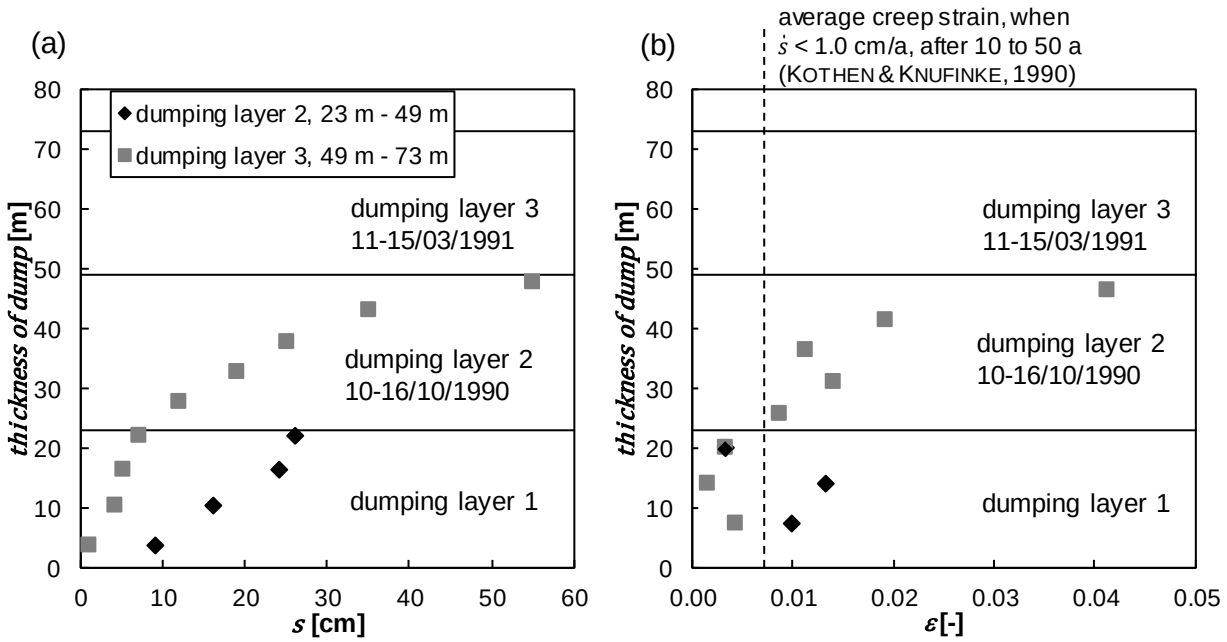

Figure 5.11: Instantaneous settlements (a) and strains (b) after dumping of layer 2 and layer 3 respectively, strains calculated between each level gauge

Compared to the strains of approximately 0.7% considered as the value of experience for the maximum strains occurring after end of dumping during 10 to 50 a (KOTHEN & KNUFINKE, 1990), the strains occurring due to the dumping are comparably high. The strains resulting from creep between dumping of the layers causing an overconsolidation effect are even smaller compared to the instantaneous strains and therefore the overconsolidated state is reset to a normally consolidated state. This result justifies the assumption that the dump is in a normally consolidated state after dumping of the last layer. It is supported by investigations of KOTHEN & KNUFINKE (1990) in the Renish lignite mining area, who evaluated the relation between the thickness of the last dumping layer and the measured maximum settlements at the point in time where the settlement rate falls below the value of 1.0 cm/a. They found that the amount of maximum settlements depends on the thickness of the last dumping layer. Their evaluation is presented in Figure 5.12. Especially between thicknesses of the last dumping layer of 5 to 20 m the maximum strains increase significantly from about 0.20 to 0.55% for the considered dumps with depths between 50 to 300 m. At larger thicknesses of the last dumping layer up to 35 m the increase becomes much smaller from about 0.55 to 0.65%. This indicates, that a dumping layer with a thickness between approximately 5 to 20 m cannot fully reactivate the creep potential in the entire dump, but layers thicker than approximately 20 m induce a large enough stress change and therefore deformation to reactive the full creep potential. The necessary thickness of the last dumping layer depends of course on the thickness of the dump and can therefore only be defined roughly. It depends on the boundary conditions in the dump.

Therefore, close attention needs to be paid to the thickness of the last dumping layer when determining the zero point in time for determination of the creep-coefficient. This is also numerically verified in Section 6.5.1.

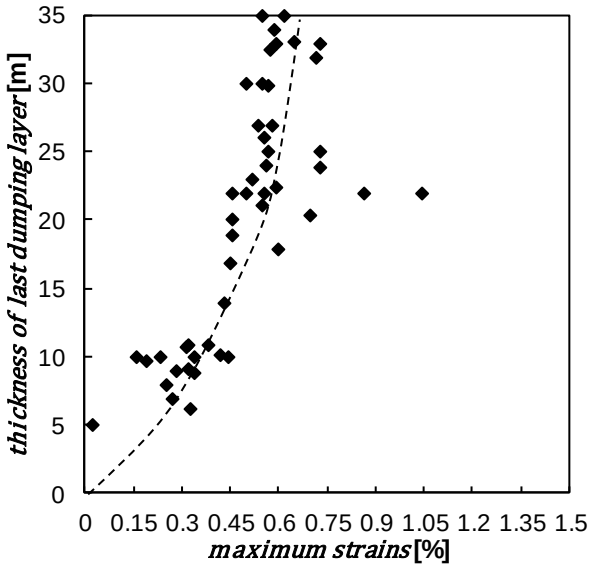

Figure 5.12: Maximum strain occurring after the end of dumping until $\dot{s}$ < 1.0 cm/a in dependence of the thickness of the last dumping layer (data from KOTHEN & KNUFINKE, 1990)

The definition of the end of dumping as the zero point in time t_{zero} makes evaluations of the data comparable. The influence of a shift in t_{zero} is presented in Figure 5.13. Actual data from a level gauge was taken and the end of dumping was virtually altered by pretending that the measurement started 50 d or 100 d after dumping ended. The shift of the end of dumping by 50 d and 100 d is equivalent to assuming that the dump is 50 d respectively 100 d older than it actually is. The observed creep rate is therefore associated to the wrong age of the dump and leads to an overestimation of the creep-coefficient. The gradients of the creep curves are initially very different and converge with increasing observation time. For the given example a combination of the shift in t_{zero} and an observation time of less than approximately 600 d can lead to a deviating determination of the creep-coefficient.

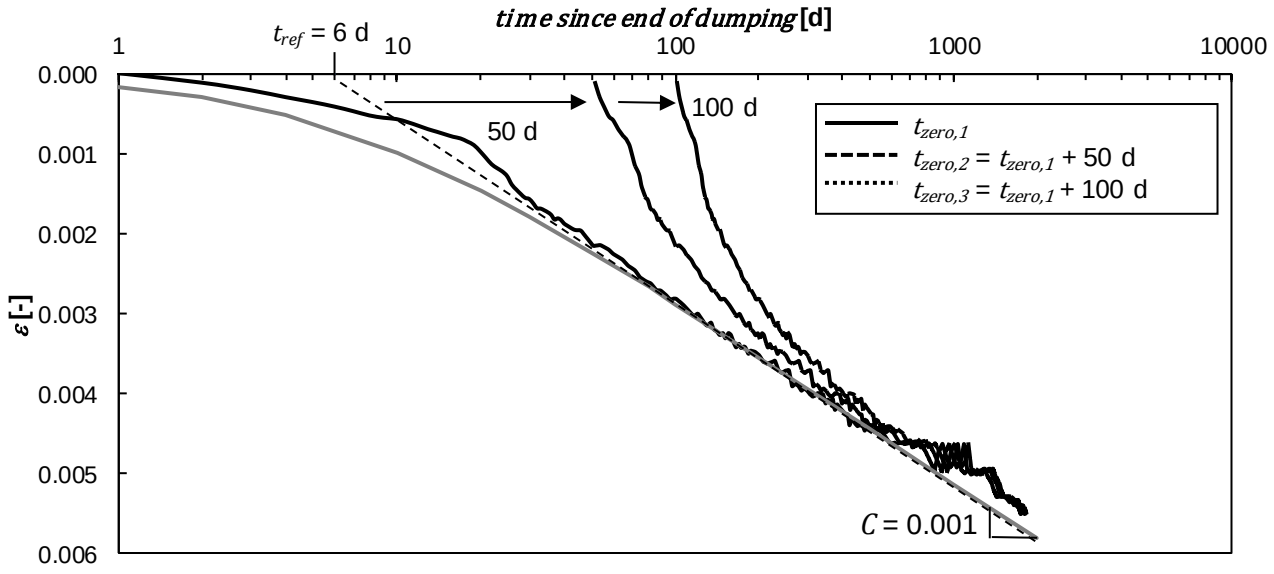

Figure 5.13: Influence of a shift in the time of end of dumping t_{zero} on the determination of the creep-coefficient C

The determination of the end of dumping exact to the day is not possible, because dumping is a continuous process and even if the dumping at one location has reached the final height, it still continues in adjacent locations influencing the deformation behaviour in the vicinity. Therefore, the zero point in time must be chosen in a way that the considered location of interest is not influenced by ongoing dumping in adjacent locations of the open cast mine.

If t_{zero} is determined correctly and the observation starts shortly after t_{zero} the creep curve can be described by

$$\varepsilon - \varepsilon_{ref} = C \cdot \ln \frac{t_{ref} + t}{t_{ref}} \qquad \text{with } t > 0. \tag{5.5}$$

t_{ref} can be determined by fitting a tangent to the linear section of the creep curve and determining the intersection point with the ε = 0 axis. In the presented case this leads to a reference time of t_{ref} = 6 d (cf. Figure 5.13). The creep-coefficient is the gradient of the tangent and is in this case C = 0.001. Generally, the creep-coefficient should be determined at a time $t >> t_{ref}$, because influences of a wrong determination of t_{zero} and as a consequence also of t_{ref} become smaller with increasing t. This can be shown by determining the derivative of (5.5) to

$$\dot{\varepsilon} = \frac{C}{t_{ref} + t} = \frac{C}{t\left(t_{ref}/t + 1\right)} \ . \tag{5.6}$$

For $t >> t_{ref}$ (5.6) approaches

$$\dot{\varepsilon} = \frac{C}{t} \tag{5.7}$$

or

$$C = \dot{\varepsilon} \cdot t \ , \tag{5.8}$$

which is independent of t_{ref}.

5.2.1.2 Analysis of field measurements from the Garzweiler opencast mining dump

The discussed influences regarding the evaluation procedure of data from surface settlement measurements are analyzed by the results of the settlement measurements from an area of the Garzweiler open cast mining dump, where the thickness of the dump body is nearly constant but the age of the dump and also the observation time changes. The data of 234 level gauges at the surface of the dump were evaluated for this purpose. The level gauges are positioned within a 3 km long section of the cross section in Figure 5.2 between the stations 4000 m and 7500 m with a distance of approximately 50 m between the level gauges. The results from CPTs in this area indicate a rather homogeneous loose relative density of the dump (cf. Figure 5.8). The soil type beneath the gauges is similar. The thickness of the dump lies between 132 m and 156 m (cf. Figure 5.14). The homogeneity

regarding soil type, relative density and depth of the dump makes it possible to evaluate the influence of observation time period and age of the dump.

The observation start t_{obs} of most gauges lies within the first month after the end of dumping. The end of dumping for each level gauge is known with an accuracy of a few days. The observation time of the dump reduces between station 4500 m and 7000 m from approximately 8.4 a to 1.5 a (cf. Figure 5.14).

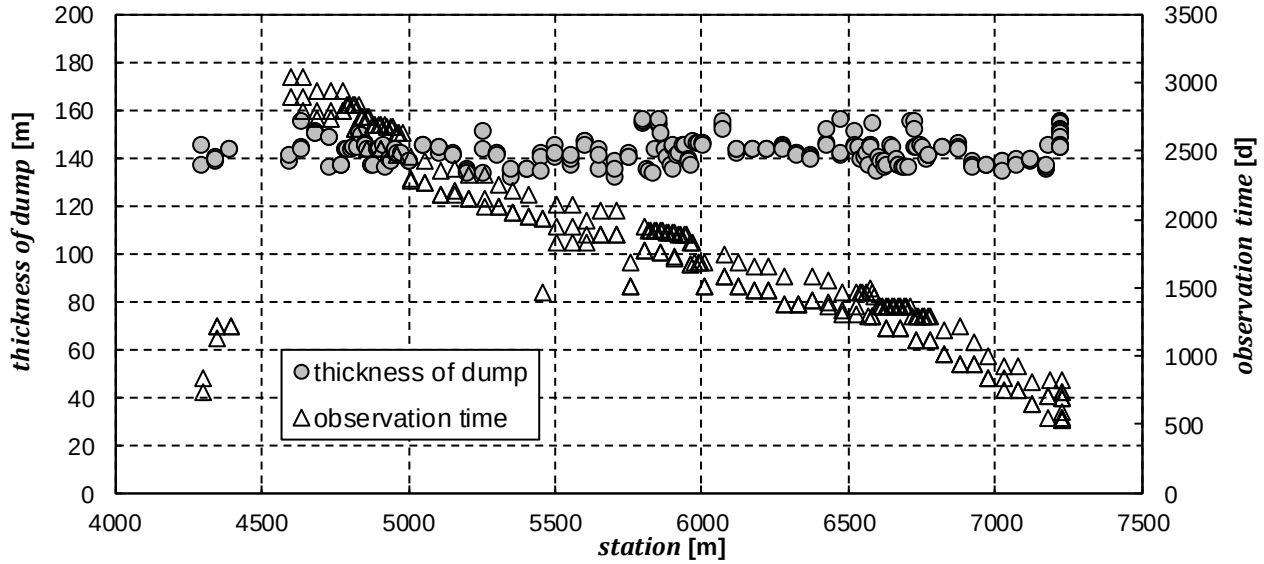

Figure 5.14: Thickness of dump and observation time at level gauge stations

Figure 5.15 (a), (c) and (e) show the strains over log-time of 77 representative level gauges. Figure 5.15 (a/b) show gauges between stations 4780 and 4960 m, Figure 5.15 (c/d) between stations 5810 and 6010 m and Figure 5.15 (e/f) between stations 6500 and 6800 m. For clarity, only 77 representative data sets out of the total of 234 level gauges are displayed. The time axis presents the elapsed time since the end of dumping of each level gauge. The maximum strain is 0.57% in 8.4 a, which corresponds to a settlement of about 82 cm. As can be seen from the diagrams, the creep-strains converge within approximately 10 to 100 d after the end of dumping towards a linear trend on the logarithmic time scale. The final gradient can be represented by a constant creep-coefficient C. A reference time t_{ref} in the sense of (5.5) can be determined for curves with approximately $t_{obs} \leq 20$ d. If $t_{obs} > 20$ d, most curves already follow a linear trend with the logarithm of time. t_{ref} ranges from 4 d to approximately 40 d. Figure 5.15 (b), (d) and (f) show the creep curves on a normalized time axis with t/t_{ref}^{*}, where $t_{ref}^{*} = t_{ref}$ for $t_{obs} \leq 20$ d and $t_{ref}^{*} = t_{obs}$ for $t_{obs} > 20$ d. The normalization causes the creep curves to lie within a relatively narrow range whose gradient can be assumed to be a constant creep-coefficient. The creep-coefficients vary from $C = 0.001$ between stations 4780 and 4960 m to $C = 0.0007$ between stations 6500 and 6800 m.

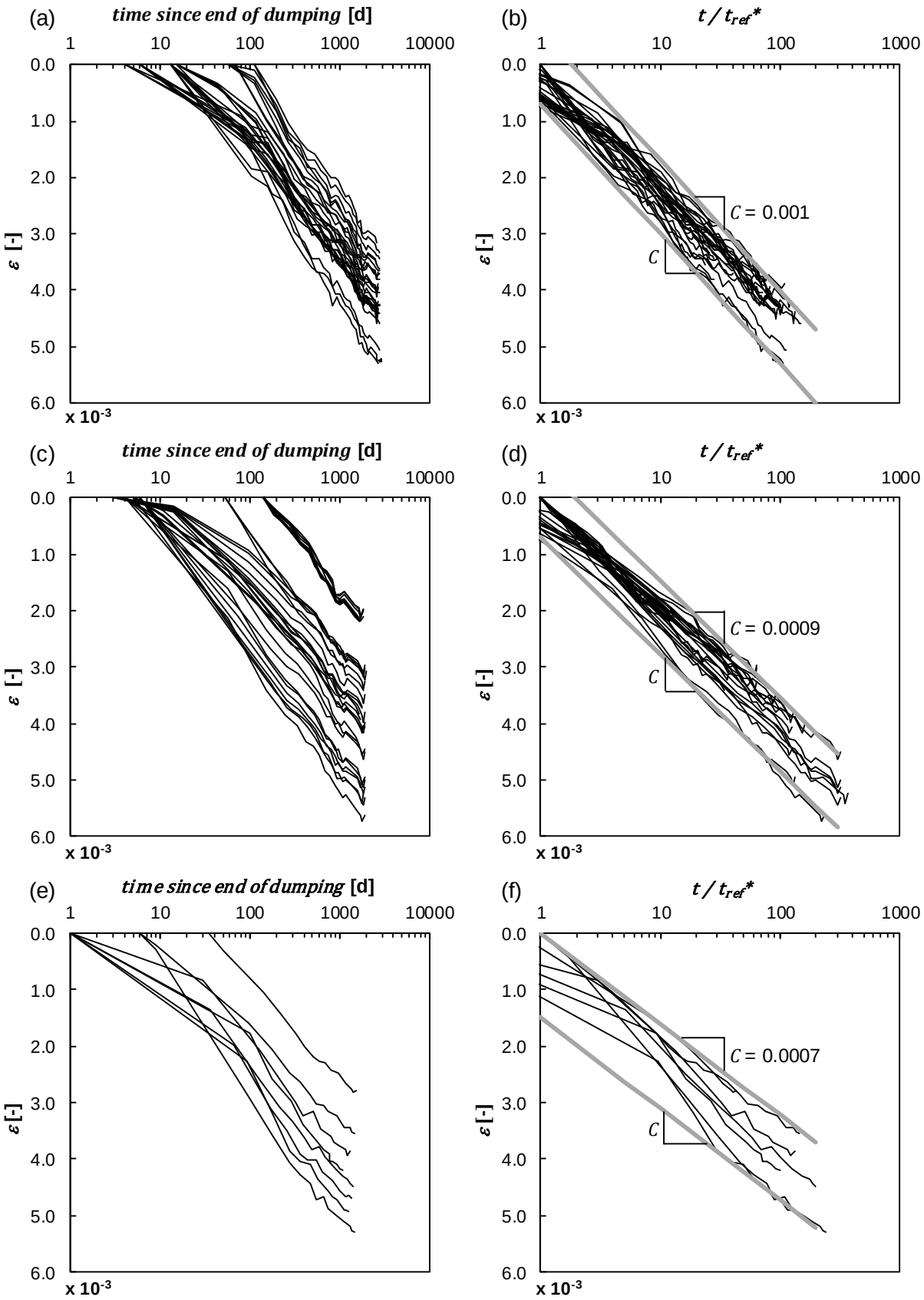

Figure 5.15: Creep strains on a logarithmic time scale of 77 out of 234 level gauges on the dump surface: (a/b) stations 4780 – 4960 m, (c/d) stations 5810 – 6010 m and (e/f) stations 6500 – 6800 m

Evaluation of the creep-coefficients at each of the 234 level gauges is presented in Figure 5.16. Between stations 4500 and 7000 m the creep-coefficients are rather similar with a slight decrease from 0.001 at 4500 m to approximately 0.0006 at station 6500 m. This confirms that influences due to different soil types, relative densities or the depth of the dump are small in this case. Noticable is the increased variance in creep-coefficients at stations > 7000 m, which can be attributed to the reduced observation time of these gauges. An analysis showing the determined creep-coefficients versus the observation time in Figure 5.17 indicates that an observation time of more than approximately 800 d is recommendable to determine representative creep-coefficients for the considered dump. The age of the dump has no significant influence on the creep-coefficients determined in the described way. Despite of the finding from Figure 5.15 showing a convergance of the creep curves towards a linear trend after 10 to 100 d, the observation time of 800 d is necessary to reduce the influence of the determination of the end of dumping and therefore zero point in time as well as fluctuations in measurements on the determined creep coefficients to a small enough level.

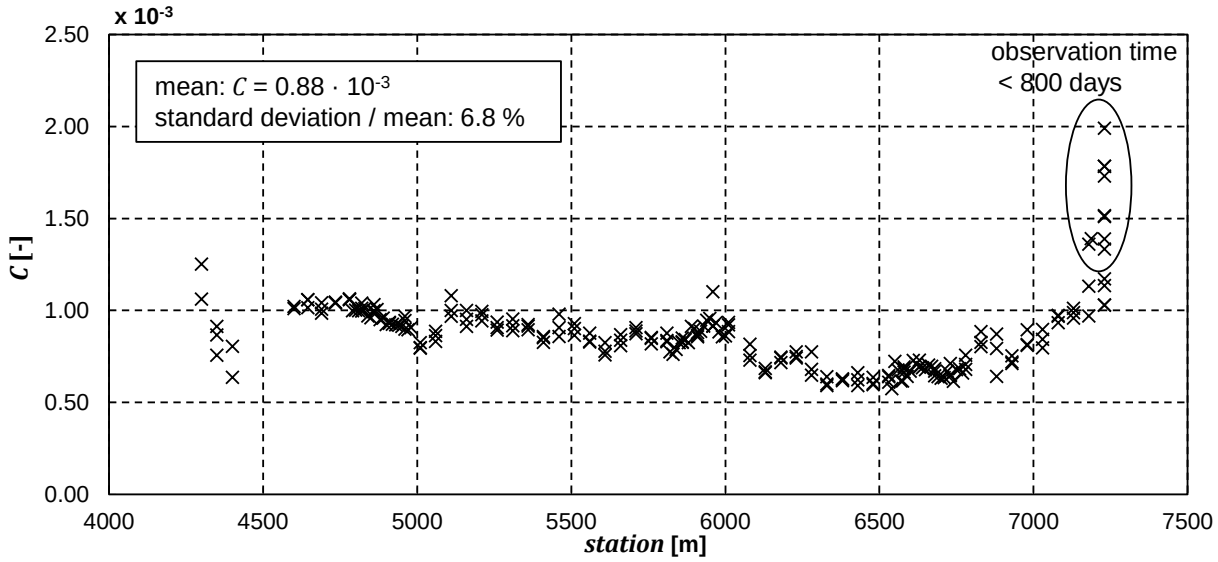

Figure 5.16: Creep-coefficients determined at each level gauge

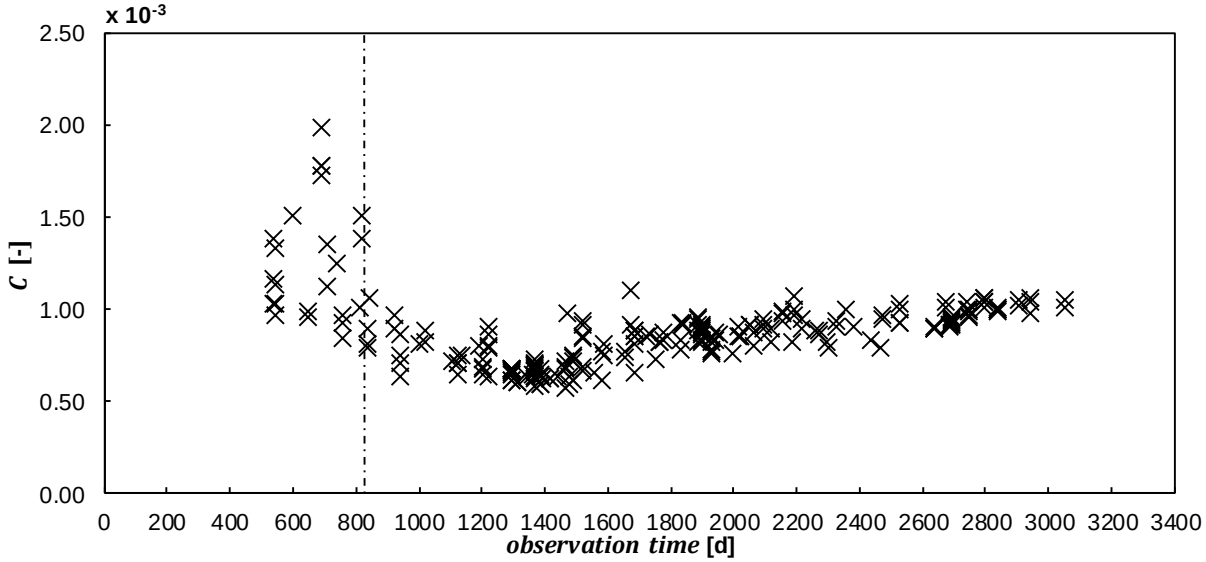

Figure 5.17: Creep-coefficient C evaluated at t > 365 d after end of dumping versus observation time

5.2.2 Long-term settlements of transmission towers on the Garzweiler open cast mining dump

This section analyzes settlement measurements at the foundations of 22 transmission towers of a 110 kV power line constructed on a part of the Garzweiler open cast mining dump with an age beween 9.5 a and more than 23 a. The data was recorded between 08/09/2005 and 12/12/2012 respectively 15/03/2015. The transmission towers stand with a distance of approximately 250 m between each other and cover a length of 5.25 km on the dump. The state of the dump under each transmission tower has not been investigated in detail. Nevertheless, since the transmission towers are located in the vicinity of the well explored part of the dump and the vast majority of the dumped overburden in Garzweiler are sands, it can be assumed that the conditions of the dumped materials are comparable with those previously described. The data are used for evaluation of the influence of the age and the thickness of the dump on the deformation characteristics. Measurements were carried out at approximately annual intervals by means of Global Positioning System (GPS) measurements in relation to a stationary reference point. The settlement of each transmission tower was measured on four measuring points on the flat foundations of the towers. The measurement results are given in Appendix A.10. In order to evaluate the measurement results, the settlement data of the four measuring points on each of the four footings of a tower were averaged and the strains were calculated by diving the measured settlements by the thickness of the dump. The age of the dump at t_{EOM} and the thickness of the dump at each tower is shown in Figure 5.18. The age of the dump was defined as the period between the end of dumping and the end of measuring t_{EOM}. For the towers 1 to 9, 21 and 22 the measurements ended on 12/12/2012 and for the towers 10 to 20 they ended on 15/03/2012. The age at t_{EOM} between the towers 1 to 6 is not known exactly, because the end of dumping was not recorded. It is however more than 23 a. Between the towers 7 to 10 the age at t_{EOM} decreases from 22 to 19 a, between the towers 11 to 20 it is approximately 12 a and at the towers 21 and 22 it is about 9.5 a. The largest thickness of the dump is 140 m between tower 14 and 19 and the smallest thickness with 60 m lies at tower 22.

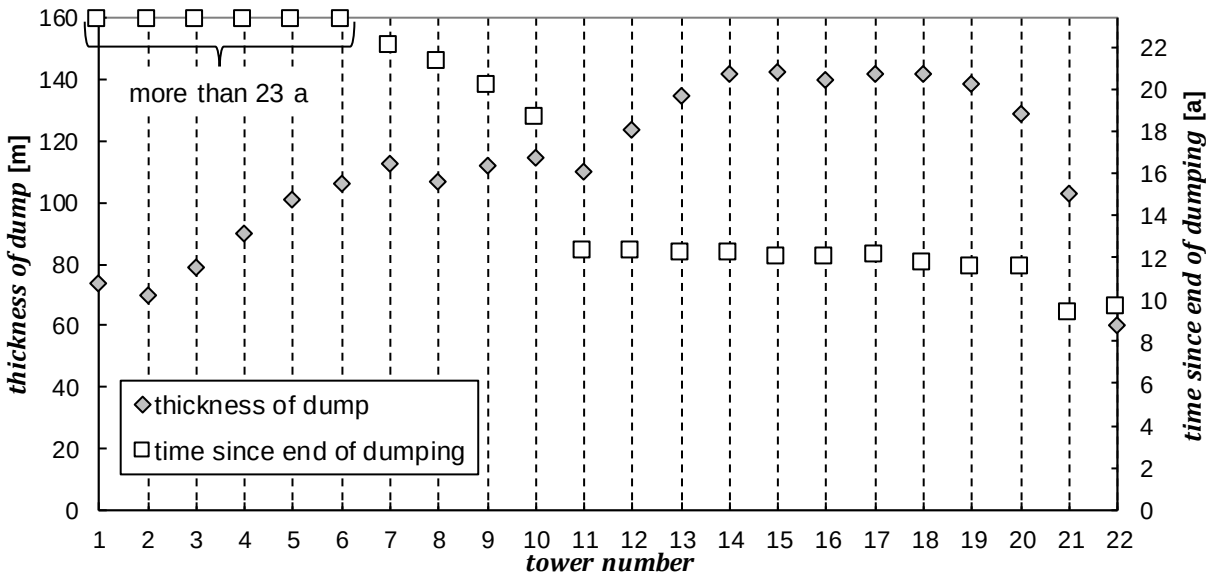

Figure 5.18: Thickness and age of the dump at the positions of the transmission towers

The time-dependent compressive strains calculated from the settlement measurements are shown for the towers 1 to 10 in Figure 5.19 and for the towers 11 to 22 in Figure 5.20. The dates of end of dumping are also given on the time axis for illustration of the time period between the end of dumping and the start of observation, which began for all towers significantly later. The towers 1 to 10 show compressive strains of maximum 0.055% between 08/09/2005 and 12/12/2012. Towers 11 to 22 show maximum strains of 0.2% in the same time interval, which demonstrates the influence of the age of the dump on the creep-strains. At towers 1 to 10 it becomes evident that although the strain rate reduces significantly, creep of the dump does not cease, at least not in a time period of up to 23 a. The variations in the measurement results of the towers 1 to 10, which show apparent uplift are related to the inaccuracy of the GPS measurements with respect to the small rate of settlement. Fluctuations in the measuring data can be traced back to time-variable measuring influences (e.g. atmospheric composition, weather conditions). This also leads to apparent accelerations of the strain rate observable in the data, which is however just a consequence of the measurement inaccuracy. The towers 20, 21 and 22 also do not show a decrease in the settlement-rate between 23/09/2008 and 12/12/2012, which cannot be explained by measurement inaccuracy, because of the much larger strain rate. According to information provided by the RWE Power AG this was probably caused by construction activities near the towers in the respective time interval. These towers are therefore excluded from the further analysis.

For evaluation of a possible influence of the age of the dump on the creep-coefficient C, the measurement data is evaluated between the start of observation t_{obs} and the end of measuring t_{EOM}. The zero point in time is the end of dumping. Figure 5.21 shows the creep deformations of towers 7 to 8 and 11 to 19 on a logarithmic time scale. The time period between the end of dumping and the start of observation varies for the towers 7 to 10 between 9.2 and 12.6 a and for the towers 11 to 19 between 2.1 and 2.8 a. The strain curves can be approximated by a logarithmically linear interpolation according to (5.5).

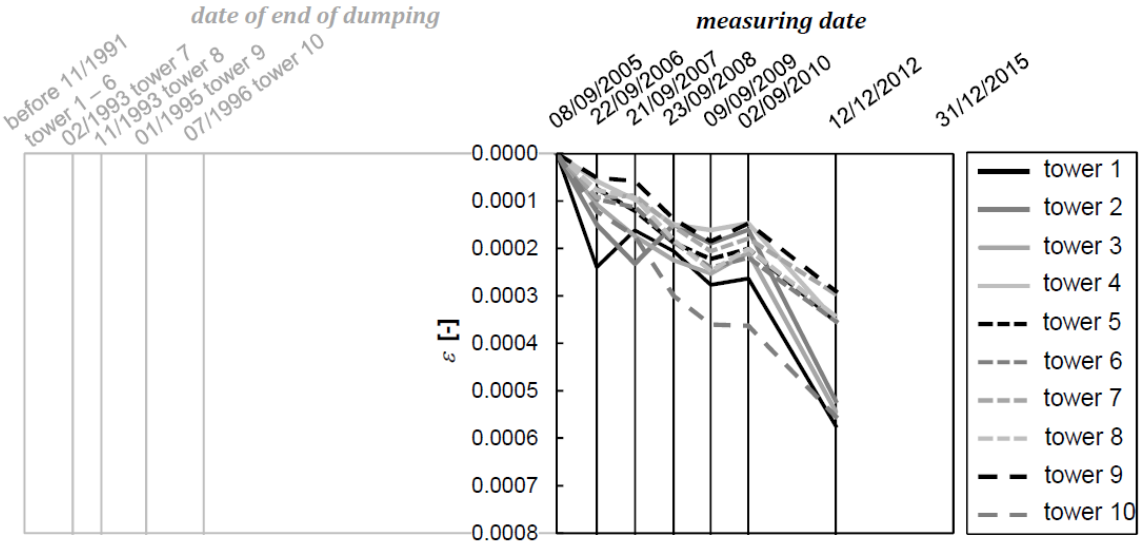

Figure 5.19: Compressive strains at the towers 1 to 10 with indication of the respective dates of end of dumping

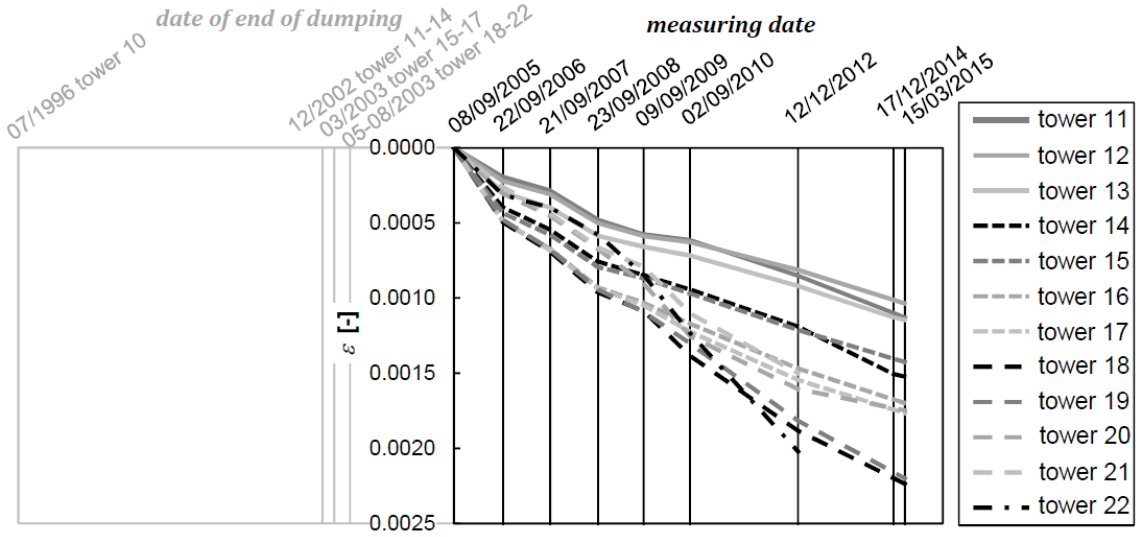

Figure 5.20: Compressive strains at the towers 11 to 22 with indication of the respective dates of end of dumping

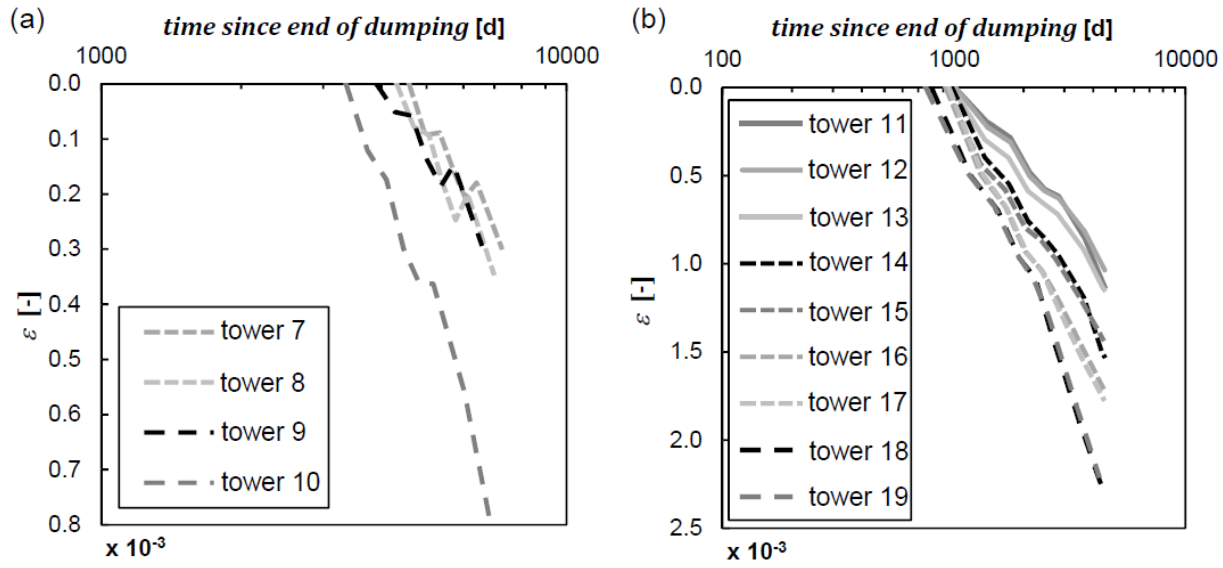

Figure 5.21: Compressive strains on a logarithmic time scale of (a) towers 7 to 10 and (b) towers 11 to 22

Figure 5.22 (a) presents the creep-coefficients as a function of the thickness of the dump and Figure 5.22 (a) presents them as a function of the age of the dump at t_{EOM}. Increasing thickness of the dump leads to an increase of overburden stress in the depth of the dump. The increase of the stress between 110 m and 145 m depth, which are the minimum and maximum depths at the towers, can be estimated to be $\Delta\sigma'$ = 546 kPa, considering a unit weight of the soil of γ = 15.6 kN/m^3 (cf. Section 5.1.3). As the results in Section 4 and results from literature (cf. Section 3.3) show, the creep-coefficient increases with increasing stress. Despite of the scattering of the results, this trend is confirmed by Figure 5.22 (a), which shows an increase between $\Delta C = 2.2 \cdot 10^{-4}$ and $\Delta C = 6.6 \cdot 10^{-4}$ of the creep-coefficient with increasing dump thickness. Comparing this increase to the results of laboratory tests

for the same stress increment (cf. Sections 4.6 and 4.7.1), the change of the creep-coefficient lies in the same range, i.e. $\Delta C = 1.2 \cdot 10^{-4}$ for sand MS and $\Delta C = 2.0 \cdot 10^{-4}$ for sand SU.
As expected, the age of the dump does not appear to have an influence on the creep-coefficient (cf. Figure 5.22 (b)). This was also shown for a younger part of the dump in Section 5.2.1.

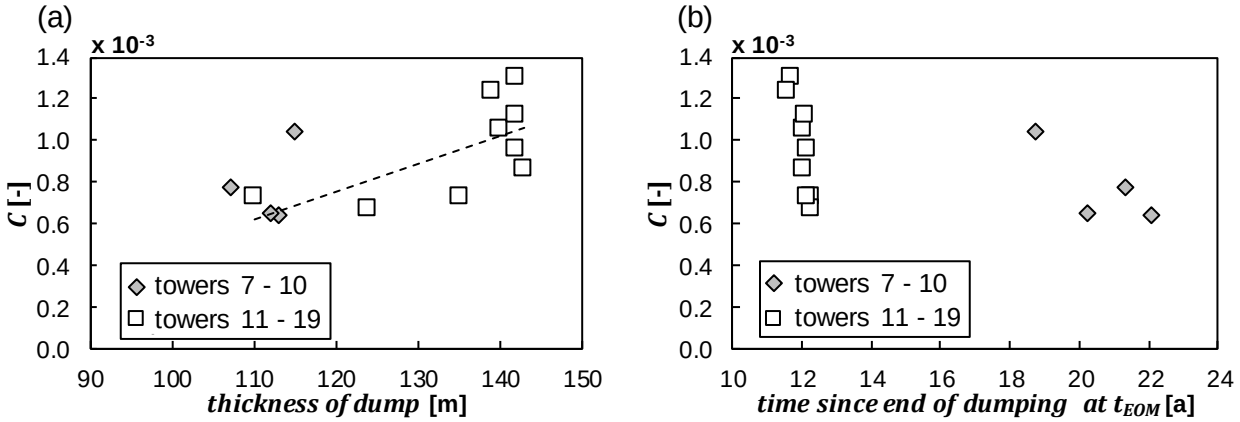

Figure 5.22: (a) Creep-coefficient over thickness of the dump and (b) creep-coefficient over the age of the dump at t_{EOM}

5.2.3 Settlement gauge V2 at open cast mine Zukunft West

5.2.3.1 Measuring system and boundary conditions

For a better understanding of the evolution of settlements in open cast mines, a settlement gauge called V2, which measured the deformations in different depths of the dump was installed by the RWE Power AG in the open cast mine Zukunft West in the Renish lignite mining area. Its purpose was to understand the evolution of instantaneous and creep settlements at different depths of the dump. The gauge reaches a maximum depth of 77 m below the dump surface. The lowest level gauge V2.1 rests on the unscathed ground, which allows an evaluation of the compressive strains of the dumped material independent of the deformation of the natural soil. The data from the settlement gauge V2 was already mentioned in Section 5.2.1 in the context of the evaluation of the creep behaviour of open cast mining dumps.

Installation of the level gauges ran in parallel to the dumping process in the years 1990 and 1991. Each vertical 5 m a measuring level was installed. The level gauges were connected by a plastic pipe, which was prolongated as the dump surface rose and thereby ensured access to the measuring levels. The pictures in Figure 5.23 show the installation process of the settlement gauge V2. The measuring system used in the settlement gauge comprised a metal plate at each level that transferred the deformation of the soil to a measuring sensor which was guided by the plastic pipe and determined the change of the distance between the metal plates. The relative measurements were related to the head of the settlement gauge at the surface of the dump during the dumping process. These relative measurements were referenced to a stationary reference point, which was not affected by the dumping. Measurement accuracy of the sensor that monitored the change of displacement of the measuring levels in good conditions, i.e. no disturbance of the sensor for instance by magnetic fields,

is +/- 2.0 mm according to information of the manufacturer. Measurement accuracy of the system of the settlement gauge V2 was however estimated to be +/- 1.0 cm.

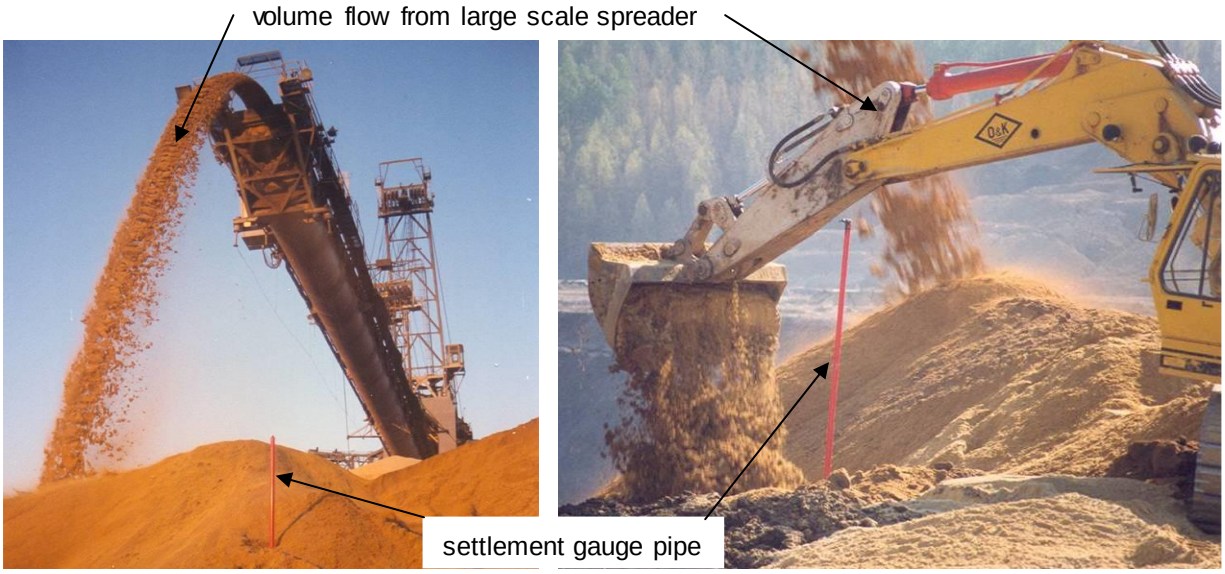

Figure 5.23: Pictures from the installation process of the settlement gauge V2, printed with permission from RWE Power AG

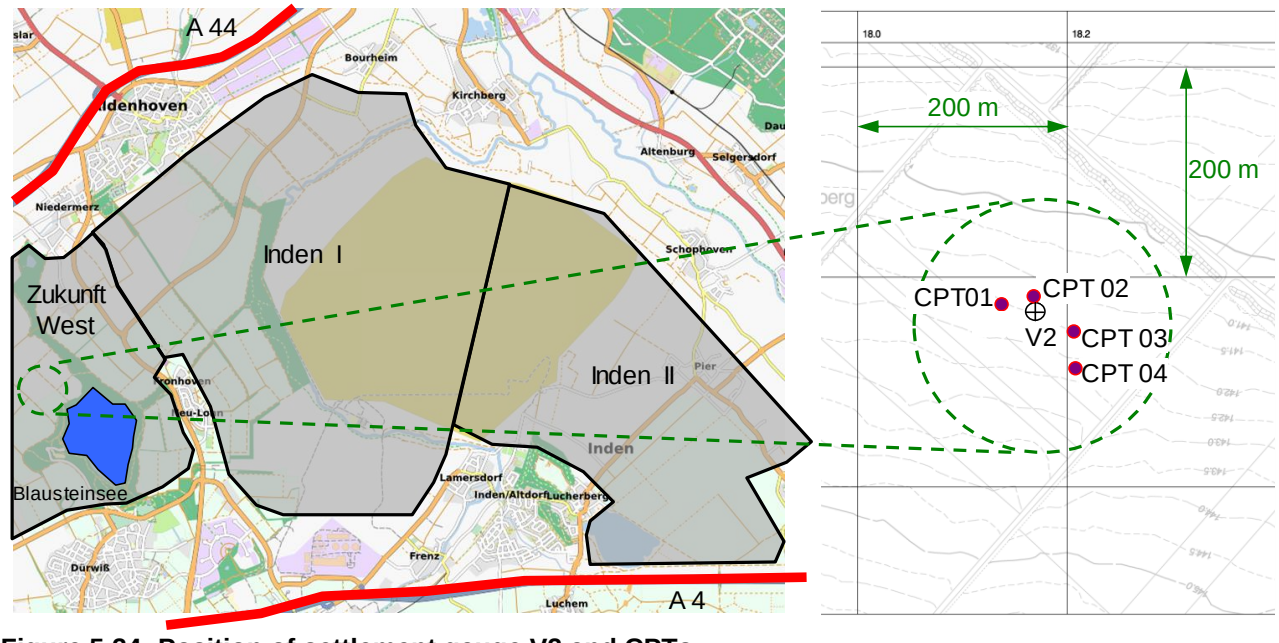

Figure 5.24: Position of settlement gauge V2 and CPTs

No samples were retrieved during dumping and no exploration drillings were performed in the area of the settlement gauge V2. The only information about the ground conditions is provided by four CPTs within a radius of 50 m around the gauge (cf. Figure 5.24). The deepest CPT reached a depth of 70 m and is almost as deep as the bottom of the settlement gauge with 77 m. The CPTs were interpreted with respect to the relative density and the soil type. The soil type was determined by the SBT method of ROBERTSON (2010) (cf. Section 5.1.2). The input parameters for the CPT evaluation with the software CPET-IT version 1.7.6.42 are summarized in Table A.8.1 in Appendix A.8.1.

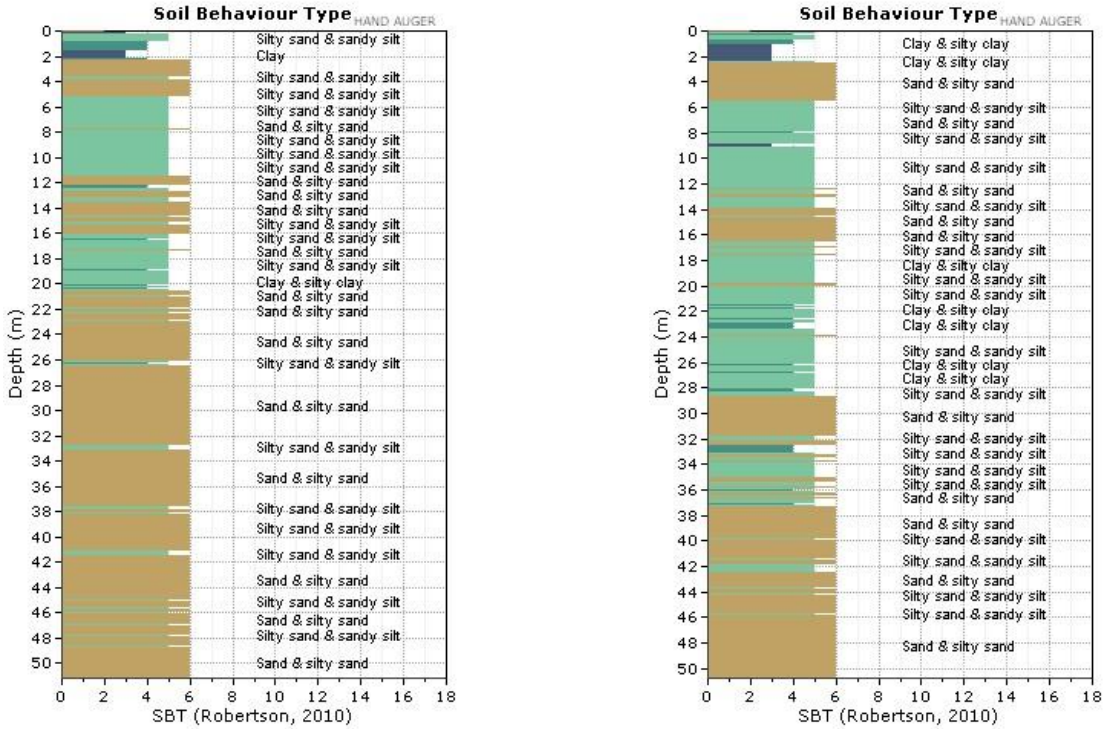

Figure 5.25: SBT determination at settlement gauge V2 (CPT 1, left and CPT 2, right)

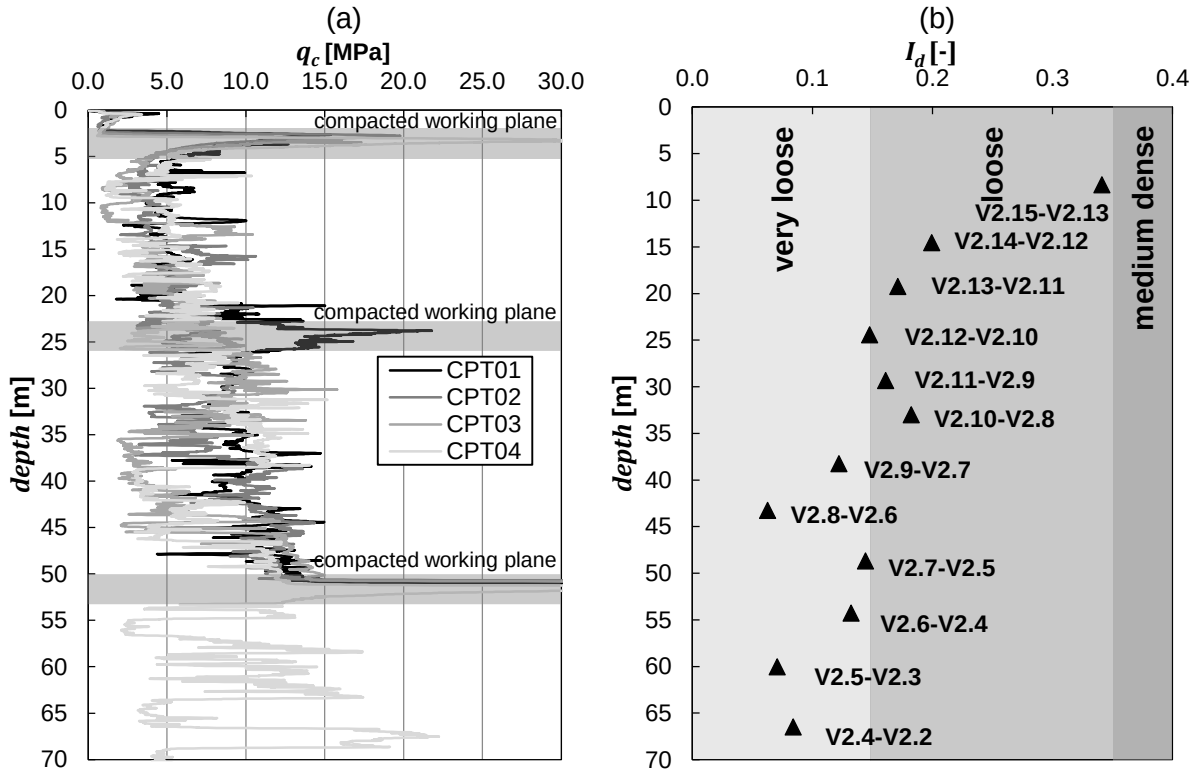

Figure 5.26: (a) Cone penetration tip resistance q_c and (b) evaluated relative densities averaged between every second level gauge determined with method proposed by CUDMANI (2001)

The results for CPT 1 and 2, which are closest to settlement gauge V2 (cf. Figure 5.24), are presented in Figure 5.25. CPT 1 classifies mostly sandy silt at the top and clean sand to silty sand in the deeper part of the dump. CPT 2 shows comparably more silty sand and partly clay and silty clay.

Like in Section 5.1.3, the relative densities were determined by the method proposed by CUDMANI (2001), assuming a homogenous soil type, which is justified by the SBT results, and the same parameter set like in Section 5.1.3 (cf. Appendix A.9). For a better overview the relative densities calculated from the tip resistance of the CPTs presented in Figure 5.27 (a) were averaged over all CPTs and between every second level gauge (cf. Figure 5.27 (b)). The evaluation shows that the relative density decreases with the depth from approximately I_d = 0.3 to I_d = 0.1.

Figure 5.27 shows the installation process of the settlement gauge V2 between March 1990 and August 1991. Dumping took place in six steps on 15/03/1990, 09/04/1990, 10-16/10/1990, 11-15/03/1991, 08/05/1991 and 05/08/1991. The main part of the dump was deposited in three layers in April and October 1990 and March 1991. These main three layers had a thickness of 21.5 m (layer 1), 24.5 m (layer 2) and 30.0 m (layer 3). Measurements were taken over a period of 18 a between 15/03/1990 and 10/09/2008 in different time intervals. During the dumping process, measurements were carried out daily and after dumping finished the intervals were increased first to monthly and then gradually to yearly intervals. The last dumping layer was deposited on 05/08/1991. After that, undisturbed creep deformations of the dump were measured until approximately January 1998. Afterwards, the deformation data is probably influenced by the rising ground water table. The rising of the groundwater table is presented at different dates in Figure 5.27. It reached the height of the level gauge V2.1 in December 1995 and rose up to level gauge V2.7 in October 2008. The instantaneous settlements measured during the dumping of the upper two main layers were already evaluated in Section 5.2.1 (cf. Figure 5.11). The evaluation presented here focuses on the creep settlements of the dump.

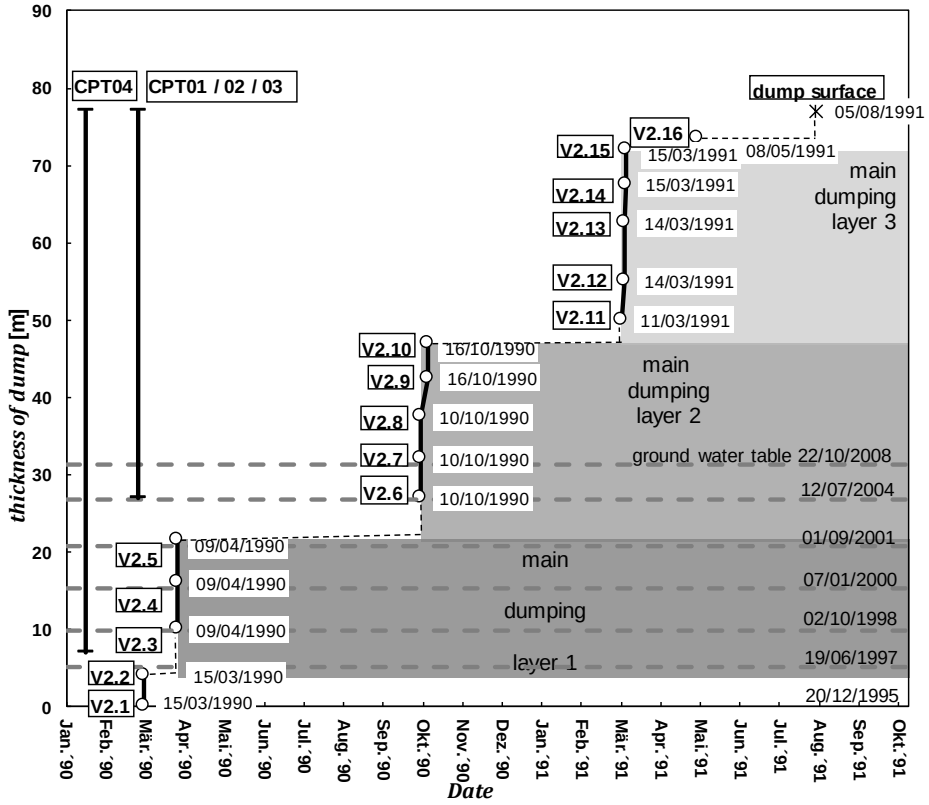

Figure 5.27: Dumping at position of settlement gauge V2 over time with positions of each measuring level and depth of the CPTs as well as the development of the ground water table

5.2.3.2 Evaluation of measured settlements

Figure 5.29 shows the measured settlements at the different level gauges on a logarithmic time scale. The displayed data are corrected by the settlements measured at level gauge V2.1, caused by the deformations of the unscathed naturally deposited ground beneath it. As can be observed in Figure 5.28, the naturally deposited soil shows significant instantaneous settlements of about 50 cm due to dumping of the soil. However, the time-dependent settlements after dumping of the last layer are too small to be detected by the settlement gauge.

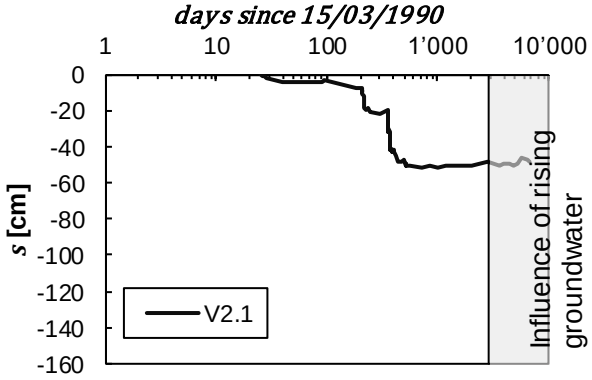

Figure 5.28: Settlements of level gauge V2.1 from 09/04/1990

The settlements are presented for each main dumping layer in a separate diagram in Figure 5.29. The data recorded after January 1998 is marked by a grey shading to indicate the influence of the rising ground water table. The measuring data shows an apparently simultanous heave in all levels after January 1998. After that, the settlement rates reduce to a value not detectable with the applied measuring system. The instantaneous settlements resulting from the dumping of the three main layers are clearly recognizable. The level gauges in the main dumping layer 3 are influenced by the three comparably thin layers that were dumped between 08/04/1991 and 05/08/1991. These layers together had a thickness of only 5.0 m. The influence of the three layers can be seen in the initially high gradient of the settlement curves (cf. Figure 5.29 (c)). Only after the dumping ceased on 05/08/1991, the settlements follow a trend according to a constant creep-coefficient C as defined by (5.5).

For evaluation of the influence of the vertical effective stress on the creep strains at different depths of the dump, the strains were calculated between every second level gauge over a vertical distance of approximately 10 m. The distance between every second level gauge was chosen to compensate the rather low accuracy of the applied measuring system of +/- 1.0 cm. The strains were evaluated after dumping of the third main layer finished on 15/03/1991. The results are presented separately for each main dumping layer in Figure 5.30. Layer 1 and layer 2 show no clear effect of the dumping of the smaller layers on 08/04/1991, 08/05/1991 and 05/08/1991, whereas the influence on layer 3 is visible, especially between the top level gauges V2.13 and V2.15.

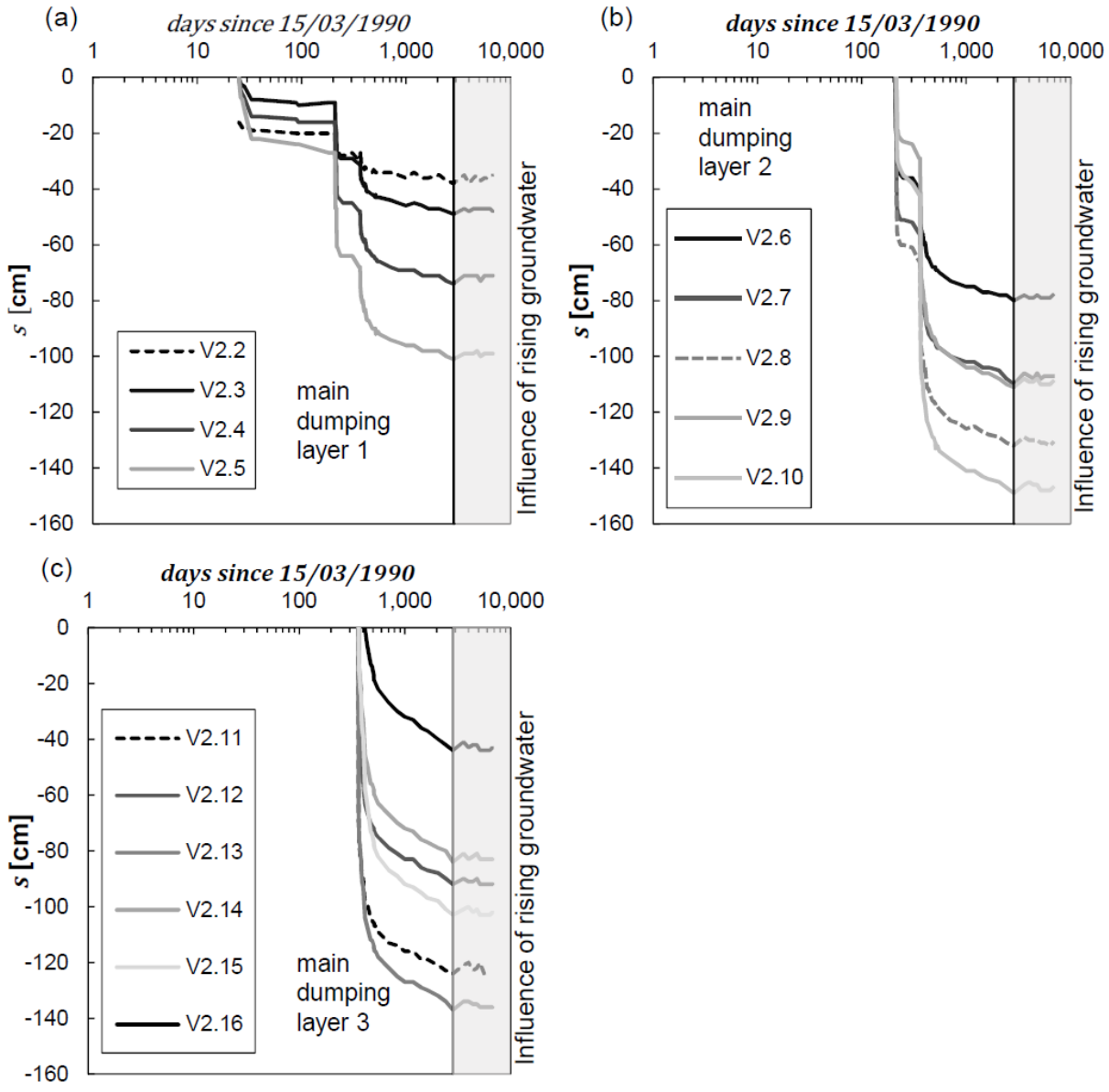

Figure 5.29: (a) Settlements of gauges V2.2 to V2.4 (dumping layer 1), (b) settlements of gauges V2.5 to V2.10 (dumping layer 2) and settlements of gauges V2.11 to V2.15 (dumping layer 3), $s = s$(V2.x) – s(V2.1)

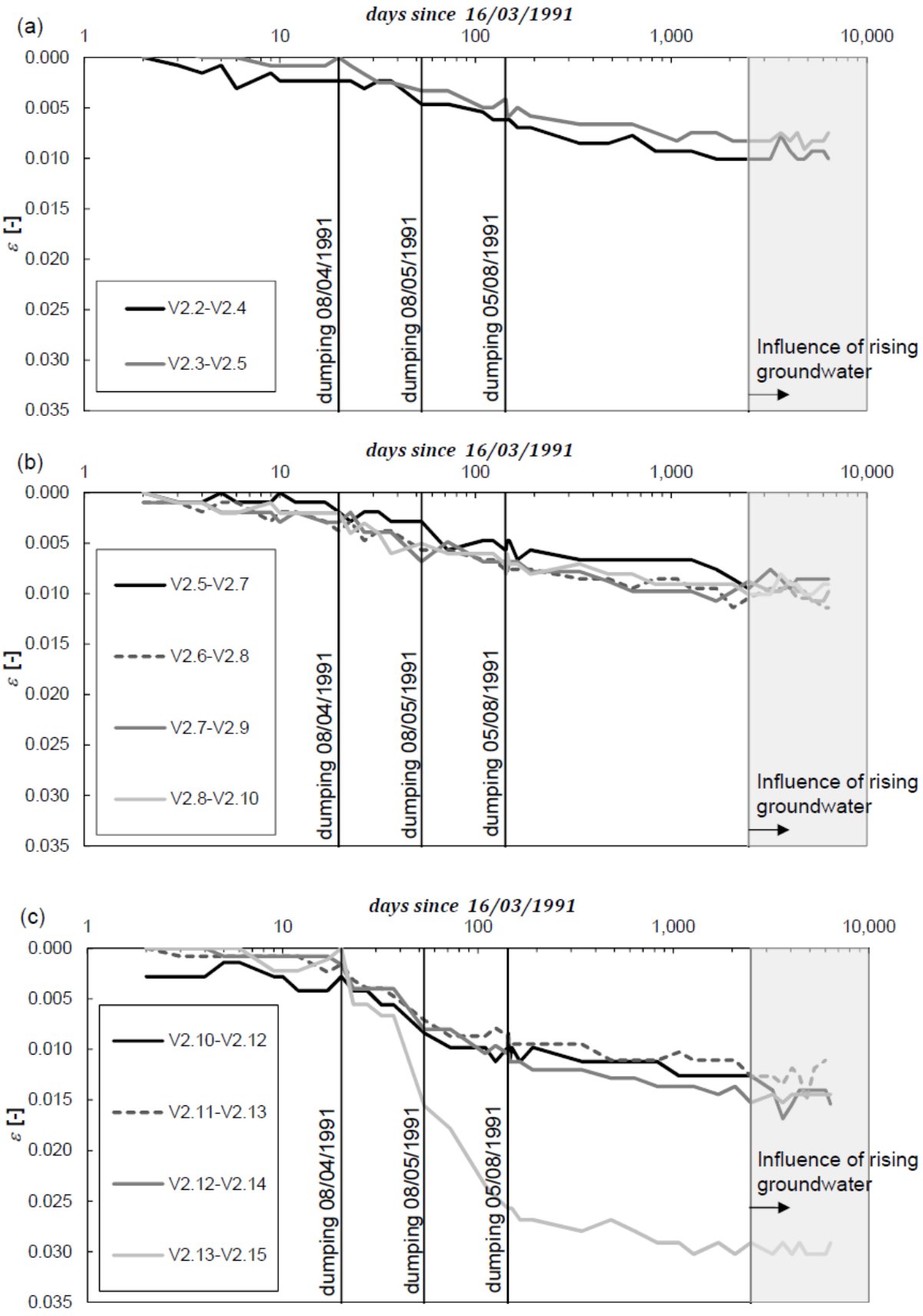

Figure 5.30: (a) Strains between every second level gauge of (a) main dumping layer 1, (b) main dumping layer 2 and (c) main dumping layer 3 from bottom to top of the dump

For a more detailed analysis the creep-coefficients according to (5.5) are evaluated from the data in Figure 5.30. The zero point in time for evaluation of creep is in this case not a unique value for the entire dump, because the layers 1 and 2 did not show a significant settlement due to the dumping of the last three thinner layers. Therefore, their state was not reset to a normal-consolidated state and the zero point in time for layer 1 and 2 must be the end date of dumping of layer 3, which was the 15/03/1991. The creep-coefficients of layers 1 and 2 were evaluated from 10 d after 15/03/1991. Contrary, layer 3 shows instantaneous settlements due to the dumping of the thin top layers and its zero point in time is therefore the end of all dumping activity on 05/08/1991. The creep-coefficients of layers 3 and 2 were evaluated from 49 d after 05/08/1991 to guarantee the convergence towards a linear trend of the strain-curves in $\log$-time (cf. Figure 5.29 (c)). All data was evaluated until January 1998, when the rising groundwater apparantly started to influence the deformation behaviour. Figure 5.31 presents the evaluated creep-coefficients C with respect to the depth of the evaluated level gauges. Also indicated are the main dumping layers. The creep-coefficients C show an increasing trend with rising depth, which is equivalent to a rising overburden stress σ_v (cf. Figure 5.31 (b)). The increase in the creep-coefficient in this case is mainly due to the vertical effective stress increase ($\Delta\sigma \approx 1000$ kPa), since the relative density change with depth is comparatively small (cf. Figure 5.26 (b)). This result confirms the findings of the oedometer tests in Section 4, showing that the creep of granular soils depends on the stress level.

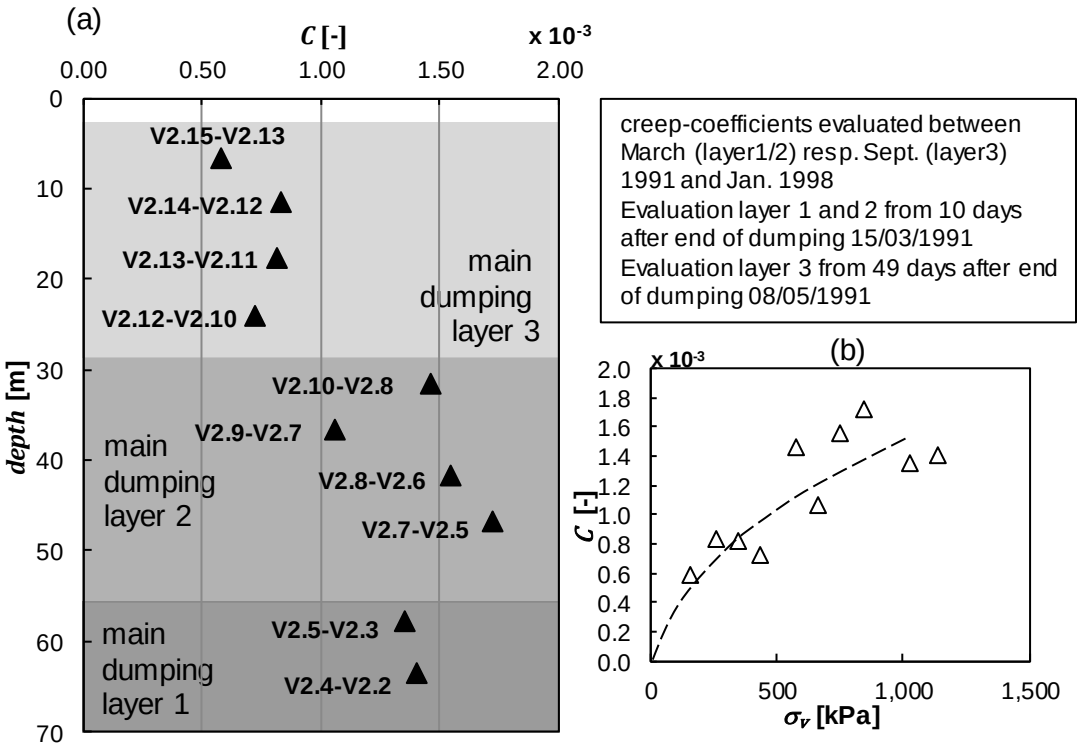

Figure 5.31: (a) Creep-coefficient as a function of the depth evaluated between every second level gauge and (b) as a function of the resulting overburden stress

5.2.3.3 Application of the empirical concept for creep-coefficient evaluation

Having shown that the soil in the dump at settlement gauge V2 shows similar creep behaviour like the samples tested in oedometer tests presented in Section 4, the empirical concept for the creep-coefficient determination introduced in Section 4.6.3 shall be tested. Settlement gauge V2 is well suited for this purpose, because the stress state at the gauge resembles an oedometric stress state. As no data from oedometer tests conducted on samples of the dump at settlement gauge V2 are available, the data of the soil from Garzweiler open cast mine (cf. Section 4), which is geologically very similar, are used. The samples cover a range of representative soils found in the Garzweiler dump.

The parameter sets needed for the empirical concept are presented for the sands MS, SU and FS in Table 5.2. The empirical concept in Section 4.6.3 is based on C_α, which is referenced to the void ratio and $\log_{10}$ (cf. Equation (3.36)). Since the void ratio in the dump is not known, creep of the dump was evaluated using C, which is based on the strain and $\ln$. For determination of the reference creep-coefficient $C_{ref,0}$ at the minimum void ratio e_{min} and reference pressure p'_{ref}, the value $C_{\alpha,ref,0}$ given in Section 4.6.3 is converted to $C_{ref,0}$. The following approach is valid for small strains and applies here:

$$C_{ref,0} = \frac{C_{\alpha,ref,0}}{(1+e_{min}) \cdot ln10}. \tag{5.9}$$

The minimum void ratio e_{min} was determined at nearly zero effective pressure. The change of e_{min} with the mean stress increase from zero to p'_{ref} = 300 kPa is not taken into account here, but this does not have significant influence on the calculated $C_{ref,0}$.

Table 5.2: Parameters for determination of the creep-coefficient C by the empirical approach presented in Section 4.6.3

	θ	ω	$C_{ref,0}$	p'_{ref} [kPa]
MS	0.07	0.0012	0.00016	300
SU	0.30	0.0009	0.00015	300
FS	0.25	0.0010	0.00012	300

To estimate the influence of the vertical stress σ_v on the creep-coefficient, the unit weight γ of the dumped soil has to be known. For this purpose the relative void ratio r_e of the dump at the settlement gauge V2 is assessed using the data from the CPTs presented in Figure 5.26. The relative void ratio can be directly calculated from the results using (3.15). The critical state ($e_c = e_{max}$) and densest state ($e_d = e_{min}$) void ratios used in (3.15) as well as the density of the solid particles ρ_s were taken from sand MS (cf. Table 4.1). The results are presented in Figure 5.32 (a) showing that the relative void ratio r_e does not change significantly along the settlement gauge V2. The unit weight γ is calculated via

$$\gamma = (1+w)\frac{\rho_s}{1+e} \cdot g \tag{5.10}$$

with ρ_s the density of the solid particles, w the water content and g the gravity. The in situ water content of the investigated soils in the Garzweiler dump varies between w = 10.2 and 6.0% and the

density of the solid particles between ρ_s = 2.604 and 2.630 g/cm³. According to this data, the unit weight changes from a minimum of γ = 14.7 kN/m³ to a maximum of 16.4 kN/m³. For the further analysis the mean value of γ = 15.6 kN/m³ along settlement gauge V2 is considered.

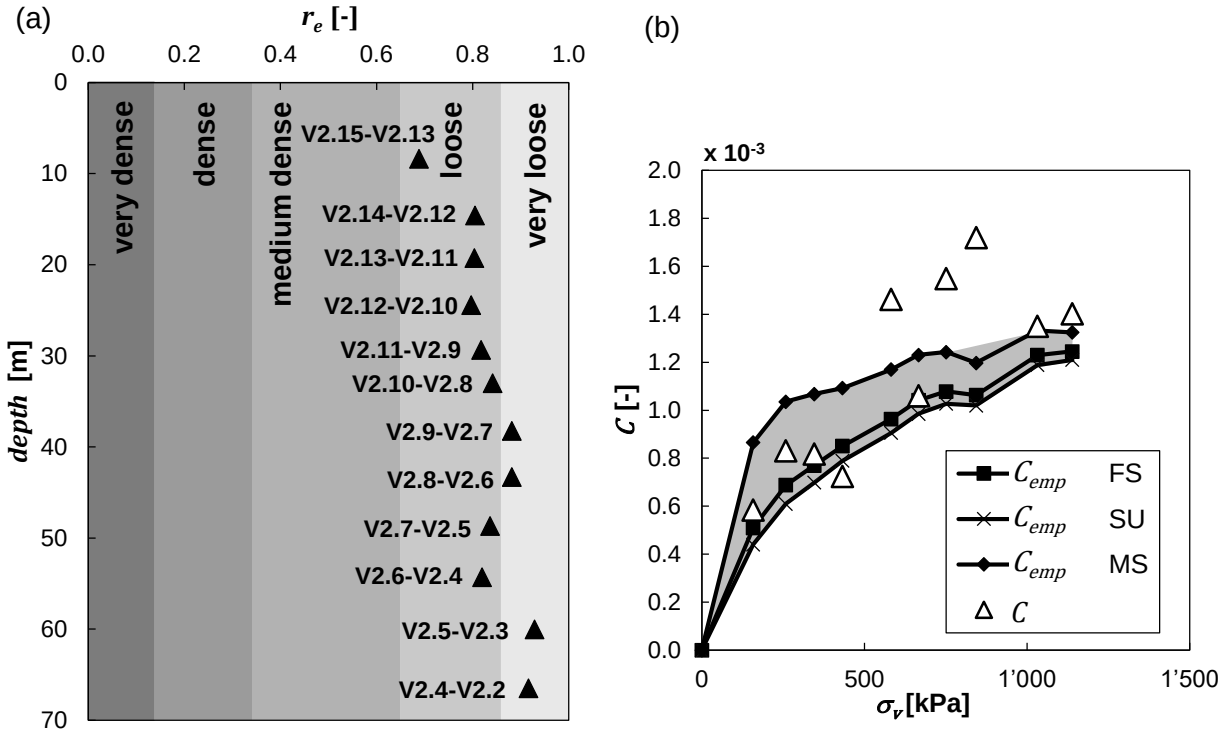

Figure 5.32: (a) Relative void ratio between every second level gauge as a function of the depth and (b) comparison between the stress-dependent creep-coefficient C determined from measurement data of settlement gauge V2 and the creep-coefficient C_{emp} determined according to the empirical concept presented in Section 4.6.3

Figure 5.32 (b) presents the creep-coefficients C_{emp} calculated with the empirical concept (grey shaded area) together with the creep-coefficients C (triangles) evaluated from the field measurement data as a function of the vertical overburden stress σ_v in the dump. σ_v was calculated using the determined unit weight of the soil. C_{emp} were determined using the parameters from Table 5.2 in combination with the relative density in the field determined from CPT tests. Considering the fact that the type of soil at the position of the settlement gauge is not exactly known and therefore the parameters could only be estimated, the empirical approach covers the range of measured creep-coefficients very well. The creep-coefficients of the dump can be estimated by determining the relative density of the soil in the field, e.g. by CPT, and the parameters for the empirical approach from oedometer tests without the need of long-term deformation measurements on the dump surface.

5.2.4 Comparison between creep behaviour in the field and in the laboratory

The purpose of laboratory tests is to depict the state of the soil and its behaviour in the field as realistic as possible and to provide input parameters for the prediction of soil behaviour. In case of the open cast mining dumps, this is necessary, if for instance field measurements are not available and the long-term deformation behaviour has to be predicted based on the test results from the laboratory.

This section compares the evaluation of field measurements from open cast mining dumps presented in Sections 5.2.1 and 5.2.2 with the results of oedometer tests presented in Section 4 with soils representative of those encountered in the open cast mining dump Garzweiler. The results on time-dependent creep behaviour are compared on the basis of the evaluated creep-coefficients.
Figure 5.33 presents the span of results from field measurements and laboratory tests over the range of investigated stresses and densities. The overburden stress in the field was estimated from the densities derived from CPT measurements. As shown in Figure 5.33, the creep-coefficients C determined in the laboratory are in average more than 50% smaller than the coefficients determined from field measurements. Even at the maximum vertical stresses applied in the standard oedometer tests of 7500 kPa, the coefficients from the laboratory are still in average smaller than the ones observed in the field.

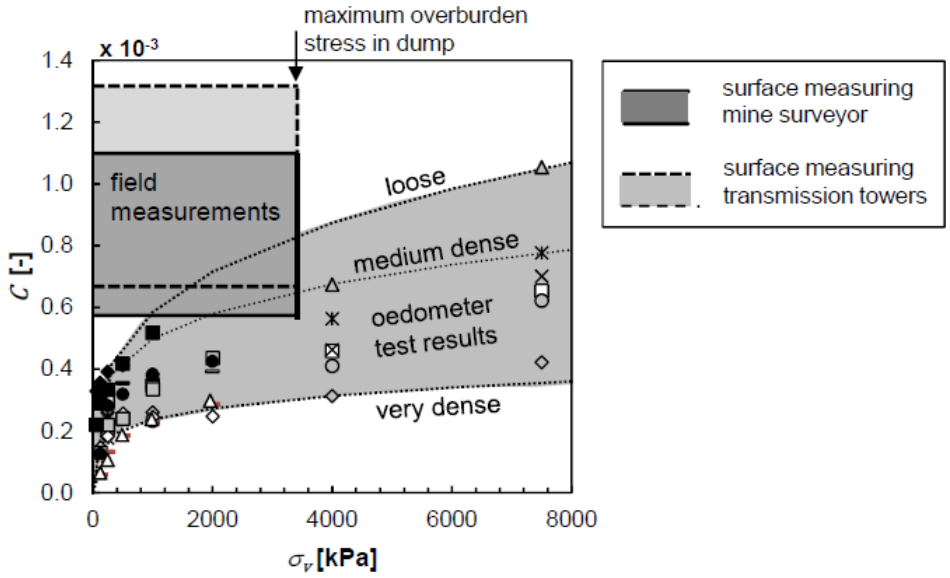

Figure 5.33: Creep-coefficients C from representative oedometer test results of the sands MS, FS, SU and SU* from the open cast mine Garzweiler as a function of the investigated vertical stresses as well as measuring results from the mining dump: surface measuring by mine surveyors (cf. Section 5.2.1), surface measuring on transmission towers (cf. Section 5.2.2)

The deviations between field measurements and laboratory results can be caused by several factors, most importantly the different density and structure of the soils in situ compared to the samples in the laboratory, as will be explained in the following. In addition, the oedometer test shows limitations that were already addressed in Section 4.1.1. In particular, the friction between the soil sample and the steel ring of the oedometer device has a reducing influence on the measured creep strain.
As CPT measurements showed, the relative densities in the field are in average very loose to loose (cf. Sections 5.1.3 and 5.2.3). Such low densities could not be reproduced in the laboratory by the chosen preparation technique (cf. Section 4.4) and are one reason for the larger creep in the field. Furthermore, the structure of the soil, which results from the dumping process of partially saturated sands by large scale spreaders, also contributes to the comparably high creep deformations of the dumps. The dumping process of partially saturated sands can create a soil structure with macropores due to the effect of suction. The macropores are of the size of several diameters of the mean grain size as indicated by Figure 5.34. A time-dependent collapse of macropores could explain, besides

the generally lower density, the larger creep rate observed in the field. The collapse can be induced by changes of the water content, changes of the vertical stress from seapage forces of infiltrating water, changes of temperature, changes of the athmospheric pressure and micro-seismic events.

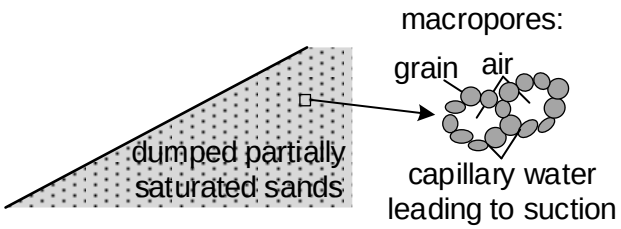

Figure 5.34: Formation of air-filled macropores in dumped sands

The macroporic soil structure of open cast mining dumps was disclosed by PRALLE (2002) by means of analyses of undisturbed sand samples extracted beneath the ground water table with the freezing technique in an open cast mining dump in Lusatia, Brandenburg (Germany). The mining and dumping techniques and also the geology are different compared to the Renish lignite mining area. Nevertheless, the dumped soils are also mainly poorly graded medium to fine sands with low fine content. The dumped soils were deposited in a partially saturated state and flooded as the ground water table rose after shut down of the well points. This most certainly led to collapse of some macropores. But even beneath the phreatic level, the samples showed a large number of air-filled and water-filled macropores with diameters of up to $40 \cdot d_{50}$. It can therefore be assumed that the macroporous structure in the investigated Garzweiler dump is similar or even more pronounced, since the phreatic level lies still beneath the bottom of the dump.

It was tried in this study to reproduce the macroporic soil structure in the laboratory by the moist tamping method, but the test results showed fluctuating results in terms of stress-dependent and time-dependent compression and no clear trends could be identified nor were the creep rates significantly higher than in the samples prepared by funnel deposition. This was most probably caused by the more inhomogeneous density of the samples compared to the samples prepared by funnel deposition, which was also recognized by JANG & FROST (1998). It was therefore not possible to quantify the contribution of macropores on the difference between creep in the field and in the laboratory, but it is highly likely that they contribute to the difference to some extent.

Ultimately, the difference between the laboratory test results and the measurements in the field cannot be attributed to a single reason but are caused by a combination of shortcomings of the oedometer tests, more specifically the boundary effects caused by the oedometer test device and insufficient sample preparation to reflect field conditions. However, the results from Section 5.2.3 showed that the creep-coefficients of the soil in the field can be determined using the empirical concept for creep-coefficient determination presented in Section 4.6.3 (cf. Figure 5.32). This indicates that the parameters of the empirical concept are not significantly influenced by the insufficiencies of the oedometer test, the difference in structure between the laboratory samples and the soil in the field or the higher densities of the laboratory samples. Therefore, the creep-coefficients in the field can be predicted with the help of the empirical concept by using the relative density in the field as input parameter. This also shows that the deviating structure between the laboratory samples and the soil in situ must have a small influence compared to the deviating relative density.

5.2.4.1 Application of the empirical concept for creep-coefficient evaluation

The above conclusion is additionally verified by comparison of the creep-coefficients C_{emp} determined with the empirical concept and the creep-coefficients determined from field measurements on the Garzweiler dump (cf. Sections 5.2.1 and 5.2.2). C_{emp} were determined using the input parameters for the empirical concept determined in the laboratory for the sands FS, MS and SU (cf. Table 5.2) and the relative void ratios determined from CPT results from the Garzweiler dump (cf. Section 5.1.3). The creep-coefficients C_{emp} determined by the empirical concept and the ranges of creep-coefficients C determined from field measurements are presented in Figure 5.35. The axis of the vertical stress σ_v covers the range of maximum stresses at the deepest points in the Garzweiler dump. The creep-coefficients C_{emp} were determined with an average relative void ratio of r_e = 0.8 (loose). They cover the range of creep-coefficients C determined from field measurements very well.
This confirms the result from Section 5.2.3 that the empirical concept for the pressure and density dependent determination of the creep-coefficient can be used as a tool to estimate the creep-coefficients of open cast mining dumps using laboratory tests, if the relative density in the field is known. It also confirms that the different relative densities in laboratory tests and in the field are the most important reason for the deviations in the creep behaviour.

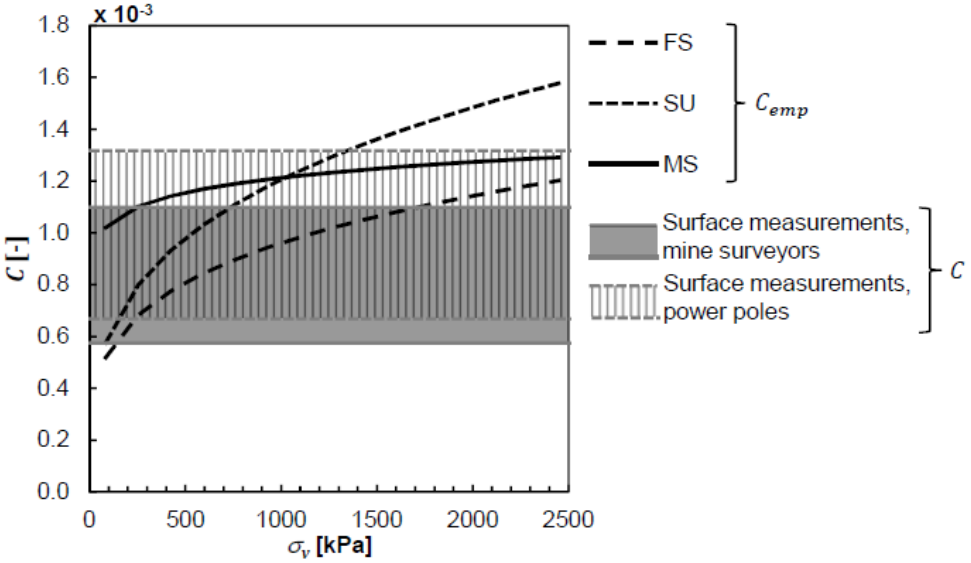

Figure 5.35: Comparison between ranges of creep-coefficients C from field measurements and creep-coefficients C_{emp} determined with the empirical concept presented in Section 4.6.3 based on the relative void ratios r_e from the field and the concept parameters determined with oedometric laboratory tests

5.3 Conclusions

The conclusions from Section 5 are summarized in the following:

– The soils in the considered part of the Garzweiler open cast mining dump are rather homogenous in terms of GSD, soil type and relative density. Field measurement data collected over a large area of the dump can therefore be analyzed as resulting from the same dump material.

– The application of the SBT-method proposed by ROBERTSON (2010) led to a realistic soil classification of the dumped materials based on the results of CPT.

– The evolution of dump settlements over time reach a linear trend using a logarithmic time scale at about 10 to 100 d after the end of deposition. In the measurements this linear trend holds over the considered measuring periods of as long as 10 a on dumps with an age of more than 23 a.

– The entire dump can be considered as normally consolidated at the end of dumping, if the thickness of the last dumping causes a large enough stress change and settlement to reset overconsolidation created by previous creep. In case of the considered Garzweiler dump the layer thickness should exceed about 15 m.

– The determination of the end of dumping and therefore zero point in time as well as fluctuations in measurements have influence on the determination of creep-coefficients for small observation times. In case of the Garzweiler dump, an observation time of more than 800 d is recommendable to reduce these influences.

– The creep-coefficients determined from field measurements in the open cast mining dump Zukunft West increase with the depth, i.e. with the overburden stress, confirming qualitatively the results from laboratory tests.

– Creep-coefficients determined from laboratory tests are about 50% smaller than the ones derived from field measurements.

– The creep-coefficients in the field can be estimated from laboratory tests when using the empirical concept for the creep-coefficient determination (cf. Section 4.6.3) together with information about the in situ relative density of the soil from CPTs and the overburden stress.

6 Modelling of time-dependent behaviour

So far, constitutive models describing the time-dependent behaviour of soil focus on soft fine grained soils. In this section, three models are analyzed on an element test basis to investigate their suitability for the simulation of the viscous behaviour of granular soils described in Section 4. The comparison is limited to oedometric compression paths.

The subsequently presented models after VERMEER & NEHER (1999) and NIEMUNIS (2002) are based on the isotache-concept developed by ŠUKLJE (1957) and others (cf. Section 3.3.2) and an overstress approach (PERZYNA, 1963), using a transient yield surface. The model after GUDEHUS (2004) relies on the BAUER compression law and does not follow a classical isotache-concept. Furthermore, all three models distinguish between virgin- respectively un- and reloading and apply the definition of $OCR = p'_e/p'$ using the mean stress p' and an equivalent stress p'_e (or p'^{eq}), which is calculated by means of a reference compression line (RCL).

First, the three models are introduced by the modelling of element compression tests. The model after GUDEHUS (2004) is analyzed in more detail especially with respect to its time-dependent behaviour introducing a modification of the model, enabling the modelling of compression tests on sand at normally consolidated states with $e_{ini} < e_i$. Afterwards, oedometric laboratory compression tests (cf. Section 4) with creep, relaxation and sudden changes of the loading strain rate are modelled.

Finally, the time-dependent settlements of an open cast mining dump (cf. Section 5) are modelled with the finite-element method and the Soft Soil Creep model by VERMEER & NEHER (1999) and NEHER (2008). The suitability and limitations of this model, developed for soft fine-grained soils, in simulating the creep behaviour of the open cast mining dump are discusssed.

6.1 Soft Soil Creep model after VERMEER & NEHER (1999)

The elasto-viscoplastic Soft Soil Creep (SSC) model by VERMEER & NEHER (1999) is an extension of the Modified Cam Clay Model by ROSCOE & BURLAND (1968) to account for the time-dependent behaviour. A detailed description of the model can be found in NEHER (2008).

The most important assumptions and relationships are presented here again. The strain[4] is first split into an elastic, a plastic and a viscous part similar to (3.38), for isotropic compression

$$\varepsilon = \varepsilon^e + \varepsilon^{pl} + \varepsilon^{vis} = \kappa^* \cdot \ln\frac{p'}{p'_0} + (\lambda^* - \kappa^*) \cdot \ln\frac{p'_{ee}}{p'_{e0}} + \mu^* \cdot \ln\frac{\tau_p + t'}{\tau_p} \quad (t' > 0)\,, \tag{6.1}$$

where, at strains below approx. 15% (cf. Figure 3.15), κ^* relates to C_s via $\kappa^* = 2C_s/(1+e)/\ln(10)$, λ^* relates to C_c via $\lambda^* = C_c/(1+e)/\ln(10)$, $\mu^* = C$ is the creep-coefficient, τ_p is the time at the end of primary consolidation, p'_0 is the initial stress and p'_{ee} is an equivalent stress on the reference

[4] $\varepsilon = \varepsilon_v$ in Section 6.1.

isochrone $\tau_{ref} = \tau_p$ corresponding to the end of primary consolidation (cf. Figure 6.1(a)). By introducing an equivalent stress p'_e, which evolves with the viscous strains, the plastic and the viscous strains can be combined and (6.1) takes the form (cf. Figure 6.1(b))

$$\varepsilon = \varepsilon^e + \varepsilon^{vis} = \kappa^* \cdot \ln\frac{p'}{p'_0} + (\lambda^* - \kappa^*) \cdot \ln\frac{p'_e}{p'_{e0}} \qquad \text{with} \quad p'_e = p'_{e0} \cdot \exp\left(\frac{\varepsilon^{vis}}{\lambda^* - \kappa^*}\right). \tag{6.2}$$

By equating (6.1) and (6.2), the viscous strains can be expressed as

$$\mu^* \cdot \ln\frac{\tau_p + t'}{\tau_p} = (\lambda^* - \kappa^*) \cdot \ln\frac{p'_e}{p'_{ee}} \qquad \text{or} \quad \left(\frac{\tau_p + t'}{\tau_p}\right)^{\mu^*} = \left(\frac{p'_e}{p'_{ee}}\right)^{(\lambda^* - \kappa^*)} . \tag{6.3}$$

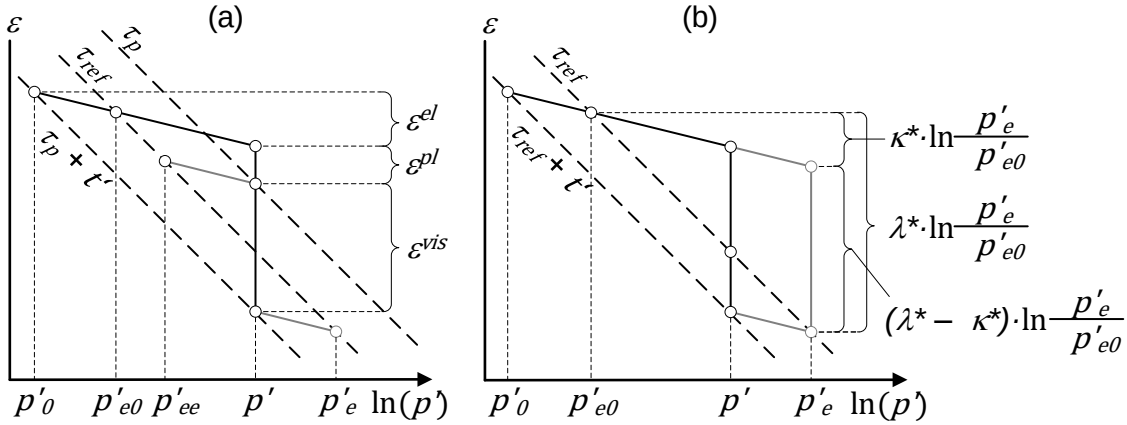

Figure 6.1: Graphical representation of (a) (6.1) and (b) (6.2) as basis of the SSC model

Inserting $\dot{\varepsilon}^{vis} = \mu^*/(\tau_p + t')$ into (6.3) gives

$$\dot{\varepsilon}^{vis} = \frac{\mu^*}{\tau_p} \cdot \left(\frac{p'_{ee}}{p'_e}\right)^{\frac{\lambda^* - \kappa^*}{\mu^*}} . \tag{6.4}$$

On the reference isochrone τ_{ref} applies $\tau_p + t' = \tau_{ref}$ and $p'_e = p'$. It follows from (6.3)

$$\left(\frac{\tau_{ref}}{\tau_p}\right)^{\mu^*} = \left(\frac{p'}{p'_{ee}}\right)^{(\lambda^* - \kappa^*)} . \tag{6.5}$$

Inserting (6.5) into (6.4) gives

$$\dot{\varepsilon}^{vis} = \frac{\mu^*}{\tau_{ref}} \cdot \left(\frac{p'}{p'_e}\right)^{\frac{\lambda^* - \kappa^*}{\mu^*}} \qquad \text{with } p'_e \text{ from (6.2) where} \quad \varepsilon^{vis} = \int \dot{\varepsilon}^{vis} dt \tag{6.6}$$

and the viscosity factor

$$f_{v,SSC} = \left(\frac{p'}{p'_e}\right)^{\frac{\lambda^* - \kappa^*}{\mu^*}} . \tag{6.7}$$

The ratio p'/p'_e corresponds to $1/OCR$. For deviatoric stress states p' and p'_e must be replaced by equivalent stresses, which project the deviatoric stress state onto the isotropic stress axis point. This is done by means of the Modified Cam Clay yield surface with

$$p'^{eq} = \frac{q^2}{M^2(p' + c' \cdot cot\varphi')} + p' + c' \cdot cot\varphi' \qquad \text{and} \tag{6.8}$$

$$p'^{eq}_e = p'^{eq}_{e0} \cdot \exp\left(\frac{\varepsilon_v^{vis}}{\lambda^* - \kappa^*}\right) \qquad \text{with} \quad \varepsilon_v^{vis} = \int \dot{\varepsilon}_v^{vis} dt\,. \tag{6.9}$$

Furthermore, the SSC model applies a MOHR-COULOMB limit condition with a non-associated flow rule. At the yield-cap an associated flow rule is applied as by $g = p'^{eq}$. The entire constitutive differential equation then reads

$$\dot{\boldsymbol{\varepsilon}} = \dot{\boldsymbol{\varepsilon}}^e + \dot{\boldsymbol{\varepsilon}}^{vis} = \mathbf{E^{-1}}\dot{\boldsymbol{\sigma}}' + \frac{1}{\alpha}\frac{\mu^*}{\tau_{ref}} \cdot \left(\frac{p'^{eq}}{p'^{eq}_e}\right)^{\frac{\lambda^* - \kappa^*}{\mu^*}} \frac{\partial p'^{eq}}{\partial \boldsymbol{\sigma}'} \tag{6.10}$$

with p'^{eq}_e and p'^{eq} from (6.9) respectively (6.8),

$$\boldsymbol{E} = \frac{1}{E_{ur}}\begin{bmatrix} 1 & -\nu_{ur} & -\nu_{ur} \\ -\nu_{ur} & 1 & -\nu_{ur} \\ -\nu_{ur} & -\nu_{ur} & 1 \end{bmatrix} \quad \text{and} \tag{6.11}$$

$$\alpha = \frac{\partial p'^{eq}}{\partial \sigma_1'} + \frac{\partial p'^{eq}}{\partial \sigma_2'} + \frac{\partial p'^{eq}}{\partial \sigma_3'}\,. \tag{6.12}$$

E_{ur} and ν_{ur} are the stiffness and the POISSON's ratio in un- and reloading respectively with

$$E_{ur} = 3(1 - 2\nu_{ur})\frac{p'}{\kappa^*}\,. \tag{6.13}$$

6.2 Visco-hypoplastic models

6.2.1 Introduction to Hypoplasticity

The hypoplastic model proposed by VON WOLFFERSDORFF (1996) is the basis for the viscous models by NIEMUNIS (2002) and GUDEHUS (2004). Hypoplastic models are based on the assumption of simple grain skeletons, which consist of permanent grains (no grain crushing). The granular skeleton is istropic and physicochemical effects as well as influences of cementation and structural anisotropy are neglected. Therefore, the material state can be described by its density and stress state only. Hypoplasticity belongs to the group of incrementally non-linear models. The main difference to the widely used elastoplastic models, like SSC, is that the soil response is modelled by one tensorial function, with no explicit distinction between elastic and plastic strain rates and no explicit formulations of a yield criterion, flow rule or plastic potential function. The general form of the hypoplastic constitutive equation reads

$$\dot{\boldsymbol{T}} = f_b f_e \left(\underbrace{\boldsymbol{L}:\boldsymbol{D}}_{\substack{\text{hypoelastic} \\ \text{response}}} + \underbrace{f_d \boldsymbol{N} \|\boldsymbol{D}\|}_{\substack{\text{"switch between} \\ \text{hypoelastic and hypoplastic} \\ \text{response"}}} \right), \tag{6.14}$$

in which

$$\boldsymbol{L} = \frac{1}{tr\left(\hat{\boldsymbol{T}} \cdot \hat{\boldsymbol{T}}\right)} \left(F^2 \boldsymbol{I} + a^2 \hat{\boldsymbol{T}} \hat{\boldsymbol{T}}\right) \qquad \text{(“linear stiffness tensor”),} \tag{6.15}$$

where $\boldsymbol{I}$ is the unit tensor, $\hat{\boldsymbol{T}} = \boldsymbol{T}/tr(\boldsymbol{T})$ (normalized stress tensor), $\hat{\boldsymbol{T}}^* = \hat{\boldsymbol{T}} - 1/3\boldsymbol{I}$ (deviator tensor),

$$a = \frac{\sqrt{3}(3 - sin\varphi_c)}{2\sqrt{2} sin\varphi_c} \qquad \text{(incorporating the MATSUOKA-NAKAI limit condition) and} \tag{6.16}$$

$$F = \sqrt{\frac{1}{8} tan^2\psi + \frac{2 - tan^2\psi}{2 + \sqrt{2} tan\psi \cdot cos3\vartheta}} - \frac{1}{2\sqrt{2}} tan\psi \tag{6.17}$$

with $tan\psi = \sqrt{3}\left\|\hat{\boldsymbol{T}}^*\right\|$ and $cos3\vartheta = -\sqrt{6}\frac{tr\left(\hat{\boldsymbol{T}}^* \cdot \hat{\boldsymbol{T}}^* \cdot \hat{\boldsymbol{T}}^*\right)}{\left[tr\left(\hat{\boldsymbol{T}}^* \cdot \hat{\boldsymbol{T}}^*\right)\right]^{3/2}}$.

Furthermore,

$$\boldsymbol{N} = \frac{a \cdot F}{tr\left(\hat{\boldsymbol{T}} \cdot \hat{\boldsymbol{T}}\right)} \left(\hat{\boldsymbol{T}} + \hat{\boldsymbol{T}}^*\right) \qquad \text{(“non-linear stiffness tensor”),} \tag{6.18}$$

$\boldsymbol{D}$ is the strain rate tensor and $\|\boldsymbol{D}\|$ is its EUCLIDIAN norm, which functions as a switch between loading and unloading states.

$$f_b = \frac{h_s}{n} \left(\frac{1 + e_i}{e_i}\right) \left(\frac{e_{i0}}{e_{c0}}\right)^{\beta} \left(\frac{tr\boldsymbol{T}}{h_s}\right)^{1-n} \left[3 + a^2 - a\sqrt{3} \left(\frac{e_{i0} - e_{d0}}{e_{c0} - e_{d0}}\right)^{\alpha}\right]^{-1} \tag{6.19}$$

is a factor incorporating the dependency of the soil response on the stress level (barotropy factor) and

$$f_e = \left(\frac{e_c}{e}\right)^{\beta} \tag{6.20}$$

as well as

$$f_d = \left(\frac{e - e_d}{e_c - e_d}\right)^{\alpha} \tag{6.21}$$

are factors for the dependency of the response on the void ratio (pycnotropy factor) where h_s is the granular hardness, n is the exponent of the compression law, φ_c is the critical state friction angle, e_{c0} is the critical state void ratio at zero stress, e_{d0} is the void ratio at maximum density and zero stress, e_{i0} is the void ratio at minimum density and zero stress and α as well as β are density dependency factors (pycnotropy). These are the eight necessary model parameters for the general Hypoplasticity.

HERLE (1997) gives a detailed description of the procedure to calibrate the parameters. The limiting void ratios are connected by the compression law for virgin loading presented by BAUER (1996) (cf. Equation (3.26)) and define the space of void ratios, which are permissible in Hypoplasticity via

$$\frac{e_i}{e_{i0}} = \frac{e_c}{e_{c0}} = \frac{e_d}{e_{d0}} = 1/\exp\left[\left(\frac{tr\boldsymbol{T}}{h_s}\right)^n\right] = 1/\exp\left[\left(\frac{3p'}{h_s}\right)^n\right]. \tag{6.22}$$

The tensorial function of Hypoplasticity can be simplified for oedometric conditions. The stress and stretching rate tensor take the form

$$\boldsymbol{T} = \begin{pmatrix} T_{11} & & \\ & K_0 T_{11} & \\ & & K_0 T_{11} \end{pmatrix} \tag{6.23}$$

where $K_0 = T_{33}/T_{11}$ and

$$\boldsymbol{D} = D_{11}\boldsymbol{I}\,. \tag{6.24}$$

According to HÜGEL (1995) the tensors $\hat{\boldsymbol{T}}$ and $\hat{\boldsymbol{T}}^*$ simplify to

$$\hat{\boldsymbol{T}} = \begin{pmatrix} \frac{1}{1+2K_0} & & \\ & \frac{K_0}{1+2K_0} & \\ & & \frac{K_0}{1+2K_0} \end{pmatrix} \tag{6.25}$$

and

$$\hat{\boldsymbol{T}}^* = \begin{pmatrix} \frac{2(1-K_0)}{3(1+2K_0)} & & \\ & \frac{K_0-1}{3(1+2K_0)} & \\ & & \frac{K_0-1}{3(1+2K_0)} \end{pmatrix}. \tag{6.26}$$

It follows

$$L_{11} = \frac{(1+2K_0)^2}{1+2{K_0}^2}\left[1 + a^2\frac{1}{(1+2K_0)^2}\right], \tag{6.27}$$

$$L_{21} = \frac{(1+2K_0)^2}{1+2{K_0}^2}\cdot a^2\frac{K_0}{(1+2K_0)^2}, \tag{6.28}$$

$$N_{11} = \frac{(1+2K_0)^2}{1+2{K_0}^2}\cdot\frac{a}{3}\cdot\frac{5-2K_0}{1+2K_0} \qquad \text{and} \tag{6.29}$$

$$N_{22} = \frac{(1+2K_0)^2}{1+2{K_0}^2}\cdot\frac{a}{3}\cdot\frac{4K_0-1}{1+2K_0}. \tag{6.30}$$

The constitutive differential equation (6.14) can be rewritten to

$$\dot{T}_{11} = f_b f_e \frac{(1+2K_0)^2}{1+2K_0{}^2}\left[D_{11} + a^2 \frac{D_{11}}{(1+2K_0)^2} + f_d \frac{a}{3} \cdot \frac{5-2K_0}{1+2K_0} D_{11}\right] \tag{6.31}$$

and

$$\dot{T}_{22} = f_b f_e \frac{(1+2K_0)^2}{1+2K_0{}^2}\left[a^2 \frac{K_0 D_{11}}{(1+2K_0)^2} + f_d \frac{a}{3} \cdot \frac{4K_0-1}{1+2K_0} D_{11}\right] \tag{6.32}$$

and it follows that the earth pressure coefficient at rest is a function of the density and the critical state friction angle according to

$$K_0 = \frac{T_{33}}{T_{11}} = \frac{f_d a}{3 + f_d a}\,. \tag{6.33}$$

6.2.2 Visco-hypoplastic model after NIEMUNIS (2002)

NIEMUNIS (2002) used the framework of VON WOLFFERSDORFF Hypoplasticity (cf. Section 6.2) and modified it for the modelling of soft soil behaviour, which is characterized by low critical state friction angles. For these soils the VON WOLFFERSDORFF model predicts a too low shear stiffness (HERLE & KOLYMBAS, 2004). NIEMUNIS splits strains and strain rates in elastic and viscoplastic parts, meaning all irreversible strains are viscous,

$$\boldsymbol{D} = \boldsymbol{D}^e + \boldsymbol{D}^{vis}\,. \tag{6.34}$$

He uses the logarithmic strain measure from (3.22), which differs at large deformations from the engineering strains, and the double-logarithmic compression law proposed by BUTTERFIELD (1979) from (3.23) (cf. Section 3.2).
To modify (6.14) according to (6.34), the density dependency factors f_d and f_e are set to unity and the non-linear term $-\boldsymbol{L}^{-1}\!:\boldsymbol{N}\|\boldsymbol{D}\|$ is replaced by the viscous strain rate $\boldsymbol{D}^{vis}$ leading to

$$\dot{\boldsymbol{T}} = f_b \boldsymbol{L}\!:\left(\boldsymbol{D} - \boldsymbol{D}^{vis}\right). \tag{6.35}$$

$\boldsymbol{L}$ from (6.15) is simplified by removing $1/tr\left(\widehat{\boldsymbol{T}} \cdot \widehat{\boldsymbol{T}}\right)$ to

$$\boldsymbol{L} = F^2 \boldsymbol{I} + a^2 \widehat{\boldsymbol{T}}\widehat{\boldsymbol{T}}\,. \tag{6.36}$$

According to NIEMUNIS (2002) this simplification is possible for fine grained soils, since the stress ratio has only little influence on the compressibility of the soil. The pressure dependency factor f_b must now describe the unloading-reloading path rather than the virgin loading one as in (6.19). NIEMUNIS therefore modified it for isotropic stress to

$$f_b = \frac{tr\boldsymbol{T}}{(1 + a^2/3)\kappa^*}\,, \tag{6.37}$$

where κ^* is the isotropic unloading-reloading coefficient from the BUTTERFIELD compression law. For oedometric conditions f_b can be written as

$$f_b = \frac{tr\boldsymbol{T}}{\left(1 + a^2/(1 + 2K_0)\right)\kappa^{*0}} \,, \tag{6.38}$$

where κ^{*0} is the BUTTERFIELD coefficient of oedometric unloading and reloading. Since oedometric tests are more convenient to perform than isotropic tests, NIEMUNIS advises to use (6.38).
The viscous strain rate is calculated via a NORTON (1929) approach, which depends on the overconsolidation ratio OCR,

$$\boldsymbol{D}^{vis} = D_r \vec{\boldsymbol{B}} \left(\frac{1}{OCR}\right)^{1/I_v} \tag{6.39}$$

with the viscosity factor

$$f_{v,Nie} = \left(\frac{1}{OCR}\right)^{1/I_v} . \tag{6.40}$$

The OCR changes with a change in the stress state as well as with time under constant effective stress. D_r is a reference strain rate, which corresponds to the isotache respectively isochrone defined as the RCL (OCR = 1). Often this reference line is chosen to be the end of primary consolidation. According to NIEMUNIS (2002), there is no need or objective criterion of taking any particular value of D_r. However, it could be determined from an isotropic compression test via

$$D_r = \frac{\lambda^* - \kappa^*}{\lambda^*} \|\boldsymbol{D}\| \tag{6.41}$$

and is often chosen as D_r = 10^{-6}.
The tensor $\vec{\boldsymbol{B}}$ is the potential function (flow rule), that defines the direction of the creep strains

$$\vec{\boldsymbol{B}} = \frac{\boldsymbol{L^{-1}}\!:\boldsymbol{N}}{\|\boldsymbol{L^{-1}}\!:\boldsymbol{N}\|} \quad \text{and} \tag{6.42}$$

I_v is the viscosity index defined by (3.45), which is slightly different from the definition by GUDEHUS & LEINENKUGEL (1978) in (3.44). For general stress states the deviatoric stress component has to be considered when calculating OCR. NIEMUNIS' approach is based on the yield surface defined by the Modified Cam Clay Model similar to the approach by VERMEER & NEHER (1999):

$$f(p', q, p'^{+}_{e}) = q^2 - M^2 p' \left(p'^{+}_{e} - p'\right) = 0 \,. \tag{6.43}$$

The OCR is calculated via two equivalent mean stresses,

$$OCR = p'_e / p'^{+}_{e} \,. \tag{6.44}$$

p'_e can be calculated from the BUTTERFIELD compression law (3.23)

$$p'_e = \left(\frac{1+e}{1+e_{e0}}\right)^{1/\lambda^*} \cdot p'_{e0}\,, \tag{6.45}$$

where e_{e0} and p'_{e0} are the chosen parameters for determination of the RCL and p'^{+}_{e} can be determined from (6.43) with

$$p'^{+}_{e} = p'\left(1+\left(\frac{q}{Mp'}\right)^2\right). \tag{6.46}$$

NIEMUNIS (2002) proposes yet another way to determine p'^{+}_{e} with distinction between states above and below the critical state line, which will however not be addressed here.
Equation (6.35) can be written for oedometric conditions. The linear part of the stress tensor from the VON WOLFFERSDORFF model can be written as

$$L_{11} = \left[1 + a^2\frac{1}{(1+2K_0)^2}\right] \quad \text{and} \tag{6.47}$$

$$L_{21} = a^2\frac{K_0}{(1+2K_0)^2} \tag{6.48}$$

and for the constitutive differential equation follows

$$\dot{T}_{11} = f_b\left(1 + a^2\frac{1}{(1+2K_0)^2}\right)\left(D_{11} - D_r\left(\frac{1}{OCR}\right)^{1/I_v}\right) \quad \text{and} \tag{6.49}$$

$$\dot{T}_{22} = f_b a^2\frac{K_0}{(1+2K_0)^2}\left(D_{11} - D_r\left(\frac{1}{OCR}\right)^{1/I_v}\right). \tag{6.50}$$

6.2.3 Visco-hypoplastic model after GUDEHUS (2004)

GUDEHUS (2004) formulated a viscous model for soft soils based on the Hypoplasticity framework developed for granular soils with limit void ratios for the loosest, densest and critical state, e_i, e_d and e_c. A comparison between the NIEMUNIS and the GUDEHUS model was presented by PUNLOR (2004). The rate dependency was incorporated by introducing a rate dependent granular hardness h_s according to

$$\frac{h_s}{h_{sr}} = 1 + I_v \cdot \ln\left(\frac{\mathrm{D}}{D_r}\right), \tag{6.51}$$

where h_{sr} is a reference value of the granular hardness, which corresponds to the reference viscous strain rate D_r. The constitutive relation reads

$$\dot{\boldsymbol{T}} = f_b f_e \boldsymbol{L}\colon\left(\boldsymbol{D} + \boldsymbol{L}^{-1} f_d \boldsymbol{N} D^{vis}\right), \tag{6.52}$$

with $\boldsymbol{L}$ and $\boldsymbol{N}$ from (6.15) and (6.18) as well as f_b from (6.19), f_e from (6.20) and f_d from (6.21), which are all rate-dependent via (6.51). D^{vis} is calculated from

$$D^{vis} = D_r \cdot f_{v,Gu} \tag{6.53}$$

with the viscosity factor

$$f_{v,Gu} = \exp\left(\frac{1/OCR - 1}{I_v}\right). \tag{6.54}$$

The overconsolidation ratio OCR depends again on an equivalent pressure p'_e, which is determined via the BAUER compression law from (3.26):

$$OCR = \frac{p'_e}{p'} \quad \text{and} \tag{6.55}$$

$$p'_e = \frac{1}{3} h_{sr} [-\ln(e f_T / e_{c0})]^{1/n} \qquad \text{where} \tag{6.56}$$

$$f_T = \frac{e_{c0}}{e_{d0}} - \left(\frac{e_{c0}}{e_{d0}} - 1\right) \cdot \left(-\frac{\lambda_\sigma}{k_c}\right)^m. \tag{6.57}$$

e_{c0}/f_T determines the RCL. The factor m defines the loosest state isotropic compression curve as the reference compression line via

$$m = \ln\left(\frac{1/e_{d0} - 1/e_{i0}}{1/e_{d0} - 1/e_{c0}}\right) / \ln\left(\frac{1}{9k_c}\right). \tag{6.58}$$

f_T reduces upon isotropic compression to $f_T = e_{c0}/e_{i0}$ (cf. Appendix A.11). And when inserting this into (6.56), it yields

$$p'_e = \frac{1}{3} h_{sr} [-\ln(e/e_{i0})]^{1/n} \qquad \text{or} \quad e = e_i = e_{i0} \cdot 1/\exp\left[\left(\frac{3p'_e}{h_{sr}}\right)^n\right], \tag{6.59}$$

which corresponds to the BAUER compression curve for the loosest state. Under compression with $\dot{\varepsilon}_1 = \dot{\varepsilon}_2 = D_r/\sqrt{3}$, $h_s = h_{sr}$ is obtained and it follows $p' = p'_e$, OCR = 1.0 and $f_{v,Gu}$ = 1.0. Consequently, any initial state denser than the loosest state is treated as overconsolidated in compression (cf. Figure 6.2).

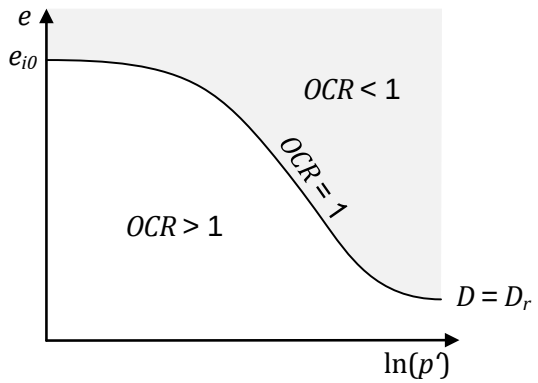

Figure 6.2: Consolidation states in Visco-Hypoplasticity after GUDEHUS (2004)

The expression λ_σ/k_c in (6.57) incorporates the MATSUOKA-NAKAI limit condition where k_c is a factor dependent on the critical state friction angle and λ_σ is the ratio of the second and third invariant of the tensor $\hat{\boldsymbol{T}}$ (BAUER, 2000):

$$\lambda_\sigma + k_c = \frac{\hat{I}_3}{\hat{I}_2} + \frac{cos^2\varphi_c}{9 - sin^2\varphi_c} = 0 \qquad \text{with} \tag{6.60}$$

$$\hat{I}_2 = \frac{\left(tr\hat{\boldsymbol{T}}^2 - 1\right)}{2} \qquad \text{and} \quad \hat{I}_3 = \frac{tr\hat{\boldsymbol{T}}^3}{3} - \frac{tr\hat{\boldsymbol{T}}^2}{2} + \frac{1}{6}\,.$$

In shearing the factor λ_σ/k_c and therefore f_T converge to 1.0, as the void ratio approaches the critical state void ratio. Hence, the e_c-compression curve becomes the reference compression curve (cf Figure 6.3). f_T controls also the volumetric behaviour of the model.

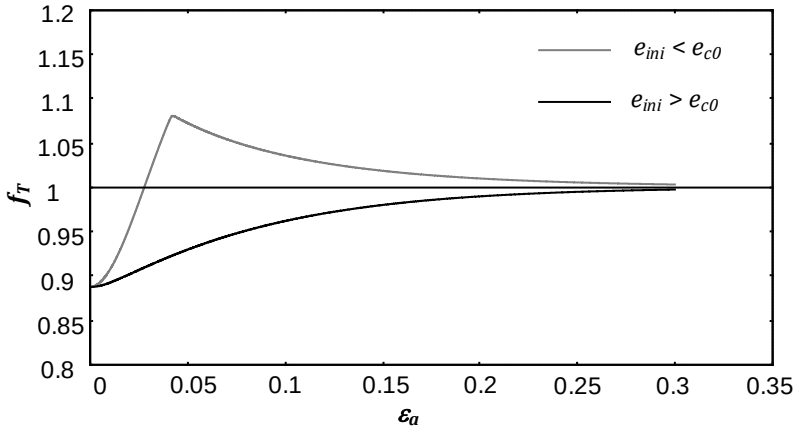

Figure 6.3: Development of factor f_T in shearing

For oedometric conditions (6.52) can be simplified to

$$\dot{T}_{11} = f_b f_e \frac{(1+2K_0)^2}{1+2K_0{}^2}\left[D_{11} + a^2\frac{D_{11}}{(1+2K_0)^2} + f_d\frac{a}{3}\cdot\frac{5-2K_0}{1+2K_0}\cdot f_v D_r\right] \tag{6.61}$$

and

$$\dot{T}_{22} = f_b f_e \frac{(1+2K_0)^2}{1+2K_0{}^2}\left[a^2\frac{K_0 D_{11}}{(1+2K_0)^2} + f_d\frac{a}{3}\cdot\frac{4K_0-1}{1+2K_0}\cdot f_v D_r\right]. \tag{6.62}$$

6.2.4 Definition of a reference state

The three presented models use the state-dependent variable $OCR = p'_e/\,p'$ based on an equivalent pressure p'_e, which is the projection of the stress state onto the hydrostatic axis, to describe creep. In the e - p space, the relationship between e and p'_e is defined by a reference compression line (RCL), which is in fine-grained materials the isotropic consolidation line. Prerequisite for the applicability of this relationship is the existence of a unique RCL where OCR = 1.0 and which defines the equivalent pressure $p'_e = p'$ as a function of the void ratio for a reference strain rate D_r. The uniqueness of the

p' - e - D - relationship is however not given for granular soils as was shown in Section 4. In the following, the definition of the RCL in fine grained soils is explained for comparison purposes. Afterwards, the concept of the RCL is adapted for granular soils.

Reference state in fine grained soil

Figure 6.4 (a) shows the isotropic loading of a fine grained soil with the reference strain rate (→1), following the compression law of (3.20) respectively (3.21). As schematically shown, a state below the RCL starting from e_{i0} can be reached by loading, unloading (→1'→2) and by creep (→1→2) from a certain pressure level. In either case the soil is overconsolidated ($OCR > 1$) at state 2. Upon isotropic reloading with the reference strain rate, the soil will remain in an overconsolidated state and behave stiffer until it reaches the RCL (2→1'). When further loaded at constant volumetric strain rate, the soil will remain on the RCL (1'→3).

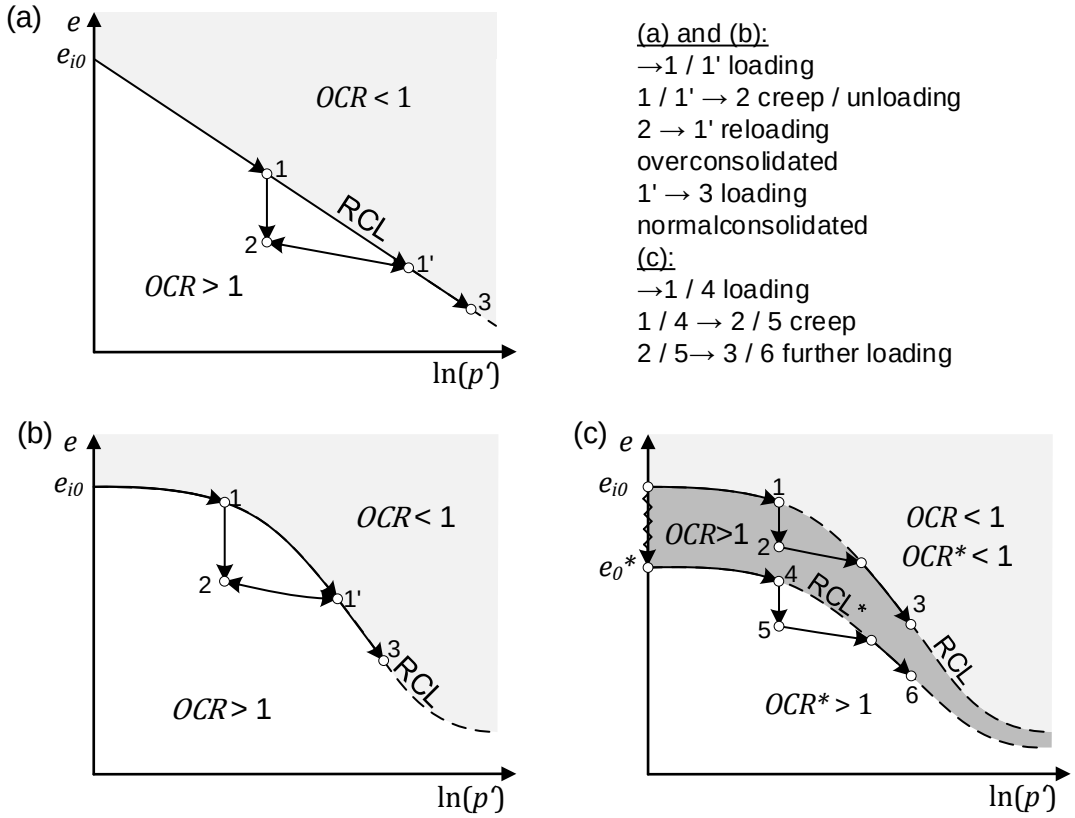

Figure 6.4: Idealized compressive behaviour of (a) a fine grained, (b) a granular soil after creep (1→2) or unloading (1'→2) as well as compression and (c) creep of a granular soil from different initial densities (1/1'→2/2'→3/3')

Reference state in granular soil

The compression behaviour of a granular soil follows the BAUER-compression law given by (3.26) (cf. Figure 6.4 (b)). A state below a RCL defined by an initial void ratio of e_{i0} and (3.26) can be reached either by loading, unloading (→1'→2) or creep (→1→2) as drawn in Figure 6.4 (b). The granular soil at point 2 will be overconsolidated, as shown for a fine grained soil (cf. Figure 6.4 (a)). Upon reloading according to Figure 6.4 (a) and (b), the soil behaviour is stiffer until the stress reaches point 1' and

by further loading, the granular soil state moves along the RCL as given by Figure 6.4 (b) in a similar way like the fine grained soil (cf. Figure 6.4 (a)).
On the contrary, if compression starts from a denser state at $e_0{}^*$, as displayed in Figure 6.4 (c), it will reach the point 4 along the RCL*, unlike a fine grained soil, without a creep or unloading process, because it is not necessarily in an overconsolidated state. From point 4 after a creep phase (4→5) the granular soil will approach the RCL* upon further loading (5→6). Clearly, the RCL cannot be unique in granular soils, but depends on the initial density of the soil. This is confirmed by the experimental results presented in Section 4 and results from other researchers (e.g. BAUER, 1992, YAMAMURO *et al.*, 1996, HERLE & GUDEHUS, 1999) (cf. Section 3.2). The dependence of the compression curve on the initial density is also a very important assumption used in the framework of Hypoplasticity (GUDEHUS, 1996).

In the e - $\ln p'$ - plane the compressive behaviour of granular soils can be described by a band of compression curves as was shown in Figure 3.11 or Figure 4.60. They can be mathematically defined for instance by (3.26). Each of these curves can be considered as a RCL depending on the initial state of the soil. As shown in Figure 6.4 (c), the reference line changes from RCL to RCL*, if the compression starts from a denser initial state $e_0{}^*$. Knowing the initial value of the three variables OCR, e and p' the RCL can be determined and the compressive and creep behaviour can be simulated.

6.3 Review of the models

The models by VERMEER & NEHER (1999), NIEMUNIS (2002) and GUDEHUS (2004) are capable of modelling the viscous behaviour of soft soils. In this section, the predictions of the three models are compared, in order to judge their suitability to model viscous behaviour of sands under compression. For the presented simulations, element test implementations of the different models were used. The most important features of the models are summarized here:

SSC:
- Splitting of strains into elastic and viscoplastic parts.
- Limit condition by MOHR-COULOMB with non-associated flow rule.
- Modified Cam Clay yield surface with associated flow rule.
- BUTTERFIELD compression law.
- Determination of the viscous strain rate with a NORTON-approach using a stress ratio p'^{eq}/p'^{eq}_e of equivalent stresses, representing the effective stress state p'^{eq} and an equivalent stress state on a reference compression curve p'^{eq}_e.
- Determination of the equivalent stress p'^{eq}_e via the accumulated viscous strains (hardening rule).

Visco-Hypoplasticity after NIEMUNIS (2002):
- Splitting of strains into hypoelastic (incrementally elastic) and viscoplastic parts.
- Limit condition by MATSUOKA-NAKAI.
- BUTTERFIELD compression law.

– Determination of the viscous strain rate with a NORTON-approach using a stress ratio p'_e/p'^+_e of equivalent stresses, representing the effective stress state p'_e and an equivalent stress state on a reference compression curve p'^+_e.
– Determination of the equivalent stress p'^+_e via the Modified Cam Clay yield surface.

Visco-Hypoplasticity after GUDEHUS (2004):
– Splitting of strains into hypoelastic and viscoplastic parts.
– Limit condition by MATSUOKA-NAKAI.
– BAUER compression law.
– Determination of the viscous strain rate with an exponential approach using a stress ratio p'/p'_e of equivalent stresses, representing the effective stress state p' and an equivalent stress state on a reference compression curve p'_e.
– Determination of the equivalent stress p'_e via a modified BAUER compression law.
– It is based on asymptotic states of extreme void ratios e_i, e_d and e_c.

In the following, the models will be compared with respect to stress-dependent compression behaviour. First the SSC and the NIEMUNIS model will be compared, because they both use the same compression law. Afterwards, the GUDEHUS model's stress-dependent compression is reviewed. In order to model virgin compression behaviour from states below the loosest state (e_i), the model needs to be modified, allowing the definition of any RCL (cf. Section 6.2.4). Viscous behaviour is analyzed by comparing the different viscosity factors from (6.7), (6.40) and (6.54) as well as looking at the predicted creep strains, the rate-dependent behaviour and stress relaxation separately.

6.3.1 Comparison of stress-dependent compression

As was presented in Sections 3.2 and 4, the compressive behaviour on a logarithmic stress scale of sand and also of sand with very high fine content is highly non-linear in common geotechnical stress ranges. A constant compression index can only be applied in very small stress intervals. The models after VERMEER & NEHER (1999) and NIEMUNIS (2002) both apply a constant compression index. The GUDEHUS (2004) model uses the BAUER-compression law, which yields a density and stress-dependent compression index C_c via

$$C_c = e \cdot n \left(\frac{3p'}{h_s}\right)^n \cdot \ln(10) \qquad \text{(HERLE, 1997).} \tag{6.63}$$

For demonstration of the different compressive behaviours of the models, oedometer tests on sand MS with a medium dense and a very dense initial state presented in Figure 4.44 were simulated. The tests were CRS tests with a strain rate in loading, unloading and reloading of 0.5%/min. The unloading started from preconsolidation stresses of 125, 250, 500, 1000, 2000, 4000 and 7500 kPa. Reloading always started from 50 kPa.

6.3.1.1 Models after VERMEER & NEHER (1999) and NIEMUNIS (2002)

The compression and swelling indices of SSC and Visco-Hypoplasticity after NIEMUNIS (2002) are not material constants, but have to be adapted for each initial density state separately. The models

also do not consider a change of C_c and C_s with stress. Therefore, mean values in the pressure range from 10 to 7500 kPa evaluated from the test results were used. This large stress range is just to emphasize the shortcomings of the two models when modelling compression in a large stress range. The model parameters are summarized in Table 6.1.

Table 6.1: Model parameters for comparative element test simulations

SSC	NIEMUNIS (2002)
medium dense $\lambda^* = 0.0183$, $\kappa^* = 0.0028$ $\mu^* = 4.4 \cdot 10^{-4}$ $e_0 = 0.950$ (at $p' \approx 0$ kPa)	medium dense $\lambda^* = 0.0183$, $\kappa^* = 0.0028$ $I_v = 0.015$ $e_0 = 0.950$ (at $p' \approx 0$ kPa)
very dense $\lambda^* = 0.0105$, $\kappa^* = 0.0028$ $\mu^* = 3.13 \cdot 10^{-4}$ $e_0 = 0.697$ (at $p' \approx 0$ kPa)	very dense $\lambda^* = 0.0105$, $\kappa^* = 0.0028$ $I_v = 0.020$ $e_0 = 0.697$ (at $p' \approx 0$ kPa)
$\varphi' = 30°$ $\tau_{ref} = 1$ d => $D_r = 5.1 \cdot 10^{-9}$ 1/s (medium dense) and $D_r = 3.6 \cdot 10^{-9}$ 1/s (very dense) $\dot{\varepsilon}_a = 8.35 \cdot 10^{-5}$ 1/s $\sigma_{a.ini} = 10$ kPa, $\sigma_{r,ini} = 5$ kPa $e_{ini,\ medium\ dense} = 0.875$, $e_{ini,very\ dense} = 0.671$	$\varphi_c = 30°$ $D_r = 8.35 \cdot 10^{-5}$ 1/s $\dot{\varepsilon}_a = 8.35 \cdot 10^{-5}$ 1/s $\sigma_{a,ini} = 10$ kPa, $\sigma_{r,ini} = 5$ kPa, $e_{ini,\ medium\ dense} = 0.875$, $e_{ini,very\ dense} = 0.671$

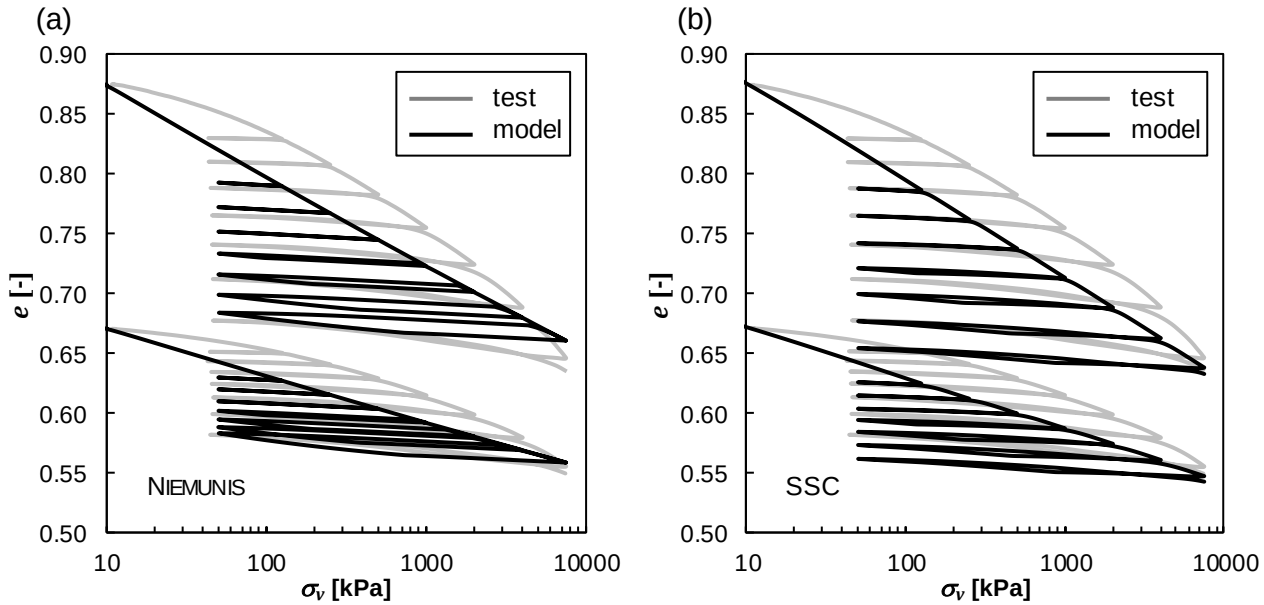

Figure 6.5: Modelled and measured compression behaviour of medium dense and very dense sand MS during CRS compression at 0.5%/min: (a) Visco-Hypoplasticity after NIEMUNIS (2002) and (b) SSC

The simulation results of both models are presented in Figure 6.5. The behaviour is very similar. It can be observed that the compression law used in both models cannot capture the virgin compression behaviour of sand MS in a wide stress range. With the same λ^* and κ^* SSC estimates slightly

larger compression than the visco-hypoplastic model. This is caused by the different approaches of calculating the viscous strain rate. In unloading and reloading both models predict a hysteretic behaviour, like the experiments. In Visco-Hypoplasticity the hysteresis increases significantly with the preconsolidation stress and overestimates the real behaviour. SSC captures the hysteretic behaviour quite well. The swelling index κ^* from experiments increases with the preconsolidation stress (cf. Figure 4.44 (b)), which cannot be reproduced by the models. Therefore, both models do not appear to be suitable to predict the compression behaviour of granular soil in a large stress range.

6.3.1.2 Model after GUDEHUS (2004)

Adaptation of the model

It was mentioned in Section 6.2.3 that the visco-hypoplastic model after GUDEHUS (2004) uses a fixed RCL, which is defined as the loosest state e_i isotropic compression curve. It is therefore not possible to model normally-consolidated compressive behaviour of sands from states that have a lower initial void ratio than the loosest state void ratio at p'= 0 kPa. The loosest state void ratio of sand MS can be estimated with e_{i0} = 1.15 · e_{max} = 1.15 · 1.09 = 1.31 (cf. Section 3.1.5). The void ratios at p' = 0 kPa of the two tests in Figure 4.44 are e_0 = 0.950 for the medium dense and e_0 = 0.697 for the very dense sample. Accordingly, the model needs to be modified in order to simulate normally consolidated behaviour from these two initial states and to apply a RCL with $e_0 < e_i$. This was done by replacing the expression e_{c0}/f_T in (6.56) by an arbitrary void ratio e_0 at effectively p'= 0 kPa , which leads to

$$p'_e = \frac{1}{3} h_{sr} [-\ln(e/e_0)]^{1/n} . \tag{6.64}$$

Due to this modification the influence of a deviatoric stress is no longer taken into account in the calculation of p'_e and shearing behaviour can no longer be modelled. h_s and n are defined for isotropic compression and need to be adapted here for the oedometric compression paths. Furthermore, they are no longer independent of the initial density, but need to be determined for each initial state independently like the parameters λ^* and κ^* in SSC and the visco-hypoplastic model after NIEMUNIS (2002).
In order to incorporate the influence of a deviatoric stress path in any anisotropic loading, the parameter f_T needs to be changed. However, this change goes beyond the scope of this study. The modified version of the model is only capable to model the behaviour under compression.

Application of the model

It is recommended by HERLE (1997) to determine n from a loose oedometer test with (4.10) (cf. Figure 4.18) and h_s via

$$h_s = 3p' \left(\frac{n \cdot e}{C_c} \right)^{1/n} . \tag{6.65}$$

n controls the curvature and h_s the inclination of the compression curve (cf. Figure 3.16). This fitting gives a first estimation of the range of the parameters, but is not sufficient to provide an exact parameter set. It is therefore necessary to determine the parameters by iteratively fitting the compression curves within the determined parameter range. $C_\alpha/C_c = I_v$ was determined as a mean value from the creep tests presented in Section 4.7.1. The fitted visco-hypoplastic parameters for the medium dense and very dense samples of sand MS are summarized in Table 6.2.

Table 6.2: Visco-hypoplastic constitutive parameters of sand MS for comparative element test simulations

	medium dense	very dense
h_{sr} [MPa]	750	1650
n	0.285	0.340
I_v	0.019	
φ_c [°]	30	
e_0	0.950	0.697
e_{d0}	0.630	
e_{c0}	1.090	
e_{i0}	1.310	
D_r	$8.33 \cdot 10^{-5}$ = 0.5%/min	
$\sigma_{ini,\,a}$ [kPa]	10	
$\sigma_{ini,\,r}$ [kPa]	5	
e_{ini}	0.875	0.671

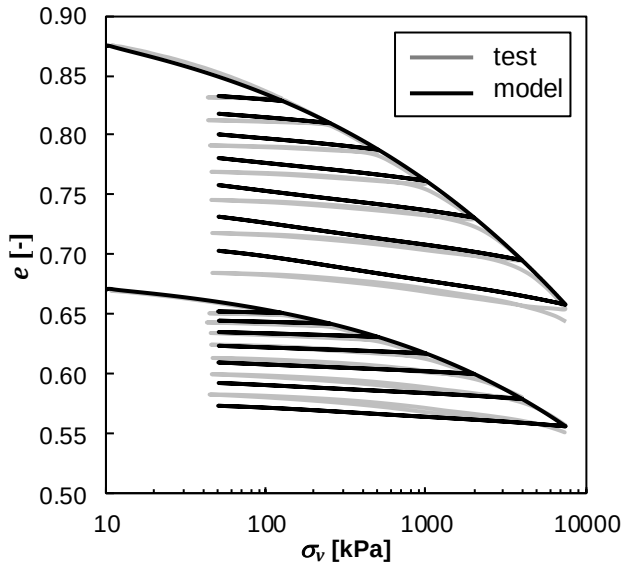

Figure 6.6: Modelled and measured compression behaviour of medium dense and very dense sand MS during CRS compression at 0.5%/min: Modified Visco-Hypoplasticity after GUDEHUS (2004)

The modelling results of the modified visco-hypoplastic model along with the test results are presented in Figure 6.6. With the two parameter sets the behaviour of sand MS in virgin compression can be very well reproduced. Un- and reloading in the GUDEHUS model cannot be calibrated with corresponding parameters like in SSC or the NIEMUNIS model, but is calculated model-inherently by the combination of the tensors $\boldsymbol{L}$ and $\boldsymbol{N}$. The behaviour of the model in unloading and reloading shows

practically no hysteretic behaviour. This deviation is negligible, because the hysteresis in the tests is very small. At low densities the un- and reloading stiffness is slightly underestimated and at higher densities it is overestimated.
It can be concluded that the modified version of the Visco-Hypoplasticity after GUDEHUS (2004) is most suited for predicting the stress-dependent compression behaviour of granular soil. This was expected, as the BAUER compression law used in the model was developed for granular materials.

6.3.2 Comparison of the viscous behaviour

First, the viscosity factors from (6.7), (6.40) and (6.54) responsible for modelling of the viscous behaviour shall be compared. The three approaches for calculating the viscosity factors are given again below. All of them are controlled by the overconsolidation ratio OCR and a viscosity index I_v or $(\lambda^* - \kappa^*)/\mu^*$. They govern the simulation of the viscous response of the models:

SSC: $$f_{v,SSC} = \left(\frac{1}{OCR}\right)^{\frac{\lambda^*-\kappa^*}{\mu^*}} \underbrace{=}_{for\ \varepsilon < approx.\ 15\%} \left(\frac{1}{OCR}\right)^{\frac{C_c-C_s}{C_\alpha}} \tag{6.66}$$

NIEMUNIS: $$f_{v,Nie} = \left(\frac{1}{OCR}\right)^{1/I_v} = \left(\frac{1}{OCR}\right)^{\frac{C_c}{C_\alpha}} \tag{6.67}$$

GUDEHUS: $$f_{v,Gu} = \exp\left(\frac{1/OCR - 1}{I_v}\right) = \exp\left(\frac{C_c(1/OCR - 1)}{C_\alpha}\right) \tag{6.68}$$

Under consideration of (3.43), the equality of $(\lambda^* - \kappa^*)/\ \mu^*$ and $(C_c - C_s)/C_\alpha$ for strains below approximately 15% and the assumption of the same OCR-development, the three viscosity factors can be compared. Figure 6.7 presents the development of the different viscosity factors with the OCR for two cases. Figure 6.7 (a) was calculated with data of a highly compressible organic clayey silt taken from KRIEG (2000) (cf. Table 6.3) and Figure 6.7 (b) was derived using data from sand MS (cf. Table 6.2 and Section 4). They represent a wide range of viscosity in soil. The GUDEHUS approach compared to the NIEMUNIS approach yields larger viscosity factors at the same OCR. In SSC the decrease of $f_{v,SSC}$ depends on the difference between the compression index C_c (or λ^*) and the swelling index C_s (or κ^*) in the exponent $(C_c - C_s)/C_\alpha$. Considering the validity of $I_v = C_\alpha/C_c$, SSC will predict larger viscosity factors than the NIEMUNIS model at the same OCR > 1.0. In case of the very viscous organic silt all three viscosity factors become very small for OCR > 2.0. For sand MS they already become negligibly small at OCR > 1.2.

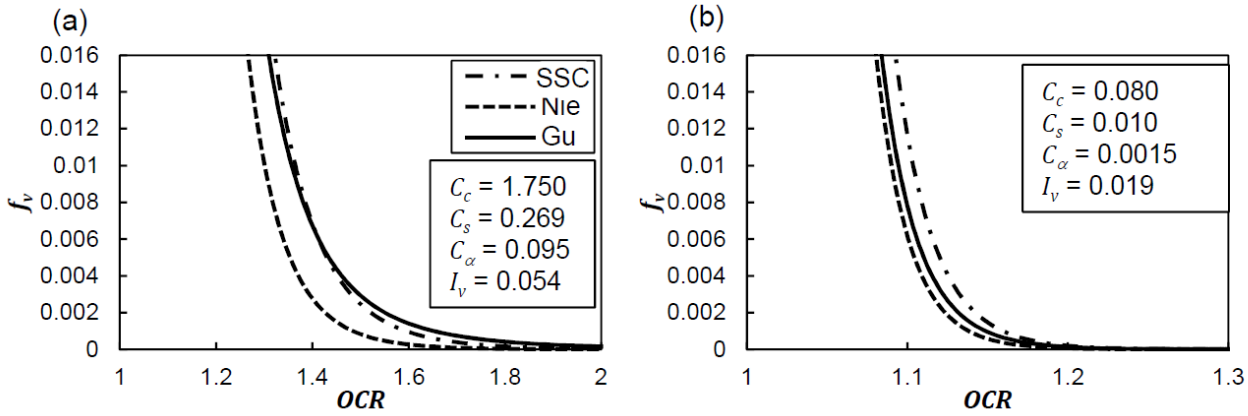

Figure 6.7: Comparison between different viscosity factors of SSC, NIEMUNIS (2002) (Nie) and GUDEHUS (2004) (Gu), (a) with data of an organic clayey silt from KRIEG (2000), (b) with data from medium dense quartz sand MS at 250 kPa effective vertical stress

In the following, the influence of the different models shall be analyzed with respect to

1. development of creep strains,
2. strain rate dependency and
3. relaxation behaviour.

The constitutive parameters used in the simulations for comparison of the viscous behaviour are derived from experimental results on the already mentioned organic clayey silt by KRIEG (2000). This data set was chosen, because the soil is highly compressible and shows large viscous effects, making the behaviour well visible in the simulations. The parameters are summarized in Table 6.3. The compression and swelling index of SSC and the NIEMUNIS model are equal due to the same applied compression law. I_v was estimated from the experimental results and C_α respectively μ^* were calculated according to $I_v = C_\alpha/C_c$. In case of SSC, the model-inherent reference isochrone is fixed to one day. The reference strain rate is accordingly $D_r = \mu^*/t_{ref} = \mu^*/86400 = 0.01/86400 = 1.16 \cdot 10^{-7}$ 1/s. In the two visco-hypoplastic models the reference strain rate can be chosen by the user. Here they were chosen as $D_r = \dot{\varepsilon}_a = 2.6 \cdot 10^{-6}$ 1/s for maintaining an $OCR = 1.0$ condition on initiation of the simulation. The SSC-routine was also adapted and tested using this reference strain rate instead of the model-inherent one for comparison. Compression started from $e_{ini} = 3.32$ on the e_i - compression curve. This way the behaviour starting from a normally consolidated state could be modelled without any changes of the visco-hypoplastic model after GUDEHUS (2004) like they were presented in Section 6.3.1. The viscous response of the original model can thereby be evaluated. The simulations were performed until maximum stresses of 500 kPa to test the soft soil models in their usually applied stress range.

Table 6.3: Model parameters of organic clayey silt taken from KRIEG (2000) for comparative element test simulations

VERMEER & NEHER (1999)	NIEMUNIS (2002)	GUDEHUS (2004)
$\lambda^* = 0.187$ or $C_c = 1.750$ $\kappa^* = 0.029$ or $C_s = 0.269$ $\mu^* = 0.01$ or $C_\alpha = 0.095$ $\varphi' = 44°$ $c' = 70$ kPa $e_{ini} = 3.32$ $D_r = \frac{\mu^*}{\tau_{ref}} = \frac{0.01}{86400} =$ 1.16·10^{-7} 1/s and $D_r = 2.6 \cdot 10^{-6}$ 1/s $\dot{\varepsilon}_a = 2.6 \cdot 10^{-6}$ 1/s $\sigma_{a,ini} = 100$ kPa, $\sigma_{r,ini} = 30$ kPa	$\lambda^* = 0.187$ or $C_c = 1.750$ $\kappa^* = 0.029$ or $C_s = 0.269$ $I_v = 0.054$ $\varphi_c = 44°$ $e_{ini} = 3.32$ $D_r = 2.6 \cdot 10^{-6}$ 1/s $\dot{\varepsilon}_a = 2.6 \cdot 10^{-6}$ 1/s $\sigma_{a,ini} = 100$ kPa, $\sigma_{r,ini} = 30$ kPa	$h_{sr} = 510$ kPa $n = 0.30$ $I_v = 0.054$ $\varphi_c = 44°$ $e_{ini} = 3.32$ $e_{d0} = 3.75$ $e_{c0} = 6.00$ $e_{i0} = 7.20$ $D_r = 2.6 \cdot 10^{-6}$ 1/s $\dot{\varepsilon}_a = 2.6 \cdot 10^{-6}$ 1/s $\sigma_{a,ini} = 134$ kPa, $\sigma_{r,ini} = 43$ kPa
$w = 184\%$ $w_L = 220\%$ $w_P = 106\%$ Organic content 33 wt-%		

6.3.2.1 Creep tests

To compare the three models with respect to developing creep strains, 10-day oedometric creep periods at vertical effective stresses of 172 kPa and 344 kPa were simulated. The SSC-model was tested with two different reference times with τ_{ref} = 1 d as recommended by VERMEER & NEHER (1999) and NEHER (2008) and τ_{ref} = 0.0445 d in order to have the same reference strain rate $D_r = 2.6 \cdot 10^{-6}$ 1/s and to start from the same OCR = 1.0 as the models by NIEMUNIS and GUDEHUS. Figure 6.8 (a) depicts the creep strain over the 10-day creep period and Figure 6.8 (b) shows the development of the OCR. According to NEHER (2008) the reference time of one day in SSC was chosen, as generally most creep phases performed in oedometer tests have a duration of 24 h. However, the difference in reference times in SSC does not cause a difference in the predicted creep strains, because the developments of OCR compensate the difference in the reference times. At τ_{ref} = 1 d OCR = 1.0 is reached exactly after one day of creeping when the creep strain rate equals D_r. On a logarithmic time scale, SSC and the NIEMUNIS model converge to the same constant gradient of creep strains. The resemblance of SSC and the NIEMUNIS model in terms of the predicted creep strains comes from the similar approach for calculating the viscosity factor. The slightly larger creep strains predicted by SSC are caused by the different exponents in (6.66) and (6.67), which leads to a larger viscosity factor in SSC (cf. Figure 6.7 (a)). The GUDEHUS model predicts the smallest creep strains. At the higher vertical effective stress 344 kPa all models show the same change in void ratio as at 172 kPa, corresponding to an isotache behaviour. The predicted creep strains are independent of the stress level in the tested stress range.

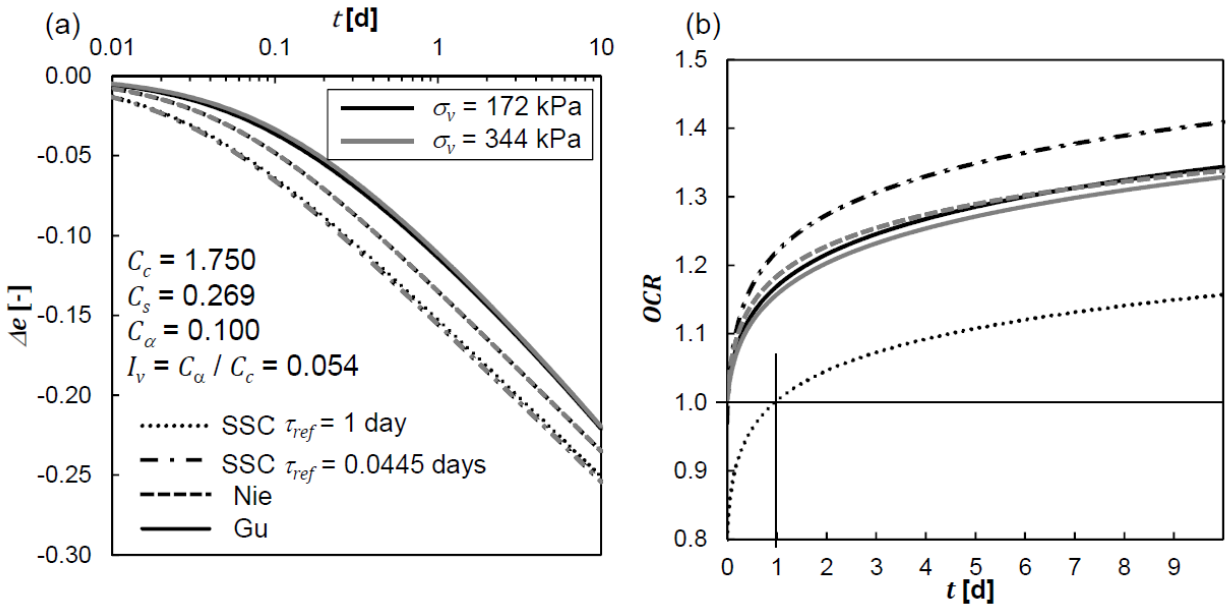

Figure 6.8: (a) Change in void ratio in a 10 d creep period at vertical effective stresses of 172 kPa and 344 kPa as well as (b) development of the OCR in the same time period and at the same stresses

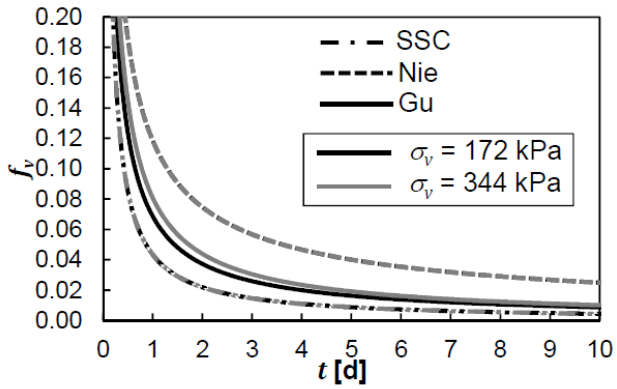

Figure 6.9: Development of the viscosity factors at vertical effective stresses of 172 kPa and 344 kPa in a 10-day creep period

6.3.2.2 Constant rate of strain tests

Figure 6.10 shows simulation results of CRS oedometric loading tests with different strain rates. All three models show an isotache behaviour with parallel lines of equal strain rate in the stress range up to 500 kPa. The GUDEHUS model shows isotaches with constant slope and the NIEMUNIS model with a slightly decreasing slope on a logarithmic stress scale. The SSC model converges towards a constant slope of the isotaches. The difference in the shape of the compression curves compared to the simulations of the tests on sand in Section 6.3.1 are caused by the very much higher compressibility of the organic clayey silt. In the case of the hypoplastic model after GUDEHUS, this is discussed in more detail in Section 6.3.2.5.

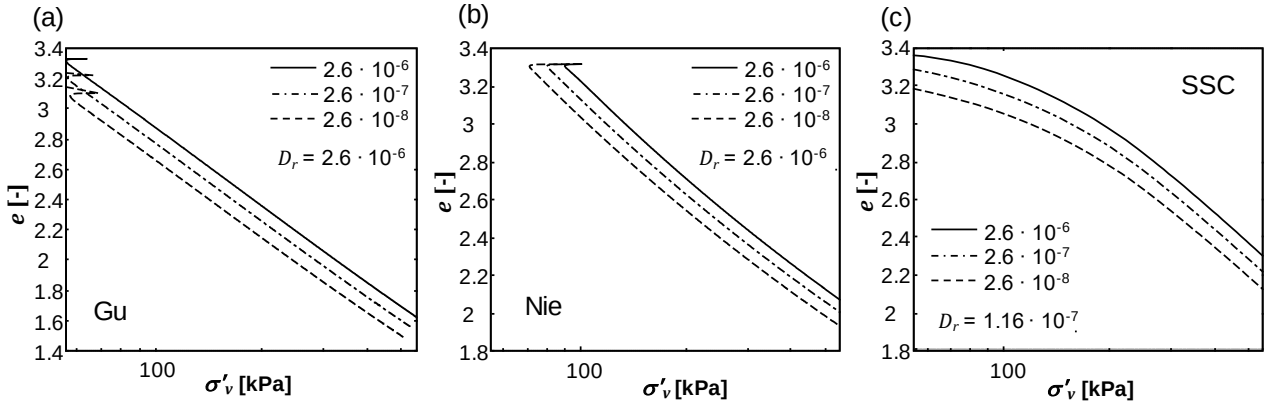

Figure 6.10: Numerical CRS oedometric loading tests modelled with (a) the model after GUDEHUS, (b) the model after NIEMUNIS and (c) SSC

6.3.2.3 Tests with sudden changes in the strain rate

Oedometric element tests with sudden in- or decrease of the strain rate were simulated for comparison of the strain rate-dependent behaviour. The applied axial strain rates were

$\dot{\varepsilon}_a = D_r$ until $\sigma_v = 172.34$ kPa,
$\dot{\varepsilon}_a = 0.1 \cdot D_r$ until $\sigma_v = 199.71$ kPa,
$\dot{\varepsilon}_a = 0.01 \cdot D_r$ until $\sigma_v = 254.54$ kPa,
$\dot{\varepsilon}_a = 0.1 \cdot D_r$ until $\sigma_v = 339.41$ kPa and
$\dot{\varepsilon}_a = D_r$ until $\sigma_v = 452.52$ kPa.

The results are presented in Figure 6.11. Upon reduction of the strain rate the models show a stress decrease and an OCR increase and with increase of the strain rate stress increases and OCR decreases. Qualitatively, the models show a similar behaviour with respect to a jump of the strain rate. The GUDEHUS model predicts a slightly larger stress change upon strain rate jump at identical viscous parameters, which is in agreement with the generally larger viscosity factor of the model. SSC and the NIEMUNIS model show almost identical stress changes after the jump. As expected, all models show isotache behaviour in the considered stress range up to 500 kPa.

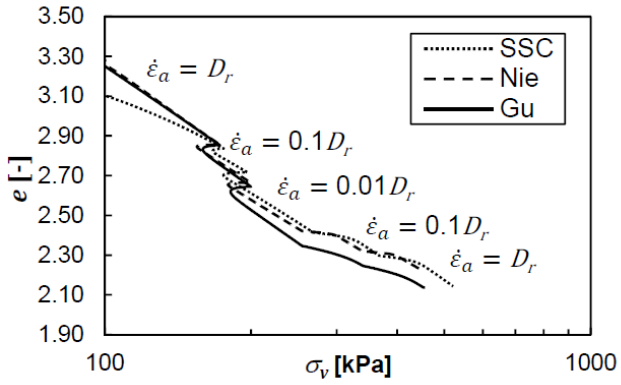

Figure 6.11: Numerical oedometric loading tests with jumps in the strain rate

6.3.2.4 Stress relaxation tests

In relaxation tests the strain rate is set to zero and the constitutive equations for the primary stress rate under oedometric conditions can be written as follows:

SSC:

$$\dot{T}_{11} = -E_{ur} \cdot \frac{\mu^*}{\tau_{ref}} \cdot f_{v,SSC} \qquad \text{with } f_{v,SSC} \text{ from (6.66),} \tag{6.69}$$

NIEMUNIS:

$$\dot{T}_{11} = -f_b \left(1 + a^2 \frac{1}{(1+2K_0)^2}\right) f_{v,Nie} D_r \qquad \text{with } f_{v,Nie} \text{ from (6.67) and} \tag{6.70}$$

GUDEHUS:

$$\dot{T}_{11} = f_b f_e \frac{(1+2K_0)^2}{1+2{K_0}^2} \left[-f_d \frac{a}{3} \cdot \frac{5-2K_0}{1+2K_0} \cdot f_{v,Gu} D_r\right] \qquad \text{with } f_{v,Gu} \text{ from (6.68).} \tag{6.71}$$

The stress rate in SSC and the NIEMUNIS model depends on the unloading-reloading stiffness E_{ur} respectively κ through f_b from (6.37) and the OCR. Furthermore, μ^* respectively I_v influence the stress rate. In the GUDEHUS model the relaxation stress rate is controlled by h_s and n through f_b from (6.19), I_v and also the OCR.

The relaxation behaviour was reviewed with the same test conditions like the previously simulated creep test. The creep phase of ten days at 172 kPa was replaced by a relaxation phase of ten days. The results are presented in Figure 6.12. SSC shows the largest stress relaxation followed by the NIEMUNIS and then the GUDEHUS model. After ten days the maximum difference between SSC and the GUDEHUS model lies at about 10%. The GUDEHUS model predicts the lowest stiffnes upon unloading and therefore the lowest stress relaxation (cf. Section 6.3.1). The difference between SSC and the NIEMUNIS model results from the difference of the exponents in the viscosity factors in (6.66) and (6.67), which control the development of OCR. Furthermore, despite the same un- and reloading stiffness parameter κ^* in both models, their stiffness in un- and reloading is different as can be observed in the results in Section 6.3.1. This is due to the different approaches of calculating the un- and reloading behaviour via (6.13) in case of SSC and (6.37) respectively (6.38) in the NIEMUNIS model.

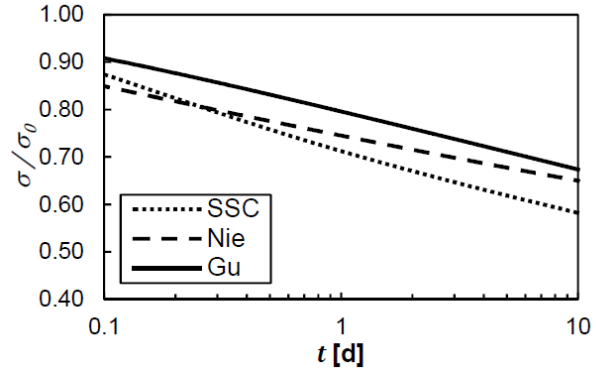

Figure 6.12: Normalized stress change in relaxation over a period of ten days

6.3.2.5 Detailed analysis of the GUDEHUS model

The model after GUDEHUS shows the best estimation of the stress-dependent compression behaviour. Therefore, the evaluation of its time-dependent predictions were extended to effective vertical stresses of 7500 kPa applied in the oedometer tests in Section 4. Two parameter sets for medium dense sand MS (cf Table 6.2) and organic clayey silt (cf. Table 6.3) were compared.
Oedometric CRS tests with loading strain rates $\dot{\varepsilon}_a = D_r$, $\dot{\varepsilon}_a = 0.1\ D_r$ and $\dot{\varepsilon}_a = 0.01\ D_r$ were simulated (cf. Figure 6.13). The medium dense sand MS shows much smaller viscous effects than the organic clayey silt, which can be observed by the different vertical distances between the isotache-lines, each being characterized by a constant OCR. The different isotaches are each calculated with a constant exponent n and different granular hardnesses h_s determined via (6.51) depending on the applied strain rate. As shown in Figure 3.16 (a), the compression curves with different h_s and constant n diverge in the lower stress range and converge in the higher stress range. The transition lies at the turning point of the BAUER compression law at $p' = h_s$ (cf. Figure 3.16 (b)). A section around the turning point can be considered as a range of nearly parallel compression curves on a logarithmic stress scale. The extent of the sections depends on the magnitude of the granular hardness. The sand and the silt reach the different sections at very different stress levels, because of their by several orders of magnitude different h_{sr} (cf. Figure 6.13). The sand is still in the diverging range at the maximum vertical effective stress of 7500 kPa, while the silt is already in the converging range. The viscous behaviour simulated by the model is different depending on the stress range. In case of creep, this means in the diverging range the soil has a lower OCR at the higher stress after the same creep strain increment than at the lower stress and thus shows a higher creep strain rate. Creep therefore increases at higher stresses. In the parallel range it will remain nearly constant and the model follows the classical isotache-concept. In the converging range creep strains in the same time interval will decrease at higher stresses, because OCR increases faster at higher stresses in the converging range.

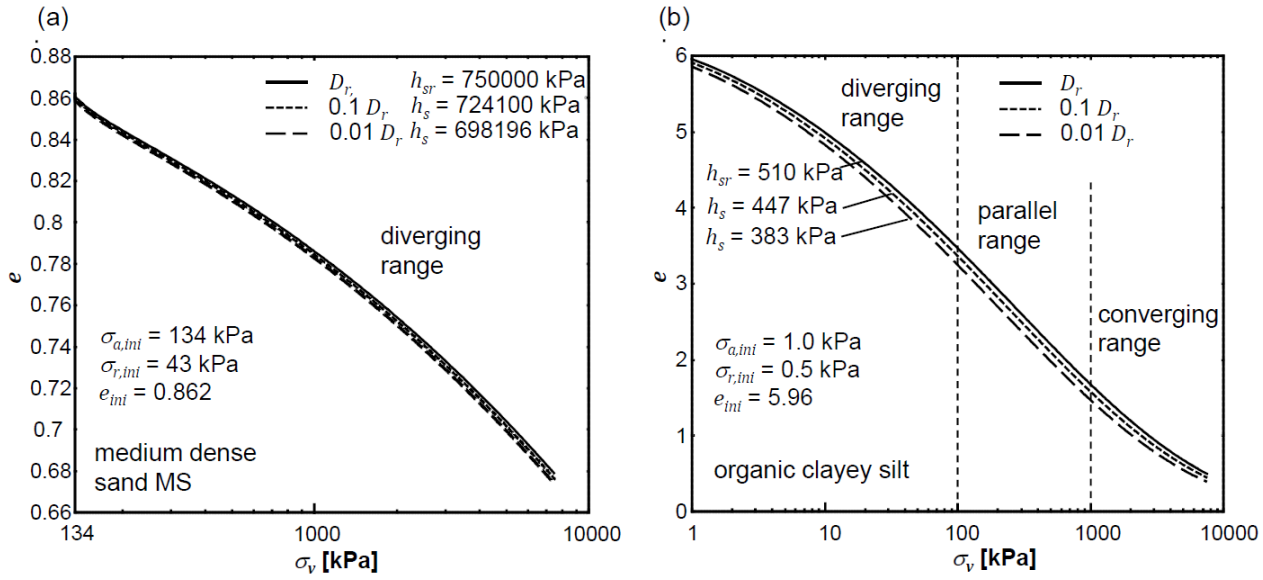

Figure 6.13: CRS compression at different strain rates of (a) medium dense sand MS and (b) organic clayey silt

The transition point from the diverging range to the parallel range for the silt can be estimated at σ_v' = 100 kPa, which corresponds under consideration of φ' = 44° and the JAKY (1948) approach for calculating K_0 to a mean stress of p' = 54 kPa ≈ 1/10 h_{sr}. The converging range of the silt can be estimated to start from σ_v' = 1000 kPa (p' = 537 kPa ≈ h_{sr}). The previously compared simulations of creep on the organic clayey silt at 172 and 344 kPa (cf. Figure 6.8) are therefore in the parallel range and the predicted creep strains are nearly identical at the two stress levels. A slight difference however is observable in the development of the OCR, which shows a higher OCR for the lower stress after the same creep time interval, because the applied stresses are lower than p' = h_s, which marks the turning point of the BAUER compression law. In case of the modelled medium dense sand MS with h_{sr} = 750000 kPa the parallel range of the isotaches lies at stresses, which are far higher than the applied stresses of σ_v' = 7500 kPa.
It can be concluded that the GUDEHUS model follows a stress-dependent isotache-concept resulting from the applied compression law. When modelling the behaviour of sands within normal geotechnical stress ranges, the predicted behaviour will be always in the diverging range of the isotaches and thus show larger creep strain and stress jumps upon strain rate jumps at higher stresses.

6.3.3 Conclusions

– When applying large stress increments the SSC-model and the NIEMUNIS model cannot predict the compressive behaviour of granular soils satisfactorily.

– The GUDEHUS model uses the BAUER compression law, which was developed for sands, and can therefore predict the compressive behaviour of granular soil realistically.

– The un- and reloading stiffness in the GUDEHUS model cannot be calibrated with corresponding parameters as in SSC or the NIEMUNIS models, but depends on the model parameters via the tensors $\boldsymbol{L}$ and $\boldsymbol{N}$ as well as the barotropy and pycnotropy functions. At low relative density this can lead to an underestimation and at high relative density to an overestimation of the un- and reloading stiffness.

– The predicted viscous behaviour of SSC and the NIEMUNIS model are very similar and strictly follow the isotache-concept. Differences are caused by the different definitions of the viscosity factors and the reference state.

– In all models the stress relaxation is influenced by the unloading behaviour.

– The GUDEHUS model does not use a NORTON approach like SSC and the NIEMUNIS model for the viscosity factor but an exponential approach. It does not follow the classical isotache-concept, due to the applied BAUER compression law. Depending on the applied stress, the isotaches have a diverging range, a parallel range and a converging range. The viscous behaviour is different depending on the stress range. Modelling of sands will always be in the diverging range at geotechnically relevant stresses.

– The GUDEHUS model is considered most suited for the application to granular soils, because of the more appropriate compression law, the dependence on the void ratios e_i, e_c and e_d and the ability to consider the stress dependency of the viscous behaviour.

6.4 Simulation of oedometric compression tests

In this section oedometer tests presented in Section 4 are modelled with the visco-hypoplastic model after GUDEHUS (2004) to further evaluate its capabilities and limitations. As presented, the GUDEHUS model does not follow the classical isotache-concept but considers with the BAUER compression law a stress dependency of the viscous response. The findings from element tests presented in Sections 3.3 and 4 contradict the classical isotache-concept in several ways. The main findings from Section 4 are summarized here again. Figure 6.14 presents them graphically.

a) Creep strains increase with increasing stress. As a consequence, the isochrone lines are not parallel anymore (cf. Figure 6.14 (a)).
b) Isotaches and isochrones are not identical in granular soils. Due to the changing viscous response at different stress levels, the equivalency of the lines in the sense of (3.53) or (4.16) is not given.
c) The creep and relaxation isochrones are not identical (cf. Figure 6.14 (b)).
d) CRS tests on sand with initially different loading strain rates do not show a rate effect (cf. Section 4.7.3).
e) The effect of a sudden strain rate change is only temporary in the stress-strain response (cf. Figure 6.14 (c)). The relationship between σ', e and $\dot{\varepsilon}$ is not unique.
f) A unique reference state cannot be defined.

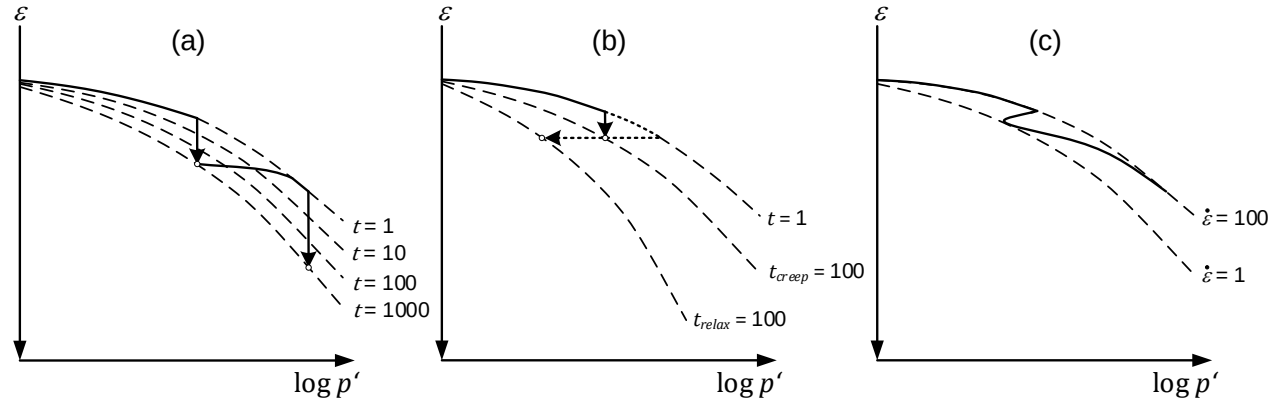

Figure 6.14: Schematic viscous behaviour of granular materials in creep (a), relaxation (b) and rate dependency (c)

In the following, simulation results of oedometric tests of the types depicted in Figure 6.14 (creep, stress relaxation and strain rate jump) are compared to the laboratory test results from Section 4. The parameter set used for all calculations is presented in Table 6.2.

6.4.1 Creep tests

Tests on medium dense and very dense samples of sand MS presented in Section 4.7.1 were simulated for analysis of the creep behaviour. The reference strain rate D_r in the simulations was identical to the loading strain rate in the tests to guarantee OCR = 1.0 at the beginning of creep. The simulation results presented in Figure 6.15 show that the model can realistically capture the stress-dependent creep behaviour of sand MS using a mean value of the evaluated $C_\alpha/C_c = I_v$ values from creep tests

on medium dense and very dense specimen in a wide range of stresses. Despite the finding from Section 4 that a constant C_α/C_c ratio alone is not capable of describing the oedometric creep behaviour of sand, in combination with the BAUER compression law the stress and density dependent creep behaviour can be modelled.

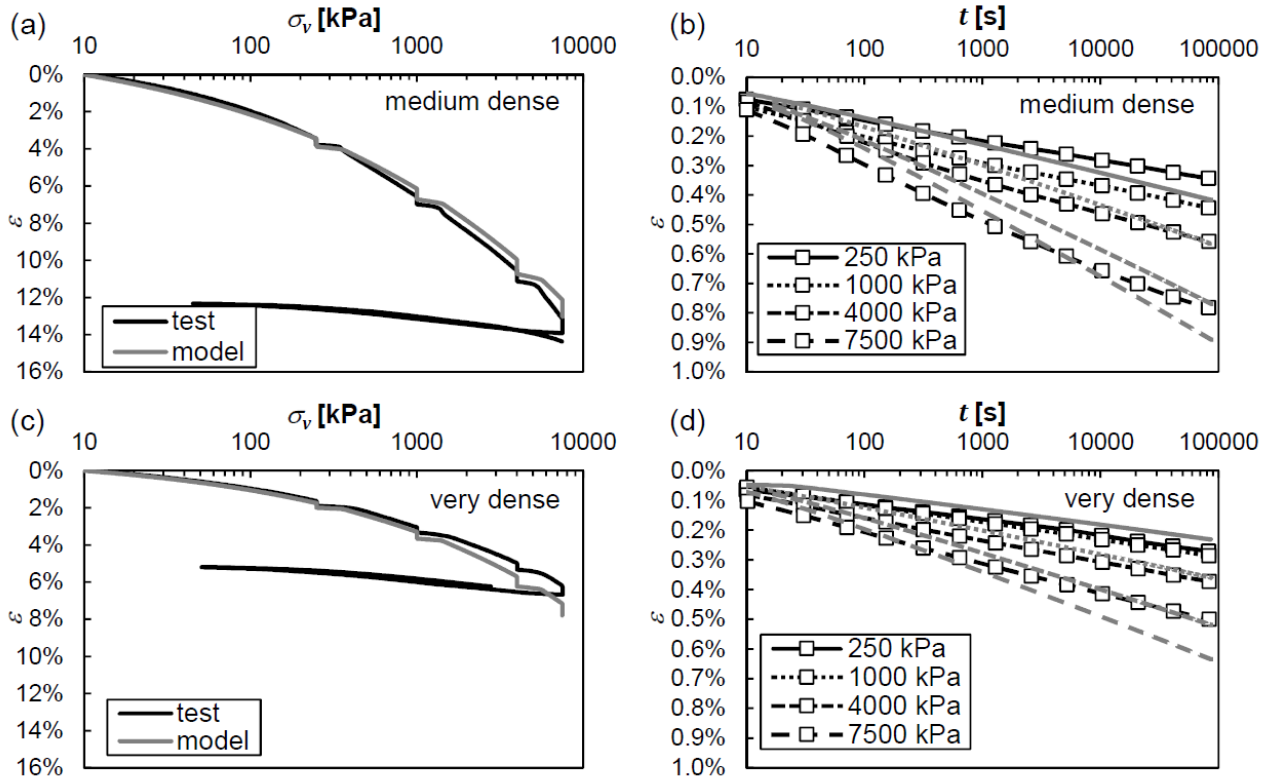

Figure 6.15: Simulation of creep tests with CRS loading at 1.0%/min of (a)/(b) medium dense and (c)/(d) very dense sand MS

6.4.2 Stress relaxation tests

The stress relaxation tests on medium dense and very dense sand MS from Section 4.7.5 were simulated with the same parameter combination as the previously presented creep tests. Note that this viscosity index is significantly smaller than the viscosity index that results from relaxation tests (cf. Figure 4.56 (a)). The index from creep tests was chosen to emphasize the fact that with the chosen constitutive model the creep and relaxation behaviour of sands cannot be modelled by the same parameter set. The reference strain rate D_r was again identical to the loading strain rate to ensure OCR = 1.0 at the beginning of relaxation. The simulation results presented in Figure 6.16 show that the stress relaxation is strongly underestimated for the lower preconsolidation stresses of 250 and 1000 kPa. Stress relaxation at the preconsolidation stresses of 4000 and 7500 kPa is modelled satisfyingly as the viscosity index from creep and relaxation tests become similar at high stresses (cf. Figure 4.56 (a)). Qualitatively, the model can also capture the decreasing normalized stress relaxation σ/σ_0 at higher stresses. The model predicts an increase of the swelling index κ^0 and therefore a reduction of the rate of stress change with increasing preconsolidation stress (cf. Section 4.7.5). The κ^0 values determined from the simulation results are presented in Figure 6.17. Their trend fits

qualitatively and quantitatively very well with the κ^0 values determined from experiments (cf. Figure 4.44 (b)). Despite that, the model underestimates the relative stress relaxation at lower stresses due to the constant viscosity index determined from creep tests.

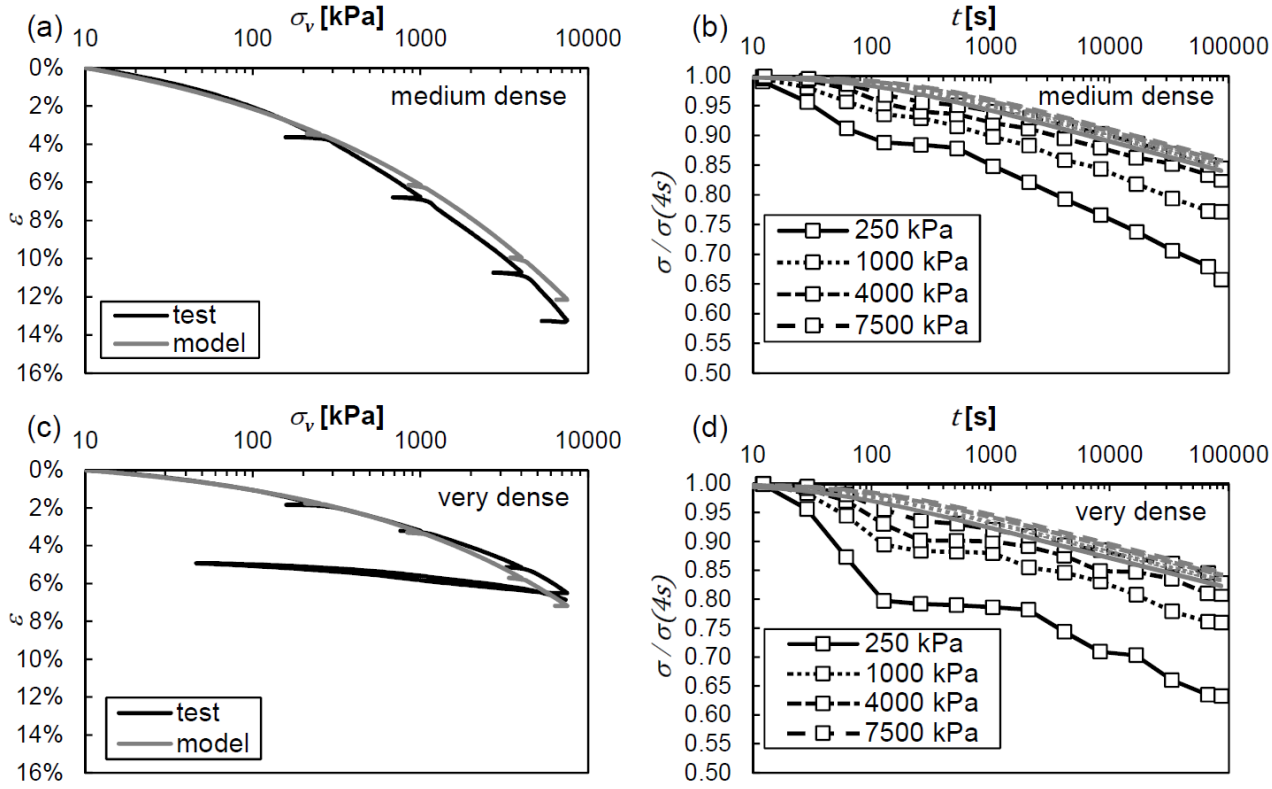

Figure 6.16: Simulation of stress relaxation tests with CRS loading at 0.01%/min of (a)/(b) medium dense and (c)/(d) very dense sand MS

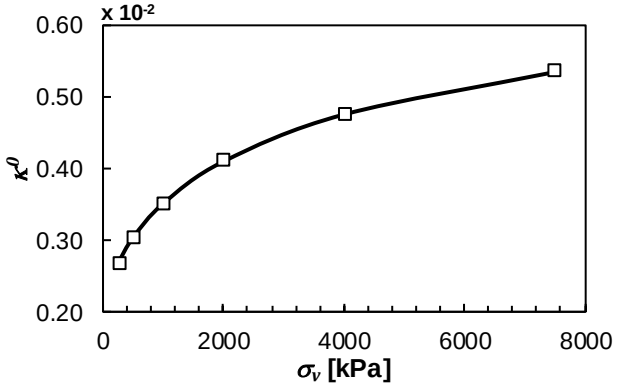

Figure 6.17: Swelling index κ^0 determined from simulation of CRS test with un- and reloading phases on medium dense sand MS presented in Figure 6.6

6.4.3 Test with sudden changes of strain rate

Figure 6.18 shows the comparison of the laboratory test result and the simulation with medium dense sand MS with sudden 1000-fold changes in loading strain rate. It is obvious that the stress jump upon a sudden change of loading strain rate is constant in the simulation while the laboratory test behaviour

can be identified as TESRA (cf. Sections 3.3.2. and 4.7.4). To represent TESRA or other rate-dependent responses (cf. Section 3.3.2) the viscosity index I_v should decay with the strain ($I_v = f(\varepsilon - \varepsilon_j)$) starting from the strain ε_j at which the strain rate jump occured. Such decay functions were proposed by TATSUOKA *et al.* (2008), but are difficult to calibrate and apply in constitutive models.

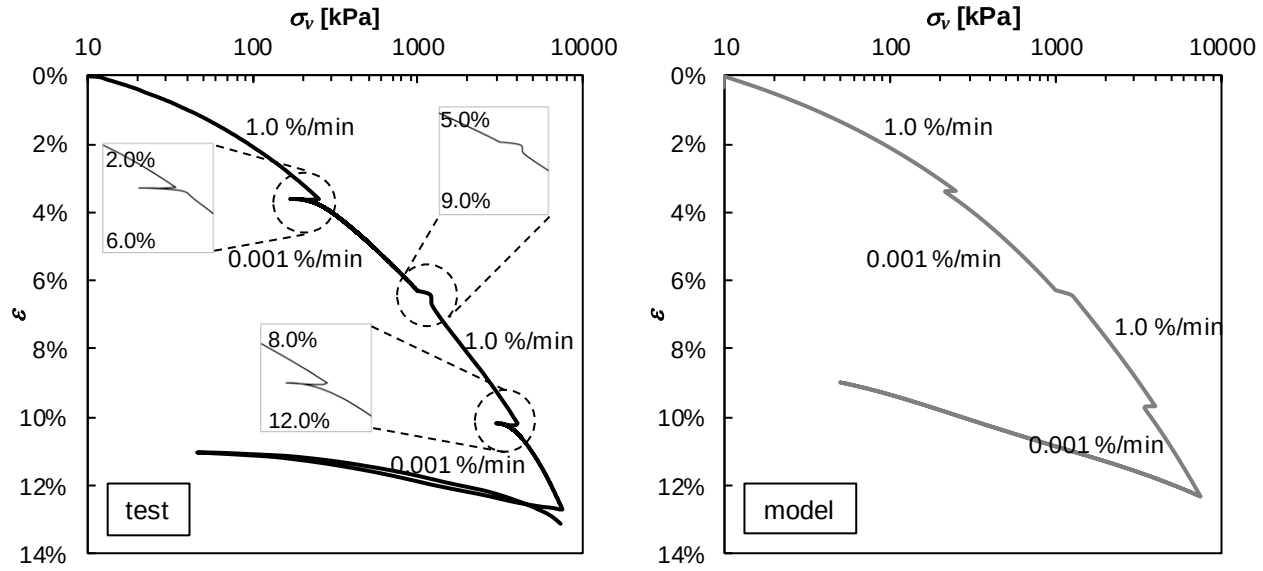

Figure 6.18: Simulation of test with sudden changes of strain rate on medium dense sand MS

6.5 Finite-Element-Modelling of the time-dependent deformations of an open cast mining dump

In this section, creep settlements of open cast mining dumps in the Renish lignite mining area (cf. Section 5.2) are predicted using the SSC-model after VERMEER & NEHER (1999). As was presented in Section 4, sands do not follow the same stress- and time-dependent compression behaviour as soft soils. Models, which are based on the behaviour of fine grained soils, like all models following the isotache-concept, can therefore only be applied under consideration of some limitations and prerequisites. Three different models – SSC, the NIEMUNIS model and the GUDEHUS model – were reviewed in the previous sections with respect to their stress and time-dependent compression behaviour. The GUDEHUS model is most suited for granular soils. Nevertheless, so far the investigations with this model are limited to oedometric compression and it is not available yet for modelling boundary value problems. However, it is shown in the following that particularly in the case of the described open cast mines the observed creep settlements can be modelled by classical isotache models as the SSC-model.

6.5.1 Modelling of dump surface settlements

Most important prereqisite for a successful modelling of the creep strains in the dump is the correct determination of the creep-coefficient characterizing the viscous response of the soil. This can be done using long-term surface settlement measurements (cf. Section 5.2.1) or by the help of oedometer tests (cf. Section 5.2.3), if no long-term measurements are available. Another important aspect is the consideration of the dumping process, when modelling the dump settlements. This was already

addressed in Section 5.2.1. The end of dumping is usually chosen as the zero point in time for evaluating the creep-coefficient. At this point in time the dump can usually be considered to be in a normally consolidated state, because dumping of the last layer resets all previously developed overconsolidation due to creep. The last layer needs to have a sufficient thickness to ensure the reset (cf. Section 5.2.1). In cases where this is not certain, the modelling of the dumping process ensures the correct consideration of the age of the deeper dumping layers in the settlement prediction.
To exemplify this, the dumping process and subsequent creep settlement of the transmission towers 13 and 14, whose settlement data were analyzed in Section 5.2.2, is modelled using SSC. The dumping sequence at the two towers is presented in Figure 6.19. The dump was constructed at both tower locations between the year 1996 and January 2003 with a total thickness of 135 and 142 m at transmission tower 13 and 14 respectively. The two sites were chosen, because the thickness of the last dumping layer is significantly different. At transmission tower 13 the last dumping layer has a thickness of 9 m and at transmission tower 14 of 27 m.

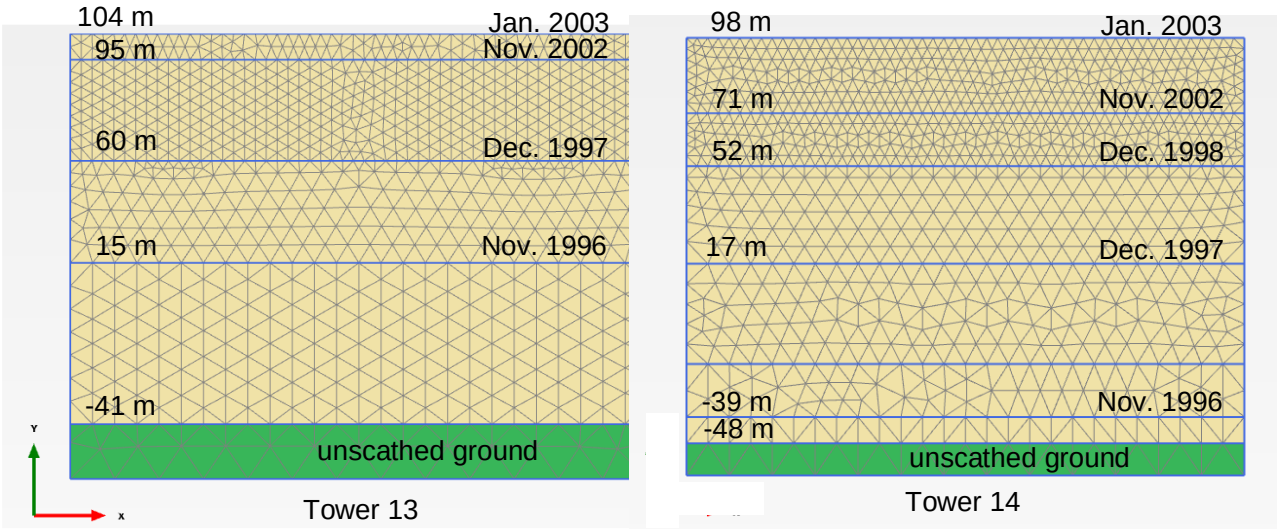

Figure 6.19: Dumping sequence at transmission towers 13 and 14

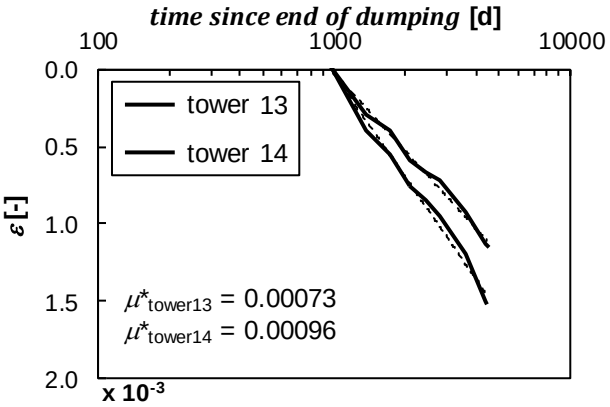

Figure 6.20: Long-term measurement data of transmission towers 13 and 14 along with the derived creep-coefficients

The constitutive model parameters for the towers are summarized in Table A.12.1. The creep-coefficients were calibrated using the measurement data presented in Section 5.2.2. The data is given again in Figure 6.20 along with the derived creep-coefficients. The measurements started both about

2.7 a after dumping ended and lasted for 9.5 a. The unscathed ground beneath the dump was modelled as a material with no time-dependent deformations (cf. Section 5.2.3).
The data does not give a perfectly linear trend on a logarithmic time scale, but can be nevertheless very well approximated by a logarithmically linear approach. The remaining parameters were calibrated using measurement data of test loads, deformation measurements of erected structures on the dump and laboratory element tests. Transmission tower 13 shows less creep deformations in the measurement period than tower 14, although the measurements started both at nearly the same time after the end of dumping. This can be explained by the smaller thickness of the last dumping layer at tower 13.

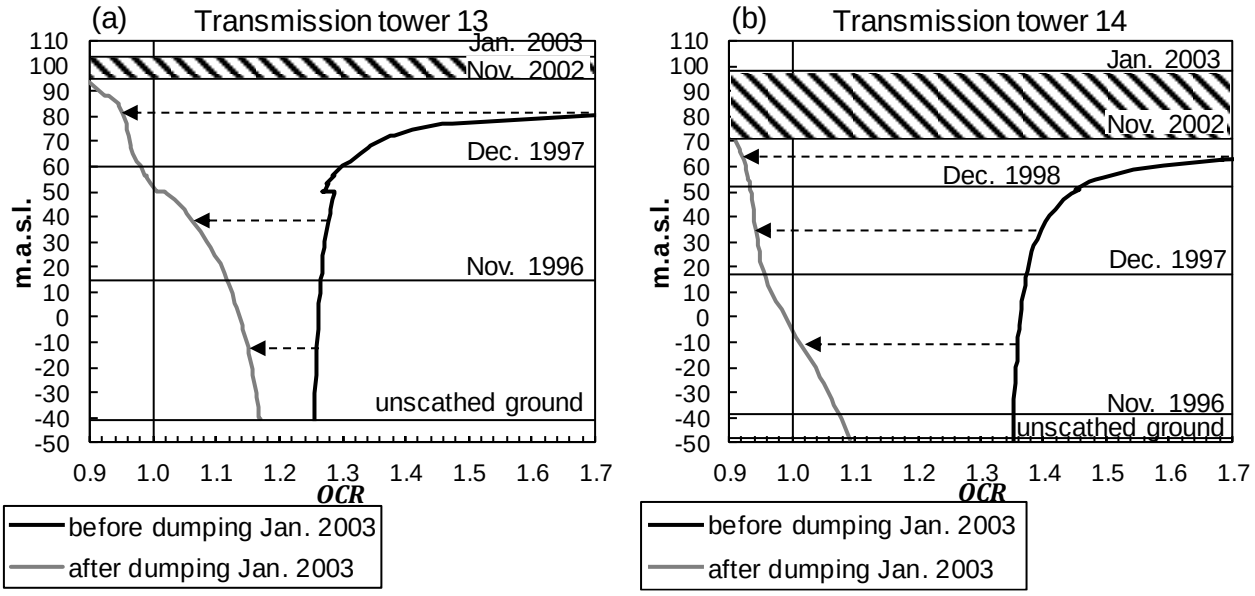

Figure 6.21: Resetting effect of the overconsolidation ratio caused by dumping of the last dumping layer: (a) transmission tower 13 and (b) transmission tower 14

The simulation results in Figure 6.21 show the effect of the last dumping layer on the overconsolidation state of the dump. It shows the OCR over the depth before and after dumping of the last layer. In both cases, the last layer has the effect that the overconsolidated state, which is generated by the creep deformations between the dumping sequences, is moved towards and beyond the normally consolidated state. However, in the case of tower 13, where the last dumping layer has only a thickness of 9 m, the effect is much less pronounced and OCR remains larger than at tower 14. At tower 14 only the lower dumping layer remains partly overconsolidated and the dump can be assumed to be in average in a normally consolidated state with OCR = 1.0. The simulation results only give a qualitative picture of the state of the soil and clarify the mechanism. The difference in the OCR also explains, why the measured creep strains at tower 13, despite of the comparable soil conditions, are lower than at tower 14.
Furthermore, an important condition for the successful prediction of the dump settlements is that the stress change caused by the load from a structure is significantly smaller than the mean stress level in the dump body and the creep-coefficient can be assumed to be a constant material parameter. Otherwise the stress change could lead to larger creep-coefficients, which cannot be considered by the SSC-model. For example, the mean effective vertical stress in the Garzweiler dump, which is

mostly around 140 to 150 m thick, is 1.2 to 1.3 MPa. Therefore, this condition is usually fulfilled in dumps of open cast mines as stress changes due to structural loads will be much smaller than these values.
On the contrary, in the vicinity of piles or permanent anchors stress changes induced by structural loads can be larger in comparison with the initial stress state and the long-term creep deformations experienced by these geotechnical structures can be significant. In these cases, the influence of the stress change on the creep-coefficient must be taken into account and the SSC-model would not be sufficient to capture the creep behaviour.

6.5.2 Measuring field with hydrostatic measuring line

In order to investigate the applicability of SSC, the measurement results of a hydrostatic measuring line installed in the Garzweiler open cast mining dump are calculated.

Measuring system

The hydrostatic measuring system was developed by LHOTZKY + PARTNER ENGINEERING COMPANY LTD.. The measuring principle of the hydrostatic line measurement is based on the discontinuous measurement of the hydrostatic pressure between predefined equidistant points (e.g. 25 cm) in a measuring hose installed along the measuring profile. The measurement of the hose is related to a reference point. At the beginning of the measurement, the hose is filled with water. After starting the measurement, the water is pumped out of the measuring hose between predefined equidistant points. If an increment is emptied, the hydrostatic pressure level between the current measuring point and the reference level is measured with a pressure sensor. The pressure level and the current values of the temperature probes are stored and the settlements are calculated by comparison of the hydrostatic pressure heads between the measurement cycles. The settlement measurements are compensated with respect to density variations of the water due to temperature fluctuations along the measuring line. The measuring accuracy of the system lies at +/- 1.0 mm. Figure 6.22 presents the measuring principle.

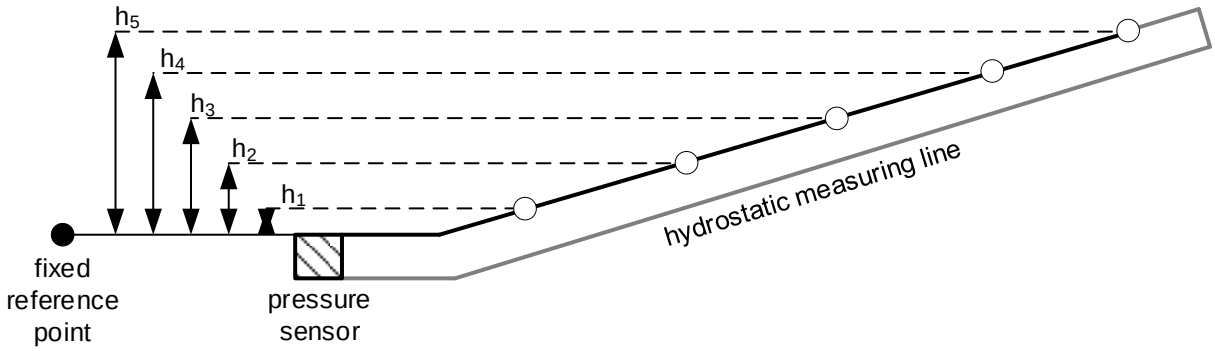

Figure 6.22: Measuring principle of the hydrostatic measuring line (adapted from LHOTZKY + PARTNER ENGINEERING COMPANY LTD.)

Installation

The measuring line in the Garzweiler dump was installed in January 2010 with a length of 160 m beneath the top most dumping layer. Pictures of the installation process are shown in Appendix A.12.1. In March 2010 the line was prolonged by an additional 100 m to a total length of 260 m. A detailed cross section through the measuring field with all installed sensors is shown in Figure 6.23. In addition to the measuring systems, the dumping sequence above the measuring line is presented. Dumping took place between 19th of January and 26th of May 2010 with a thickness above the hydrostatic measuring line of 13.2 m in the south and 16 m in the north. A cross section showing the entire dump beneath the measuring line is shown in Figure 6.24. The main dump body with a thickness of about 140 m was constructed between the years 2006 and 2011. Dumping in the vicinity of the measuring field ended in April 2011.

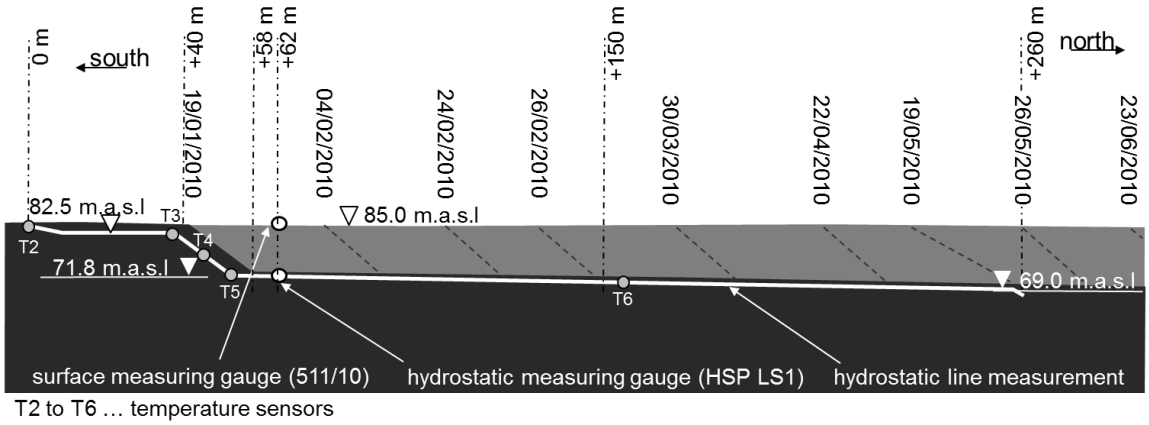

T2 to T6 … temperature sensors

Figure 6.23: Cross section along the measuring field with representation of the dumping process above the hydrostatic measuring line

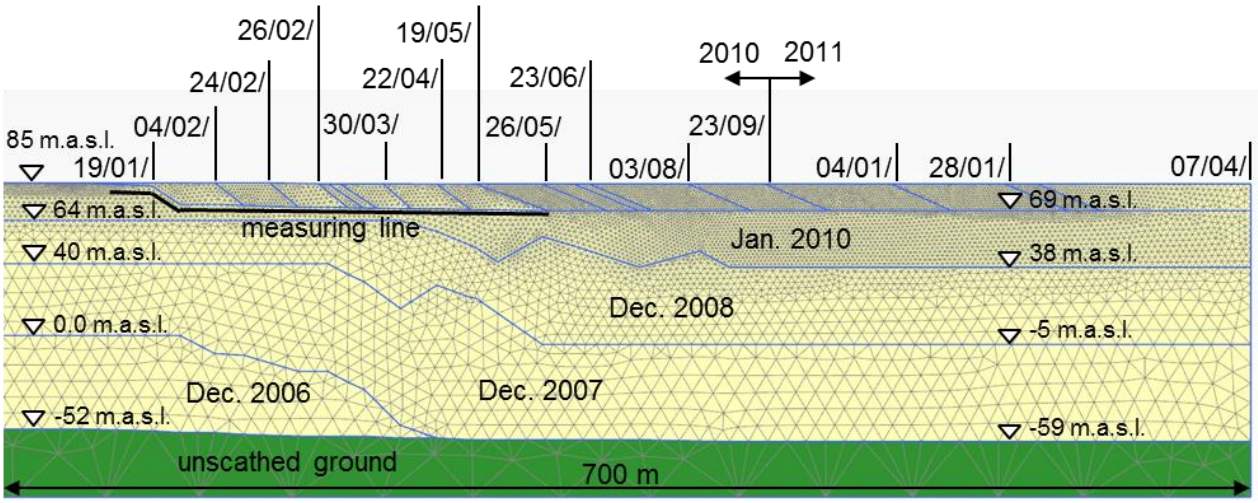

Figure 6.24: Cross section through the entire dump in the vicinity of the measuring field

Measurements

The settlement measuring data was recorded with the aid of the hydrostatic measuring line, a hydrostatic measuring gauge (HSP-LS1) and a surface measuring gauge (511/10). The measuring data of the level gauges HSP-LS1 and 511/10 were automatically recorded in daily intervals. For the hydrostatic measuring gauge HSP-LS1 measurement data are available starting from 19/01/2010 and for

the surface measuring gauge 511/10 starting from 31/01/2010. The last available measurement for both gauges was taken on 13/11/2014. The recorded data of HSP-LS1 and 511/10 is displayed in Figure 6.25. The measurement of the reference point for the hydrostatic measuring line and the hydrostatic measuring level HSP-LS01 as well as the determination of the vertical position of the surface measuring point 511/10 (in each case absolute values [m.a.s.l.]) was carried out with the help of GPS measurements. GPS data are influenced by atmospheric and temperature fluctuations. To compensate the influences, temperature and air pressure were measured. The temperature sensors (T2 to T6) are shown in Figure 6.23. Atmospheric pressure was measured at the surface of the dump. The recordings of temperature and atmospheric pressure during the measurement period are shown in Figure A.12.1. Despite compensation, fluctuations in the measurement data remain due to the measurement inaccuracy. This can be seen in the measurement results of HSP-LS1 and 511/10 after 800 d since start of observation, where the deformation rate is so small that measurement inaccuracy is visible. The measurement inaccuracy of the GPS measurements also affects the recordings of the hydrostatic measuring line. As mentioned, the accuracy of the line lies at +/- 1.0 mm. But the data is always related to a fixed reference point, which is also measured by GPS. The overall inaccuracy of the system is the inaccuracy of the GPS measurement plus the one from the measuring line and can be estimated at +/- 1.0 cm.

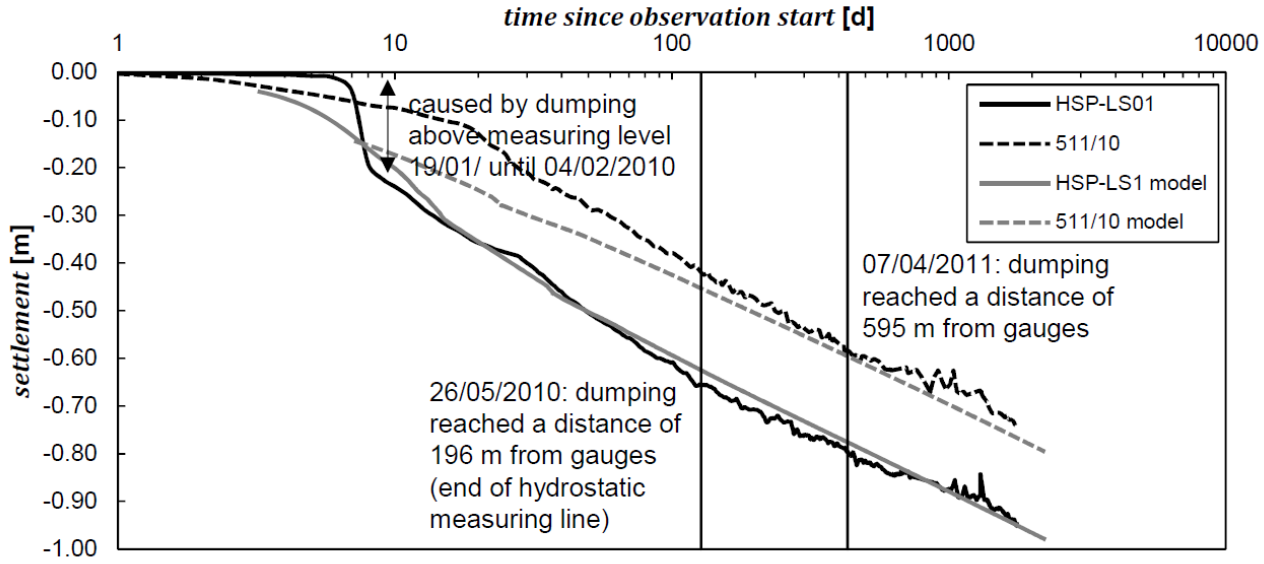

Figure 6.25: Settlements recorded at HSP-LS1 and 511/10 and their simulation using the SSC model

The measuring data in Figure 6.25 show that both gauges converge to a parallel almost linear trend on a logarithmic time scale. In the data of HSP-LS1 the instant settlements of approximately 25 cm due to the dumping above the gauge are clearly visible. The logarithmic gradient, i.e. the creep-coefficient, of both lines decreases slightly with increasing time. This is because dumping gradually moves away and the settlements are still influenced by it. The point at which the dumping horizon reached a distance of more than 595 m is marked in Figure 6.25. Beyond that no detailed informations about the dumping process are available, but it can be assumed that the settlements are no longer influenced by the dumping process.

The initial measurement for the first 160 m long section of the hydrostatic measuring line was carried out on 19/01/2010 and the initial measurement for the entire measuring line with a length of 260 m was carried out on 26/02/2010. In the beginning, the measurement intervals were approximately half a year and later increased to approximately one year intervals. The last measurement of the line was taken on 02/02/2016, which gives a measurement period of almost six years. The subsequently presented analysis only considers the measurement data starting from 26/02/2010, when the dumping already reached about half of the length of the hydrostatic measuring line (cf. Figure 6.24). The measurement data is presented in Figure 6.26. The measurements of the 4th and 5th following measurement (FM) and of the 6th and 7th FM both almost coincide, indicating that some error in the measurements occured. They may be influenced by the inaccuracy of the measuring system, which leads to the apparent stagnation of the settlements, which actually does not occur. This conlusion is supported by the long-term surface measurements on transmission towers in areas of the dump with an age of more than 23 a (cf. Section 5.2.2). These measurements showed no stagnation of the creep settlements.

Modelling

The calibration of the constitutive model parameters for the measuring field was done by back calculation of the settlement data of gauges HSP-LS1 and 511/10, which are a combination of stress- and time-dependent settlements. The results are presented in Figure 6.25. The determined parameter combination is listed in Table A.12.2. The creep-coefficient was determined by regression analysis of the linear section of the compression curve using (3.37). The compression index was determined by simulating the settlements of HSP-LS01, which showed instant settlements due to the dumping above it. The swelling index was estimated to be $\kappa^* = \lambda^* / 4.5$. The unscathed ground beneath the dump was modelled as a material with no time-dependent deformations (cf. Section 5.2.3).
Using this parameter combination, the settlements recorded by the hydrostatic measuring line were simulated. The simulation was performed with the assumption of homogenous soil conditions in terms of relative density and soil type in the dump. This assumption is supported by the classification results presented in Section 5.1. Additionally, the calibration of the model using surface measurement data, which in itself gives average straining behaviour over the entire depth of the dump, implies a homogenization of the dump properties. The simulation results are presented in Figure 6.26. They are only displayed from station 55 m, because this is the section of interest. The measurement and simulation data can be divided into two different parts. The first section until station 120 m was dumped prior to the initial measurement on 26/02/2010 and thus the data displays creep settlements, which are only slightly influenced by the adjacent dumping. Beyond station 120 m the measurements recorded the instantaneous settlements caused by the dumping process, which can be recognized by the more uneven course of the measurement curves. The settlement troughs produced by the dumping sections can partly be recognized in the measurements and are also visible in the simulation results. Of course, the exact settlements cannot be predicted by the simulation, because the dumping process is only roughly modelled. But still, the agreement between measurement data and simulation is very good, considering the complex interaction between stress- and time-dependent settlements.

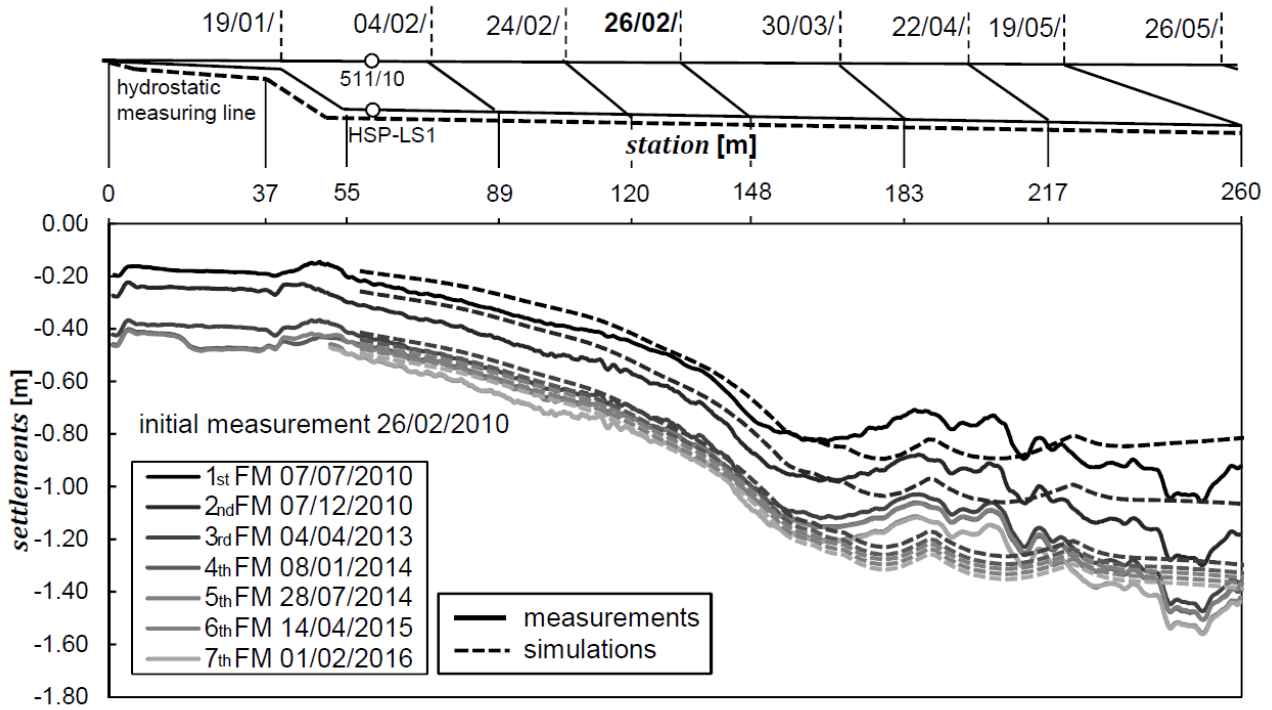

Figure 6.26: Settlement measurements and simulation of the hydrostatic measuring line between initial measurement at 26/02/2010 and 01/02/2016

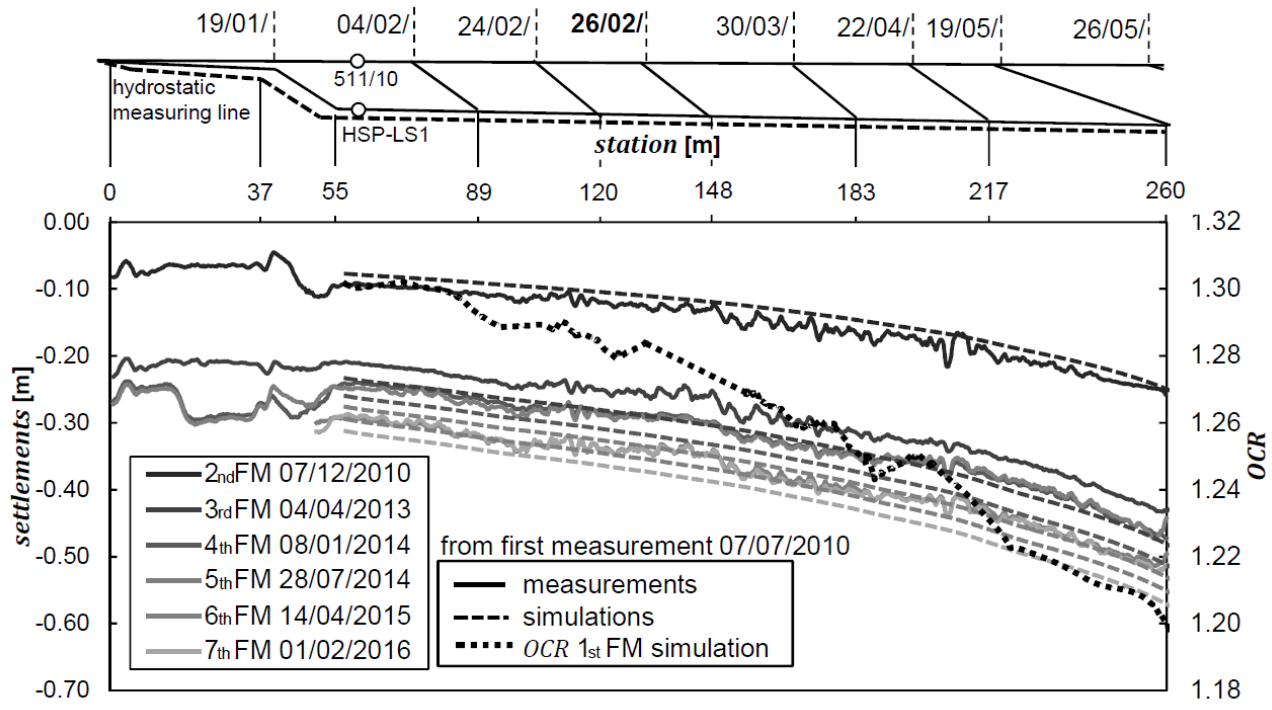

Figure 6.27: Settlement measurements and simulation of the hydrostatic measuring line between first measurement after the initial measurements at 07/07/2010 and 01/02/2016

For a better insight into the modelling results on time-dependent creep settlements of the hydrostatic measuring line, the settlements are also evaluated starting from the 1st FM on 07/07/2010. The measurement and simulation results are presented in Figure 6.27. Also displayed is the OCR along

the hydrostatic measuring line determined in the simulation. Again, the agreement between simulated and measured settlements is very good, although the simulation overestimates the deformations with increasing observation time. The model can capture the higher creep rate towards the north of the line, which comes from the more recent dumping and therefore lower OCR in this direction. The OCR decreases from 1.31 at station 55 m to 1.20 at station 260 m.

6.5.3 Conclusions

The SSC model is able to simulate the complex time- and stress-dependent evolution of settlements during and after dumping. The model parameters controlling the viscous behaviour can be determined from field measurements and the construction phases of the dump need to be realistically considered in the simulation.

Isotache models like SSC can be used to predict the creep deformations of the dump after the end of dumping despite the findings in Section 4, if the following prerequisites are fulfilled:

– The last dumping layer causes the state of the soil to approach a normally consolidated state and the creep-coefficient can correctly be determined with the zero point at the end of dumping where $OCR \approx 1.0$,
– the dumping process is known and can be modelled to account for the different age of the layers and
– the stress state of the dump does not significantly change compared to the mean stress in the dump in the time interval of the prediction and therefore the creep-coefficient can be assumed constant.

7 Summary, discussion and outlook

7.1 Summary

In this study, the time-dependent behaviour of sands was investigated by means of oedometric compression tests and the evaluation of long-term field measurements on open cast mining dumps in the Renish lignite mining area. Three constitutive models were reviewed with respect to their capabilities of modelling the stress and time-dependent compression behaviour of sands.

The viscous behaviour of sands is governed by the time-dependent degradation of grains at their contacts, so-called static fatigue. Depending on the stress level this can be grinding of asperities, breaking or crushing of particle surface protrusions or shattering of entire particles. In turn, this leads to rearrangements of the transmitting force chains and to creep deformations under constant macroscopic stresses or stress relaxation at constant soil volume. The viscous behaviour depends on material properties like the grain size distribution, mineral hardness, particle shape, strength and stiffness. Furthermore, state variables such as density and the stress state influence the viscous response of the sands.

In this study, six different sands were evaluated regarding their viscous behaviour under oedometric loading conditions. The three mechanisms of time-dependent behaviour, creep, strain rate dependency and stress relaxation were investigated. Furthermore, the behaviour after different loading and unloading paths was studied. Besides the influence of the material properties, also the influence of the initial density, stress state at low and high pressure, strain rate, loading history, duration of loading and the water content were investigated. A challenging aspect of the tests was the repeatability of the initial conditions of the soil and the control of the test conditions in the load frames, especially in stress relaxation tests.

The oedometric creep rate is highly dependent on the density of the sand and the stress level. Higher stresses and lower density yield larger creep strains. A classical isotache approach is not suited for description of such creep behaviour. Isotaches and isochrones are not equivalent in sands. Description of the creep behaviour by a constant ratio C_α/C_c is only applicable at fine contents of the sand larger than approximately 14wt-%.

By evaluation of many oedometer tests with incremental loading and CRS loading on several sands with different initial densities and under stresses up to 7500 kPa, an empirical approach was developed to predict the oedometric creep-coefficient in a large stress and density range. The concept is valid at stresses where level I to level II grain degradation occurs, without significant changes of the GSD.

An extended test series on creep, strain rate-dependency and stress relaxation was performed on three sands from the Garzweiler open cast mine, one clean sand and two sands with 14 respectively 25wt-% fine content. CRS creep tests with different loading strain rates revealed that in sands, just like in soft fine grained soils, the initial creep rate depends on the previous loading strain rate yielding larger initial creep rates at higher loading strain rates. Despite of that, the creep curves converge at

each stress level to a constant gradient on a logarithmic time scale, i.e. a constant creep-coefficient. On the other hand, CRS loading tests on clean sand with a 1000-fold difference in strain rate showed no dependency of the stress-strain response on the strain rate as it would be expected for soft soils. In contrast, sand with 46wt-% content of fines showed the expected dependency of higher stiffness at higher loading strain rate. Tests with sudden changes of the loading strain rates revealed a TESRA type response for the clean sand and an isotache type response for sands with more than 14wt-% fine content.

Stress relaxation tests were also analyzed with respect to the stress and density dependency and the influence of the loading strain rate on the subsequent relaxation rate. The tests showed that relaxation in all soils is nearly independent of the relative density. The clean sand showed strongly decreasing normalized relaxation σ/σ_0 in 24 h and viscosity indices with increasing preconsolidation stress, while the other two sands showed constant viscosity indices. The reference time increased with the vertical effective stress in all sands. Assuming the decomposition of the strain rate into an elastic and a viscous part, the smaller normalized relaxation σ/σ_0 at higher vertical effective stresses can be explained by increasing swelling indices κ^0 at higher preconsolidation stresses observed for the clean sand.

The influence of the loading strain rate on stress relaxation was tested with the clean sand. Larger loading strain rates yield higher initial relaxation rates and vice versa, similar to the creep rate. The corresponding reference time increases with decreasing loading strain rate.

Additionally to the tests on the four Garzweiler sands studying creep, strain rate-dependency and stress relaxation, several test series were performed to investigate other influencing factors on the viscous behaviour. The behaviour of sand in long-term creep tests, under high pressure of up to 340 MPa and the influence of the mean grain size as well as of the water content were tested.

The long-term creep tests on clean sand revealed an under-linear trend of the compression curve on a logarithmic time scale ultimately leading to stagnation of the creep deformations. The time interval in which a stagnation happens is strongly dependent on the soil properties and external influences. Clean sands showed much faster stagnation than the sands with large fine content. Long-term relaxation tests on the other hand showed no deviation from a linear trend in the logarithm of time. This indicates that the deformations that happen during creep, but not during stress relexation, contribute to the stagnation of the logarithmic creep strains.

High pressure tests showed that the stress-dependent compression behaviour of sand is independent of the initial density at very high stress levels, where the grain material strength dominates the compression behaviour. The tests revealed static fatigue as the creep mechanism in the grain assembly. At very high vertical effective stresses above 50 MPa, creep strains start to decrease, as the increase of contact points and the influence of the smooth surfaces of the freshly broken grains outweighs the increased external loading of the samples. This reduces the contact forces between the grains leading to less degradation and creep.

Tests on the influence of the GSD on creep revealed decreasing creep strains with increasing d_{50}. The creep-coefficient is inversely proportial to d_{50}, considering constant soil properties regarding mineralogy and grain shape. Despite of the fact that the single particle strength decreases with larger

grain size, the reduced number of potentially failing asperities of the grains in assemblies of larger grains is the dominating influence and reduces creep.
The water content influences the creep behaviour. Upon full saturation, creep increases due to intensified grain degradation caused by increased “stress corrosion cracking” (ATKINSON, 1979).

The motivation for this study originated from the necessity to give accurate predictions for creep deformations of sandy open cast mining dumps in the Renish lignite mining area near Cologne (Germany). Fortunately, ample data of long-term settlement recordings were available from these dumps. They were analyzed with respect to the creep behaviour of the dump body and different properties influencing the deformations. The age of the dump, its thickness, the dumping process and the start as well as the duration of the measurements were evaluated. Futhermore, the data of a settlement gauge capable of recording settlements in different depths of the dump were evaluated with respect to the influence of the overburden stresses on creep.
Long-term settlement recordings revealed a linear creep behaviour on a logarithmic time scale even for dumps with an age of more than 23 a. The determination of the creep-coefficient for use in simulations of the dump deformations was presented. Most important is the choice of the zero point in time. The dump can be assumed to be in a normally consolidated state at the end of dumping, if the thickness of the last dumping layer exceeds a certain thickness and induces large enough settlements to reset the overconsolidation due to creep to $OCR \approx 1.0$. For the Garzweiler dump a thickness of approximately 20 m is sufficient. The end of dumping can then be chosen as the zero point in time for evaluation of the creep coefficients, making results comparable.
The evaluation of the data of the settlement gauge capable of recording settlements in different depths of the dump proved the stress dependency of the creep strains. The increase in creep with the overburden stress can be described by the empirical approach for the stress and density dependent determination of the creep-coefficient presented in Section 4.6.3.
The comparison of creep strains of Garzweiler sands measured in the laboratory and in the field showed that the strains from the laboratory are about 50% smaller than the ones determined from field measurements. The creep in the field can however be determined via laboratory tests when using the empirical method presented in Section 4.6.3 together with information about the in situ relative density of the soil determined from CPTs. This indicates that the generally higher density of the laboratory samples compared to the field is the main reason for the difference in creep behaviour.

The presented findings on the viscous behaviour of granular soil make its modelling in the framework of a constitutive continuum model very complex. It can no longer be described by the isotache-concept using the viscosity index I_v as a constant soil property. It still does not exist a constitutive model, which can model creep with its stress and density dependency, stress relaxation, which is more pronounced than creep and the different strain rate dependent behaviour types within one unified approach.
Three models designed for the prediction of soft fine grained soil behaviour were reviewed with respect to their stress and time-dependent behaviour. The visco-hypoplastic model after GUDEHUS (2004), which uses the BAUER compression law, was found to be most suited to model the stress and time-dependent compression behaviour of sands. The original model is referenced to a fixed e_i – compression curve, which was modified to consider different RCL related to initial states different

from e_i. The model predicts a stress-dependent creep behaviour by the BAUER compression law. It is able to predict the creep behaviour of medium dense and very dense sand observed in oedometer tests using a constant viscosity index I_v. However, using the same I_v, stress relaxation is strongly underestimated. Furthermore, the model predicts an isotach-type behaviour upon sudden changes of loading strain rate with a remaining relative stress change with continued straining. Contrary, the tested clean sand showed TESRA type behaviour, which cannot be predicted by the model.
Finally, it was tested under which prerequisites the creep deformations of the Garzweiler dump can be predicted by using a classical isotache model like SSC. Three major conditions were detected:

1. The last dumping layer causes the state of the soil to approach a normally consolidated state and the creep-coefficient can correctly be determined with the zero point at the end of dumping where $OCR \approx 1.0$,
2. the dumping process is known and can be modelled to account for the different age of the layers and
3. the stress state of the dump does not significantly change compared to the mean stress in the dump in the time interval of the prediction and therefore the creep-coefficient can be assumed constant.

7.2 Discussion and outlook

Creep deformations of sands can be neglected in most building projects, but under special boundary conditions they have to be considered. Until now no constitutive model is available, which can be applied in Finite Element analysis for the prediction of all discovered aspects of time-dependent granular soil behaviour. This study is a contribution towards a better understanding and provides an experimental data base for the development of a model to predict such behaviour in the future. The limitation to oedometric loading paths leaves room to extent the findings to triaxial loading cases. To realize a similar laboratory inspection of the viscous phenomena of creep, rate dependency and stress relaxation in triaxial testing, which is still missing in literature, should be the next step. The sensitivity of the viscous effects to external changes of the test conditions makes precise laboratory experiments necessary. It requires careful preparation of the samples and close monitoring of the external conditions such as temperature and possible vibrations acting on the soil. The fulfilment of the test conditions like constant stress or constant volumetric strain need to be very precise to ensure reliable test results.

The comprehensive modelling of the discovered behaviour within a continuum model faces the problem of balancing the applicability of the model with its capability to simulate all aspects of the behaviour. Models, which tried to capture for instance the manifold types of the rate-dependent response of sand, are very hard to calibrate and their use in practice is questionable. This leaves room for future developments.

Predictions of long-term creep deformations, stress relaxation and strain rate dependent behaviour of granular soil are just one aspect, which needs further investigations and research. Another issue is the relation between ageing and viscous effects in granular soils. Finding ways to predict ageing effects by quantifying and qualitatively evaluating viscous properties of granular soil is a promising field for future studies. The consideration of ageing effects, for example on the bearing capacity of displacement piles, could lead to more efficient and economically beneficial designs of structures.

References

Antonyuk, S., Tomas, J., Heinrich, S. and Mörl, L. (2005) *Breakage behaviour of spherical granulates by compression*, Chemical Engineering Science, 60(14), pp. 4031–4044.

Atkinson, B. K. (1979) *A fracture mechanics study of subcritical tensile cracking of quartz in wet environments*, Pure and Applied Geophysics, 117(5), pp. 1011–1024.

Atkinson, B. K. and Meredith, P. G. (1981) *Stress corrosion cracking of quartz: a note on the influence of chemical environment*, Tectonophysics, 77, pp. T1–T11.

Augustesen, A., Liingaard, M. and Lade, P. V. (2004) *Evaluation of time-dependent behavior of soils*, ASCE Int. J. Geomech., 4(3), pp. 137–156.

Bauer, E. (1992) *Zum mechanischen Verhalten granularer Stoffe unter vorwiegend oedometrischer Beanspruchung*. Universität Fridericiana Karlsruhe.

Bauer, E. (1996) *Calibration of a Comprehensive Hypoplastic Model for Granular Materials.*, Soils and Foundations, 36(1), pp. 13–26.

Bauer, E. (2000) *Conditions for embedding Casagrande's critical states into hypoplasticity*, Mechanics of Cohesive-Frictional Materials, 5(2), pp. 125–148.

Di Benedetto, H., Tatsuoka, F. and Ishihara, M. (2002) *Time-dependent shear deformation characteristics of sand and their constitutive modelling*, Soils and foundations, 42(2), pp. 1–22.

Bjerrum, L. (1967) *Engineering Geology of normally-consolidated Norwegian Marine Clays as related to settlement of buildings*, Geotechnique, 17, pp. 81–118.

Bowman, E. T. and Soga, K. (2003) *Creep, Ageing and Microstructural Change in Dense Granular Materials*, Soils and Foundations, 43(4), pp. 107–117.

Brandl, H. (2015) *Vom Grundbau zur Bodenmechanik - von der Bodenmechnik zur Geotechnik*, in Aktuelle Forschung in der Bodenmechnik 2015, Tagungsband zur 2. Deutschen Bodenmechnik Tagung. Bochum: Schanz, T., Hettler, A., pp. 3–23.

Brzesowsky, R. H., Hangx, S. J. T., Brantut, N. and Spiers, C. J. (2014) *Compaction creep of sands due to time-dependent grain failure : effects of chemical environment , applied stress and grain size*, Journal of Geophysical Research: Solid Earth, 119.

Buisman, K. (1936) *Results of long duration settlement tests*, in Proceedings of the 1st International Conference on Soil Mechanics and Foundation Engineering. Cambridge, Mass., pp. 103–107.

Butterfield, A. (1979) *A new compression law for soils (an advance on e-log p')*, Geotechnique, 29, pp. 469–480.

Cavarretta, I. ., O'Sullivan, C. and Coop, M. R. (2017) *The relevance of roundness to the crushing strength of granular materials*, Géotechnique, 67(4), pp. 301–312.

Charles-Cruz, C. A., Cousens, T. W. and Stewart, D. I. (2008) *Compressibility and Creep Behaviour of Hydraulically Placed PFA and Mine Tailings Fills*, in Proceedings of the 12th Conference of the International Association for Computer Methods and Advances in Geomechanics.

Cho, G.-C., Dodds, J. and Santamarina, J. C. (2006) *Particle Shape Effects on Packing Density, Stiffness, and Strength: Natural and Crushed Sands*, Journal of Geotechnical and Geoenvironmental Engineering, 132(5), pp. 591–602.

Christie, I. F. and Tonks, D. M. (1985) *Developments in the time lines theory of consolidation*, in Proceedings of the XIth International Conference on Soil Mechanics and Foundation Engineering. San Francisco, pp. 423–426.

Chuhan, F. a, Kjeldstad, A., Bjørlykke, K. and Høeg, K. (2003) *Experimental compression of loose sands: relevance to porosity reduction during burial in sedimentary basins*, Canadian Geotechnical Journal, 40(5), pp. 995–1011.

Colliat-Dangus, J. L., Desrues, J. and Foray, P. (1988) *Triaxial testing of granular soil under elevated cell pressure*, in Advanced triaxial testing of soil and rock, ASTM. Philadelphia, pp. 290–310.

Cudmani, R. (2001) *Statische, alternierende und dynamische Penetration in nichtbindigen Böden*. Universität Fridericiana Karlsruhe.

Cudmani, R., Jörger, R. and Wolski, K. (2011) *Hafenerweiterung Port Botany: Wirtschaftliche Lösungen für höchste geotechnische Anforderungen*, in 7. Hans-Lorenz-Symposium, pp. 231–

250.
Degago, S. A., Grimstad, G., Jostad, H. P., Nordal, S. and Olsson, M. (2011) *Use and misuse of the isotache concept with respect to creep hypotheses A and B*, Geotechnique, 61(10), pp. 897–908.
Duttine, A. and Tatsuoka, F. (2009) *Viscous Properties of Granular Materials Having Different Particle Shapes in Direct Shear*, Soils and foundations, 49(5), pp. 777–796.
Eber, W. (2006) *Measurements on the Structural Contribution to Friction in Granular Media*. Technische Universität München.
Enomoto, T., Kawabe, S., Tatsuoka, F., Di Benedetto, H., Hayashi, T. and Duttine, A. (2009) *Effects of Particle Characteristics on the Viscous Properties of Granular Materials in Shear*, Soils and Foundations, 49(1), pp. 25–49.
Fraunhofer Institut ISE (2018) *Nettostromerzeugung in Deutschland in 2018*. https://www.energy-charts.de/energy_pie_de.htm (Accessed: 17 October 2018).
Garlanger, J. E. (1972) *The consolidation of soils exhibiting creep under constant effective stress*, Geotechnique, 22(1), pp. 71–78.
Glasstone, S., Laidler, K. and Eyring, H. (1941) *The Theory of Rate Processes*. New York: McGraw-Hill.
Goldscheider, M. (1972) *Spannungen in Sand bei räumlicher, monotoner Verformung*. Universität Fridericiana Karlsruhe.
Grünthal, G. and Bosse, C. (1996) *Probabilistische Karte der Erdbebengefährdung der Bundesrepublik Deutschland - Erdbebenzonierungskarte für das Nationale Anwendungsdokument zum Eurocode 8*. Geoforschungszentrum Potsdam.
Gudehus, G. (1974) *Monotone Zeitabhängige Vorgänge im Baugrund*, in Spezialsitzung der Baugrundtagung. Frankfurt am Main, pp. 234–236.
Gudehus, G. (1996) *A Comprehensive Constitutive Equation for Granular Materials*, Soils and Foundations, 36(1), pp. 1–12.
Gudehus, G. (2004) *A visco-hypoplastic constitutive relation for soft soils*, Soils and Foundations, 44(4), pp. 11–25.
Gudehus, G. (2006) *Seismo-hypoplasticity with a granular temperature*, Granular Matter, 8(2), pp. 93–102.
Gudehus, G. (2011) *Physical Soil Mechanics*. Springer Heidelberg Dordrecht London New York.
Gudehus, G., Goldscheider, M. and Winter, H. (1977) *Mechanical properties of sand and clay and numerical integration methods: Some sources of errors and bounds of accuracy*, in Finite Elements in Geomechanics. Wiley, pp. 150–212.
Gudehus, G. and Leinenkugel, H. J. (1978) *Fließdruck und Fließbewegung in bindigen Böden: Neue Methoden*, in Vorträge der Baugrundtagung 1978 in Berlin, pp. 411–429.
Hagerty, M. M., Hite, D. R., Ullrich, C. R. and Hagerty, D. J. (1993) *One-dimensional high-pressure compression of granular media*, Journal of Geotechnical Engineering, 119(1), pp. 1–18.
Hardin, B. (1985) *Crushing of Soil Particles*, Journal of Geotechnical Engineering, 111(10), pp. 1177–1192.
Herle, I. (1997) *Hypoplastizität und Granulometrie einfacher Korngerüste*. Universität Fridericiana in Karlsruhe.
Herle, I. and Gudehus, G. (1999) *Determination of parameters of a hypoplastic constitutive model from properties of grain assemblies*, Mechanics of Cohesive-Frictional Materials, 4(5), pp. 461–486.
Herle, I. and Kolymbas, D. (2004) *Hypoplasticity for soils with low friction angles*, Computers and Geotechnics, 31(5), pp. 365–373.
Herrmann, H. J. (1993) *On the thermodynamics of granular media*, Journal de Physique, 3(4), pp. 427–433.
Hertz, H. (1881) *Über die Berührung fester elastischer Körper*, Journal für die reine und angewandte Mathematik, 92, pp. 156–171.
Hryciw, R. D., Zheng, J. and Shetler, K. (2016) *Particle Roundness and Sphericity from Images of Assemblies by Chart Estimates and Computer Methods*, Journal of Geotechnical and Geoenvironmental Engineering, 142(9).
Hügel, H. M. (1995) *Prognose von Bodenverformungen*. Universität Fridericiana in Karlsruhe.
Jaky, J. (1948) *Pressure in silos*, in 2nd International Conference on Soil Mechanics and Foundation

Engineering. London, pp. 103–107.
Janbu, N. (1969) *The resistance concept applied to deformation of soils*, in Proceedings of the VIIth International Conference on Soil Mechanics and Foundation Engineering. Mexico City, pp. 191–196.
Jang, D.-J. and Frost, J. D. (1998) *Sand structure differences resulting from specimen preparation procedures.*, in Proceedings of the Specialty Conference on Geotechnical Earthquake Engineering and Soil Dynamics. Seattle, WA, USA, pp. 234–245.
Janssen, H. A. (1895) *Versuche über Getreidedruck in Silozellen*, Zeitschr. d. Vereines deutscher Ingenieure, pp. 1045–1049.
Johnson, K. L. (1985) *Contact Mechanics*. Cambridge: Cambridge University Press.
Karimpour, H. and Lade, P. V. (2010) *Time Effects Relate to Crushing in Sand*, Journal of Geotechnical and Geoenvironmental Engineering, 136(9), pp. 1209–1219.
Karimpour, H. and Lade, P. V (2013) *Creep behavior in Virginia Beach sand*, Canadian Geotechnical Journal, 50(11), pp. 1159–1178.
Karlsrud, K. (2012) *Prediction of load-displacement behaviour and capacity of axially loaded piles in clay based on analyses and interpretation of pile load test results*. Norwegian University of Science and Technology.
Kikkawa, N., Pender, M. J., Orense, R. P., StGeorge, J. D. and Matsushita, E. (2012) *K0 Compression and Stress Relaxation of Pumice Sand*, Journal of Geotechnical and Geoenvironmental Engineering, 138(5), pp. 625–628.
Klobe, B. (1992) *Eindimensionale Kompression und Konsolidation und darauf basierende Verfahren zur Setzungsprognose*. Universität Fridericiana in Karlsruhe.
Klostermann, J. (2010) *Geologie des Rheinischen Braunkohlereviers*, in Tagungsband zum Bergschadensforum. Niederzier: RWE Power AG, p. 59.
Kothen, H. and Knufinke, H. U. (1990) *Restsetzungen auf Neulandflächen*, Braunkohle, 10, pp. 24–29.
Krieg, S. (2000) *Viskoses Verhalten von Mudden, Seeton und Klei*. Universität Fridericiana in Karlsruhe.
Krumbein, W. C. and Sloss, L. L. (1963) *Stratigraphy and Sedimentation. 2nd edn*. San Franscisco: Freeman, W.H.
Kuhn, M. R. and Mitchell, J. K. (1993) *New Perspectives on Soil Creep*, Journal of Geotechnical Engineering, 119(3), pp. 507–524.
Kuwano, R. (2001) *Time and stress history dependency of creep strain vector for granular materials*, in Proceedings of the 15th International Conference on Soil Mechanics and Geotechnical Engineering. Istanbul, pp. 175–178.
Kuwano, R. and Jardine, R. J. (2002) *On measuring creep behaviour in granular materials through triaxial testing*, Canadian Geotechnical Journal, 39(5), pp. 1061–1074.
Kwok, C. Y. and Bolton, M. D. (2013) *DEM simulations of soil creep due to particle crushing*, Géotechnique, 63(16), pp. 1–12.
Lacerda, W. and Houston, W. N. (1973) *Stress Relaxation in Soils*, in Proc. VIIIth. ICOSOMEF. Moscow, pp. 221–227.
Lade, P. V. and Karimpour, H. (2014) *Stress relaxation behavior in Virginia Beach sand*, Canadian Geotechnical Journal, 52(7), pp. 813–835.
Lade, P. V., Liggio, C. D. and Nam, J. (2009) *Strain Rate, Creep, and Stress Drop-Creep Experiments on Crushed Coral Sand*, Journal of Geotechnical and Geoenvironmental Engineering, 135(7), pp. 941–953.
Lade, P. V. and Liu, C.-T. (1998) *Experimental Study of Drained Creep Behavior of Sand*, Journal of Engineering Mechanics, 124(8), pp. 912–920.
Lade, P. V., Nam, J. and Liggio, C. D. (2010) *Effects of Particle Crushing in Stress Drop-Relaxation Experiments on Crushed Coral Sand*, Journal of Geotechnical and Geoenvironmental Engineering, 136(3), pp. 500–509.
Lade, P. V (2009) *Creep , stress relaxation , and rate effects in sand*, in Hamza, M., Shahien, M., and El-Mossallamy, Y. (eds) Proceedings of the 17th International Conference on Soil. Amsterdam: IOS Press, pp. 264–267.
Lambe, T. W. and Whitman, R. V. (2012) *Soil Mechanics*. New York: John Wiley & Sons.
Lange, S. (1986) *Building on uncompacted dumps in the Rhenish brown coal area of the Federal*

Republic of Germany, in Building on Marginal and Derelict Land. London, pp. 137–153.
Leinenkugel, H. J. (1976) *Deformations- und Festigkeitsverhalten bindiger Erdstoffe; Experimemtelle Ergebnisse und ihre physikalische Deutung*. Universität Fridericiana in Karlsruhe.
Leung, C. F., Lee, F. H. and Yet, N. S. (1996) *The role of particle breakage in pile creep in sand*, Canadian Geotechnical Journal, 33(6), pp. 888–898.
Levin, F. and Vogt, S. (2015) *Creep of Sand in Filled Open Cast Mining Pits*, in Dijkstra, J., Karstunen, M., Gras, J.-P., and Karlsson, M. (eds) International conference on Creep and Deformation Characteristics in Geomaterials. Gothenburg: Chalmers University of Technology, pp. 47–49.
Lv, Y., Li, F., Liu, Y., Fan, P. and Wang, M. (2017) *Comparative study of coral sand and silica sand in creep under general stress states*, Canadian Geotechnical Journal, 54(11), pp. 1601–1611.
Mayne, P. W. and Kulhawy, F. H. (1982) *K0-OCR relationships in soil*, Journal of Geotechnical Engineering, 108(6), pp. 851–872.
Mc Dowell, G. R. and Amon, A. (2000) *The application of Weibull statistics to the fracture of soil particles*, Soils and Foundations, 40(3), pp. 131–141.
McDowell, G. R. and Khan, J. J. (2003) *Creep of granular materials*, Granular Matter, 5(3), pp. 115–120.
Mejia, C. A. and Vaid, Y. P. (1988) *Time dependet behaviour of sand*, in Keedwell, M. J. (ed.) International Conference on Rheology and Soil Mechanics. Coventry, pp. 312–326.
Mesri, G; Godlewski, P. M. (1977) *Time- and Stress-Compressibility interrelationship*, Journal of the Geotechnical Engineering Devision, 103(May), pp. 417–430.
Mesri, G. and Castro, A. (1987) *Ca-Cc Concept and K0 During Secondary Compression*, Journal of Geotechnical and Geoenvironmental Engineering, 113(3), pp. 230–247.
Mesri, G. and Choi, Y. K. (1979) *Excess Pore Water Pressures During Consolidation*, in Proc. 6th Asian Conference on Soil Mechanics and Foundation Engineering. Singapore, pp. 151–154.
Mesri, G., Feng, T. W. and Benak, J. M. (1990) *Postdensification Penetration Resistance of Clean Sands*, Journal of Geotechnical Engineering, 116(7), pp. 1095–1115.
Mesri, G. and Vardhanabhuti, B. (2009) *Compression of granular materials*, Canadian Geotechnical Journal, 46(4), pp. 369–392.
Michalowski, R. L., Wang, Z. and Nadukuru, S. S. (2018) *Maturing of contacts and ageing of silica sand*, Géotechnique, 68(2), pp. 133–145.
Michalowski, R. and Nadukuru, S. (2012) *Static fatigue, time effects, and delayed increase in penetration resistance after dynamic compaction of sands*, Journal of Geotechnical and Geoenvironmental Engineering, 138(5), pp. 564–574.
Mitchell, James K; Soga, K. (2005) *Chapter04*, in Fundamentals of Soil Behhavior. 3rd edn, pp. 83–108.
Mitchell, J. K. (1986) *Practical Problems from Surprising Soil Behaviour*, Journal of Geotechnical Engineering, 112(3), pp. 255–289.
Mitchell, J. K. and Soga, K. (2005) *Fundamentals of soil behaviour. 3rd Editio*. Hoboken: John Wiley & Sons.
Mitchell, J. K. and Solymar, Z. V. (1984) *Time-dependent strength gain in freshly deposited or densified sand*, Journal of Geotechnical and Geoenvironmental Engineering, 110(11), pp. 1559–1576.
Miura, K., Maeda, K., Furukawa, M. and Toki, S. (1997) *Physical characteristics of sands with different primary properties*, Soils and Foundations, 37(3), pp. 53–64.
Miura, K., Maeda, K., Furukawa, M. and Toki, S. (1998) *Mechanical characteristics of sands with different primary properties*, Soils and Foundations, 38(4), pp. 159–172.
Miura, N. and Yamanouchi, T. (1975) *Effect of water on the behavior of a quartz-rich sand under high stress*, Soils and Foundations, 15(4), pp. 23–34.
Moore, A. L., McAdoo, B. G. and Ruffman, A. (2000) *Landward fining from multiple sources in a sand sheet deposited by the 1929 Grand Banks tsunami*, Sedimentary Geology, 200(3–4), pp. 336–346.
Muhs, H. and Kany, M. (1954) *Einfluss von Fehlerquellen beim Kompressionsversuch*. Technische Universität Berlin.
Murakami, Y. (1979) *Excess pore pressure and preconsolidation effect developed in normally consolidated clays of some age*, Soils and Foundations, 19(4), pp. 17–29.
Murayama, S., Michihiro, K. and Sakagami, T. (1984) *Creep Characteristics of Sand*, Soils and

Foundations, 24(2), pp. 2–15.
Nakata, Y., Hyde, A. F. L., Hyodo, M. and Murata, H. (1999) *A probabilistic approach to sand particle crushing in the triaxial test*, Geotechnique, 49(5), pp. 567–583.
Nakata, Y., Hyodo, M., Hyde, A. F. L., Kato, Y. and Murata, H. (2001) *Microscopic Particle Crushing of Sand Subjected to High Pressure One-Dimensional Compression.*, Soils and Foundations, 41(1), pp. 69–82.
Neher, H. P. (2008) *Zeitabhangiges Materialverhalten und Anisotropie von weichen Böden - Theorie und Anwendung*. Universität Stuttgart.
Neuroth, M., Lokay, P. and Schüngel, M. (2016) *Kontrolle der Belagsbildung bei der Verfeuerung rheinischer Braunkohlen in Kraftwerkskesseln*, in Tagungsband zum 48. Kraftwerkstechnischen Kolloquium. Dresden, pp. 395–406.
Niemunis, A. (2002) *Extended hypoplastic models for soils*. Mitteilungen Institut für Grundbau und Bodenmechanik Heft 34, Ruhr-Universität Bochum.
Niemunis, A. and Krieg, S. (1997) *Viscous behaviour of soil under oedometric conditions*, Canadian Geotechnical Journal, 34(1), pp. 161–162.
Norton, F. H. (1929) *The Creep of Steel at High Temperatures*. New York: Mc Graw-Hill.
Ohde, J. (1939) *Zur Theorie der Druckverteilung im Baugrund*, Der Bauingenieur, 20, pp. 451–459.
Ostermayer, H. (1976) *Das Verhalten gemischtkörniger Böden im einachsigen Formänderungszustand*. Technische Universität München.
Peng, F., Li, F., Tan, Y. and Kongkitkul, W. (2010) *FEM simulation of viscous properties for granular materials considering the loading rate effect*, Granular Matter, 12(6), pp. 555–568.
Pestana, J. M. and Whittle, A. J. (1995) *Compression model for cohesionless soils*, Geotechnique, 45(4), pp. 611–631.
Pestana, J. M. and Whittle, A. J. (1998) *Time effects in the compression of sands*, Geotechnique, 48(5), pp. 695–701.
Pham Van Bang, D., Di Benedetto, H., Duttine, A. and Ezaoui, A. (2007) *Viscous behaviour of dry sand*, International Journal for Numerical and Analytical Methods in Geomechanics, 31, pp. 1631–1658.
Powers, M. C. (1953) *A new roundness scale for the sedimentary particles*, Journal of Sedimentary Petrology, 23, pp. 117–119.
Pralle, N. (2002) *Mechanisms in Nearly Saturated Sandy Soils under Quasi-static and Dynamic Loading*. Universität Fridericiana Karlsruhe.
Punlor, A. (2004) *Numerical Modelling of the Visco-plastic Behaviour of Soft Soils*. Universität Fridericiana in Karlsruhe.
Radjai, F., Jean, M., Moreau, J. J. and Roux, S. (1996) *Force distributions in dense two-dimensional granular systems*, Phys. Rev. Lett., 77, pp. 274–277.
Robertson, P. K. (1986) *In situ testing and its application to foundation engineering*, Canadian Geotechnical Journal, 23(4), pp. 573–594.
Robertson, P. K. (1990) *Soil classification using the cone penetration test*, Canadian Geotechnical Journal, 27(1), pp. 151–158.
Robertson, P. K. (2009) *Interpretation of Cone Penetration Tests - a Unified Approach*, Canadian Geotechnical Journal, 46(11), pp. 1337–1355.
Robertson, P. K. (2010) *Soil behaviour type from the CPT: an update*, in Proceedings of the 2nd International Symposium on Cone Penetration Testing. Huntington Beach.
Roscoe, K. H. and Burland, J. B. (1968) *On the generalized stress–strain behaviour of 'wet clay'*, in A.Leckie, J. H. and F. (ed.) Engineering plasticity. Cambridge University Press, pp. 535–609.
Schanz, T., Vermeer, P. A. and Bonnier, P. G. (1999) *The Hardening Soil Model: Formulation And Verification*, in Beyond 2000 in Computational Geotechnics - 10 Years of PLAXIS. Balkema, Rotterdam: Balkema, pp. 1–16.
Schmertmann, J. H. (1991) *The mechanical ageing of soils*, Journal of Geotechnical Engineering, 117(9), pp. 1288–1330.
Von Soos, P. (2009) *Eigenschaften von Boden und Fels; ihre Ermittlung im Labor*, in Grundbautaschenbuch. 7th editio. Berlin: Ernst & Sohn.
Stocks-Fischer, S., Galinat, J. K. and Bang, S. S. (1999) *Microbiological precipitation of CaCO3*, Soil Biology and Biochemistry, 31(11), pp. 1563–1571.
Suarez, N. R. (2012) *Micromechanical Aspects of Aging in Granular Soils*. Virginia Polytechnic

Institute and State University.
Suklje, L. (1957) *The Analysis Of The Consolidation Process By The Isotaches Method*, in Proceedings of the 4th International Conference on Soil Mechanics and Foundation Engineering. London, pp. 200–206.
Tatsuoka, F., Di Benedetto, H., Enomoto, T., Kawabe, S. and Kongkitkul, W. (2008) *Various Viscosity Types of Geomaterials in Shear and Their Mathematical Expression*, Soils and Foundations, 48(1), pp. 41–60.
Tatsuoka, F., Ishihara, M., Di Benedetto, H. and Kuwano, R. (2002) *Time-Dependent Shear Deformation Characteristics of Geomaterials and their Simulation*, Soils and Foundations, 42(2), pp. 103–129.
Taylor, D. W. (1948) *Fundamentals of Soil Mechanics*. New York: Wiley.
Terzaghi, K. (1925) *Erdbaumechanik auf bodenphysikalischer Grundlage*. Leipzig / Wien: Franz Deuticke.
Verdugo, R. (1992) *Characterization of Sandy Soil Behavior under Large Deformation*. University of Tokyo.
Verdugo, R. and Ishihara, K. (1996) *The Steady State of Sandy Soils*, Soils and Foundations, 36(2), pp. 81–91.
Vermeer, P. A. and Neher, H. P. (1999) *A soft soil model that accounts for creep*, in Proceedings of the International Symposium "Beyond 2000 in Computational Geotechnics". Amsterdam, pp. 249–261.
Vogt, N., Heyer, D., Birle, E., Vogt, S., Dahmen, D., Karcher, C., Vinzelberg, G. and Eidam, F. (2013) *Special Aspects for Building a Motorway on a 185 m Deep Dump*, in Proceedings of the 18th International Conference on Soil Mechanics and Geotechnical Engineering. Paris, pp. 1377–1380.
Vogt, S. (2017) *Zeitabhängiger Verformungswiderstand weicher Böden und seine Berücksichtigung bei der Tragfähigkeitsprognose stabilitätsgefährdeter Pfähle*. Technical University of Munich.
Wang, Z. and Michalowski, R. L. (2015) *Contact fatigue in silica sand-Observations and modeling*, Geomechanics for Energy and the Environment. Elsevier Ltd, 4, pp. 88–99.
von Wolffersdorff, P. A. (1996) *Hypoplastic relation for granular materials with a predefined limit state surface*, Mechanics of Cohesive-Frictional Materials, 1(3), pp. 251–271.
Yamamuro, J. A., Bopp, P. A. and Lade, P. V (1996) *One-dimensional compression of sands at high pressures*, Journal of Geotechnical and Geoenvironmental Engineering, 122(2), pp. 147–154.
York, B. D. L., Brusey, W. G., Clemente, F. M. and Law, S. K. (1995) *Setup and relaxation on glacial sand*, Journal of Geotechnical Engineering, 120(9), pp. 1498–1513.

National standards

ASTM D4254-16, *Standard Test Methods for Minimum Index Density and Unit Weight of Soils and Calculation of Relative Density*, ASTM International, West Conshohocken, PA, 2016.

ASTM D6913 / D6913M-17, *Standard Test Methods for Particle-Size Distribution (Gradation) of Soils Using Sieve Analysis*, ASTM International, West Conshohocken, PA, 2017.

DIN EN ISO 17892-4, *Geotechnische Erkundung und Untersuchung - Laborversuche an Bodenproben - Teil 4: Bestimmung der Korngrößenverteilung* (ISO 17892-4:2016); Deutsche Fassung EN ISO 17892-4:2016*,* Berlin, Beuth.

DIN 18126:1996-11, *Baugrund, Untersuchung von Bodenproben - Bestimmung der Dichte nichtbindiger Böden bei lockerster und dichtester Lagerung,* Berlin, Beuth.

Appendix

A.1 List of figures

A.2 List of tables

A.3 Parameters for the 3D FE-simulation of the stress and strain distribution in an oedometer test

Table A.3.1: Constitutive model parameters for the Mohr-Coulomb constitutive model for the soil in the 3D FE-simulation of the stress and strain distribution in an oedometer test

Parameter combination			
Constitutive model			Mohr-Coulomb
Unit weight	γ	[kN/m³]	0
YOUNG's modulus	E	[MN/m²]	50
POISSON's ratio	ν		0.3
Cohesion	c'	[kPa]	1
Friction angle	φ'	[°]	30
Dilatancy angle	ψ	[°]	7

Table A.3.2: Linear elastic parameters for the steel of the oedometer apparatus in the 3D FE-simulation of the stress and strain distribution in an oedometer test

Parameter combination			
Constitutive model			Linear elastic
Unit weight	γ	[kN/m³]	0
YOUNG's modulus	E	[MN/m²]	200,000
POISSON's ratio	ν		0.3

Surface interface at steel wall of oedoemter: Coarseness factor 0.5

Mesh: 138,745 nodes, 98,574 volume triangular elements

A.4 Oedometer tests

Table A.4.1: List of oedometer tests on soils MS, FS, SU, SU*, SW and SU2

test type	Test number	soil	$D_{R,ini}$	e_{ini}	$\sigma_{v,ini}$ [kPa]	saturation	test procedure + stress sequence [kPa]	action
Creep after incremental loading, influence of initial density	03-FS15-D031	FS	0.35	1.014	2.00	air-dry	62.5 - 125 - 250 - 500 - 1000	creep 24h at each stress
	04-FS15-D039	FS	0.44	0.984	2.00	air-dry	62.5 - 125 - 250 - 500 - 1000	creep 24h at each stress
	05-FS15-D047	FS	0.52	0.954	2.00	air-dry	62.5 - 125 - 250 - 500 - 1000	creep 24h at each stress
	06-FS15-D056	FS	0.61	0.921	2.00	air-dry	62.5 - 125 - 250 - 500 - 1000	creep 24h at each stress
	02-FS15-D032	FS	0.36	1.011	2.00	air-dry	125 - 250 - 500 - 1000 - 2000 - 1000 - 500	creep 24h at each stress except unloading
	07-FS15-D042	FS	0.48	0.969	2.00	air-dry	125 - 250 - 500 - 1000 - 2000 - 1000 - 500	creep 24h at each stress except unloading
	08-FS15-D102	FS	0.77	1.020	2.00	air-dry	125 - 250 - 500 - 1000 - 2000 - 1000 - 500	creep 24h at each stress except unloading
	01-FS15-D040	FS	0.45	0.977	2.00	air-dry	125 - 250 - 500 - 1000 - 2000 - 1750	creep 24h at each stress except unloading
	02-FS15-D056	FS	0.61	0.918	2.00	air-dry	125 - 250 - 500 - 1000 - 2000 - 1750	creep 24h at each stress except unloading
	03-FS15-D075	FS	0.79	0.977	2.00	air-dry	125 - 250 - 500 - 1000 - 2000 - 1750	creep 24h at each stress except unloading
	04-FS15-D095	FS	0.96	0.791	2.00	air-dry	125 - 250 - 500 - 1000 - 2000 - 1750	creep 24h at each stress except unloading
	05-FS15-D114	FS	1.12	0.733	2.00	air-dry	125 - 250 - 500 - 1000 - 2000 - 1750	creep 24h at each stress except unloading
	04-MS15-D049	MS	0.55	0.834	2.00	air-dry	62.5 - 125 - 250 - 500 - 1000	creep 24h at each stress
	05-MS15-D042	MS	0.48	0.866	2.00	air-dry	62.5 - 125 - 250 - 500 - 1000	creep 24h at each stress
	06-MS15-D069	MS	0.74	0.747	2.00	air-dry	62.5 - 125 - 250 - 500 - 1000	creep 24h at each stress
	01-MS15-D080	MS	0.84	0.703	2.00	air-dry	62.5 - 125 - 250 - 500 - 1000	creep 24h at each stress
	02-MS15-D040	MS	0.46	0.876	2.00	air-dry	62.5 - 125 - 250 - 500 - 1000	creep 24h at each stress
	03-MS15-D036	MS	0.42	0.895	2.00	air-dry	62.5 - 125 - 250 - 500 - 1000	creep 24h at each stress
	05-MS15-D090	MS	0.92	0.664	2.00	air-dry	62.5 - 125 - 250 - 500 - 1000	creep 24h at each stress
	02-MS15-D042	MS	0.47	0.864	2.00	air-dry	125 - 250 - 500 - 1000 - 2000 - 1750 - 500 - 1750	creep 24h at each stress except unloading
	08-MS15-D100	MS	1.00	0.628	2.00	air-dry	125 - 250 - 500 - 1000 - 2000 - 1750 - 500 - 1750	creep 24h at each stress except unloading
	03-MS15-D056	MS	0.62	0.802	2.00	sat. at 2000 kPa	125 - 250 - 500 - 1000 - 2000 - 1000 - 500	creep 24h at each stress except unloading
	01-MS15-D047	MS	0.54	0.839	2.00	air-dry	125 - 250 - 500 - 1000 - 2000 - 1750 - 1000	creep 24h at each stress except unloading
	02-MS15-D045	MS	0.58	0.823	2.00	air-dry	125 - 250 - 500 - 1000 - 2000 - 1750 - 1000	creep 24h at each stress except unloading
	03-MS15-D070	MS	0.75	0.745	2.00	air-dry	125 - 250 - 500 - 1000 - 2000 - 1750 - 1000	creep 24h at each stress except unloading
	04-MS15-D086	MS	0.89	0.678	2.00	air-dry	125 - 250 - 500 - 1000 - 2000 - 1750	creep 24h at each stress except unloading
	05-MS15-D109	MS	1.07	0.596	2.00	air-dry	125 - 250 - 500 - 1000 - 2000 - 1750 - 1000	creep 24h at each stress except unloading
	01-SU15b-D006	SU	0.07	1.125	2.00	air-dry	62.5 - 125 - 250 - 500 - 1000	creep 24h at each stress
	02-SU15b-D009	SU	0.11	1.111	2.00	air-dry	62.5 - 125 - 250 - 500 - 1000	creep 24h at each stress
	03-SU15b-D030	SU	0.34	1.017	2.00	air-dry	62.5 - 125 - 250 - 500 - 1000	creep 24h at each stress
	04-SU15b-D049	SU	0.54	0.938	2.00	air-dry	62.5 - 125 - 250 - 500 - 1000	creep 24h at each stress
	05-SU15b-D070	SU	0.74	0.859	2.00	air-dry	62.5 - 125 - 250 - 500 - 1000	creep 24h at each stress
	01-SU15b-D030	SU	0.34	1.017	2.00	air-dry	125 - 250 - 500 - 1000 - 2000 - 1750 - 500 - 1750	creep 24h at each stress except unloading
	07-SU15b-D100	SU	1.00	0.756	2.00	air-dry	125 - 250 - 500 - 1000 - 2000 - 1750 - 500 - 1750	creep 24h at each stress except unloading
	01-SU15b-D034	SU	0.38	1.000	2.00	sat. at 2000 kPa	125 - 250 - 500 - 1000 - 2000 - 1000 - 500	creep 24h at each stress except unloading
	01-SU15b-D042	SU	0.47	0.965	2.00	air-dry	125 - 250 - 500 - 1000 - 2000 - 1750 - 500	creep 24h at each stress except unloading
	02-SU15b-D043	SU	0.48	0.962	2.00	air-dry	125 - 250 - 500 - 1000 - 2000 - 1750 - 500	creep 24h at each stress except unloading
	03-SU15b-D075	SU	0.79	0.840	2.00	air-dry	125 - 250 - 500 - 1000 - 2000 - 1750 - 500	creep 24h at each stress except unloading
	04-SU15b-D097	SU	0.98	0.765	2.00	air-dry	125 - 250 - 500 - 1000 - 2000 - 1750 - 500	creep 24h at each stress except unloading
	05-SU15b-D112	SU	1.10	0.715	2.00	air-dry	125 - 250 - 500 - 1000 - 2000 - 1750 - 500	creep 24h at each stress except unloading
	04-SU63526-D045	SU2	0.52	0.933	2.00	air-dry	62.5 - 125 - 250 - 500 - 1000	creep 24h at each stress
	05-SU63526-D030	SU2	0.37	1.007	2.00	air-dry	62.5 - 125 - 250 - 500 - 1000	creep 24h at each stress
	06-SU63526-D078	SU2	0.82	0.776	2.00	air-dry	62.5 - 125 - 250 - 500 - 1000	creep 24h at each stress
	01-SU63526-D035	SU2	0.42	0.983	2.00	air-dry	125 - 250 - 500 - 1000 - 2000 - 1750 - 500	creep 24h at each stress except unloading
	02-SU63526-D048	SU2	0.55	0.914	2.00	air-dry	125 - 250 - 500 - 1000 - 2000 - 1750 - 500	creep 24h at each stress except unloading
	03-SU63526-D066	SU2	0.72	0.827	2.00	air-dry	125 - 250 - 500 - 1000 - 2000 - 1750 - 500	creep 24h at each stress except unloading
	04-SU63526-D081	SU2	0.85	0.759	2.00	air-dry	125 - 250 - 500 - 1000 - 2000 - 1750 - 500	creep 24h at each stress except unloading
	05-SU63526-D099	SU2	1.00	0.685	2.00	air-dry	125 - 250 - 500 - 1000 - 2000 - 1750 - 500	creep 24h at each stress except unloading

test type	Test number	soil	$D_{R,ini}$	e_{ini}	$\sigma_{v,ini}$ [kPa]	saturation	test procedure + stress sequence [kPa]	action
Load controlled creep tests influence of the mean grain size d_{50}	01S-79288+79746-D030-Sr0	SW	0.35	0.590	2.00	air-dry	125 - 250 - 500 - 1000 - 2000	creep 24h at each stress
	06S-79288+79746-D080-Sr0	SW	0.83	0.435	2.00	air-dry	125 - 250 - 500 - 1000 - 2000	creep 24h at each stress
	01S-79288+79746-Mix größer 2-D030-Sr0	SW >2mm	0.33	0.646	2.00	air-dry	125 - 250 - 500 - 1000 - 2000	creep 24h at each stress
	02S-79288+79746 Mix größer 2-D080-Sr0	SW >2mm	0.82	0.535	2.00	air-dry	125 - 250 - 500 - 1000 - 2000	creep 24h at each stress
	03S-79288+79746 Mix0,5-2-D030-Sr0	SW 0.5-2mm	0.33	0.723	2.00	air-dry	125 - 250 - 500 - 1000 - 2000	creep 24h at each stress
	04S-79288+79746 Mix0,5-2-D080-Sr0	SW 0.5-2mm	0.82	0.580	2.00	air-dry	125 - 250 - 500 - 1000 - 2000	creep 24h at each stress
	05S-79288+79746 Frakt 0,2-0,5-D030-Sr0	SW 0.2-0.5mm	0.33	0.875	2.00	air-dry	125 - 250 - 500 - 1000 - 2000	creep 24h at each stress
	06S-79288+79746 Frakt 0,2-0,5-D080-Sr0	SW 0.2-0.5mm	0.82	0.760	2.00	air-dry	125 - 250 - 500 - 1000 - 2000	creep 24h at each stress
	07S-79288+79746 Frakt kleiner 0,2-D030-Sr0	SW 0.063-0.2mm	0.36	0.911	2.00	air-dry	125 - 250 - 500 - 1000 - 2000	creep 24h at each stress
	08S-79288+79746 Frakt kleiner 0,2-D080-Sr0	SW 0.063-0.2mm	0.84	0.682	2.00	air-dry	125 - 250 - 500 - 1000 - 2000	creep 24h at each stress
	05S-79288+79746Mix kleiner 0,063-G185-Sr0	SW <0.063mm	-	-	2.00	air-dry	125 - 250 - 500 - 1000 - 2000	creep 24h at each stress
	06S-79288+79746Mix kleiner 0,063-G205-Sr0	SW <0.063mm	-	-	2.00	air-dry	125 - 250 - 500 - 1000 - 2000	creep 24h at each stress
Load controlled creep tests influence of saturation	01-SU15b-D000-Sr1	SU	0.00	1.154	2.00	S_r = 1	125 - 250 - 500 - 1000 - 2000	creep 24h at each stress
	02-SU15b-D006-Sr1	SU	0.07	1.125	2.00	S_r = 1	62.5 - 125 - 250 - 500 - 1000	creep 24h at each stress
	03-SU15b-D026-Sr1	SU	0.30	1.034	2.00	S_r = 1	62.5 - 125 - 250 - 500 - 1000	creep 24h at each stress
	04-SU15b-D046-Sr1	SU	0.51	0.950	2.00	S_r = 1	62.5 - 125 - 250 - 500 - 1000	creep 24h at each stress
	05-SU15b-D066-Sr1	SU	0.70	0.873	2.00	S_r = 1	62.5 - 125 - 250 - 500 - 1000	creep 24h at each stress
	06-SU15b-D095-Sr1	SU	0.96	0.772	2.00	S_r = 1	62.5 - 125 - 250 - 500 - 1000	creep 24h at each stress
	01-SU15b-D006	SU	0.07	1.125	2.00	S_r = 1	62.5 - 125 - 250 - 500 - 1000	creep 24h at each stress
	01-SU15b-D009	SU	0.11	1.111	2.00	S_r = 1	62.5 - 125 - 250 - 500 - 1000	creep 24h at each stress
	01-SU15b-D030	SU	0.34	1.017	2.00	S_r = 1	62.5 - 125 - 250 - 500 - 1000	creep 24h at each stress
	01-SU15b-D049	SU	0.54	0.938	2.00	S_r = 1	62.5 - 125 - 250 - 500 - 1000	creep 24h at each stress
	01-SU15b-D070	SU	0.74	0.859	2.00	S_r = 1	62.5 - 125 - 250 - 500 - 1000	creep 24h at each stress
	01-MS15-D003	MS	0.05	1.067	2.00	S_r = 0.15	125 - 250 - 500 - 1000 - 2000	creep 24h at each stress
	02-MS15-D021	MS	0.25	0.971	2.00	S_r = 0.16	125 - 250 - 500 - 1000 - 2000	creep 24h at each stress
	03-MS15-D043	MS	0.49	0.862	2.00	S_r = 0.18	125 - 250 - 500 - 1000 - 2000	creep 24h at each stress
	04-MS15-D094	MS	0.95	0.651	2.00	S_r = 0.24	125 - 250 - 500 - 1000 - 2000	creep 24h at each stress
	05-MS15-D087	MS	0.90	0.673	2.00	S_r = 0.24	125 - 250 - 500 - 1000 - 2000	creep 24h at each stress
Creep after constant rate of strain, influence of initial density	180503_MS15_D030_1%min	MS	0.46	0.877	10.00	air-dry	1%/min, 250 - 1000 - 4000 - 7500 - 50 - 7500	creep 24h at each stress
	180525_MS15_D085_1%min_Creep	MS	0.85	0.697	10.00	air-dry	1%/min, 250 - 1000 - 4000 - 7500 - 50 - 7500	creep 24h at each stress except unloading
	180703_SU15b_D030_1%min_Creep	SU	0.51	0.951	10.00	air-dry	1%/min, 250 - 1000 - 4000 - 7500 - 50 - 7500	creep 24h at each stress except unloading
	180820_SU15b_D085_1%min_Creep	SU	1.04	0.741	10.00	air-dry	1%/min, 250 - 1000 - 4000 - 7500 - 50 - 7500	creep 24h at each stress except unloading
	180801_SUStern_D030_1%min_Creep	SU*	0.41	0.950	10.00	air-dry	1%/min, 250 - 1000 - 4000 - 7500 - 50 - 7500	creep 24h at each stress except unloading
	180910_SUStern_D055_1%min_Creep	SU*	0.62	0.836	10.00	air-dry	1%/min, 250 - 1000 - 4000 - 7500 - 50 - 7500	creep 24h at each stress except unloading
Creep after different strain-rates	180503_MS15_D030_1%min_Creep	MS	0.46	0.877	10.00	air-dry	0.1%/min, 250 - 1000 - 4000 - 7500 - 50 - 7500	creep 24h at each stress except unloading
	180727_MS15_D030_01%min_Creep	MS	0.44	0.884	10.00	air-dry	0.1%/min, 250 - 1000 - 4000 - 7500 - 50 - 7500	creep 24h at each stress except unloading
	180727_MS15_D030_001%min_Creep	MS	0.44	0.884	10.00	air-dry	0.01%/min, 250 - 1000 - 4000 - 7500 - 50 - 7500	creep 24h at each stress except unloading
Constant rate of strain tests	06-11-320-MS15-CRS D-0.30	MS	0.35	0.925	13.00	air-dry	1%/min upto 2000 kPa	-
	06-11-320-MS15-CRS D-0.30	MS	0.35	0.925	13.00	air-dry	0.01%/min upto 2000 kPa	-
	18-01-320-MS15-CRS D-0.30	MS	0.35	0.925	13.00	air-dry	1%/min upto 2000 kPa	-
	18-01-320-1-MS15-CRS D-0.30	MS	0.35	0.925	13.00	air-dry	1%/min upto 2000 kPa	-
	05-11-321-MS15-CRS-D-0.27	MS	0.32	0.940	13.00	air-dry	0.1%/min upto 2000 kPa	-
	15-01-321-MS15-CRS-D-0.27	MS	0.32	0.940	13.00	air-dry	1%/min upto 2000 kPa	-
	18-01-321-MS15-CRS-D-0.27	MS	0.32	0.940	13.00	air-dry	1%/min upto 2000 kPa	-
	10-11-321-MS15-CRS-D-0.38	MS	0.44	0.884	13.00	air-dry	1%/min upto 2000 kPa	-
	10-11-321-MS15-CRS-D-0.38	MS	0.44	0.885	13.00	air-dry	0.001%/min upto 2000 kPa	-
	09-11-321-MS15-CRS-D-0.77	MS	0.81	0.714	13.00	air-dry	1%/min upto 2000 kPa	-
	09-11-321-MS15-CRS-D-0.77	MS	0.81	0.714	13.00	air-dry	0.1%/min upto 2000 kPa	-
	06-11-321-MS15-CRS-D-0.77	MS	0.81	0.714	13.00	air-dry	0.01%/min upto 2000 kPa	-
	11-01-320-SU63526 D-0.30	SU2	0.36	1.014	13.00	air-dry	1%/min upto 2000 kPa	-
	08-01-320-SU63526 D-0.30	SU2	0.36	1.014	13.00	air-dry	0.1%/min upto 2000 kPa	-
	11-03-320-SU63526 D-0.30	SU2	0.36	1.014	13.00	air-dry	0.01%/min upto 2000 kPa	-
	12-01-320-SU63526 D-0.81	SU2	0.85	0.762	13.00	air-dry	1%/min upto 2000 kPa	-
	13-01-320-SU63526 D-0.81	SU2	0.85	0.762	13.00	air-dry	1%/min upto 2000 kPa	-
	11-03-320-SU63526 D-0.75	SU2	0.80	0.788	13.00	air-dry	1%/min upto 1000 kPa	-
	11-01-321-SU63526-D-0.77	SU2	0.80	0.788	13.00	air-dry	1%/min upto 2000 kPa	-
	12-01-321-SU63526-D-0.77	SU2	0.80	0.788	13.00	air-dry	0.01%/min upto 2000 kPa	-
	1 - 321-SU63526-D-0.75	SU2	0.80	0.788	13.00	air-dry	1%/min upto 2000 kPa	-
	2 - 321-SU63526-D-0.75	SU2	0.80	0.788	13.00	air-dry	1%/min upto 2000 kPa	-
	3 - 321-SU63526-D-0.75	SU2	0.80	0.788	13.00	air-dry	1%/min upto 2000 kPa	-
	4 - 321-SU63526-D-0.75	SU2	0.80	0.788	13.00	air-dry	1%/min upto 2000 kPa	-
	1 - 321-SU63526-D-0.75	SU2	0.80	0.788	13.00	air-dry	0.01%/min upto 2000 kPa	-
	2 - 321-SU63526-D-0.75	SU2	0.80	0.788	13.00	air-dry	0.01%/min upto 2000 kPa	-

test type	Test number	soil	$D_{R,ini}$	e_{ini}	$\sigma_{v,ini}$ [kPa]	saturation	test procedure + stress sequence [kPa]	action
Tests with sudden changes in strain-rate	15-02-320-SU63526 D-0.75	SU2	0.80	0.788	13.00	air-dry	1%/min-0.01%/min, 62.5 - 250 - 500 - 1000	jump at 62.5, 250, 500 kPa
	15-02-320-SU63526 D-0.75	SU2	0.80	0.788	13.00	air-dry	1%/min-0.005%/min, 62.5 - 250 - 500 - 1000	jump at 62.5, 250, 500 kPa
	02-170512-1-ChRS-SU63526-D-0.75	SU2	0.80	0.788	13.00	air-dry	5%/min-0.005%/min, 62.5 -125 - 250 - 500 - 1000 - 2000	jump at 62.5, 125, 250, 500, 1000 kPa
	04-11-320-MS15-ChRS-D-0.30	MS	0.35	0.925	13.00	air-dry	1%/min-0.01%/min, 125 - 250 - 500 - 1000	jump at 125, 250, 500 kPa
	13-01-320-MS15-D0.30	MS	0.35	0.925	13.00	air-dry	1%/min-0.005%/min, 62.5 - 125 - 250 - 500 - 1000 - 2000	jump at 62.5, 125, 250, 500, 1000 kPa
	14-01-320-MS15-D0.30	MS	0.35	0.925	13.00	air-dry	1%/min-0.005%/min, 62.5 - 125 - 250 - 500 - 1000 - 2000	jump at 62.5, 125, 250, 500, 1000 kPa
	13-01-321-MS15-D0.27	MS	0.32	0.940	13.00	air-dry	1%/min-0.005%/min, 62.5 - 125 - 250 - 500 - 1000 - 2000	jump at 62.5, 125, 250, 500, 1000 kPa
	14-01-321-MS15-D0.27	MS	0.32	0.940	13.00	air-dry	1%/min-0.005%/min, 62.5 - 125 - 250 - 500 - 1000 - 2000	jump at 62.5, 125, 250, 500, 1000 kPa
	04-11-321-MS15-CRS-D-0.77	MS	0.81	0.714	13.00	air-dry	0.1%/min-0.01%/min, 62.5 - 125 - 250 - 500 - 1000	jump at 62.5, 125, 250, 500 kPa
	05-11-321-MS15-CRS-D-0.77	MS	0.81	0.714	13.00	air-dry	1%/min-0.005%/min, 62.5 - 125 - 250 - 500 - 1000	jump at 62.5, 125, 250, 500 kPa
	180514_MS15_D030_1%min_jump	MS	0.46	0.878	10.00	air-dry	1%/min-0.001%/min, 250 - 1000 - 4000 - 7500 - 50 - 7500	jump at 250, 1000, 4000 kPa
	180611_MS15_D085_1%min_jump	MS	0.85	0.697	10.00	air-dry	1%/min-0.001%/min, 250 - 1000 - 4000 - 7500 - 50 - 7500	jump at 250, 1000, 4000 kPa
	180713_SU15b_D030_1%min_Jump	SU	0.46	0.969	10.00	air-dry	1%/min-0.001%/min, 250 - 1000 - 4000 - 7500 - 50 - 7500	jump at 250, 1000, 4000 kPa
	180827_SU15b_D085_1%min_Jump	SU	0.95	0.775	10.00	air-dry	1%/min-0.001%/min, 250 - 1000 - 4000 - 7500 - 50 - 7500	jump at 250, 1000, 4000 kPa
	180820_SUStern_D030_1%min_Jump	SU*	0.46	0.924	10.00	air-dry	1%/min-0.001%/min, 250 - 1000 - 4000 - 7500 - 50 - 7500	jump at 250, 1000, 4000 kPa
	180914_SUStern_D055_1%min_Jump	SU*	0.62	0.833	10.00	air-dry	1%/min-0.001%/min, 250 - 1000 - 4000 - 7500 - 50 - 7500	jump at 250, 1000, 4000 kPa
Relaxation after constant rate of strain, influence of initial density + Relaxation after different strain- rates	180508_MS15_D030_1%min_	MS	0.45	0.881	10.00	air-dry	1%/min, 250 - 1000 - 4000 - 7500 - 50 - 7500	relax 24h at each stress
	180529_MS15_D085_1%min_relax	MS	0.85	0.697	10.00	air-dry	1%/min, 250 - 1000 - 4000 - 7500 - 50 - 7500	relax 24h at each stress except unloading
	180830_MS15_D030_001%min_Relax	MS	0.46	0.875	10.00	air-dry	0.01%/min, 250 - 1000 - 4000 - 7500 - 50 - 7500	relax 24h at each stress except unloading
	180910_MS15_D030_01%min_Relax	MS	0.51	0.855	10.00	air-dry	1%/min, 250 - 1000 - 4000 - 7500 - 50 - 7500	relax 24h at each stress except unloading
	180919_MS15_D030_001%min_Relax	MS	0.47	0.871	10.00	air-dry	0.01%/min, 250 - 1000 - 4000 - 7500 - 50 - 7500	relax 24h at each stress except unloading
	180919_MS15_D085_001%min_Relax	MS	0.92	0.665	10.00	air-dry	0.01%/min, 250 - 1000 - 4000 - 7500 - 50 - 7500	relax 24h at each stress except unloading
	180709_SU15b_D030_1%min_Relax	SU	0.51	0.949	10.00	air-dry	1%/min, 250 - 1000 - 4000 - 7500 - 50 - 7500	relax 24h at each stress except unloading
	180824_SU15b_D085_1%min_Relax	SU	0.94	0.777	10.00	air-dry	1%/min, 250 - 1000 - 4000 - 7500 - 50 - 7500	relax 24h at each stress except unloading
	180924_SU15b_D030_001%min_Relax	SU	0.47	0.965	10.00	air-dry	0.01%/min, 250 - 1000 - 4000 - 7500 - 50 - 7500	relax 24h at each stress except unloading
	180924_SU15b_D085_001%min_Relax	SU	0.94	0.778	10.00	air-dry	0.01%/min, 250 - 1000 - 4000 - 7500 - 50 - 7500	relax 24h at each stress except unloading
	180801_SUStern_D030_1%min_Relax	SU*	0.40	0.955	10.00	air-dry	1%/min, 250 - 1000 - 4000 - 7500 - 50 - 7500	relax 24h at each stress except unloading
	180914_SUStern_D055_1%min_Relax	SU*	0.63	0.831	10.00	air-dry	1%/min, 250 - 1000 - 4000 - 7500 - 50 - 7500	relax 24h at each stress except unloading
	180110_SUStern_D030_001%min_Relax	SU*	0.45	0.932	10.00	air-dry	0.01%/min, 250 - 1000 - 4000 - 7500 - 50 - 7500	relax 24h at each stress except unloading
	181001_SUStern_D055_001%min_Relax	SU*	0.62	0.833	10.00	air-dry	0.01%/min, 250 - 1000 - 4000 - 7500 - 50 - 7500	relax 24h at each stress except unloading
Combined tests	180518_MS15_D030_Combi	MS	0.43	0.889	10.00	air-dry	cf. Table 3.8, Section 3.7.7	-
	180703_MS15_D085_Combi	MS	1.35	0.466	10.00	air-dry	cf. Table 3.8, Section 3.7.7	-
	180808_MS15_D030_Combi	MS	0.37	0.920	10.00	air-dry	cf. Table 3.8, Section 3.7.7	-
	190112_MS15_D030_Combi190112	MS	0.47	0.871	10.00	air-dry	cf. Table 3.8, Section 3.7.7	-
	180719_SU15b_D030_Combi	SU	0.50	0.956	10.00	air-dry	cf. Table 3.8, Section 3.7.7	-
	180808_SUStern_D030_Combi	SU*	0.42	0.947	10.00	air-dry	cf. Table 3.8, Section 3.7.7	-
	190118_SUStern_D030_Combi190112	SU*	0.42	0.944	10.00	air-dry	cf. Table 3.8, Section 3.7.7	-
Long term creep and relaxation test	180614_MS15_D030_long term_Relax+Creep	MS	0.38	0.912	10.00	air-dry	1%/min, 4000 - 7500 - 50 - 7500	relax 168h at 4000 kPa, creep 168h at 7500 kPa
Constant rate of strain high pressure tests	180108-A	MS	0.63	0.796	1273.00	air-dry	1.67%/min, up to 340 MPa	-
	180809-A	MS	0.92	0.664	1273.00	air-dry	1.67%/min, up to 340 MPa	-
	180109-B	FS	0.41	0.992	1273.00	air-dry	1.67%/min, up to 340 MPa	-
	180109-C	FS	1.15	0.720	1273.00	air-dry	1.67%/min, up to 340 MPa	-
	180111-1	SU	0.51	0.950	1273.00	air-dry	1.67%/min, up to 340 MPa	-
	180111-2	SU	0.99	0.759	1273.00	air-dry	1.67%/min, up to 340 MPa	-
	180116-5	SU	0.51	0.950	1273.00	air-dry	1.67%/min, up to 10 MPa	-
	150116-6	SU	0.51	0.950	1273.00	air-dry	1.67%/min, up to 50 MPa	-
	180116-7	SU	0.51	0.950	1273.00	air-dry	1.67%/min, up to 100 MPa	-
	180116-8	SU	0.51	0.950	1273.00	air-dry	1.67%/min, up to 200 MPa	-
	180116-1	MS	0.30	0.950	1273.00	air-dry	1.67%/min, up to 10 MPa	-
	180116-2	MS	0.30	0.950	1273.00	air-dry	1.67%/min, up to 50 MPa	-
	180116-3	MS	0.30	0.950	1273.00	air-dry	1.67%/min, up to 100 MPa	-
	180116-4	MS	0.30	0.950	1273.00	air-dry	1.67%/min, up to 200 MPa	-
	180201-1	MS	0.30	0.950	1273.00	air-dry	1.67%/min, up to 300 MPa	-

test type	Test number	soil	$D_{R,ini}$	e_{ini}	$\sigma_{v,ini}$ [kPa]	saturation	test procedure + stress sequence [kPa]	action
Creep after constant rate of strain high pressure tests	180117-1	MS	0.66	0.786	1273.00	air-dry	1.67%/min, up to 10 MPa	1h creep at maximum stress
	180117-2	MS	0.66	0.786	1273.00	air-dry	1.67%/min, up to 50 MPa	1h creep at maximum stress
	180117-3	MS	0.66	0.786	1273.00	air-dry	1.67%/min, up to 100 MPa	1h creep at maximum stress
	180117-4	MS	0.66	0.786	1273.00	air-dry	1.67%/min, up to 300 MPa	1h creep at maximum stress
	181115-1	MS	0.75	0.745	1273.00	air-dry	1.67%/min, up to 10 MPa	1h creep at maximum stress
	181115-2	MS	0.75	0.745	1273.00	air-dry	1.67%/min, up to 50 MPa	1h creep at maximum stress
	181115-3	MS	0.76	0.738	1273.00	air-dry	1.67%/min, up to 100 MPa	1h creep at maximum stress
	181116-1	MS	0.73	0.751	1273.00	air-dry	1.67%/min, up to 200 MPa	1h creep at maximum stress
	181204-1	MS	0.70	0.764	1273.00	air-dry	1.67%/min, up to 300 MPa	1h creep at maximum stress
	181204-2	MS	1.10	0.582	1273.00	air-dry	1.67%/min, up to 10 MPa	1h creep at maximum stress
	181204-3	MS	1.09	0.588	1273.00	air-dry	1.67%/min, up to 50 MPa	1h creep at maximum stress
	181205-1	MS	1.05	0.604	1273.00	air-dry	1.67%/min, up to 100 MPa	1h creep at maximum stress
	181205-2	MS	1.03	0.616	1273.00	air-dry	1.67%/min, up to 200 MPa	1h creep at maximum stress
	181205-3	MS	1.00	0.627	1273.00	air-dry	1.67%/min, up to 300 MPa	1h creep at maximum stress
	181212-1	SU	0.95	0.774	1273.00	air-dry	1.67%/min, up to 10 MPa	1h creep at maximum stress
	181212-2	SU	0.95	0.775	1273.00	air-dry	1.67%/min, up to 50 MPa	1h creep at maximum stress
	181212-3	SU	0.97	0.768	1273.00	air-dry	1.67%/min, up to 100 MPa	1h creep at maximum stress
	181212-4	SU	0.95	0.775	1273.00	air-dry	1.67%/min, up to 200 MPa	1h creep at maximum stress
	181213-1	SU	1.63	0.502	1273.00	air-dry	1.67%/min, up to 300 MPa	1h creep at maximum stress
	181213-2	SU	1.29	0.638	1273.00	air-dry	1.67%/min, up to 10 MPa	1h creep at maximum stress
	181213-3	SU	1.38	0.604	1273.00	air-dry	1.67%/min, up to 50 MPa	1h creep at maximum stress
	181217-1	SU	1.37	0.609	1273.00	air-dry	1.67%/min, up to 100 MPa	1h creep at maximum stress
	181217-2	SU	1.38	0.604	1273.00	air-dry	1.67%/min, up to 200 MPa	1h creep at maximum stress
	181218-1	SU	1.38	0.604	1273.00	air-dry	1.67%/min, up to 300 MPa	1h creep at maximum stress

Oedometer tests with measurement of lateral stress	180720_RB	MS	0.30	0.950	13.00	air-dry	50 kPa/min, up to 4000 kPa, 50 kPa/min unloading 110 kPa	continuous K_0-measurement
	180820_RB	MS	0.85	0.697	13.00	air-dry	50 kPa/min, up to 4000 kPa, 50 kPa/min unloading 110 kPa	continuous K_0-measurement
	180821_RB	FS	0.30	1.034	13.00	air-dry	50 kPa/min, up to 4000 kPa, 50 kPa/min unloading 110 kPa	continuous K_0-measurement
	180821_RB2	FS	0.85	0.831	13.00	air-dry	50 kPa/min, up to 4000 kPa, 50 kPa/min unloading 110 kPa	continuous K_0-measurement
	180821_RB3	SU	0.30	1.034	13.00	air-dry	50 kPa/min, up to 4000 kPa, 50 kPa/min unloading 110 kPa	continuous K_0-measurement
	180822_RB	SU	0.85	0.815	13.00	air-dry	50 kPa/min, up to 4000 kPa, 50 kPa/min unloading 110 kPa	continuous K_0-measurement

A.5 Drained triaxial compression tests

Table A.5.1: List of drained triaxial compression tests on soils MS, FS and SU

test type	Test number	soil	$D_{R,ini}$	e_{ini}	sample preparation	consolidation stress [kPa] + test procedure
drained triaxial compression tests	Ausw_FS15-81417-2b_ld055	FS	0.55	0.942	dry funnel deposition, water saturation after replacing air by CO_2, B-values > 0.95	100, 300, 500, 700; 0.024%/min up to 20% axial strain at each consolidation stress
	Ausw_MS15-81412-2_ld050	MS	0.50	0.858		100, 300, 500, 700; 0.024%/min up to 20% axial strain at each consolidation stress
	Ausw_SU15b-81414_ld060	SU	0.60	0.915		100, 300, 500, 700; 0.024%/min up to 20% axial strain at each consolidation stress

The determined friction angles are summarized in Table A.9.2.

A.6 Empirical concept for the creep-coefficient evaluation

Validation of empirical concept for stress and density dependent determination of the creep-coefficient. Comparison of approach to test data from incremental LC tests on sands MS and SU presented in Section 4.6.

(a)

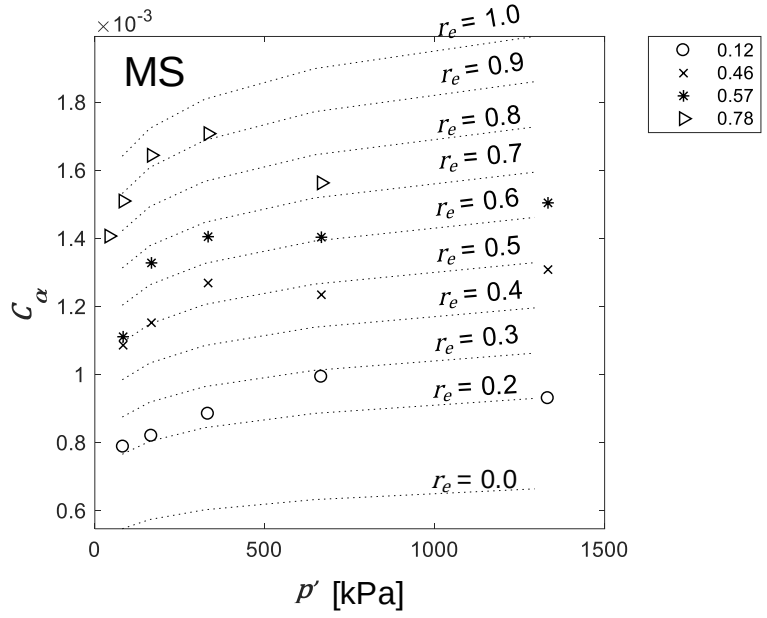

(b)

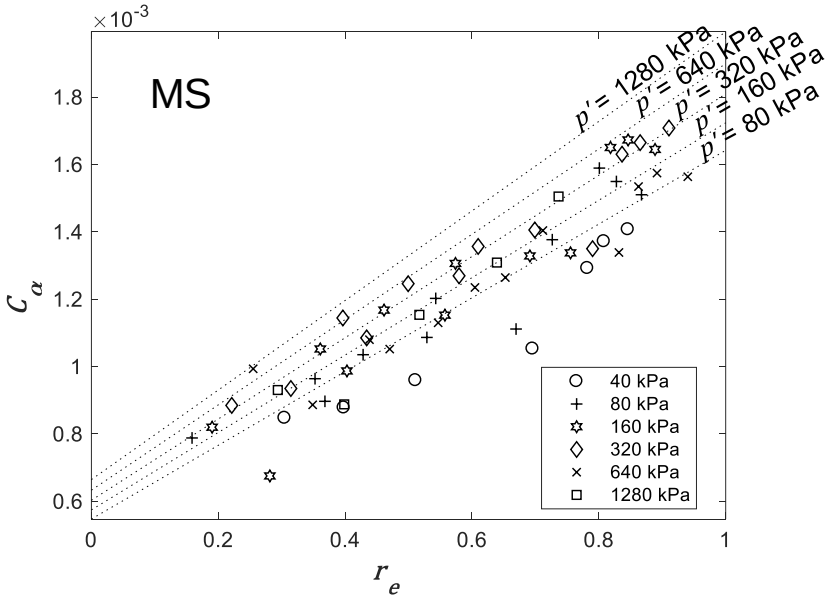

Figure A.6.1: (a) Development of C_α with the pressure p' and (b) with the relative void ratio r_e of sand MS calculated with ω = 0.0012, θ = 0.07, p'_{ref} = 300 kPa and $C_{\alpha,ref,0}$ = 0.0006

(a)

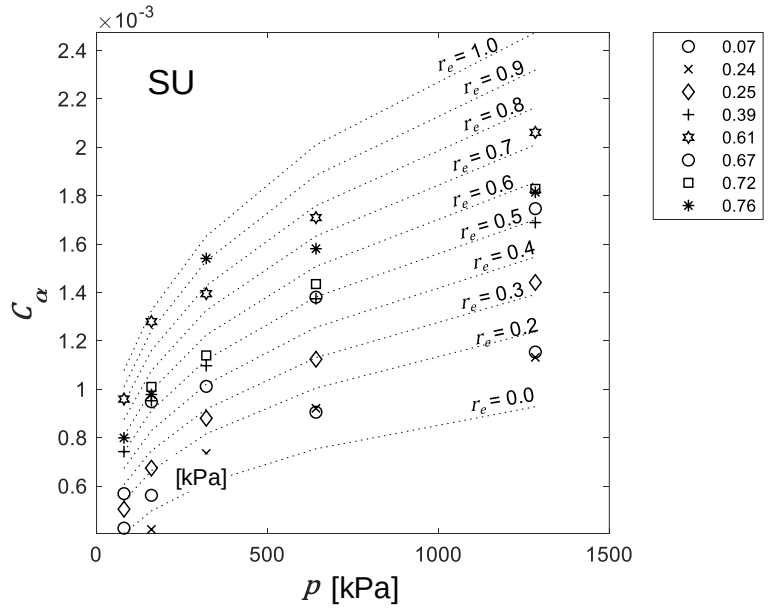

(b)

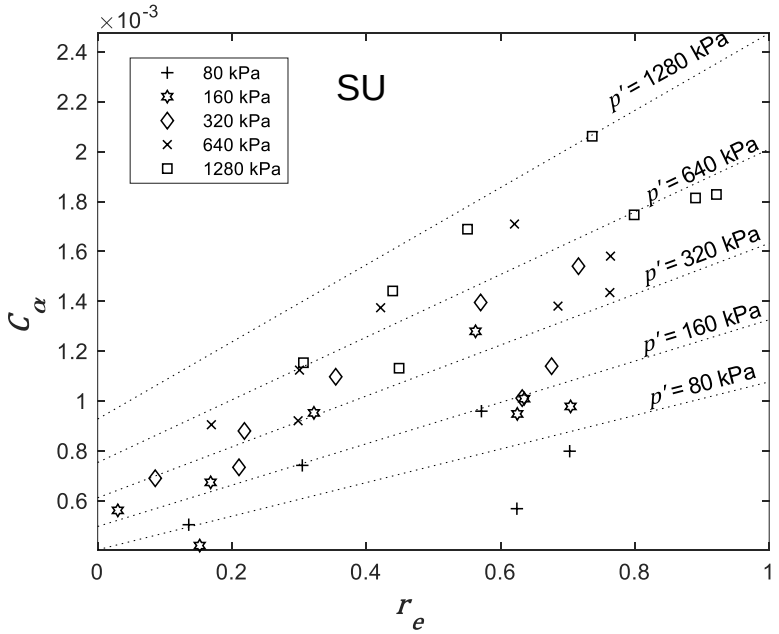

Figure A.6.2: (a) Development of C_α with the pressure p' and (b) with the relative void ratio r_e of sand SU calculated with ω = 0.0009, θ = 0.30, p'_{ref} = 300 kPa and $C_{\alpha,ref,0}$ = 0.0006

A.7 Top view of continuous sampling along highway A44n on the Garzweiler open cast mining dump

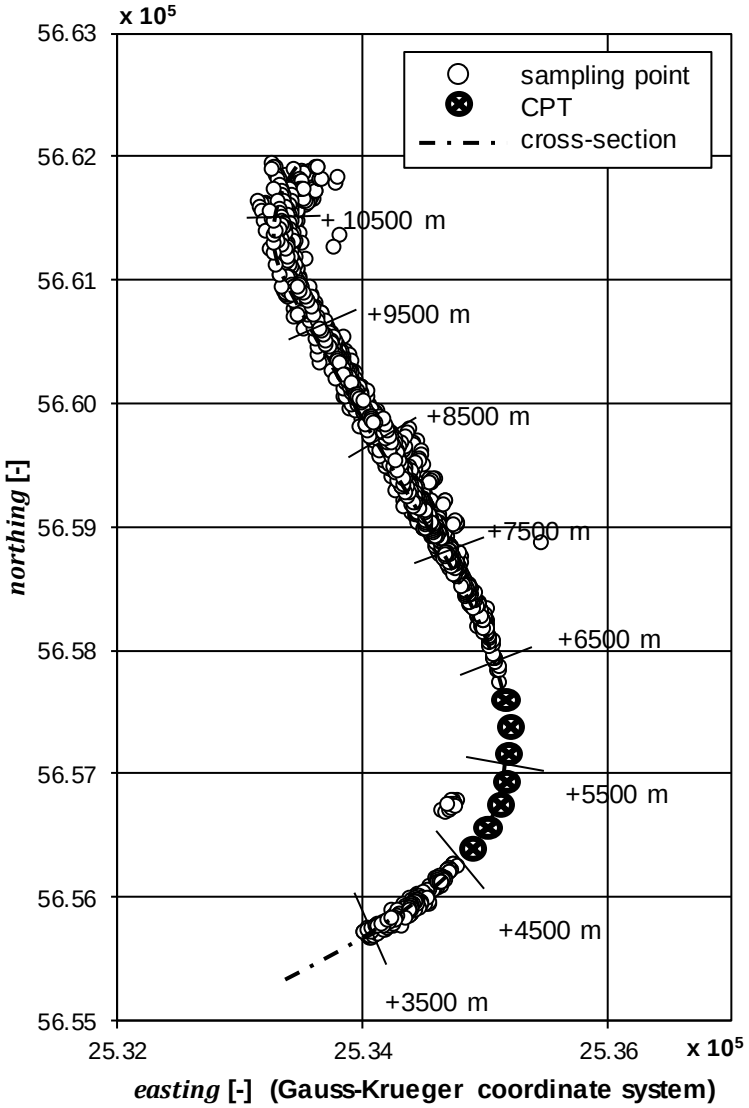

Figure A.7.1: Top view of continuous sampling points along highway A44n cross-section

A.8 Comparison of CPT evaluation for SBT determination by ROBERTSON (1990) and ROBERTSON (2010)

Analysis of CPTs in Garzweiler open cast mining dump (cf. Figure 5.3) with respect to Soil Behaviour Type after ROBERTSON (1990) and ROBERTSON (2010) using the software CPET-IT version 1.7.6.42. The input parameters for the software are listed in Table 5.1.

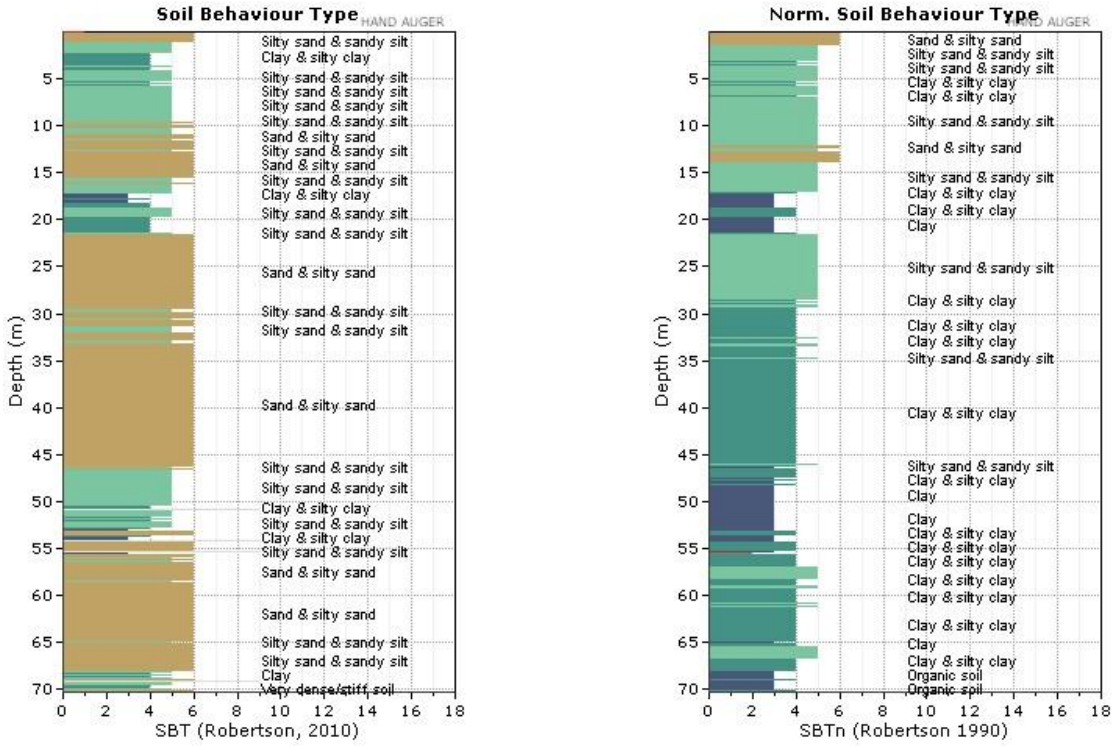

Figure A.8.1: CPT 2

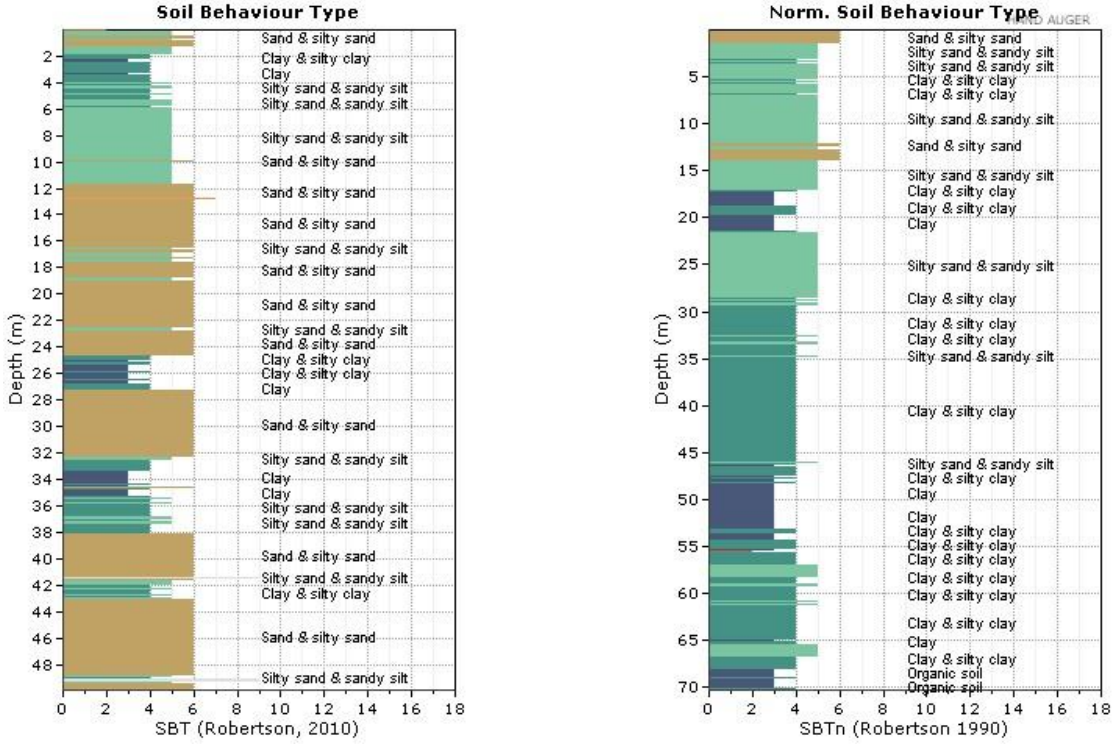

Figure A.8.2: CPT 3

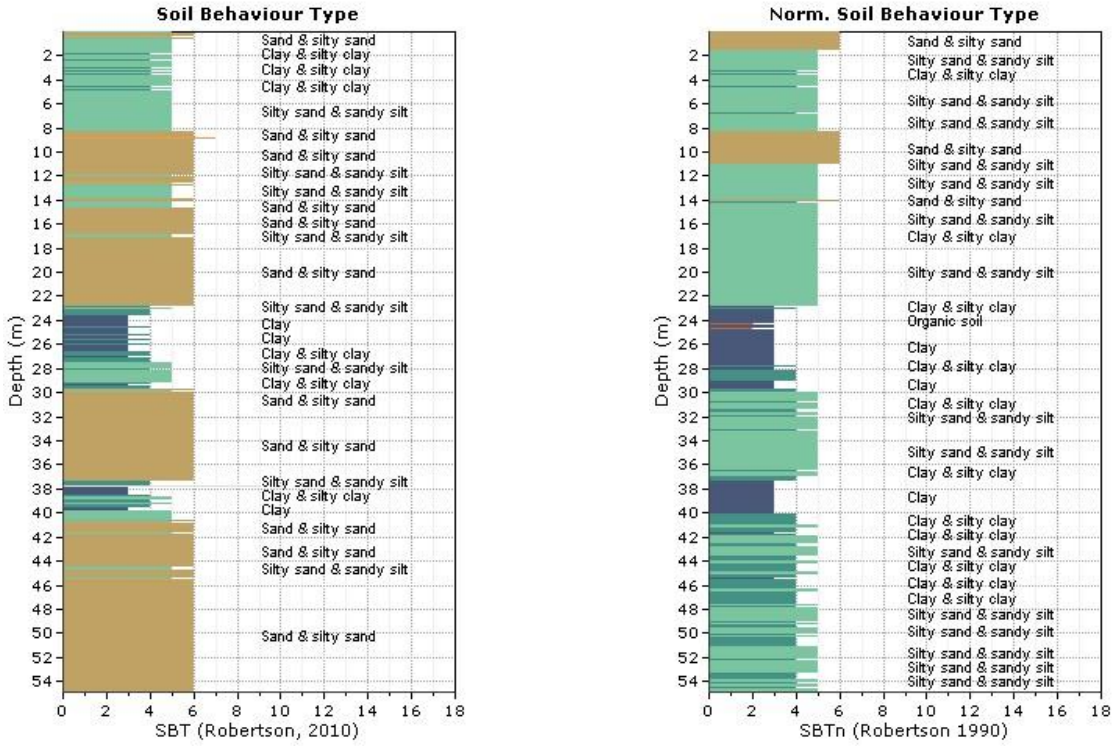

Figure A.8.3: CPT 4

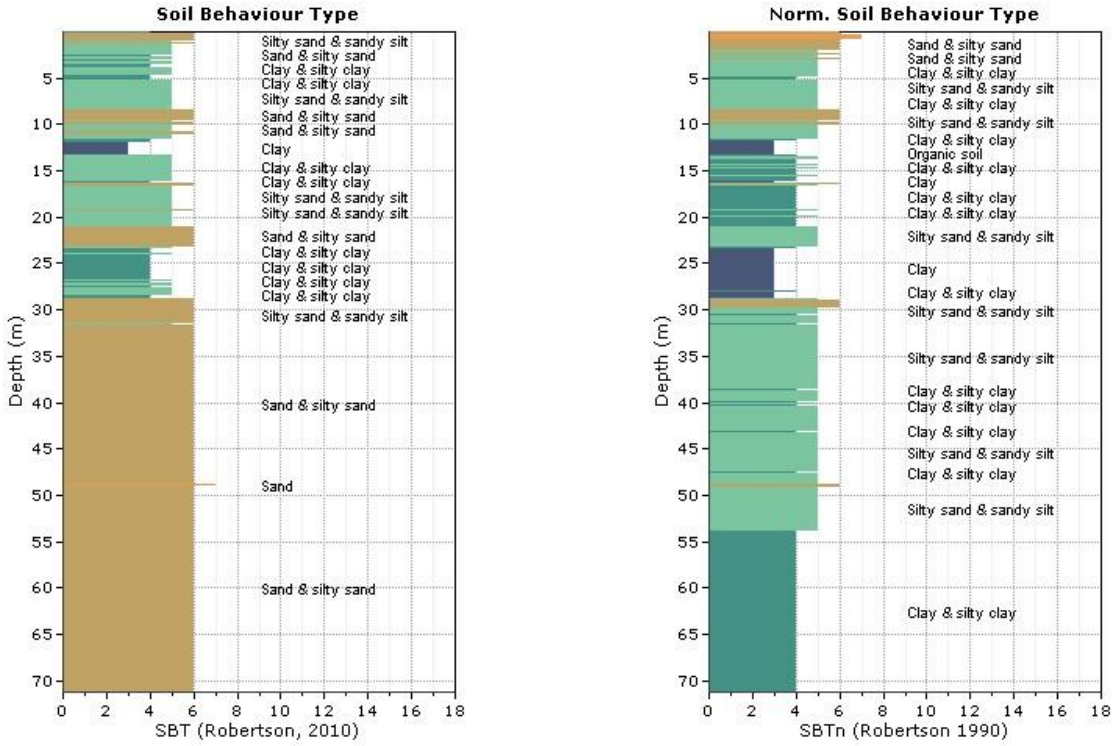

Figure A.8.4: CPT 5

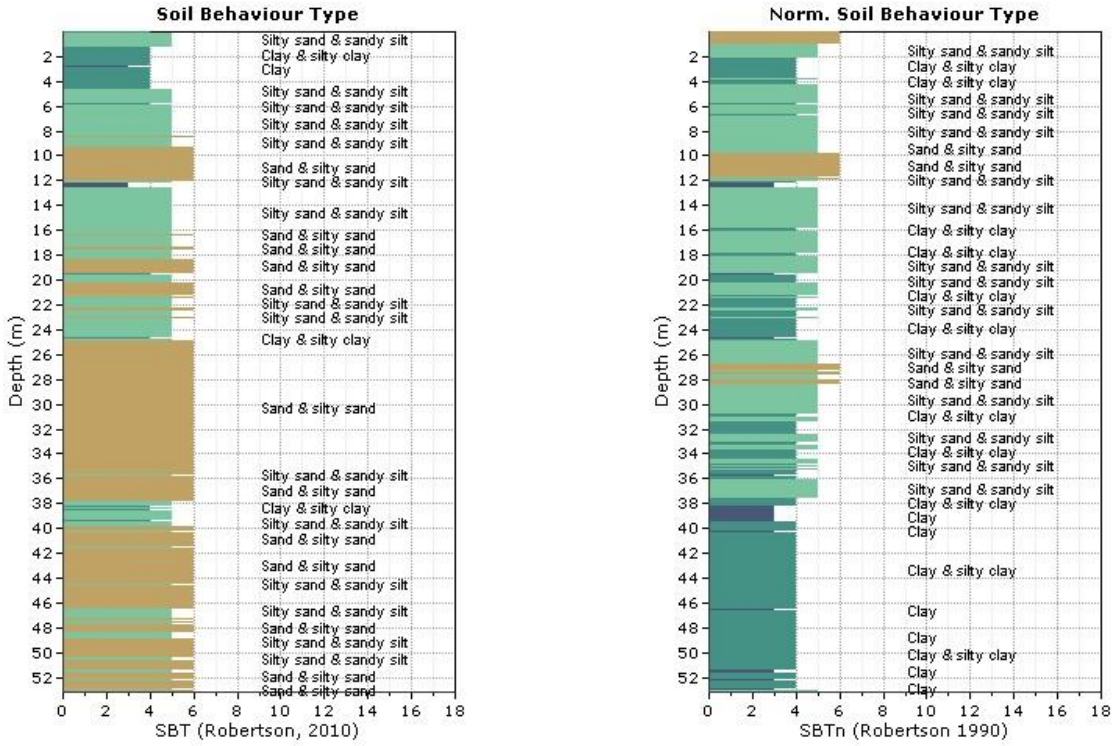

Figure A.8.5: CPT 6

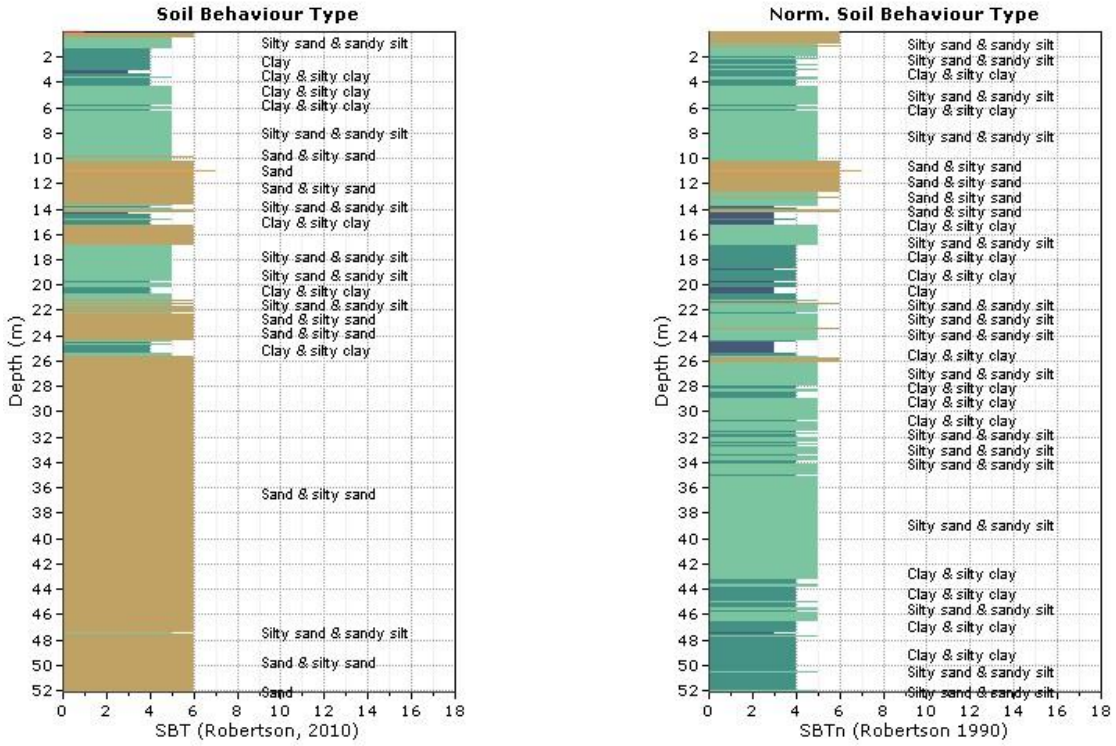

Figure A.8.6: CPT 7

A.8.1 Determination of SBT at settlement gauge V2 at open cast mine Zukunft West

Table A.8.1: Input parameters for CPT evaluation with the software CPET-IT version 1.7.6.42

Average interval	3
Ground elevation	0
Ground water table	46 m below surface
Probe radius	0.0219 m
Cone area ratio	0.80
OCR	1.0
Unit weight of water	10 kN/m^3
Unit weight (of soil)	15.6 kN/m^3

A.9 Parameters for determination of relative density from CPT after CUDMANI (2001)

Table A.9.1: Constants a_i and b_i for determination of the spherical limit pressure

	a_1	a_2	a_3	b_1	b_2	b_3
MS	6.739	-3.749	-1.963	0.9867	0.2118	-1.761
FS	4.946	-5.267	-2.382	0.992	0.229	-2.023
SU	1.713	-8.963	-0.9	0.9715	0.4396	-1.843

Table A.9.2: Hypoplastic constitutive parameters for the three Garzweiler sands MS, FS and SU

	φ_c[°]	e_{i0}	e_{d0}	e_{c0}	h_s[MPa]	n	α	β
MS	30	1.310	0.630	1.09	380	0.22	0.30	2.08
FS	32	1.370	0.770	1.140	900	0.18	0.30	2.12
SU	32.5	1.383	0.755	1.153	30	0.5	0.25	1.56

Table A.9.3: Parameters for determination of β for the three Garzweiler sands MS, FS and SU

	E_{s1} [MPa]	E_{s2} [MPa]	e_1	e_2	K_{01} loose[5]	K_{02} dense	K_0 (JAKY,1948)
MS	15.25	36.36	0.770	0.590	0.53 (0 – 500 kPa)	0.50 (0 – 500 kPa)	0.50
FS	13.25	29.62	0.862	0.689	0.49 (0 – 500 kPa)	0.37 (0 – 500 kPa)	0.47
SU	11.07	25.31	0.821	0.663	0.42 (0 – 500 kPa)	0.38 (0 – 500 kPa)	0.46

[5] The K_0-values were determined with a soft oedometer equipped with strain gauges.

A.10 Measurement results of long-term surface settlement measurements on transmission towers

110 kV power line, tower 1

settlement measurements

Nr.	date of measurement	reference point number	reference point m.a.s.l.	NT 1 m.a.s.l.	NT 1 delta last measurement [mm]	NT 1 delta initial measurement [mm]	NT 2 m.a.s.l.	NT 2 delta last measurement [mm]	NT 2 delta initial measurement [mm]	NT 3 m.a.s.l.	NT 3 delta last measurement [mm]	NT 3 delta initial measurement [mm]	NT 4 m.a.s.l.	NT 4 delta last measurement [mm]	NT 4 delta initial measurement [mm]	remarks
1	08.09.2005	300/85	66.668	62.135			62.137			62.113			62.113			m.a.s.l. (+38 mm)
2	22.09.2006	300/85	66.658	62.089	-46	-46	62.128	-9	-9	62.105	-8	-8	62.105	-8	-8	m.a.s.l. (+38 mm)
3	21.09.2007	300/85	66.655	62.122	33	-13	62.124	-4	-13	62.102	-3	-11	62.102	-3	-11	m.a.s.l. (+38 mm)
4	23.09.2008	300/85	66.651	62.120	-2	-15	62.121	-3	-16	62.098	-4	-15	62.098	-4	-15	m.a.s.l.
5	09.09.2009	300/85	66.648	62.114	-6	-21	62.116	-5	-21	62.093	-5	-20	62.093	-5	-20	m.a.s.l.
6	02.09.2010	300/85	66.649	62.115	1	-20	62.117	1	-20	62.094	1	-19	62.094	1	-19	m.a.s.l.
7	12.12.2012	300/85	66.627	62.092	-23	-43	62.094	-23	-43	62.071	-23	-42	62.071	-23	-42	m.a.s.l.

110 kV power line, tower 2

settlement measurements

Nr.	date of measurement	reference point number	reference point m.a.s.l.	NT 1 m.a.s.l.	NT 1 delta last measurement [mm]	NT 1 delta initial measurement [mm]	NT 2 m.a.s.l.	NT 2 delta last measurement [mm]	NT 2 delta initial measurement [mm]	NT 3 m.a.s.l.	NT 3 delta last measurement [mm]	NT 3 delta initial measurement [mm]	NT 4 m.a.s.l.	NT 4 delta last measurement [mm]	NT 4 delta initial measurement [mm]	remarks
1	08.09.2005	300/85	66.668	62.261			62.288			62.285			62.292			m.a.s.l. (+38 mm)
2	22.09.2006	300/85	66.658	62.251	-10	-10	62.277	-11	-11	62.274	-11	-11	62.282	-10	-10	m.a.s.l. (+38 mm)
3	21.09.2007	300/85	66.655	62.245	-6	-16	62.271	-6	-17	62.268	-6	-17	62.277	-5	-15	m.a.s.l. (+38 mm)
4	23.09.2008	300/85	66.651	62.281	36	20	62.267	-4	-21	62.264	-4	-21	62.272	-5	-20	m.a.s.l.
5	09.09.2009	300/85	66.648	62.278	-3	17	62.265	-2	-23	62.260	-4	-25	62.270	-2	-22	m.a.s.l.
6	02.09.2010	300/85	66.649	62.280	2	19	62.267	2	-21	62.262	2	-23	62.272	2	-20	m.a.s.l.
7	12.12.2012	300/85	66.627	62.255	-25	-6	62.242	-25	-46	62.236	-26	-49	62.247	-25	-45	m.a.s.l.

110 kV power line, tower 3

settlement measurements

Nr.	date of measurement	reference point number	reference point m.a.s.l.	NT 1 m.a.s.l.	NT 1 delta last measurement [mm]	NT 1 delta initial measurement [mm]	NT 2 m.a.s.l.	NT 2 delta last measurement [mm]	NT 2 delta initial measurement [mm]	NT 3 m.a.s.l.	NT 3 delta last measurement [mm]	NT 3 delta initial measurement [mm]	NT 4 m.a.s.l.	NT 4 delta last measurement [mm]	NT 4 delta initial measurement [mm]	remarks
1	08.09.2005	300/85	66.668	64.239			64.268			64.283			64.271			m.a.s.l. (+38 mm)
2	22.09.2006	300/85	66.658	64.231	-8	-8	64.26	-8	-8	64.274	-9	-9	64.262	-9	-9	m.a.s.l. (+38 mm)
3	21.09.2007	300/85	66.655	64.227	-4	-12	64.255	-5	-13	64.268	-6	-15	64.256	-6	-15	m.a.s.l. (+38 mm)
4	23.09.2008	300/85	66.651	64.221	-6	-18	64.251	-4	-17	64.265	-3	-18	64.253	-3	-18	m.a.s.l.
5	09.09.2009	300/85	66.648	64.220	-1	-19	64.248	-3	-20	64.263	-2	-20	64.250	-3	-21	m.a.s.l.
6	02.09.2010	300/85	66.649	64.223	3	-16	64.252	4	-16	64.266	3	-17	64.254	4	-17	m.a.s.l.
7	12.12.2012	300/85	66.627	64.196	-27	-43	64.226	-26	-42	64.240	-26	-43	64.227	-27	-44	m.a.s.l.

110 kV power line, tower 4

settlement measurements

		reference point		NT 1			NT 2			NT 3			NT 4			
Nr.	date of measurement	number	m.a.s.l.	m.a.s.l.	delta last measurement [mm]	delta initial measurement [mm]	m.a.s.l.	delta last measurement [mm]	delta initial measurement [mm]	m.a.s.l.	delta last measurement [mm]	delta initial measurement [mm]	m.a.s.l.	delta last measurement [mm]	delta initial measurement [mm]	remarks
1	08.09.2005	300/85	66.668	74.943			74.935			74.947			74.934			**m.a.s.l. (+38 mm)**
2	22.09.2006	300/85	66.658	74.938	-5	-5	74.93	-5	-5	74.942	-5	-5	74.928	-6	-6	**m.a.s.l. (+38 mm)**
3	21.09.2007	300/85	66.655	74.935	-3	-8	74.927	-3	-8	74.938	-4	-9	74.924	-4	-10	**m.a.s.l. (+38 mm)**
4	23.09.2008	300/85	66.651	74.930	-5	-13	74.922	-5	-13	74.933	-5	-14	74.920	-4	-14	**m.a.s.l.**
5	09.09.2009	300/85	66.648	74.929	-1	-14	74.920	-2	-15	74.933	0	-14	74.919	-1	-15	**m.a.s.l.**
6	02.09.2010	300/85	66.649	74.930	1	-13	74.922	2	-13	74.934	1	-13	74.920	1	-14	**m.a.s.l.**
7	12.12.2012	300/85	66.627	74.912	-18	-31	74.903	-19	-32	74.915	-19	-32	74.902	-18	-32	**m.a.s.l.**

110 kV power line, tower 5

settlement measurements

		reference point		NT 1			NT 2			NT 3			NT 4			
Nr.	date of measurement	number	m.a.s.l.	m.a.s.l.	delta last measurement [mm]	delta initial measurement [mm]	m.a.s.l.	delta last measurement [mm]	delta initial measurement [mm]	m.a.s.l.	delta last measurement [mm]	delta initial measurement [mm]	m.a.s.l.	delta last measurement [mm]	delta initial measurement [mm]	remarks
1	08.09.2005	300/85	66.668	84.591			84.578			84.592			84.591			**m.a.s.l. (+38 mm)**
2	22.09.2006	300/85	66.658	84.584	-7	-7	84.57	-8	-8	84.584	-8	-8	84.584	-7	-7	**m.a.s.l. (+38 mm)**
3	21.09.2007	300/85	66.655	84.579	-5	-12	84.565	-5	-13	84.579	-5	-13	84.58	-4	-11	**m.a.s.l. (+38 mm)**
4	23.09.2008	300/85	66.651	84.571	-8	-20	84.558	-7	-20	84.574	-5	-18	84.573	-7	-18	**m.a.s.l.**
5	09.09.2009	300/85	66.648	84.568	-3	-23	84.555	-3	-23	84.570	-4	-22	84.569	-4	-22	**m.a.s.l.**
6	02.09.2010	300/85	66.649	84.570	2	-21	84.557	2	-21	84.572	2	-20	84.572	3	-19	**m.a.s.l.**
7	12.12.2012	300/85	66.627	84.555	-15	-36	84.541	-16	-37	84.557	-15	-35	84.556	-16	-35	**m.a.s.l.**

110 kV power line, tower 6

settlement measurements

		reference point		NT 1			NT 2			NT 3			NT 4			
Nr.	date of measurement	number	m.a.s.l.	m.a.s.l.	delta last measurement [mm]	delta initial measurement [mm]	m.a.s.l.	delta last measurement [mm]	delta initial measurement [mm]	m.a.s.l.	delta last measurement [mm]	delta initial measurement [mm]	m.a.s.l.	delta last measurement [mm]	delta initial measurement [mm]	remarks
1	08.09.2005	300/85	66.668	87.146			87.154			87.154			87.153			**m.a.s.l. (+38 mm)**
2	22.09.2006	300/85	66.658	87.135	-11	-11	87.144	-10	-10	87.144	-10	-10	87.143	-10	-10	**m.a.s.l. (+38 mm)**
3	21.09.2007	300/85	66.655	87.133	-2	-13	87.142	-2	-12	87.143	-1	-11	87.141	-2	-12	**m.a.s.l. (+38 mm)**
4	23.09.2008	300/85	66.651	87.126	-7	-20	87.134	-8	-20	87.135	-8	-19	87.133	-8	-20	**m.a.s.l.**
5	09.09.2009	300/85	66.648	87.120	-6	-26	87.128	-6	-26	87.129	-6	-25	87.128	-5	-25	**m.a.s.l.**
6	02.09.2010	300/85	66.649	87.122	2	-24	87.131	3	-23	87.131	2	-23	87.130	2	-23	**m.a.s.l.**
7	12.12.2012	300/85	66.627	87.108	-14	-38	87.116	-15	-38	87.117	-14	-37	87.116	-14	-37	**m.a.s.l.**

110 kV power line, tower 7

settlement measurements

		reference point		NT 1			NT 2			NT 3			NT 4			
Nr.	date of measurement	number	m.a.s.l.	m.a.s.l.	delta last measurement [mm]	delta initial measurement [mm]	m.a.s.l.	delta last measurement [mm]	delta initial measurement [mm]	m.a.s.l.	delta last measurement [mm]	delta initial measurement [mm]	m.a.s.l.	delta last measurement [mm]	delta initial measurement [mm]	remarks
1	08.09.2005	300/85	66.668	90.230			90.269			90.234			90.244			**m.a.s.l. (+38 mm)**
2	22.09.2006	300/85	66.658	90.219	-11	-11	90.259	-10	-10	90.223	-11	-11	90.234	-10	-10	**m.a.s.l. (+38 mm)**
3	21.09.2007	300/85	66.655	90.219	0	-11	90.259	0	-10	90.224	1	-10	90.235	1	-9	**m.a.s.l. (+38 mm)**
4	23.09.2008	300/85	66.651	90.212	-7	-18	90.252	-7	-17	90.216	-8	-18	90.227	-8	-17	**m.a.s.l.**
5	09.09.2009	300/85	66.648	90.207	-5	-23	90.246	-6	-23	90.210	-6	-24	90.221	-6	-23	**m.a.s.l.**
6	02.09.2010	300/85	66.649	90.210	3	-20	90.249	3	-20	90.213	3	-21	90.224	3	-20	**m.a.s.l.**
7	12.12.2012	300/85	66.627	90.197	-13	-33	90.236	-13	-33	90.199	-14	-35	90.211	-13	-33	**m.a.s.l.**

110 kV power line, tower 8

settlement measurements

		reference point		NT 1			NT 2			NT 3			NT 4			
Nr.	date of measurement	number	m.a.s.l.	m.a.s.l.	delta last measurement [mm]	delta initial measurement [mm]	m.a.s.l.	delta last measurement [mm]	delta initial measurement [mm]	m.a.s.l.	delta last measurement [mm]	delta initial measurement [mm]	m.a.s.l.	delta last measurement [mm]	delta initial measurement [mm]	remarks
1	08.09.2005	300/85	66.668	89.626			89.621			89.612			89.622			**m.a.s.l. (+38 mm)**
2	22.09.2006	300/85	66.658	89.618	-8	-8	89.613	-8	-8	89.603	-9	-9	89.614	-8	-8	**m.a.s.l. (+38 mm)**
3	21.09.2007	300/85	66.655	89.617	-1	-9	89.612	-1	-9	89.601	-2	-11	89.611	-3	-11	**m.a.s.l. (+38 mm)**
4	23.09.2008	300/85	66.651	89.608	-9	-18	89.602	-10	-19	89.591	-10	-21	89.602	-9	-20	**m.a.s.l.**
5	09.09.2009	300/85	66.648	89.600	-8	-26	89.595	-7	-26	89.585	-6	-27	89.595	-7	-27	**m.a.s.l.**
6	02.09.2010	300/85	66.649	89.606	6	-20	89.600	5	-21	89.589	4	-23	89.600	5	-22	**m.a.s.l.**
7	12.12.2012	300/85	66.627	89.591	-15	-35	89.585	-15	-36	89.573	-16	-39	89.585	-15	-37	**m.a.s.l.**

110 kV power line, tower 9

settlement measurements

		reference point		NT 1			NT 2			NT 3			NT 4			
Nr.	date of measurement	number	m.a.s.l.	m.a.s.l.	delta last measurement [mm]	delta initial measurement [mm]	m.a.s.l.	delta last measurement [mm]	delta initial measurement [mm]	m.a.s.l.	delta last measurement [mm]	delta initial measurement [mm]	m.a.s.l.	delta last measurement [mm]	delta initial measurement [mm]	remarks
1	08.09.2005	300/85	66.668	89.854			89.847			89.852			89.872			**m.a.s.l. (+38 mm)**
2	22.09.2006	300/85	66.658	89.848	-6	-6	89.842	-5	-5	89.846	-6	-6	89.866	-6	-6	**m.a.s.l. (+38 mm)**
3	21.09.2007	300/85	66.655	89.847	-1	-7	89.84	-2	-7	89.846	0	-6	89.866	0	-6	**m.a.s.l. (+38 mm)**
4	23.09.2008	300/85	66.651	89.839	-8	-15	89.832	-8	-15	89.835	-11	-17	89.857	-9	-15	**m.a.s.l.**
5	09.09.2009	300/85	66.648	89.833	-6	-21	89.827	-5	-20	89.831	-4	-21	89.851	-6	-21	**m.a.s.l.**
6	02.09.2010	300/85	66.649	89.837	4	-17	89.831	4	-16	89.835	4	-17	89.856	5	-16	**m.a.s.l.**
7	12.12.2012	300/85	66.627	89.822	-15	-32	89.815	-16	-32	89.819	-16	-33	89.839	-17	-33	**m.a.s.l.**

110 kV power line, tower 10

settlement measurements

Nr.	date of measurement	reference point number	reference point m.a.s.l.	NT 1 m.a.s.l.	NT 1 delta last measurement [mm]	NT 1 delta initial measurement [mm]	NT 2 m.a.s.l.	NT 2 delta last measurement [mm]	NT 2 delta initial measurement [mm]	NT 3 m.a.s.l.	NT 3 delta last measurement [mm]	NT 3 delta initial measurement [mm]	NT 4 m.a.s.l.	NT 4 delta last measurement [mm]	NT 4 delta initial measurement [mm]	remarks
1	08.09.2005	300/85	66.668	89.029			89.037			89.06			89.068			**m.a.s.l. (+38 mm)**
2	22.09.2006	300/85	66.658	89.015	-14	-14	89.022	-15	-15	89.046	-14	-14	89.055	-13	-13	**m.a.s.l. (+38 mm)**
3	21.09.2007	300/85	66.655	89.008	-7	-21	89.014	-8	-23	89.041	-5	-19	89.051	-4	-17	**m.a.s.l. (+38 mm)**
4	23.09.2008	300/85	66.651	88.995	-13	-34	89.000	-14	-37	89.025	-16	-35	89.036	-15	-32	**m.a.s.l.**
5	09.09.2009	300/85	66.648	88.987	-8	-42	88.992	-8	-45	89.019	-6	-41	89.030	-6	-38	**m.a.s.l.**
6	02.09.2010	300/85	66.649	88.987	0	-42	88.992	0	-45	89.018	-1	-42	89.030	0	-38	**m.a.s.l.**
7	12.12.2012	300/85	66.627	88.965	-22	-64	88.970	-22	-67	88.996	-22	-64	89.008	-22	-60	**m.a.s.l.**
8	15.03.2015	1000	88.964	88.938	-27	-91	88.942	-28	-95	88.970	-26	-90	88.981	-27	-87	Connection statically measured (ETRS89)

110 kV power line, tower 11

settlement measurements

Nr.	date of measurement	reference point number	reference point m.a.s.l.	NT 1 m.a.s.l.	NT 1 delta last measurement [mm]	NT 1 delta initial measurement [mm]	NT 2 m.a.s.l.	NT 2 delta last measurement [mm]	NT 2 delta initial measurement [mm]	NT 3 m.a.s.l.	NT 3 delta last measurement [mm]	NT 3 delta initial measurement [mm]	NT 4 m.a.s.l.	NT 4 delta last measurement [mm]	NT 4 delta initial measurement [mm]	remarks
1	08.09.2005	300/85	66.668	93.443			93.444			93.47			93.452			**m.a.s.l. (+38 mm)**
2	22.09.2006	300/85	66.658	93.422	-21	-21	93.423	-21	-21	93.448	-22	-22	93.43	-22	-22	**m.a.s.l. (+38 mm)**
3	21.09.2007	300/85	66.655	93.412	-10	-31	93.413	-10	-31	93.438	-10	-32	93.42	-10	-32	**m.a.s.l. (+38 mm)**
4	23.09.2008	300/85	66.651	93.391	-21	-52	93.392	-21	-52	93.417	-21	-53	93.398	-22	-54	**m.a.s.l.**
5	09.09.2009	300/85	66.648	93.380	-11	-63	93.381	-11	-63	93.406	-11	-64	93.388	-10	-64	**m.a.s.l.**
6	02.09.2010	300/85	66.649	93.376	-4	-67	93.377	-4	-67	93.401	-5	-69	93.384	-4	-68	**m.a.s.l.**
7	12.12.2012	300/85	66.627	93.350	-26	-93	93.351	-26	-93	93.375	-26	-95	93.358	-26	-94	**m.a.s.l.**
8	15.03.2015	1000	88.964	93.319	-31	-124	93.321	-30	-123	93.345	-30	-125	93.327	-31	-125	Connection statically measured (ETRS89)

110 kV power line, tower 12

settlement measurements

Nr.	date of measurement	reference point number	reference point m.a.s.l.	NT 1 m.a.s.l.	NT 1 delta last measurement [mm]	NT 1 delta initial measurement [mm]	NT 2 m.a.s.l.	NT 2 delta last measurement [mm]	NT 2 delta initial measurement [mm]	NT 3 m.a.s.l.	NT 3 delta last measurement [mm]	NT 3 delta initial measurement [mm]	NT 4 m.a.s.l.	NT 4 delta last measurement [mm]	NT 4 delta initial measurement [mm]	remarks
1	08.09.2005	300/85	66.668	95.173			95.17			95.177			95.165			**m.a.s.l. (+38 mm)**
2	22.09.2006	300/85	66.658	95.145	-28	-28	95.143	-27	-27	95.149	-28	-28	95.137	-28	-28	**m.a.s.l. (+38 mm)**
3	21.09.2007	300/85	66.655	95.135	-10	-38	95.133	-10	-37	95.138	-11	-39	95.125	-12	-40	**m.a.s.l. (+38 mm)**
4	23.09.2008	300/85	66.651	95.111	-24	-62	95.108	-25	-62	95.115	-23	-62	95.102	-23	-63	**m.a.s.l.**
5	09.09.2009	300/85	66.648	95.100	-11	-73	95.098	-10	-72	95.104	-11	-73	95.091	-11	-74	**m.a.s.l.**
6	02.09.2010	300/85	66.649	95.095	-5	-78	95.093	-5	-77	95.098	-6	-79	95.087	-4	-78	**m.a.s.l.**
7	12.12.2012	300/85	66.627	95.072	-23	-101	95.070	-23	-100	95.076	-22	-101	95.063	-24	-102	**m.a.s.l.**
8	15.03.2015	1000	88.964	95.045	-27	-128	95.043	-27	-127	95.048	-28	-129	95.035	-28	-130	Connection statically measured (ETRS89)

110 kV power line, tower 13

settlement measurements

Nr.	date of measurement	reference point number	reference point m.a.s.l.	NT 1 m.a.s.l.	NT 1 delta last measurement [mm]	NT 1 delta initial measurement [mm]	NT 2 m.a.s.l.	NT 2 delta last measurement [mm]	NT 2 delta initial measurement [mm]	NT 3 m.a.s.l.	NT 3 delta last measurement [mm]	NT 3 delta initial measurement [mm]	NT 4 m.a.s.l.	NT 4 delta last measurement [mm]	NT 4 delta initial measurement [mm]	remarks
1	08.09.2005	300/85	66.668	96.356			96.361			96.354			96.346			**m.a.s.l. (+38 mm)**
2	22.09.2006	300/85	66.658	96.316	-40	-40	96.321	-40	-40	96.314	-40	-40	96.306	-40	-40	**m.a.s.l. (+38 mm)**
3	21.09.2007	300/85	66.655	96.302	-14	-54	96.306	-15	-55	96.3	-14	-54	96.293	-13	-53	**m.a.s.l. (+38 mm)**
4	23.09.2008	300/85	66.651	96.278	-24	-78	96.281	-25	-80	96.274	-26	-80	96.267	-26	-79	**m.a.s.l.**
5	09.09.2009	300/85	66.648	96.268	-10	-88	96.271	-10	-90	96.265	-9	-89	96.257	-10	-89	**m.a.s.l.**
6	02.09.2010	300/85	66.649	96.260	-8	-96	96.263	-8	-98	96.256	-9	-98	96.250	-7	-96	**m.a.s.l.**
7	12.12.2012	300/85	66.627	96.233	-27	-123	96.236	-27	-125	96.229	-27	-125	96.222	-28	-124	**m.a.s.l.**
8	17.12.2014	GF1412_735	96.235	96.205	-28	-151	96.207	-29	-154	96.201	-28	-153	96.194	-28	-152	Connection statically measured (ETRS89)
9	15.03.2015	1000	88.964	96.203	-2	-153	96.205	-2	-156	96.198	-3	-156	96.192	-2	-154	Connection statically measured (ETRS89)

110 kV power line, tower 14

settlement measurements

Nr.	date of measurement	reference point number	reference point m.a.s.l.	NT 1 m.a.s.l.	NT 1 delta last measurement [mm]	NT 1 delta initial measurement [mm]	NT 2 m.a.s.l.	NT 2 delta last measurement [mm]	NT 2 delta initial measurement [mm]	NT 3 m.a.s.l.	NT 3 delta last measurement [mm]	NT 3 delta initial measurement [mm]	NT 4 m.a.s.l.	NT 4 delta last measurement [mm]	NT 4 delta initial measurement [mm]	remarks
1	08.09.2005	300/85	66.668	96.740			96.741			96.733			96.742			**m.a.s.l. (+38 mm)**
2	22.09.2006	300/85	66.658	96.684	-56	-56	96.685	-56	-56	96.676	-57	-57	96.685	-57	-57	**m.a.s.l. (+38 mm)**
3	21.09.2007	300/85	66.655	96.662	-22	-78	96.663	-22	-78	96.656	-20	-77	96.665	-20	-77	**m.a.s.l. (+38 mm)**
4	23.09.2008	300/85	66.651	96.632	-30	-108	96.633	-30	-108	96.626	-30	-107	96.634	-31	-108	**m.a.s.l.**
5	09.09.2009	300/85	66.648	96.619	-13	-121	96.621	-12	-120	96.613	-13	-120	96.621	-13	-121	**m.a.s.l.**
6	02.09.2010	300/85	66.649	96.606	-13	-134	96.607	-14	-134	96.599	-14	-134	96.608	-13	-134	**m.a.s.l.**
7	12.12.2012	300/85	66.627	96.571	-35	-169	96.572	-35	-169	96.564	-35	-169	96.573	-35	-169	**m.a.s.l.**
8	14.12.2014	GF1412_735	96.235	96.523	-48	-217	96.527	-45	-214	96.522	-42	-211	96.529	-44	-213	Connection statically measured (ETRS89)
9	15.03.2015	1000	88.964	96.520	-3	-220	96.524	-3	-217	96.520	-2	-213	96.527	-2	-215	Connection statically measured (ETRS89)

110 kV power line, tower 15

settlement measurements

Nr.	date of measurement	reference point number	reference point m.a.s.l.	NT 1 m.a.s.l.	NT 1 delta last measurement [mm]	NT 1 delta initial measurement [mm]	NT 2 m.a.s.l.	NT 2 delta last measurement [mm]	NT 2 delta initial measurement [mm]	NT 3 m.a.s.l.	NT 3 delta last measurement [mm]	NT 3 delta initial measurement [mm]	NT 4 m.a.s.l.	NT 4 delta last measurement [mm]	NT 4 delta initial measurement [mm]	remarks
1	08.09.2005	300/85	66.668	95.874			95.869			95.868			95.861			**m.a.s.l. (+38 mm)**
2	22.09.2006	300/85	66.658	95.812	-62	-62	95.806	-63	-63	95.806	-62	-62	95.799	-62	-62	**m.a.s.l. (+38 mm)**
3	21.09.2007	300/85	66.655	95.790	-22	-84	95.785	-21	-84	95.786	-20	-82	95.779	-20	-82	**m.a.s.l. (+38 mm)**
4	23.09.2008	300/85	66.651	95.760	-30	-114	95.755	-30	-114	95.755	-31	-113	95.747	-32	-114	**m.a.s.l.**
5	09.09.2009	300/85	66.648	95.749	-11	-125	95.744	-11	-125	95.745	-10	-123	95.737	-10	-124	**m.a.s.l.**
6	02.09.2010	300/85	66.649	95.734	-15	-140	95.730	-14	-139	95.730	-15	-138	95.723	-14	-138	**m.a.s.l.**
7	12.12.2012	300/85	66.627	95.699	-35	-175	95.695	-35	-174	95.696	-34	-172	95.688	-35	-173	**m.a.s.l.**
8	15.03.2015	1000	88.964	95.668	-31	-206	95.665	-30	-204	95.666	-30	-202	95.657	-31	-204	Connection statically measured (ETRS89)

110 kV power line, tower 16

settlement measurements

Nr.	date of measurement	reference point number	reference point m.a.s.l.	NT 1 m.a.s.l.	NT 1 delta last measurement [mm]	NT 1 delta initial measurement [mm]	NT 2 m.a.s.l.	NT 2 delta last measurement [mm]	NT 2 delta initial measurement [mm]	NT 3 m.a.s.l.	NT 3 delta last measurement [mm]	NT 3 delta initial measurement [mm]	NT 4 m.a.s.l.	NT 4 delta last measurement [mm]	NT 4 delta initial measurement [mm]	remarks
1	08.09.2005	300/85	66.668	94.619			94.631			94.607			94.638			**m.a.s.l. (+38 mm)**
2	22.09.2006	300/85	66.658	94.551	-68	-68	94.564	-67	-67	94.537	-70	-70	94.568	-70	-70	**m.a.s.l. (+38 mm)**
3	21.09.2007	300/85	66.655	94.527	-24	-92	94.539	-25	-92	94.51	-27	-97	94.541	-27	-97	**m.a.s.l. (+38 mm)**
4	23.09.2008	300/85	66.651	94.491	-36	-128	94.504	-35	-127	94.474	-36	-133	94.505	-36	-133	**m.a.s.l.**
5	09.09.2009	300/85	66.648	94.478	-13	-141	94.490	-14	-141	94.459	-15	-148	94.490	-15	-148	**m.a.s.l.**
6	02.09.2010	300/85	66.649	94.459	-19	-160	94.472	-18	-159	94.438	-21	-169	94.470	-20	-168	**m.a.s.l.**
7	12.12.2012	300/85	66.627	94.419	-40	-200	94.431	-41	-200	94.395	-43	-212	94.427	-43	-211	**m.a.s.l.**
8	15.03.2015	1000	88.964	94.388	-31	-231	94.400	-31	-231	94.362	-33	-245	94.393	-34	-245	Connection statically measured (ETRS89)

110 kV power line, tower 17

settlement measurements

Nr.	date of measurement	reference point number	reference point m.a.s.l.	NT 1 m.a.s.l.	NT 1 delta last measurement [mm]	NT 1 delta initial measurement [mm]	NT 2 m.a.s.l.	NT 2 delta last measurement [mm]	NT 2 delta initial measurement [mm]	NT 3 m.a.s.l.	NT 3 delta last measurement [mm]	NT 3 delta initial measurement [mm]	NT 4 m.a.s.l.	NT 4 delta last measurement [mm]	NT 4 delta initial measurement [mm]	remarks
1	08.09.2005	300/85	66.668	93.359			93.356			93.34			93.35			**m.a.s.l. (+38 mm)**
2	22.09.2006	300/85	66.658	93.290	-69	-69	93.287	-69	-69	93.27	-70	-70	93.279	-71	-71	**m.a.s.l. (+38 mm)**
3	21.09.2007	300/85	66.655	93.264	-26	-95	93.26	-27	-96	93.242	-28	-98	93.251	-28	-99	**m.a.s.l. (+38 mm)**
4	23.09.2008	300/85	66.651	93.227	-37	-132	93.223	-37	-133	93.207	-35	-133	93.215	-36	-135	**m.a.s.l.**
5	09.09.2009	300/85	66.648	93.211	-16	-148	93.207	-16	-149	93.191	-16	-149	93.200	-15	-150	**m.a.s.l.**
6	02.09.2010	300/85	66.649	93.186	-25	-173	93.183	-24	-173	93.165	-26	-175	93.175	-25	-175	**m.a.s.l.**
7	12.12.2012	300/85	66.627	93.141	-45	-218	93.137	-46	-219	93.120	-45	-220	93.129	-46	-221	**m.a.s.l.**
8	15.03.2015	1000	88.964	93.109	-32	-250	93.106	-31	-250	93.089	-31	-251	93.098	-31	-252	Connection statically measured (ETRS89)

110 kV power line, tower 18

settlement measurements

Nr.	date of measurement	reference point number	reference point m.a.s.l.	NT 1 m.a.s.l.	NT 1 delta last measurement [mm]	NT 1 delta initial measurement [mm]	NT 2 m.a.s.l.	NT 2 delta last measurement [mm]	NT 2 delta initial measurement [mm]	NT 3 m.a.s.l.	NT 3 delta last measurement [mm]	NT 3 delta initial measurement [mm]	NT 4 m.a.s.l.	NT 4 delta last measurement [mm]	NT 4 delta initial measurement [mm]	remarks
1	08.09.2005	300/85	66.668	92.382			92.384			92.372			92.372			**m.a.s.l. (+38 mm)**
2	22.09.2006	300/85	66.658	92.313	-69	-69	92.314	-70	-70	92.3	-72	-72	92.301	-71	-71	**m.a.s.l. (+38 mm)**
3	21.09.2007	300/85	66.655	92.286	-27	-96	92.287	-27	-97	92.271	-29	-101	92.272	-29	-100	**m.a.s.l. (+38 mm)**
4	23.09.2008	300/85	66.651	92.247	-39	-135	92.248	-39	-136	92.232	-39	-140	92.235	-37	-137	**m.a.s.l.**
5	09.09.2009	300/85	66.648	92.230	-17	-152	92.230	-18	-154	92.216	-16	-156	92.217	-18	-155	**m.a.s.l.**
6	02.09.2010	300/85	66.649	92.186	-44	-196	92.184	-46	-200	92.175	-41	-197	92.178	-39	-194	**m.a.s.l.**
7	12.12.2012	300/85	66.627	92.112	-74	-270	92.107	-77	-277	92.107	-68	-265	92.114	-64	-258	**m.a.s.l.**
8	15.03.2015	1000	88.964	92.063	-49	-319	92.053	-54	-331	92.056	-51	-316	92.068	-46	-304	Connection statically measured (ETRS89)

110 kV power line, tower 19

settlement measurements

Nr.	date of measurement	reference point number	reference point m.a.s.l.	NT 1 m.a.s.l.	NT 1 delta last measurement [mm]	NT 1 delta initial measurement [mm]	NT 2 m.a.s.l.	NT 2 delta last measurement [mm]	NT 2 delta initial measurement [mm]	NT 3 m.a.s.l.	NT 3 delta last measurement [mm]	NT 3 delta initial measurement [mm]	NT 4 m.a.s.l.	NT 4 delta last measurement [mm]	NT 4 delta initial measurement [mm]	remarks
1	08.09.2005	300/85	66.668	89.878			89.872			89.852			89.867			**m.a.s.l. (+38 mm)**
2	22.09.2006	300/85	66.658	89.812	-66	-66	89.806	-66	-66	89.785	-67	-67	89.799	-68	-68	**m.a.s.l. (+38 mm)**
3	21.09.2007	300/85	66.655	89.785	-27	-93	89.78	-26	-92	89.757	-28	-95	89.771	-28	-96	**m.a.s.l. (+38 mm)**
4	23.09.2008	300/85	66.651	89.747	-38	-131	89.741	-39	-131	89.722	-35	-130	89.734	-37	-133	**m.a.s.l.**
5	09.09.2009	300/85	66.648	89.725	-22	-153	89.721	-20	-151	89.701	-21	-151	89.714	-20	-153	**m.a.s.l.**
6	02.09.2010	300/85	66.649	89.696	-29	-182	89.692	-29	-180	89.672	-29	-180	89.685	-29	-182	**m.a.s.l.**
7	12.12.2012	300/85	66.627	89.618	-78	-260	89.617	-75	-255	89.607	-65	-245	89.617	-68	-250	**m.a.s.l.**
8	15.03.2015	1000	88.964	89.562	-56	-316	89.561	-56	-311	89.557	-50	-295	89.566	-51	-301	Connection statically measured (ETRS89)

110 kV power line, tower 20

settlement measurements

Nr.	date of measurement	reference point number	reference point m.a.s.l.	NT 1 m.a.s.l.	NT 1 delta last measurement [mm]	NT 1 delta initial measurement [mm]	NT 2 m.a.s.l.	NT 2 delta last measurement [mm]	NT 2 delta initial measurement [mm]	NT 3 m.a.s.l.	NT 3 delta last measurement [mm]	NT 3 delta initial measurement [mm]	NT 4 m.a.s.l.	NT 4 delta last measurement [mm]	NT 4 delta initial measurement [mm]	remarks
1	08.09.2005	300/85	66.668	84.149			84.15			84.153			84.143			**m.a.s.l. (+38 mm)**
2	22.09.2006	300/85	66.658	84.109	-40	-40	84.111	-39	-39	84.114	-39	-39	84.103	-40	-40	**m.a.s.l. (+38 mm)**
3	21.09.2007	300/85	66.655	84.090	-19	-59	84.092	-19	-58	84.095	-19	-58	84.083	-20	-60	**m.a.s.l. (+38 mm)**
4	23.09.2008	300/85	66.651	84.061	-29	-88	84.062	-30	-88	84.068	-27	-85	84.056	-27	-87	**m.a.s.l.**
5	09.09.2009	300/85	66.648	84.029	-32	-120	84.032	-30	-118	84.040	-28	-113	84.028	-28	-115	**m.a.s.l.**
6	02.09.2010	300/85	66.649	83.981	-48	-168	83.983	-49	-167	83.998	-42	-155	83.986	-42	-157	**m.a.s.l.**
7	12.12.2012	300/85	66.627	83.934	-47	-215	83.937	-46	-213	83.954	-44	-199	83.941	-45	-202	**m.a.s.l.**
8	15.03.2015	1000	88.964	83.915	-19	-234	83.918	-19	-232	83.936	-18	-217	83.924	-17	-219	Connection statically measured (ETRS89)

110 kV power line, tower 21

settlement measurements

Nr.	date of measurement	reference point number	reference point m.a.s.l.	NT 1 m.a.s.l.	NT 1 delta last measurement [mm]	NT 1 delta initial measurement [mm]	NT 2 m.a.s.l.	NT 2 delta last measurement [mm]	NT 2 delta initial measurement [mm]	NT 3 m.a.s.l.	NT 3 delta last measurement [mm]	NT 3 delta initial measurement [mm]	NT 4 m.a.s.l.	NT 4 delta last measurement [mm]	NT 4 delta initial measurement [mm]	remarks
1	08.09.2005	300/85	66.668	76.130			76.137			76.132			76.143			**m.a.s.l. (+38 mm)**
2	22.09.2006	300/85	66.658	76.103	-27	-27	76.11	-27	-27	76.105	-27	-27	76.116	-27	-27	**m.a.s.l. (+38 mm)**
3	21.09.2007	300/85	66.655	76.086	-17	-44	76.093	-17	-44	76.086	-19	-46	76.097	-19	-46	**m.a.s.l. (+38 mm)**
4	23.09.2008	300/85	66.651	76.063	-23	-67	76.068	-25	-69	76.064	-22	-68	76.074	-23	-69	**m.a.s.l.**
5	09.09.2009	300/85	66.648	76.049	-14	-81	76.055	-13	-82	76.050	-14	-82	76.061	-13	-82	**m.a.s.l.**
6	02.09.2010	300/85	66.649	76.016	-33	-114	76.024	-31	-113	76.018	-32	-114	76.030	-31	-113	**m.a.s.l.**
7	12.12.2012	300/85	66.627	75.975	-41	-155	75.982	-42	-155	75.978	-40	-154	75.989	-41	-154	**m.a.s.l.**

110 kV power line, tower 22																
settlement measurements																
		reference point		NT 1			NT 2			NT 3			NT 4			
Nr.	date of measurement	number	m.a.s.l.	m.a.s.l.	delta last measurement	delta initial measurement	m.a.s.l.	delta last measurement	delta initial measurement	m.a.s.l.	delta last measurement	delta initial measurement	m.a.s.l.	delta last measurement	delta initial measurement	remarks
					[mm]	[mm]		[mm]	[mm]		[mm]	[mm]		[mm]	[mm]	
1	08.09.2005	300/85	66.668	40.126			40.12			40.12			40.112			**m.a.s.l. (+38 mm)**
2	22.09.2006	300/85	66.658	40.109	-17	-17	40.106	-14	-14	40.105	-15	-15	40.095	-17	-17	**m.a.s.l. (+38 mm)**
3	21.09.2007	300/85	66.655	40.109	0	-17	40.106	0	-14	40.105	0	-15	40.093	-2	-19	**m.a.s.l. (+38 mm)**
4	23.09.2008	300/85	66.651	40.102	-7	-24	40.099	-7	-21	40.100	-5	-20	40.086	-7	-26	**m.a.s.l.**
5	09.09.2009	300/85	66.648	40.084	-18	-42	40.083	-16	-37	40.083	-17	-37	40.070	-16	-42	**m.a.s.l.**
6	02.09.2010	300/85	66.649	40.064	-20	-62	40.063	-20	-57	40.063	-20	-57	40.049	-21	-63	**m.a.s.l.**
7	12.12.2012	300/85	66.627	40.014	-50	-112	40.014	-49	-106	40.014	-49	-106	39.999	-50	-113	**m.a.s.l.**

A.11 Derivation of isotropic reference compression line for visco-hypoplasticity after GUDEHUS (2004)

From GUDEHUS (2004):

$$f_T = \frac{e_{c0}}{e_{d0}} - \left(\frac{e_{c0}}{e_{d0}} - 1\right) \cdot \left(-\frac{\lambda_\sigma}{k_c}\right)^m$$

$$m = \ln\left(\frac{1/e_{d0} - 1/e_{i0}}{1/e_{d0} - 1/e_{c0}}\right) / \ln\left(\frac{1}{9}k_c\right)$$

$$\lambda_\sigma = \frac{2\frac{1+2K^3}{1+2K} - 3(1+2K^2) + (1+2K)^2}{3(1+2K^2) - 3(1+2K)^2}$$

with

$$K = \frac{\sigma'_2}{\sigma'_1}$$

Under isotropic compression follows K = 1.0 and $\lambda_\sigma = -1/9$.

$$f_T = \frac{e_{c0}}{e_{d0}} - \left(\frac{e_{c0}}{e_{d0}} - 1\right) \cdot \left(\frac{1}{9k_c}\right)^{\ln\left(\frac{1/e_{d0} - 1/e_{i0}}{1/e_{d0} - 1/e_{c0}}\right)/\ln\left(\frac{1}{9}k_c\right)}$$

$$= \frac{e_{c0}}{e_{d0}} - \left(\frac{e_{c0}}{e_{d0}} - 1\right) \cdot \left[\left(\frac{1}{9k_c}\right)^{1/\ln\left(\frac{1}{9}k_c\right)}\right]^{\ln\left(\frac{1/e_{d0} - 1/e_{i0}}{1/e_{d0} - 1/e_{c0}}\right)}$$

and with

$$\left(\frac{1}{9k_c}\right)^{1/\ln\left(\frac{1}{9}k_c\right)} = \left(\frac{1}{9k_c}\right)^{1/\frac{log_{\frac{1}{9k_c}}\left(\frac{1}{9k_c}\right)}{log_{\frac{1}{9k_c}}(\exp(1))}} = \left(\frac{1}{9k_c}\right)^{log_{\frac{1}{9k_c}}(\exp(1))} = \exp(1)$$

follows

$$f_T = \frac{e_{c0}}{e_{d0}} - \left(\frac{e_{c0}}{e_{d0}} - 1\right) \cdot exp\left(\ln\left(\frac{\frac{1}{e_{d0}} - \frac{1}{e_{i0}}}{\frac{1}{e_{d0}} - \frac{1}{e_{c0}}}\right)\right) = \frac{e_{c0}}{e_{d0}} - \left(\frac{e_{c0}}{e_{d0}} - 1\right) \cdot \frac{\frac{1}{e_{d0}} - \frac{1}{e_{i0}}}{\frac{1}{e_{d0}} - \frac{1}{e_{c0}}} = \frac{e_{c0}}{e_{i0}}$$

A.12 Finite-Element-Modelling of the time-dependent deformations of the Garzweiler open cast mining dump using the Soft Soil Creep model after VERMEER & NEHER (1999)

Table A.12.1: Constitutive model parameters for SSC for simulation of the dump at transmission tower 13 and 14

Parameter combination			Tower 13	Tower 14
Constitutive model			Soft soil creep	
Unit weight	γ	[kN/m³]	17	
Compression index	λ^*		0.03	
Swelling index	κ^*		0.006	
Creep-coefficient	μ^*		0.00072	0.00095
Cohesion	c'	[kPa]	5	
Angle of repose	φ'	[°]	30	
Dilatancy angle	ψ	[°]	0	
Earth pressure at rest	K_0^{NC}		0.5	
POISSON's ratio	ν_{ur}		0.15	
Overconsolidation ratio	OCR		1	
Preconsolidation stress	POP	[kPa]	0	

Table A.12.2: Constitutive model parameter for SSC for simulation of settlement gauges HSP-LS1 and 511/10

Constitutive model			Soft soil creep
Unit weight	γ	[kN/m³]	17
Compression index	λ^*		0.0275
Swelling index	κ^*		0.006
Creep-coefficient	μ^*		0.001
Cohesion	c'	[kPa]	5
Angle of repose	φ'	[°]	30
Dilatancy angle	ψ	[°]	0
Earth pressure at rest	K_0^{NC}		0.5
POISSON's ratio	ν_{ur}		0.15
Overconsolidation ratio	OCR		1
Preconsolidation stress	POP	[kPa]	0

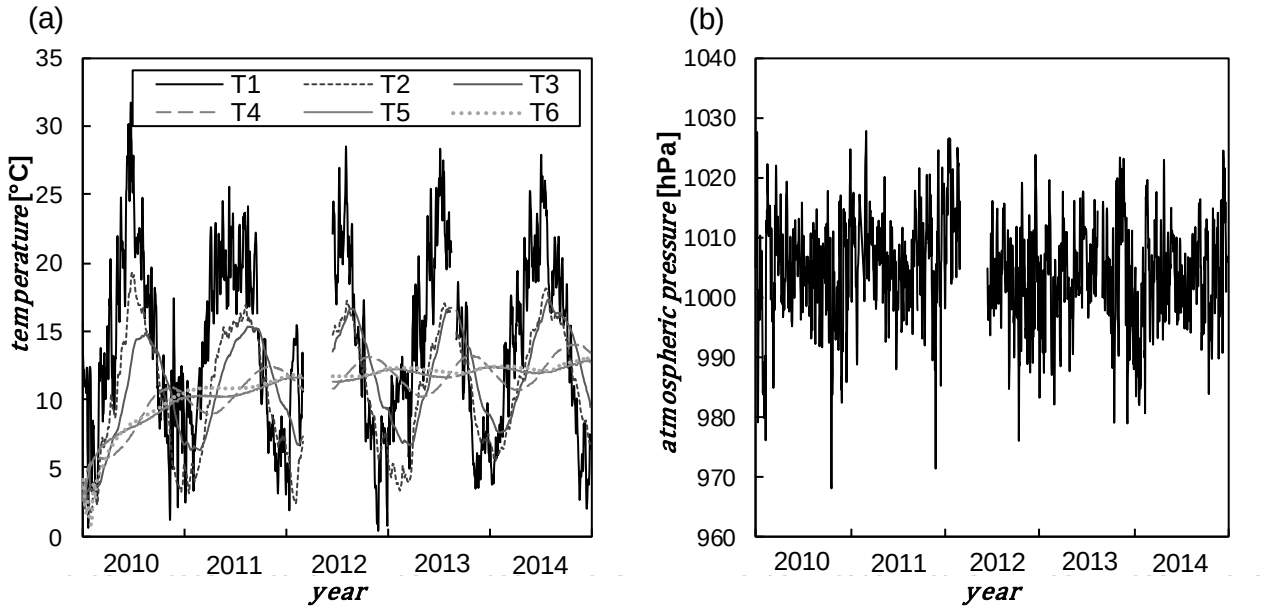

Figure A.12.1: (a) Temperature recordings of the sensor in the measuring field (cf. Figure 6.23) and (b) atmospheric pressure recordings during the observation time of HSP-LS1 and 511/10

A.12.1 Installation of the hydrostatic measuring line in the Garzweiler open cast mining dump

Figure A.12.2: Installation process of the hydrostatic measurement line, printed with permission from RWE Power AG

Figure A.12.3: Dumping above hydrostatic measuring line and measurement gauge HSP-LS1, printed with permission from RWE Power AG